RESUMEN

GOMEZ ALBA, SEBASTIAN ALEJANDRO. Estimación de imágenes de anomalías de velocidad, dispersores y campo de esfuerzos locales a partir del análisis de sismicidad generada en yacimientos de hidrocarburos en Colombia. (Bajo la dirección de PhD Carlos Alberto Vargas Jiménez).

La información producto del monitoreo sismológico de campos de hidrocarburos se ha convertido en una herramienta y fuente de información importante para determinar bajo qué circunstancias las operaciones de explotación de campos de hidrocarburos inciden en la alteración del estado natural de los parámetros elásticos de las rocas y el flujo de fluidos al interior de los yacimientos. En Colombia no ha existido una política que demande el monitoreo sismológico de campos de hidrocarburos, y el poco que ha podido ser realizado aún no ha sido ni procesado ni analizado en su totalidad. En este contexto hay un rezago respecto a la adquisición de data, análisis y apropiación de conocimiento sobre el subsuelo del país, y por ende un bajo entendimiento de los fenómenos físicos resultado de operaciones industriales.

Esta tesis se convierte en un primer paso para llenar este vacío, al hacer uso de la información disponible de los terremotos registrados desde 1993 hasta 2018 por el Servicio Geológico Colombiano (SGC), para proponer un modelo geodinámico de la esquina NW de Sur América, el primer modelo a tomografía de anisotropía sísmica para la corteza de Colombia, la primera valoración de los posibles mecanismos de activación de sismicidad antropogénica producto de la inyección de agua en yacimientos disposal en el campo de mayor producción de crudo pesado del país, y finalmente la caracterización de estructuras disipadoras de energía sísmica en yacimientos de hidrocarburos.

En el Capítulo 1 se describe en detalle el problema, su planteamiento, la justificación y la motivación de esta disertación. Igualmente se exponen los principios y antecedentes fundamentales bajo los cuales se ha venido construyendo el fundamento teórico asociado a la sismicidad antropogénica.

En el Capítulo 2 se hace un estudio de sismicidad regional de la esquina NW de Sur América para estimar tomografías de velocidad de Vp y Vs de la corteza y el manto superior, distribución de anomalías Vp/Vs en al manto superior y el mapeo de vectores de anisotropía

azimutal de onda P de la corteza. Este Capítulo ha sido sometido en la revista Seismological Research Letters (SRL).

En el Capítulo 3 se analiza la causalidad entre la producción de crudo pesado y sismicidad registrada en inmediaciones de un campo de la Cuenca de los Llanos Orientales de Colombia. Se utilizó la información reportada de los eventos para calcular mecanismos focales y determinar el tipo de fallamiento. Se estimó la energía radiada de los eventos de mayor magnitud para caracterizar los procesos de ruptura y determinar las propiedades de las fracturas generadas, incluidas la orientación, trayectoria y velocidad. Este Capítulo fue publicado en la revista Journal of South American Earth Sciences.

En el Capítulo 4 se determinó que la secuencia de eventos en el Campo de estudio (Capitulo 3) era el resultado de la liberación de la energía elástica almacenada en el yacimiento debido a la acción continua del trabajo ejercido por la inyección de agua en yacimientos disposal. Un análisis hidromecánico permitió determinar que la eficiencia energética del ciclo de inyección es baja en comparación con otras operaciones de inyección documentadas, permitiendo que la inyección a largo plazo de grandes volúmenes no haya dado lugar a eventos más importantes. Este Capítulo fue publicado en la revista Geophysical Journal International.

En el capítulo 5, se hace una recopilación de los resultados más importantes de este trabajo en forma de conclusiones y se plantean algunas futuras recomendaciones de trabajo e investigación.

ABSTRACT

GOMEZ ALBA, SEBASTIAN ALEJANDRO. Imaging velocity and attenuation anomalies, local stresses fields, based on the analysis of anthropogenic seismicity generated in hydrocarbon reservoirs in Colombia (Under the direction of PhD Carlos Alberto Vargas Jiménez).

The information achieved by the seismological monitoring of hydrocarbon fields has become an important tool and source of information to determine under what circumstances the operations of exploitation of hydrocarbon fields affect the alteration of the natural state of the elastic parameters of the rocks and the fluid flow into the reservoirs. In Colombia there has not been a policy that requires seismological monitoring of hydrocarbon fields, and the little that has been done has not yet been processed or fully analyzed. In this context, there is a gap regarding the acquisition of data, analysis and appropriation of knowledge about the subsoil of the country, and therefore a low understanding of the physical phenomena resulting from industrial operations.

This thesis is a first step to fill this gap, by making use of the information available from the earthquakes recorded from 1993 to 2018 by the Colombian Geological Service (SGC). To propose a geodynamic model of the NW corner of South America, the first seismic anisotropy tomography model for the crust of Colombia, the first assessment of the possible activation mechanisms of anthropogenic seismicity as a result of the injection of water into disposal reservoirs in the field with the highest production of heavy crude oil in the country, and finally the characterization of seismic energy dissipative structures in hydrocarbon reservoirs.

Chapter 1 describes the problem in detail, its approach, the justification, and the motivation for this dissertation. Likewise, the fundamental principles and theorical background under which anthropogenic seismicity has been built are exposed.

In Chapter 2 a regional seismicity study of the NW corner of South America is made to estimate velocity tomography of Vp and Vs of the crust and upper mantle, distribution of Vp / Vs anomalies in the upper mantle, and mapping of P wave azimuthal anisotropy vectors of the crust. This Chapter has been submitted in the Seismological Research Letters (SRL) journal.

In Chapter 3 the causality between heavy crude production and seismicity recorded in the vicinity of a field in the Llanos Orientales Basin of Colombia is analyzed. The information reported from the events was used to calculate focal mechanisms and determine the type of failure. The radiated energy of the highest magnitude events was estimated to characterize the rupture processes and determine the properties of the generated fractures, including orientation, trajectory, and velocity. This Chapter was published in the South American Earth Sciences Journal.

In Chapter 4, there is a description of the sequence of events in the oil field under study (Chapter 3) as the result of the release of the elastic energy stored in the reservoir due to the continuous action of the work exerted by the injection of water in disposal reservoirs. A hydromechanical analysis determined that the energy efficiency of the injection cycle is low compared to other documented injection operations, allowing the long-term injection of large volumes not to have led to more larger events. This Chapter was published in the Geophysical Journal International.

In Chapter 5, a compilation of the most important results of this work is made in the form of conclusions and some future work and research recommendations are proposed.

Estimación de imágenes de anomalías de velocidad, dispersores y campo de esfuerzos locales a partir del análisis de sismicidad generada en yacimientos de hidrocarburos en Colombia

por
Sebastián Alejandro Gómez Alba

Tesis presentada a la Facultad de Ciencias,
de la Universidad Nacional de Colombia
en cumplimiento parcial de la
requisitos para el grado de
Doctor en Filosofía

Geociencias

Bogotá D.C, Colombia

2022

APROBADO POR:

Carlos Alberto Vargas Jiménez
Director

Imaging of velocity and attenuation anomalies, local stresses fields, based on the analysis of anthropogenic seismicity generated in hydrocarbon reservoirs in Colombia

by
Sebastián Alejandro Gómez Alba

A dissertation submitted to Facultad de Ciencias,
of Universidad Nacional de Colombia
in partial fulfillment of the
requirements for the degree of
Doctor in Philosophy

Geosciences

Bogotá D.C, Colombia

2022

APPROVED BY:

Carlos Alberto Vargas Jiménez
Committee Chair

DEDICATION

With deep love, to my parents Nydia and Fernando, to my brother Luis Fer, my greatest support and inspiration. I also dedicate this work to all those who have not had the same opportunities as me: I hope that the results of this work contribute to the construction of an egalitarian society with better opportunities for all.

AKNOWLEDGMENTS

First of all, I want to thank my advisor, Professor Carlos Alberto Vargas, from whom I learned that the greatest satisfaction in life consists of producing new knowledge by taking every impulse of intellectual curiosity paired with scientific rigor. Thanks to all the active and non-active members of the Geophysics Research Group of the Universidad Nacional de Colombia for their support, accompaniment and sincere friendship. Likewise, to the entire administrative team of the Department of Geosciences, as through their work our research activities become easier. The following Institutions generously allowed access to the data used to write this document: Agencia Nacional de Hidrocarburos (ANH) and Servicio Geológico Colombiano (SGC). Special thanks to Colciencias and Colfuturo who, through Call 617: Becas Doctorados Nacionales, allocated funds for my academic stipend.

I would also like to acknowledge the contribution of all the comments that constructively assisted in the development of this work: all the anonymous peer-reviewers of Papers herein; to Professor Ivan Koulakov, who is the head Department of Seismic Tomography at the Institute of Petroleum Geology and Geophysics, Siberian Branch of the Russian Academy of Sciences (IPGG SB RAS), who provided great support in the development of the second chapter; to my colleague Carlos Fajardo who is co-author of the third chapter of this thesis; to Professor Arno Zang, scientist at the Seismic Hazard and Risk Dynamics Section of the Geophysics Department at the GFZ German Research Center of Geosciences, with his contributions we co-authored the fourth chapter of this thesis. Finally, to my colleague and friend Edwin Mayorga seismologist from the Colombian Geological Service (SGC) for his advice.

During my research internships, I had the opportunity to work in the research groups of Professors Guoquin Lin and Noritsimu Nakata from the Universities of Miami and Oklahoma, respectively. My sincere thanks for their hospitality, dedication and welcome in their work teams.

Finally, I would like to thank the Organizations that gave me the opportunity to show the partial results in international events, mostly thanks to their contributions from travel grants: American Geophysical Union (AGU) Fall Meeting (2014), International Union of Geodesy and Geophysics (IUGG) General Assembly (2015), Regional Assembly Latin

American and Caribbean Seismology Commission (LACSC) (2016), Workshop on Induced Seismicity organized by the Swiss Seismological Service and ETH Zurich (2017), Eastern Section SSA Annual Meeting (2017), General Assembly of the European Seismological Commission (2018), and International Union of Geodesy and Geophysics (IUGG) General Assembly (2019).

TABLE OF CONTENTS

LIST OF TABLES

LIST OF FIGURES

CHAPTER 1. INTRODUCTION: THE PROBLEM AND ANTHROPOGENIC SEISMICITY

The Problem

Energy technologies based on fossil fuels and those with potential growth in the coming decades (alternative / renewable energies) inevitably require the exploration and exploitation of subsoil resources for their production. This implies disturbing the natural state of the rock's stresses and its elastic properties. If rock is disturbed enough by human intervention, it can exceed its range of elastic behavior and fail, releasing energy in the form of earthquakes. This phenomenon is known by the name of anthropogenic seismicity. The seismic energy released during induced events is almost always very small, when compared to the energy released from natural events. The magnitude is dependent on the subsurface tectonic environment (active or inactive), and the operational parameters that rule industrial operations. If the mechanical properties of the subsoil are unknow, and without proper management and control of operational variables, it is not possible to guarantee the viability of energy projects, nor to mitigate the possible negative effects on the communities neighboring their areas of influence.

Statement of the Problem

The underlying causes of induced earthquakes depends directly on the industrial operations involved and the mechanisms of activation of seismicity. The industrial operations that have been documented as potential generators of induced events may include: mining projects, water reservoirs, geothermal operations systems, capture and injection of CO_2, dumping of wastewater in disposal reservoirs, and extraction of oil and natural gas (Hitzman et al., 2012). These industrial activities may or may not include the injection of fluids into the subsurface. Regarding those that do, some studies suggest that are the main cause of the increasing number of earthquakes in the central and eastern U.S since early 2000’s (Ellsworth, 2013; Keranen et al., 2014; Horton, 2012; Walsh and Zoback, 2015). According to the U.S Geological Survey (USGS), before 2008 there was an average of 25 earthquakes of M3+ in the central and eastern United States. Since 2009, at least 58 earthquakes of this magnitude have been recorded each year. Since 2013, the number of annual records has doubled, reaching the maximum rate of events (M3+) in 2015 close to 1000 earthquakes (Rubinstein and Mahani, 2015). A detriment was also detected in the number of events after 2015 to date. Only 130 M3+ earthquakes were recorded in 2019. Depending on the event size, some can be perceived by people, few can cause significant damage. Some moderate to large earthquakes include the M4.8 earthquake near Denver, Colorado in 1967 (Herrmann et al., 1981), the M5.3 earthquake at Raton Basin, Colorado in 2011 (Rubinstein et al., 2014), the M5.7 earthquake near Prague, Oklahoma in 2011 (Keranen et al., 2013) and the M5.8 earthquake near Pawnee, Oklahoma in 2016 (Yeck et al., 2016).

The mechanisms of activation of fluid-injection induced earthquakes do not depend on a single cause. On the contrary, different patterns interact to each other to create unique scenarios that enable the faulting of rocks (Ellsworth, 2013; Rubinstein and Mahani, 2015). According to Ellsworth (2013), the two main possible causes include: 1) increasing the pore water pressure through injecting water to a permeable reservoir close to a fault, and 2) changing the normal and shear stress condition on a fault without direct hydrologic connection. Even with a general consensus regarding the causes mentioned above, the question of why in some regions there are more induced earthquakes than in others, is of great importance for the scientific community. The distribution of induced seismicity is uneven with respect to fluid injection (Frohlich et al. 2015; Gobel 2015). High rates of injected volume do not always generate large number of events, nor great magnitudes (Keranen et al. 2014, Weingarten et al. 2015, Walsh & Zoback 2015, Goebel et al. 2016, Hornbach et al. 2016).

Instinctively it would be believed that regions with low induced seismicity may have insufficient injection rates or volumes to allow an increase in pore pressure beyond critical levels (Frohlich et al. 2015), particularly with respect to permeability of injection formations. Barriers of low transmissibility of pressure disturbances may prevent the activation of faults within the injection zones, or even further away, such as those located in the crystalline basement (Zhang et al. 2013). Aspects such as permeability variations, geological structures and injection operational designs, would control pressure diffusion, and therefore the location and time distribution of seismicity. Some aspects to consider:

a. Dissimilarities in the stress field may contribute to the observed variability in induced seismicity (King et al. 2014, Gobel 2015). If natural faults in a region are not close to their failure point, the induced pressure disturbances would be insufficient to trigger slip (Hickman et al. 1985, Zakharova & Goldberg 2014). Now, if a fault is close to its failure bound, it would have the capacity to trigger earthquakes (van der Elst et al., 2013). Theoretically, critically stressed fault regions could be mapped and provide evidence of subsurface stress conditions. In many cases, stress data on faults do not exist or are not in the public domain, so it is difficult to carry out complete analyzes that can link stress field variations and induced seismicity (Heidbach et al. 2010).

b. Fault orientation patterns may, or may not, affect the mobility of the injected fluid and its interaction with fluids confined in natural fractures (Liu et al. 1991, Townend & Zoback 2000, Lambert 2017). Earthquakes in Oklahoma primarily occur on clearly regionally aligned (well-oriented systems) fault systems (Holland 2013b, Alt & Zoback 2016, Lambert 2017), although rupture also occurs on misoriented faults. Some examples of induced earthquake sequences aligned to well-oriented systems are, the Pawnee events (Mw 5.8) and the Prague sequence (Mw 5.7), where the seismicity distribution underlies the largest mapped crystalline basement faults (Keranen et al. 2013, Sumy et al. 2014, Lambert 2017). When ruptures occur in misoriented systems, injection bottomhole pressures must operate high enough for slip to occur on nearby faults (Raleigh et al. 1976, Ake et al. 2005, Keranen et al. 2013). Due to high injection rates, the probability of connecting to fault systems is higher, and therefore misoriented fractures may also fail (Keranen et al. 2013, King et al. 2014). A helpful side effect of induced seismicity, is the possibility to map small fault systems that have not been detected. However, well-defined regional fault systems, even with well-constructed hydrogeological models, are not enough to characterize the possible seismic hazard generated by anthropogenic earthquakes.

The study and analysis of induced seismicity in Colombia has not started in detail yet, and already faces some difficulties to begin properly:

a. Anthropogenic seismicity analysis demands information from geological structures and detailed local velocity models that do not exist in most cases.

b. The distribution and magnitude of the stress field is unknown in many areas of the upper crust.
c. The deployment of seismological monitoring instruments done by the Colombian Geological Service (SGC) is designed to detect earthquakes on a regional scale. Only a small fraction (less than 1%) of the SGC equipment is available to record events associated with hydrocarbon exploration and production operations.
d. Remote monitoring of induced seismicity means that the recorded signals tend to be weak, and the signal / noise ratio is not favorable for seismic analysis (a consequence of the regional distribution of stations).
e. Injection protocols are in most cases subject to confidentiality agreements that do not ease the development of independent studies and academic analysis.

Purpose of this dissertation

This dissertation aims to analyze the phenomenon of anthropogenic seismicity with a case study of the Eastern Llanos Basin of Colombia, and explore the impact of induced earthquakes on stress field orientations. This is achieved through the following objectives:

a. To estimate velocity anomalies, large scale structures and stress orientations by the analysis of regional isotropic and anisotropic tomography in Colombia.
b. To develop a first approach on how fluid extraction, and injection, may create anomalous local stresses triggering earthquakes in areas already affected by large scale regional stress.
c. To make an energy balance between the injected potential energy versus the radiated seismic energy to comprehend some particularities of the mechanical conditions of rocks in the study area.

Davis and Frohlich (1993) proposed seven generally accepted criteria that must be met before fault reactivation is considered to be anthropogenic in origin. Below are the considerations for each claim in the case of Puerto Gaitan, taken into account when starting out this research:

a. Are these events the first known earthquakes of this character in the region? Yes. The Colombian Geological Service (SGC) has always reported high seismicity in the deformed belt of the Eastern Llanos Foothills, but not in Puerto Gaitan area. (Figure 1). According to SGC, 11 events were recorded before intense seismicity started in Puerto Gaitan in March 2013. Only one was M3 in 1997. No reports exist about felt earthquakes by people between 1993 and March 2013, so it is assumed that no earthquakes larger than M3 occurred during this period.

b. Is there a clear correlation between injection and seismicity? Yes. Reports indicated that the natural increase in the co-production of water had prevented its disposal in natural water sources. The operating company requested authorizations from Colombian environmental authorities, to reinject water into the Carbonera formation. In 2008 the injection of 900 KBWPD was permitted, by 2014 the injection volume allowable increased to 3500KBWPD. There is an apparent correlation between the approved injection volumes and the recorded seismicity.

c. Are epicenters near wells (within 5 km)? Yes. All the seismicity recorded in the Puerto Gaitán fields takes place within the areas delimited for the exploration and exploitation of heavy crude (Figure 1).

d. Do some earthquakes occur at or near injection depths? Yes. The injection formation is Carbonera, which has three target horizons: C1 (~0.51–0.57 km below surface), Intermediary (~0.55–0.61 km below surface) and Carbonera basal (~0.7–0.85 km below surface). Until 2014, the Colombian Geological Service (SGC) reported that (~31%) of the recorded events occurred less than 1 km depth.

e. If not, are there known geologic structures that may channel flow to sites of earthquakes? It is not conclusive. It is assumed that there must be local fault systems that allow migration of fluids to greater depths of the injection formation. Until 2014, the Colombian Geological Service (SGC) reported that (~69%) of the recorded events occurred at depths greater than 1 km.

f. Are changes in fluid pressures at well bottoms sufficient to encourage seismicity? It is not conclusive. The well-head and bottom-hole injection parameters is not in the public domain. It is hypothesized that the injection pressure ranges contribute to the increase in reported seismicity.

g. Are changes in fluid pressures at hypocentral distances sufficient to encourage seismicity? It is not conclusive. There was no information or previous studies in this regard. It is hypothesized that fluid pressure variations in the subsurface, within the injection horizons or deeper, contribute to the increase in reported seismicity.

The articles published as part of this dissertation (chapters 2, 3, and 4), in addition to subsequent independent studies (Molina et al., 2020), have corroborated the assessments made at the beginning of this research.

Earthquake activation within hydrocarbon fields

To adequately describe anthropogenic seismicity, researchers have introduced two definitions so far. The first one is "induced", which is used to describe the seismicity resulting from an industrial activity that causes a change in the stress state that is comparable in magnitude to the environmental shear stress that acts on a fault to cause its slip. The second term is “triggered” which is used when the stress change is only a small fraction of the environmental level (Bossu, 1996; McGarr and Simpson, 1997).

The resistance of the rocks to fracture is mainly controlled by the effective pressure of the fault (Byerlee, 1978). This statement is known as Byerlee's Law and establishes that the shear stress (τs) necessary for the frictional sliding to begin can be related to the normal stress (σ_n) to the fracture plane according to the following equation:

$$\tau_s = \mu_f \sigma_n + C$$

Where μ_f is the coefficient of friction and C is the cohesive resistance parameter. The laboratory tests carried out by Byerlee established that the laws that govern rock friction are independent of their type and must consider pore pressure (Brace and Kohlstedt, 1980; Kohlstedt et al., 1995). To model anthropogenic earthquakes, it is necessary to assume some fundamental hypotheses (Zoback and Healy, 1984; Brudy et al., 1997; Rutledge and Phillips, 2003; Suckale, 2010; Maxwell et al., 2010):

a. The crust has previous fractures.
b. Fractures have a favorable orientation for frictional sliding to occur.

c. The natural stress field conditions on the crust are always very close to the critical fault limit, so the pore pressure is almost equal to the value of the hydrostatic pressure
d. Cohesive resistance is negligible.
e. Variations in stress patterns within the injection formation are due to the extraction and injection of fluids.

The extraction of fluids can cause the compaction of the reservoir and reactivate pre-existing faults that induce small earthquakes or microseisms (Chan & Zoback, 2007; Miyazawa et al., 2008; Sarkar et al., 2008). On the contrary, water injection causes a decrease in effective stress and slip along pre-existing faults (Grasso, 1992). The induced seismicity caused by fluid injection is mainly associated with an increase in pore pressure, while that generated by fluid extraction is due to its decrease. It is not convenient to attribute the appearance or increase in seismicity to one single cause. It has been established that the combinations of factors that generate anthropogenic seismicity include some of the following aspects (Hitzman et al., 2012):

a. Significant changes in the net pore pressure in a reservoir
b. Activation of critically stressed faults and with orientations favorable to faulting, and
c. Creation of faults or fractures in formations with a high brittleness value.

Important physical mechanisms of injection-induced seismicity have been revealed from previous experimental revisions and study cases. Some important recent advances gained from previous observations also include:

a. Discrimination between Tectonic vs Induced Events: Great efforts have been made to determine robust methodologies that allow discriminating between natural and induced events. Statistical evaluations have been the most used techniques to date, mainly focused on measuring the distances between injection wells and earthquakes, temporal correlations, and analyzes of historical seismicity in the areas of interest (Davis & Frohlich, 1993; Weingarten et al., 2015). However, recent studies have shown that the spatial extent between wells and earthquakes depends on many variables, and does not always occur in the immediate vicinity of injection points (Keranen et al., 2014; King et al., 2014; Yeck et al., 2016). For instance, and as mentioned above, faults and fractures between the basement and the injection geological units can spread pressure disturbances downwards, generating earthquakes at depths much greater than the injection depths (Rubinstein et al., 2014). Temporally, induced earthquakes are observed to move analogously with fluid migration (Keranen et al., 2014). If there is no continuous and detailed monitoring of migration patterns, it will be difficult to assess detectable levels of the pressure disturbance front. The detection of migration along small faults requires catalogs with low detection thresholds, which are only possible with dense networks of local stations.

b. Temporal correlations and time delays: Earthquakes can be triggered with varying time delays, depending on well locations, faults, and conditions for pressure transmissibility. Depending on the injection technologies, the temporal correlation between operation and earthquakes may vary. For instance, in hydraulic fracturing and geothermal projects, these sequences exhibit short temporal correlations (Majer et al. 2007, Holland 2013a, Skoumal et al. 2015b). These correlations can be made shorter if there is connectivity between operating depths and nearby faults (Raleigh et al. 1976). It is also assumed that with respect to the volume of injected fluid, if it is small, the pressure region of the disturbed fluid is insignificant and there is also a short delay between injection and earthquakes. When the temporal correlation is moderate or occurs over long periods, geological features are presumed to be responsible for delaying pressure diffusion. At first it is possible to establish a rapid and straight relationship between the injection operation and the earthquakes, but then again once industrial intervention is complete, earthquakes may be recorded even years later. An example of this, is the resulting seismicity recorded in the Rocky Mountain Arsenal (RMA), which occurred up to two years after the end of water injection. Water disposal was made in a fracture zone enclosed by a low-permeability crystalline basement (Hsieh & Bredehoeft, 1981). At the Cogdell field in Texas, the seismicity befell 18 years after injection was complete. The complex stratigraphic trap limited the diffusion of fluid pressure (Davis & Pennington 1989). In fault systems, they might behave like significant deflectors for fluid flow, or as fluid pathways (Smalley & Muggeridge 2010, King et al. 2014, Wibberley et al. 2017). When faults are baffled, the structures strongly inhibit fluid pressure disparities

(Wibberley et al. 2017). Each fault requires a critical pressure threshold to reach its failure point. Thresholds would be achieved due to the multiple combinations of injection rates, pressure and permeability distribution. For geological systems with good hydraulic communication, time lags can be of the order of hours or days. These ranges would increase in inverse proportion to the lateral connectivity of the formation, allowing fluid pressure to build up for even tens of years.

c. Frequency earthquakes distribution: Possible seismicity deviations in historical earthquake frequencies in regional areas have been useful to discriminate between tectonic and induced events. Some analyzes have been done in Oklahoma and Arkansas in 2009 (Llenos & Michael 2013). Walsh and Zoback (2015) analyzed statistics within smaller regions in Oklahoma, and within some sub-regions around the 2011 Prague earthquakes. In some cases, they found that observed patterns deviated from observed regional patterns, while in others the patterns were very similar. Deviations from historical rates were identified in western Canada in 2010 (Atkinson et al. 2016).
d. b value and stress drop analysis: It is common to observe that earthquakes in volcanic geodynamic environments occur in the form of swarms, and the b values differ considerably from the values of tectonic earthquakes (Shelly et al. 2013). Applying the same logic, attempts have been made to find similar behaviors when seismicity is induced (Skoumal et al. 2015a, 2016). However, to date it has not been possible to state whether the induced earthquakes have a swarm behavior or more like an earthquake-aftershock sequence. Moreover, they have been documented in both ways. The Fairview (Mw5.0), Pawnee (Mw5.8), and many other small events in Oklahoma occur in clear main-aftershock sequences, some of which have shown to exhibit Omori-type decay sequences (Yeck et al. 2016). Stress drop analyzes seem to be also inconclusive. Joint studies of spectrum analysis, rupture area and seismic moment estimations, have recognized that the stress drops of some induced events are very small (Sumy et al. 2017, Barnhart et al. 2014). However, other studies have indicated that stress drops are on the order of those of tectonic earthquakes (Huang et al. 2016).

e. Discrimination of Induced Seismicity in Tectonically Active Regions: In regions with abundant tectonic seismicity near active faults, differentiating whether the causes of earthquakes are natural or anthropogenic is a difficult task. If stress drops are high enough, seismicity with classical migration patterns, low b values, and temporal and spatial correlations consistent with injection operations can be generated. Gobel et al. (2016) concluded that induced seismicity in hydrocarbon fields in California would elude the identification criteria of detailed seismological, geological, and hydrogeological analyses.

Towards solving the problem, conclusions and future work.

Pressure disturbances in the subsurface do not follow clear migration patterns, and are controlled by a large number of variables such as: geological structures, permeability variations, fault systems and orientation, and injection protocols. The following are agreed conclusions found in numerous experimental revisions and case studies:

a. Subsurface pressure variations associated to fluid injection are capable of inducing and triggering earthquakes.
b. High pore pressure due to fluid injection may reduce normal stress on a fault plane and slip a fault if it reaches the Coulomb failure criterion.
c. Seismicity can occur fair after injection if the well (or set of wells) and faults are linked by transmissive zones (high permeability or fractures).
d. Seismicity has been recorded years after injection ends, if pressure does not diffuse to initial levels but remains perturbed locally.
e. Pressure diffusion is inhibited by low-permeability fluid pathways or barriers.
f. Injection-induced earthquakes can reach (at least) moderate magnitudes.
g. Induced seismicity near injection wells is more sensitive to injection protocols such as injection rate and total injected volume.

Improved geological data and hydrogeological simulations will allow better evaluation and understanding of the role of geological setting in induced seismicity. Undoubtedly, the understanding of the phenomenon will imply a better evaluation of the designs of operations in geoengineering projects. Such studies will also apprise research into earthquake nucleation and fault zone processes and will be useful in understanding seismic hazard.

The capability of induced seismicity to advance an understanding of earthquake triggering mechanisms relies upon proper and constant monitoring, at the scale at which nucleation processes happens. This requires the deployment of bottomhole seismometers and dense surface recording instrumentation. To avoid signal degradation associated with near-surface site effects, well logging using three-component seismometer packages that have a wide dynamic range and wide bandwidth is recommended (Malin et al., 1988; Abercrombie, 1995). The processing and subsequent analysis of the seismic data obtained must be complemented with the results of other mechanical studies, such as information on crustal deformation before and after earthquakes (Fialko & Simons, 2000; Vasco et al., 2010; Ali et al., 2016). Monitoring of fluid saturation in the subsurface in deep wells would allow the detection of temporary changes in fluid pressure, which allows the identification of overpressure formations (Kroll et al., 2017). Geophysical data must also be included in the interpretation of structures that mitigate pressure diffusion in injection formations.

Regional studies of induced seismicity are continuously published (Keranen and Weingarten, 2018; Rubinstein et al., 2018; Skoumal et al., 2020). Many of them are carried out in cooperation between universities or industry-universities. Numerous initiatives have been created, some in the United States and Canada, to address the issue of hazard mitigation due to induced earthquakes (Atkinson et al., 2015; McGarr et al., 2015; Atkinson, 2017; Bommer et al., 2017). Some of these collaborations include the US Geological Survey (Petersen et al., 2016) and the Canadian Induced Seismicity Collaboration (Atkinson et al., 2015; Atkinson, 2017). These initiatives should seek to publish and facilitate public access to information on hydrogeological (including Poroelasticity) and geomechanics properties.

Seismic parameters, including source magnitude, seismic moment, stress drop, and radiated energy can provide useful information for establishing a causal relationship between industrial operations with the resulting seismicity. Precise hypocentral locations and magnitude estimations are essential (Spottiswoode and McGarr, 1975; McGarr, 1992). From these data it is possible to determine, for instance, information on stress fields in a particular region. Available data on stress state are insufficient for determining whether spatially varying stress fields contribute to spatial and temporal variability in induced seismicity (Schoenball and Ellsworth, 2017; Chang et al., 2018). Obtaining reliable, distributed data on principal stress magnitudes, would provide a priori guesses of the proximity of faults to failure and could help determine appropriate regions for long-term, high-volume fluid disposal (Langenbruch and Shapiro, 2015; Huang et al., 2016; Huang et al., 2017; Snee and Zoback, 2018; Wang et al., 2018; Wu et al., 2018; Bourne et al., 2018; Haddad et al., 2020; Maurer et al., 2020;). By understanding the distribution of stresses in the crust, it is easier to understand the mechanisms of activation of earthquakes and ground motion models for different fluid injection technologies (Atkinson, 2015; Bommer et al., 2016; Mignan, 2016; Bydlon et al., 2017; Dempsey and Suckale, 2017; Cremen et al., 2017; Farhadi et al., 2018; Petersen et al., 2018; Atkinson et al., 2018; Khosravikia et al., 2019; Bydlon et al., 2019; Kang et al., 2019; Chen et al., 2020; Trugman and Savvaidis, 2021). At this point, research should continue to be carried out to differentiate the effects of different injection schemes, such as short-term injection (includes hydraulic fracturing) (Skoumal et al., 2015b; Maxwell et al., 2015; Savvaidis et al., 2020; Cremen et al., 2020) and long-term like water disposal (Gono et al., 2015; Dieterich et al., 2015; Langenbruch and Zoback, 2016; Lui and Huang, 2019; Hennings et al., 2019; Alghannam and Juanes, 2020). Additionally, it is important to evaluate the effect of the type of fluids contained in an injection formation, such as those containing gas (van Thienen-Visser and Breunese, 2015). 4D seismic technology has acquire data in order to obtain dynamic high-quality images to identify the distribution of fluids phases within reservoirs, water injection fronts, and hydrocarbon production (Suckale, 2010).

Hazard analysis studies have been done in different injection scenarios (Ellsworth et al., 2015; Bommer et al., 2015; Petersen et al., 2015; Walters et al., 2015; Petersen et al., 2016; van Elk et al., 2017; Wang et al., 2017; Bommer et al., 2017; Brooks et al., 2018; Mousavi et al., 2018; Ghofrani et al., 2019; Gupta and Baker, 2019; Atkinson, 2020). Risk analysis are broadly based on analyzes associated with the generation of prediction models of earthquake generation in space, time and the magnitude of the events. The basis of these studies includes from the analysis of historical seismicity to the implementation of more complex statistical analysis. Some studies have been carried out by (Bourne and Oates, 2017; Broccardo et al., 2017; Dost et al., 2017; Gupta and Baker, 2017; Novakovic et al., 2018; Langenbruch et al., 2018; Scanlon et al., 2019; Baisch et al., 2019; Grigoratos et al., 2020a; Grigoratos et al., 2020b; Schultz et al., 2021). Finally, action protocols have been implemented for the analysis of the risk of induced earthquakes (Mignan et al., 2017; Schultz et al., 2020; Verdon and Bommer, 2020).

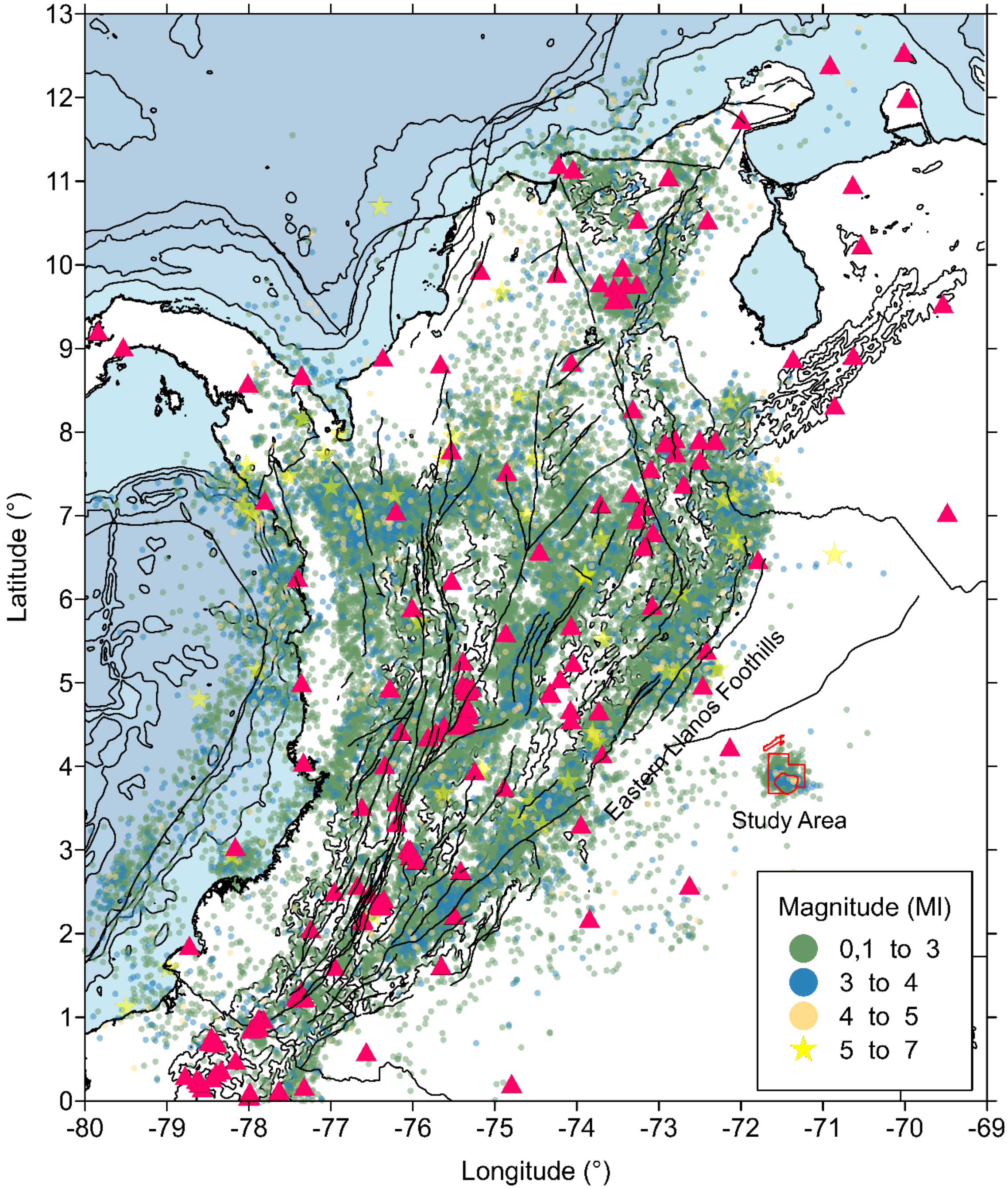

Figure 1. Seismicity of the upper crust of Colombia. The distribution of crustal seismicity is concentrated in the Andes region. The seismicity is a consequence of the processes associated with the deformation of the crust. The study area is located to the East, in the sedimentary basin of the Eastern Plains (framed by the red quadrants). This region is seismically inactive, except for the accumulation of events in the Puerto Gaitan area. The red

triangles show the regional distribution of the seismological stations in the Colombian territory. All information is public and in the domain of the Colombian Geological Service (SGC) and the National Hydrocarbons Agency (ANH).

CHAPTER 2. HIGH-RESOLUTION SEISMIC TOMOGRAPHY OF THE CONVERGING LITHOSPHERIC SYSTEM OF NW SOUTH AMERICA

Introduction

The NW corner of South America is the region where different tectonic plates, Nazca, Caribbean, and South America converge to create a zone of elastic deformation and high seismic activity (Duque-Caro, 1990; Taboada et al., 2000; Trenkamp et al., 2002; Vargas and Mann, 2013). The region is made up of three different areas: Andes, Caribbean, and Eastern (Figure 2). The current configuration of the Andes includes three mountain ranges: Eastern (EC), Central (CC) and Western (WC), and two internal valleys: Magdalena (MV) and Cauca (CV). It is bounded on the east by the Eastern Llanos foothills, on the west by the Colombian trench and the north by the South Caribbean Deformed Belt (Pennington, 1981, Adamek et al., 1988). The second area, known as the Caribbean, is a flat region composed mainly of several sedimentary basins. Finally, the Eastern Region represents an extensive foreland basin associated with the Andean orogen that overlays the Guyana craton (Farris et al., 2011).

Different models have been proposed to clear up the processes associated with the current geodynamic configuration of the region. There seems to be a concession in recognizing the existence of two different subduction plates: Nazca and Caribbean. However, the main discussions are around fundamental unknowns such as lithospheric tearing and the mechanical coupling between both slabs and the mantle. Pennington (1981) determined that the Wadati-Benioff area in the Colombian territory is located in two differentiated segments: Cauca and Bucaramanga. The Cauca segment is linked to the subduction of the Nazca Plate with a direction N35°E and 35° dip. The Bucaramanga segment is associated with the subduction of the Caribbean Plate in the direction N109°E and 20-25° dip. van der Hilst and Mann (1994) determined the convergence and superposition of both slabs between latitudes 5.2°N and 7°N based on the analysis of tomography images. This model was adopted years later by Taboada et al. (2000) and Cortés and Angelier (2005). Vargas and Mann (2013) proposed that the boundary between the oceanic crust of the Nazca Plate and the Panama arc indenter is defined by a lithospheric tearing (Caldas Tear) around 5.5°N. Salazar and Vargas

(2015) interpreted the Caldas Tear as the southern limit of the Caribbean Plate, based on seismotectonic deformation determined from ISC focal mechanisms. Tomographic interpretations of Chiarabba et al. (2016) explain this fragmentation as a change between a steep subduction angle and a flatter one, both within the Nazca plate only, which implies that the Nazca plate boundary would move much further north somewhere under the volcanic arch of Panama. Finally, Syracuse et al. (2016) presented three-dimensional models of the variations of the velocity of the P and S waves and identified the Nazca plate fragmentation in two segments similar to Chiarabba et al. (2016), but marking the Bucaramanga Seismic Nest (BN) in the second segment. The Caribbean Plate, on the other hand, would be subducting at shallower dip angle <10° in a WNW-ESE direction (Bernal-Olaya, 2015; Sanchez et al., 2015; Mora-Bohórquez et al., 2017), with no apparent partition zones. On the overriding South American Plate, foremost studies have focused on estimating the thickness crust. Poveda et al. (2015), estimated the crustal thickness based on the analysis of receiver functions. Subsequently, Syracuse et al. (2016) did so by analyzing images of the lateral variation of the P and S wave velocity between 12.5 and 55 km depth. Recently, Poveda et al. (2018) published a new analysis of the upper and middle crustal velocity structure from the reconstruction of the empirical green's functions of pairs of stations and surface wave tomographic images.

The subduction process of the Nazca and Caribbean plates under South America has a significant influence on the tectonic evolution and geological setting of the region, as well as a substantial impact on its seismic and volcanic activity. One striking feature is observed around 5.5°N, where there is a lateral eastward displacement (~ 240 km) of epicentral earthquake solutions (Pennington, 1981). To the north and south of this discontinuity, there have been identified two seismic nests. The BN to the north, which is considered one of the places that groups the highest concentration of intermediate-depth seismic events worldwide (Prieto et al., 2012). To the south is the Cauca Seismic Nest (CN), associated with the mid-depth seismicity of the Nazca Plate subduction (Chang et al., 2017). Figure 2 also shows the epicentral distribution of earthquakes in the region recorded by the Colombian Geological Service (SGC) from 1993 to date. The accumulation of earthquakes in the Andean region seems to be a consequence of the subduction processes of both Nazca and Caribbean Plates, and crustal deformation. The seismicity on the Caribbean is diffuse, and to the Eastern Region is quite inexistent. With seismicity, the volcanic activity also moves laterally to the east; even more, the active volcanic chain of the South American Andes is interrupted at ~5.5oN.

The NW corner of South America provides an outstanding research frame to comprehend how plate convergence and subduction processes interact simultaneously to fix crustal deformation and upper mantle composition. In this study, we use the local tomography algorithm LOTOS package (Koulakov, 2009), by jointly inverting the local earthquake catalog for P and S velocity waves. The velocity model and earthquake locations were also improved. This new model and distribution of seismicity reveal new insights into the complex configuration of NW South America convergent boundary setting, faulting, and slab coupling beneath the study area.

Data description and methodology

Hypocentral parameters and phases of the local seismicity of Colombia, which have been collected by the Colombian Geological Survey (SGC) since 1993 were used. From this available database, we selected earthquakes recorded between 1993 and 2017 with at least 20 registered picks and located at a horizontal distance of no more than 200 km from the nearest station. In total 15,776 seismic events from 547 stations were used. The final dataset used in the tomography enclosed 245,214 P and 221,554 S arrival times. The hypocentral distribution provides initial evidence of a good ray coverage, as shown in Figure 3. More details about recording conditions, instruments, and distribution of events are provided at the SGC website (www.sgc.gov.co).

Local earthquake tomography algorithm: LOTOS (local tomography algorithm) for simultaneous inversion of P and S velocity anomalies, source coordinates, station corrections, and origin times (Koulakov 2009) was used. The algorithm comprises three main steps. The first step is called the 1D model optimization. It consists of selecting a set of events uniformly distributed at different depths, and relocating them by using a grid search method (Figure 4) (Koulakov & Sobolev, 2006). The second step involves optimizing the 3D model. Once the location of sources is performed (first step), rays are traced using a modified bending algorithm. The algorithm is founded on the Fermat principle of travel minimization. The grid nodes are established automatically according to the distribution of the seismic rays, which means that the code is able to increase the grid density in areas of high ray number, or on the contrary, does not define any in the absence of them. Both 1D and 3D models are inverted by using the LSQR method (Van der Sluis & Van der Vorst, 1987). The last step is the inversion procedure. The inversions are done on four different grids with altered basic azimuthal alignments (0°, 22°, 45°, and 67°) to avoid any artifacts due to grid orientations. The final result in each grid corresponds to the average of adding the inversion in each of the orientations mentioned above.

Local earthquake anisotropy tomography algorithm: To estimate the azimuthal anisotropy derived for the P-wave velocity models, we used the local Source anisotropic P-wave tomography algorithm ANITA (Koulakov et al., 2009b). The algorithm is based on the general concept of the LOTOS code described above. The algorithm considers a simple approximation of azimuthal anisotropy, which is described by three parameters corresponding to the directions at 0°, 60° and 120°. The slowness along a ray is estimated by using the slowness along the corresponding azimuth with respect to a reference slowness value, and the azimuthal α and dip angle β (both measured upward from the vertical axis) calculated at each direction. The final parametrization corresponds to a pseudo-ellipse with the orthogonally oriented maximum and minimum values of slowness and azimuth of maximum slowness orientation.

The inversion solution is further controlled by smoothing and damping parameters, so the difference in the final values of neighboring nodes may be reduced to the maximum. These last restrictions were selected, taking into account the steadiness between the reduction of travel time residuals and the smoothness of the 3D velocity model obtained (Eberhart-Phillips, 1986). We choose both smoothing and damping parameters of 5.0 and 20 for Vp, and 10.0 and 20 for Vs, for both LOTOS and ANITA inversions. We show results after the fifth iteration, despite the solution was optimal after three iterations with RMS time residuals no longer significantly decreasing for both P and S velocity anomalies (Figure 5).

The LOTOS code does not presume any parametrization with cubes, but with nodes spaced every 5 km. We took the initial 1-D velocity model and Vp/Vs ratio (1.78) from

Ojeda and Havskov (2001). Table 1 displays the velocity profile They developed a regional model with three layers (0.0 km - 4.0 km, 4.0 km - 25 km and 25 km - 32.0 km) for the crust, and one single layer for the upper mantle (32.0 km – 100 km). P wave velocities of 4.8 km/s, 6.6 km/s, and 7.0 km/s for all three crustal layers, and an upper mantle velocity between 8.0 km/s and 8.1 km/s.

Synthetic tests: The accuracy of the final 3D inversion results was assessed by comparing the results of the inversion of synthetic data (using the same starting model and control parameters as for the real data), with the calculated theoretical travel times of seismic rays for an ideal model. We performed checkboard tests for horizontal sections, and additionally evaluated free shape anomaly tests for vertical sections only. The synthetic assessment could display unrestored zones where tomographic resolution is not well defined.

We tested working with 3D anomalies traditional checkboard models of different size (50 km3, 75 km3, 100 km3) alternating positive and negative anomalies of +/- 10%, in eight horizontal sections at depths of 10, 20, 30, 40, 50, 100, 150 and 200 km. The estimated synthetic travel times were also perturbed by random noise with an average standard deviation of 0.1, 0.2, and 0.5 s. The forms for the free shape anomaly test were performed to explore the capacity to resolve the slabs shapes in vertical sections.

Evidence suggests that 50 km2 anomalies can be well resolved to a maximum depth of 30 km (Figure 6). The anomalies of 75 km2 (Figure 7) and those of 100 km2 (Figure 8) up to depths of 40 km, and 50 km, respectively. The resolution is optimal in the middle of the station arrangement since there is where the highest concentration of rays occurs. Reconstruction is affected in the deeper layers, due to the decrease in the number of rays. The models for the S wave are always less constrained than the model for the P-wave due to the number of S-wave phases is lower than that of the P-wave, and the S-wave data does not always allow reliable picks. The results for synthetic travel times perturbed by random noise with an average standard deviation of 0.1, 0.2, and 0.5 s. are shown from Figure 9. Figure 10 shows synthetic test results for free shape anomalies, showing that subduction slabs structures (shapes) are well resolved. In general, it can be determined that given the results of the synthetic tests, the images of the structures and the slabs can be reliably interpreted.

The reduction obtained in the LOTOS code for the synthetic isotropic P-wave and S-wave models were also estimated. After five iterations, the model reductions are around 50.9% for P and 54.6% for S, when changing the anomaly size. The average difference between both models is close to 3.7%. The P-residuals data abridged around 0.5s, and those of the S data reduced 0.8s. More significant reduction for the S-wave velocity residuals happens because they are more sensitive to velocity anomalies. When adding random noise, the model reductions are close to 42.9% for P and 51.2% for S. The average difference between both models is almost 8.3%. P and S residuals were close to 0.4s and 0.9s, respectively.

In the case of anisotropic P-wave inversion, we performed three different checkboard models with size patterns of 50km2, 75km2 and 100 km2 for crustal depths (from 10 km to 50 km). At each point of the synthetic model, we defined the azimuth of the main anisotropy axis and two velocity values oriented along orthogonal azimuths corresponding to fastest and slowest directions. In the blue cells, we defined the maximum and minimum velocities of 5% and 15%, respectively, and the fast velocity was oriented longitudinally. For the red cells, the anomalies were -5% and -15%, and the orientation was latitudinal. Below NW corner South America, the reconstruction of the anisotropic patterns appears to be much less stable than the isotropic models. The best reconstruction was completed by the anomaly size pattern of 50km2. High quality reconstruction of the anisotropy orientations was better achieved in the central blocks. Towards the sides, the reconstruction tends to disperse. After five iterations, the reduction for P-wave anisotropic model was close to15.9% and the P-residuals decreased from 0.8385s to 0.7053s. The results are shown in Figure 11.

Such relatively high values of reduction for both models can be explained by the high quality of the data and strong heterogeneities in the models with respect to the initial 1D velocity model.

Inversion Results

The resulting isotropic models for P and S waves performed with LOTOS are presented in Figure 12 and Figure 13, respectively, in eight horizontal sections at depths of 10, 20, 30, 40, 50, 100, 150, and 200 km. The reductions obtained in the LOTOS code for the isotropic P-wave model was 43.11%, and for S-wave model was 47.08%. When comparing the locations in the starting 1D model and the final 3D anisotropic model, the residuals of P data reduced from 0.7437s to 0.4231s, and those of the S data reduced from 1.2031s to 0.6366s.

We illustrate the results of the combined analysis of earthquake relocation and seismic tomography. The distribution of seismicity in-depth shows two differentiated seismogenic zones. The first corresponds to all earthquakes located above 50 km, which are associated with crustal structures (including faults). All the seismic events below 50 km belong to the second group where hypocenter solutions are already in the upper mantle. Regarding the distribution of anomalies, it is possible to identify that in the first seismogenic layer, the velocity variations are grouped in three differentiated regions: to the north, the Caribbean domain in which low-velocity anomalies predominate for both P and S waves; an Andean region located in the central part, where high lateral tomographic variations prevail; and finally, to the east, a region where most velocity anomalies are negative for both P and S waves. Below 50 km, the dominance of high-velocity anomalies for P and S waves is determined by the upper mantle.

In the Caribbean region, the seismicity is quite diffuse throughout the first 10 km layer. As the depth decreases, the frequency of events increases and accumulates predominantly in the southern limit of this region. Low-velocity anomalies may be associated with sedimentary deposits up to the first 20 km depth. To the west of the Andean region, seismicity and velocity distributions are defined by the subduction geometry of the Nazca Plate. Earthquakes are distributed along the Colombian trench in the Pacific Ocean, and on the mantle wedge under the continental region parallel to the coast. Negative velocity anomalies define the location of the mantle wedge along the Pacific coast which is located above the subducted Nazca Plate, that reaches a latitude of ~7°N. Towards the east, velocity anomalies become negative, indicating the thickest segments of the continental crust. Moreover, seismicity is aligned SW-NE agreed to fault system directions. This alignment is more explicit on the Eastern Llanos Foothills, where seismicity reaches depths close to 30 km. This feature remarks on a geologic boundary between the Andes and the Eastern region. Finally, seismicity in the eastern region is considered non-existent, except for the Puerto

Gaitan earthquake cluster. Negative velocity anomalies on the east flank of the Eastern Llanos Foothills may be linked with large thicknesses of sedimentary deposits, which gradually decrease as they move away from the Andean Mountain range.

The second seismogenic segment is located between 100 km and 200 km depth. Here, two broad groupings of earthquakes are possible to identify. The first, parallel to the Pacific coast and located south of ~ 5 ° N. The second, located north of this latitude and displaced east ~ 250 km. Earthquakes in the southern fringe are aligned parallel to the Pacific coast and the chain of active volcanoes in the Andes. To the north, the seismicity seems to continue in this same direction, but without the presence of volcanic activity. As a whole, the hypocenters delineate two Wadatti-Benoiff planes in Colombian territory, one to the south where the Cauca seismic nest is located, and the other to the north, where the Bucaramanga seismic nest is found. Except for the immediate vicinity of the latter, all events are located on high-velocity anomalies.

Vertical sections (defined in Figure 2) through the Vp and Vs anomalies, and relocated earthquakes within ± 5 km from the cross-section lines are shown in Figure 14, and Figure 15, respectively. Profiles 1 and 2 correspond to the Caribbean segment, while profiles 3 and 4 correspond to Cauca. Vertically, the events are grouped into the seismogenic sections of the crust and upper mantle. The dotted black-line represents the boundary between the two (Mohorodovic discontinuity, Moho). Given the concentration of earthquakes and the distribution of seismic stations in the Andean region, it is possible to accurately estimate the depth of the Moho below the Andean Mountain range of around 60 km. Towards the coastal regions, it is highly probable that this discontinuity is located at a lower depth, but our results are not decisive in this regard. The distribution of earthquakes in the crust is not conclusive when establishing vertical alignments to identify specific faults. However, it does allow the identification of some accumulations of events associated with fault systems for instance, the Eastern Llanos Foothills Fault System. Below 50 km the profiles of the Bucaramanga segment show two particular characteristics regarding the distribution of the hypocenters. The first of them corresponds to a gently sloping, almost flat distribution, that extends for ~ 200 km along with both profiles. A second section corresponds to a steeper distribution with a high concentration of earthquakes, where the Bucaramanga nest is located. In the profiles associated with the Cauca segment, seismicity is a consequence of the Nazca Plate subduction process.

The resulting anisotropic P wave model performed with ANITA shows that the reductions obtained was 15.16%. When comparing the locations in the starting 1D model and the final 3D anisotropic model, the residuals of P data reduced from 0.7986s to 0.6774s. The results and analysis are jointly explained in detail in the next section.

Discussion

The Andes Subduction System is an ideal natural laboratory for studying the relationships that arise between the angle of subduction, volcanic activity, seismicity and crustal deformation (Gutscher et al. 1999, 2000; Gailler et al., 2007; Espurt et al., 2008). Particularly the NW corner of the South American continent has been subjected to rigorous analysis regarding the coupling of two different subduction segments with each other: the flat subduction of the Caribbean plate and the steep subduction of the Nazca plate, both under the South America plate.

Our results for shallow depths (10 km - 50 km) show three differentiated regions. Two of them, the Caribbean and Eastern regions, with low-velocity anomalies, and a third region corresponding to the block of the Andes where the high lateral variation of P-wave and S-wave velocities predominates. Shallow and low-velocity anomalies in the Caribbean and Eastern Llanos are mostly associated with the presence of sedimentary basins. In the Caribbean, these anomalies extend south to a latitude of ~7°N. The most representative basins in the region are Sinú- San Jacinto (SSJB), Plato-San Jorge (PSJB), and Cesar-Ranchería (CRB), where sediments thickness has been estimated of up to 12 km (Bernal-Olaya, Mann, & Escalona, 2015; Flinch, 2003; Lara et al., 2013; Montes et al., 2010). In the Eastern Llanos region, the most striking contrast occurs throughout the entire fault system on the eastern flank of the Eastern Cordillera, where the sedimentary thickness is thicker compared to its eastern extension (Farris et al., 2011).

Lateral heterogeneities in the Andean region are determined by a complex geological history as a consequence of the stacking of diverse terrains since the Paleozoic. Poveda et al., (2018) associated high S-wave velocity anomalies to the presence of Batholiths (Antioqueño and Ibague), and outcrops of the Garzón and Quetame Massifs, and with Jurassic plutonism under the Central Cordillera. At intermediate crustal depths, below 30 km and up to 40 km, the P-wave and S-wave negatives anomalies define the crustal roots of the Eastern, Central, and Western Cordilleras. Some depocenters are identified, possibly associated with the segments where the crustal root is deeper. Poveda et al. (2015) based on analysis of receptor functions, suggested that the Eastern Cordillera has a thicker crust compared to the other two. Our results are not decisive in this sense. Still, it is possible to identify the sections where the cordilleras are isostatically compensated (the anomaly is stronger), in case the interpretation of Poveda et al. (2015) is correct.

Sella et al. (2012) had proposed that segments subducting from the west below South America may have the same geological origin and that the displacement in both velocity anomalies and seismicity below 100 km (upper mantle) is the consequence of a lithospheric tear. Our results may favor this interpretation since the distribution of anomalies to the west does not show discontinuities along the Pacific coast. On the contrary, they remain continuous throughout the different layers of crust and reach extensions near 7°N (border with the Caribbean region). One of these anomalies is located on the Pacific offshore (positive anomaly) associated with the thin thickness of the oceanic crust, while the other is negative and is found along the coast linked to an accretionary wedge.

The origin of the aforementioned lithospheric tear has been interpreted by some authors who suggest a time close to 10 - 15 Ma, since when the lateral displacement began between both segments (Dengo and Covey, 1993). Currently, there are two complementary hypotheses to explain the cause of this displacement. The first is that it originated as a result of the collision between the Panama Arch with the South American Plate (Vargas and Mann, 2013); and the second, by the subduction of a volcanic arc, which intensified the coupling between the South American plate and the segment of the Nazca / Caribbean slab north of the tear (Chiarabba et al., 2015). Overall, it is a zone of weakness from the Pacific, which once penetrates into the continent causes the total tearing of the Nazca plate in-depth in the continental region. Syracuse et al. (2016) from tomographic images established that below 100 km there is no connection between the two segments.

The distribution of our velocity and seismicity anomalies in the upper mantle (depths> 100km) support this interpretation. South of 5°N the seismicity configuration and the distribution of anomalies strictly obey the subduction of the Nazca Plate, which is reflected by a high deformation of the crust and the appearance of active volcanoes chains. Specifically, anomalies of the vertical sections from profile 3 Vp and Vs (Figures 14 and 15) show the location of the negative anomalies, that right in the Central Mountain range ascend and shape the active chain of active volcanoes in the region. To the north, the seismicity coming from the south moves eastward ~250 km and volcanic activity is non-existent on the surface. The negative and outstretched anomalies in profiles 1 and 2 from 14 and 15 figures suggest stagnant and coupled volcanic activity under the Andes. In the 4 profiles out of both graphs it is possible to observe negative anomalies possibly associated with dehydration processes of the slab stone that subducts right after the trench zone.

One of the central debates regarding the configuration of the northern segment of the 5°N revolves around the coupling of the Nazca and Caribe plates and the origin of the Bucaramanga seismic nest. Some authors such as Van der Hilst and Mann (1994) and Chiarabba (2015), suggest that the seismic nest has a Nazca origin, while authors such as Taboada et al (2000), Zafiri et al. (2007), Vargas and Mann (2013) and Syracuse et al. (2016), associated the intermediate seismicity of Bucaramanga with the Caribbean Plate.

New insights of angle subduction slabs: Vp/Vs anomaly distribution and dehydration process along Nazca and Caribbean segments.

Figure 16 shows Vp/Vs anomalies at 150 km and 200 km depth and four vertical sections. The embrittlement by dehydration hypothesis is currently considered as the primary mechanism for the generation of earthquakes in zones of double seismicity. They are linked to fragile faults associated with dehydration of minerals in the slab crust and upper mantle (Houston, 2015; Brantut, 2016). South of the Caldas Tear, the Vp/Vs anomalies align parallel to the Pacific coast and the chain of active volcanoes in the Andes. Unlike the Nazca Plate, the extent of Vp/Vs anomalies in the north segment occupies a large amount of the plate area, which in our view, serves as evidence to support that the dehydration process in the Caribbean Plate spread across an entire flat plate portion. Embrittlement by dehydration has been tested mainly by thermal-petrological models and laboratory deformation experiments for hydrated minerals in subduction slabs (see, e.g., Hacker, 2003; Jung, 2004). In the Caribbean Plate, the Vp/Vs ratio is lower near the coast and relatively high within the continent at 150 km depth (Figure 16).

Although the existence of hydrated minerals in subduction slabs has been demonstrated by studies of seismic tomography (Mishra and Zhao, 2004) and receptor functions (Kawakatsu and Watada, 2007), there are still doubts about where and how water migrates in a subduction zone. Vertical sections show high Vp/Vs velocity anomalies in the Nazca Plate (Profiles 3 and 4), close to the trench. Normal failure that occurs in the Nazca slab when it bends and enters the trench zone provides the adequate mechanisms that accelerate plate dehydration by the entrance of water into the subduction system, generating an increase in Vp/Vs anomalies. The Caribbean Plate case would be explained as an old and cold plate that is resistant to flexion near to the trench. So even if there is a dehydration process, it tends to be slow, limiting the melting of the mantle wedge and the formation of a volcanic arc, far away from the trench. Hydration processes also favor the serpentinization of minerals, which in the case of the Nazca segment, have been identified by the Colombian Geological Survey (SGC) on the surface along the Western Cordillera. In the northern segment, some ferronickel outcrops relatively close to the coast and that are exploited in open-pit mines serve as evidence of the serpentinization processes that ascends to the surface. In order to support our interpretation, we used gravimetric distribution maps (Figure 17), with the aim of identifying above them, the zones where, owing to the flexion of the subduction slabs, fracturing, water ingress and mineral transformation are generated. Indeed, it is possible to identify low gravimetric density zones because of hydrothermal processes that decrease its density.

At 200 km depth, Vp/Vs anomalies become smaller, suggesting that the slab subduction angle is tilted even further in both scenarios. According to our results, the Bucaramanga nest may be the result of massive dehydration, which stimulates gravitational collapse and slab rupture. Laboratory tests have shown that the presence of the molten phase, and increased water content and temperature, should decrease the Vp while increasing the Vp / Vs ratio (Hammond and Humpreys, 2000; Takei, 2002; Faul and Jackson, 2005). We interpret the reduction in Vp in the Bucaramanga nest as being caused by a combination of temperature and fusion effects. In our model, the simultaneous increase in Vp / Vs and decrease in Vp indicate that the molten mass or water may be present within the slab between 150 km to 200 km depths. High Vp / Vs values may also be linked to elevated temperatures (Karato, 1993; Faul and Jackson, 2005). Water presence and high temperatures are necessary conditions to generate mechanisms of intermediate-depth earthquakes of embrittlement by dehydration (Kirby et al., 1996) and thermal leakage (Keleman and Hirth, 2007; Prieto et al., 2012).

Is there evidence of the coupling of the Cauca and Bucaramanga segments along with the crust?

The complete separation of the segments of the Nazca and Caribe subduction slabs, below the thickness of the crust, has been supported by studies of seismic anisotropy. Porritt et al. (2014) used data from the SGC to investigate seismic anisotropy and slab dynamics based on SKS splitting. Their results show rapid polarization perpendicular to the Colombian trench zone, which, once they enter the continent, specifically the back-arc region, they abruptly change to parallel anisotropy. Additionally, they observed that said perpendicular alignment is a tendency towards the south of the lithospheric tear at 5°N, but that once said tear towards the north is exceeded, the rotation changes abruptly. This was interpreted as a complex three-dimensional flow near the contact edge between both segments and whose patterns correspond to the flow of the mantle around the edges of subduction slabs (Jadamec and Billen, 2010). Idárraga et al. (2016) also measured the S-wave splitting of SKS and local S related to subduction slabs from information from 38 seismic stations. They determined that the flow of the mantle in the South American NW system is controlled by the presence of structures associated with lithospheric tears such as the Caldas Tear and the Malpelo Tear. They also asserted that the rapid polarization of local S-waves aligns consistently with regional faults. It implies the existence of a confined anisotropy in the upper lithosphere and the mantle wedge does not contribute significantly to the S-wave splitting.

Unlike mantle anisotropy which is controlled by the circulation of fluids during convection heat transfer processes and is explained by the orientation of the olivine crystals

(Karoto and Wu, 1993; Fouch and Rondenay, 2006), the seismic anisotropy in the crust is largely controlled by the orientation and distribution of geological structures (Bokelmann, 1995). The fault systems become the features that provide the largest anisotropic properties (Zhang and Schwartz, 1994). The results of P-wave azimuth seismic anisotropy for the crust (10 km - 50 km) are shown in Figure 18. Thus, we estimated the direction and magnitude of azimuth P-wave anisotropy for the upper crust (10 km and 20 km layers, red color) and lower crust (30 km - 50 km, blue color). The maximum anisotropy anomaly is 15%. The anisotropy in the vertical sections was not shown because only the azimuthal anisotropy was considered. At all five depths (10, 20, 30, 40, 50 km), the anisotropy exhibits regular patterns that appear to be controlled by the major geologic structures.

On the Pacific coast, the direction of the high-velocity vectors tends to align perpendicularly to the trench zone. This distribution is caused by the Nazca Plate as it subducts under South America. The convergence of the subduction favors the projection of the main stress component in the west-east orientation ($S1$). On the Caribbean coast the convergence of subduction should also favor the projection of high-velocity vectors. However, this trend does not seem to be as evident as it is in the Pacific and the vectors direction follows different patterns. It is probable that the influence of the low convergence of the Caribbean slab subduction above the seismic anisotropy patterns is not as dominant as in the Pacific. Let’s consider that northward, the anisotropy must be strongly controlled by thick sedimentary deposits, and even by geological structures covered by sediments that have not been mapped yet. To the East, two regional trends are identified; the first one to the east flank of the Eastern Cordillera where the orientation of the high-velocity vectors is aligned perpendicular to the fault system, and the second trend located further east, where the preferred orientation is in a north-south direction.

The region with the highest anisotropic heterogeneity is in the Andean Block. The magnitude and direction will preferably respond to the structural and deformation control of the mountain block. Our results show that the perpendicular direction trend of the vectors in the trench zone changes to parallel anisotropy in the back-arc region, aligning with the fault systems of the Andes Mountain range. However, there is evident a strip in the 6°N where perpendicular direction to the trench is preserved really within the continent (Segment A, Figure 8). Along segment A, the alignment of vectors would be determined by the weak area that advances towards the continent in west-east direction and would be interpreted as the contact edge between Cauca and Bucaramanga segments. To the south and north of this segment, the vectors conserve a parallel alignment to the fault systems of the Andean block. Our model proposes that the boundary between Cauca and Bucaramanga segments in the crust occurs along segment A (~6°N) and dips towards the south to the upper mantle where segment B intersects. Along this last segment, Porrit et al., (2014) had already shown change in anisotropy vectors and had interpreted their result as a possible limit between both blocks in the upper mantle. Vargas et al., (2019) show in space inversion studies of seismic attenuation that there are significant changes in the thermal structure along the volcanic arc of the Andes, and that the isotherms throughout it also dip southwards similarly to how our model does, serving as evidence to support our dip hypothesis. Figure 19 schematically shows the interpretation of our results.

To complement the proposed scenario, we superimposed the open public database of maximum horizontal compressional stress SHmax compile under the WSM Project (Heidbach et al., 2018). Each stress data record plotted in Figure 18 is accurate to within ± 25° and was obtained from a single focal mechanism solution. These solutions at the western end of segment A tend to align with the high-velocity P-wave vectors. Additionally, we incorporated the velocity field for NW South America based on GPS continuously operating reference stations in Colombia, Panama, Ecuador and Venezuela (Mora-Páez et al., 2018), to evaluate if the displacement of the tectonic blocks corresponds to the preferential direction of propagation of the P-wave. The GPS results analysis assumes that the response of the recorded relative displacement obeys the entire thickness of the crust, while our results are discriminated for different depths. The similarities would show the likeness degree that the elastic properties of the medium have, while the differences would show a high heterogeneity of them and of the rheological properties of the crust.

The superposition of the previous vectors hints at the high tectonic complexity of the NW corner of South America, which should not only be characterized by the fault systems that comprise it, but it is also essential to analyze the effect of lithological contrasts, high variations in rheological properties between the upper and lower crust, high-stress zones and thermal contrasts (Jung and Karato, 2001; Kneller et al., 2005, Vargas et al., 2019). The collection of geophysical and surface geology evidence will jointly help to gradually clarify many of the observations already analyzed and will surely propose new and better hypotheses.

Conclusions

The velocity anomalies obtained and the relocation of earthquakes coincide with previously published studies. The interpretation of our model shows high-resolution velocity anomaly patterns that allow us to identify two subduction segments. An analysis of the distribution of Vp / Vs anomalies shows that towards the south of the lithospheric tear, the subduction angle favors the hydration of minerals and the appearance of chains of active volcanoes. To the north, the distribution of these anomalies suggests that mineral dehydration occupies a vast region, suggesting that the angle of subduction is not as pronounced as it is to the south of the lithospheric tear. Our model proposes that the origin of the Bucaramanga seismic nest is the Caribbean and that it is generated by a massive dehydration process of this slab. On the other hand, making estimates of azimuth anisotropy for the P-wave, we were able to establish that the coupling of both blocks begins at the surface around 6°N and dives south to 5°N in the upper mantle where there is no longer a connection between both segments.

Data and Resources

An open-access database about the local seismicity of Colombia, which was collected by the Colombian Geological Survey, was searched and requested using www.sgc.gov.co (Last accessed in February 2018).

Acknowledgments

Thanks to the Department of Geosciences of the Universidad Nacional de Colombia for partially supporting this research. Special gratitude to the Colombian Geological Survey (SGC) for sharing seismological information. For detail, source data refer to (https://www.sgc.gov.co/). Sincere thanks to Professor Ivan Koulakov, Corr. Member of

Russian Academy of Sciences, Vice-director of the Institute of Petroleum Geology and Geophysics, SB RAS, and Head of the Department of Geophysics, who provided us with the code LOTOS, as well as giving us constructive feedback for the improvement of the paper (Website Prof.: http://www.ivan-art.com/science/). S. Gómez-Alba thanks a fellowship by COLCIENCIAS (Grant: Doctorados Nacionales 617).

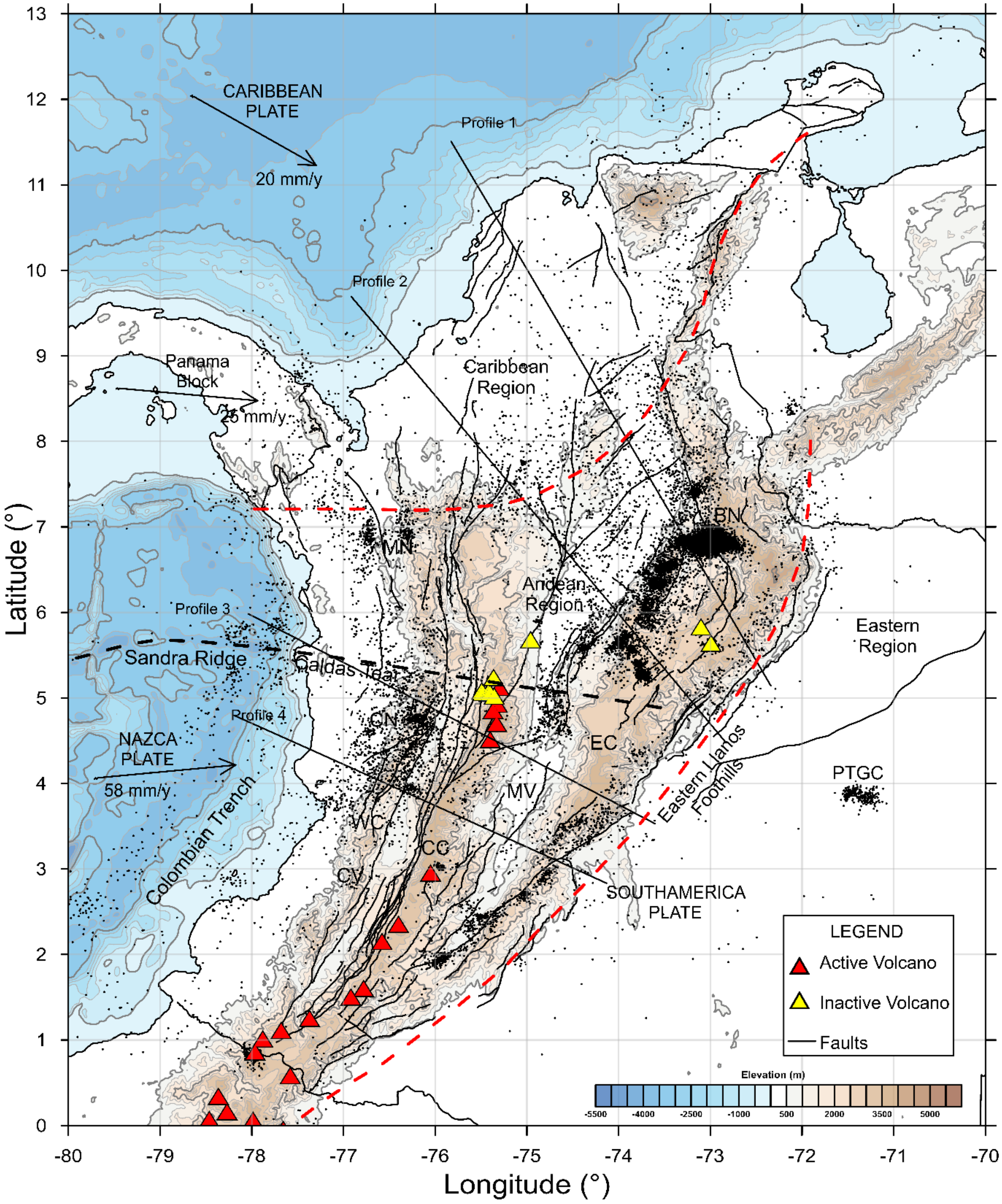

Figure 2. Tectonic setting of the northern Andes. The colored surface lines show the current topographic offshore and continental height levels of the NW corner of South America. Some topographic features on the map are: Eastern Cordillera (EC), Central Cordillera (CC),

Western Cordillera (WC), Magdalena Valley (MV) and Cauca Valley (CV). Plate motions relative to South America (Trenkamp et al, 2012) are shown as black arrows. Black lines represent major fault systems; red triangles, active volcanoes; and yellow triangles, inactive volcanoes. Three different regions have been delimited by red dotted lines: Caribbean to the north, Andean in the center, and Eastern to the right side. The black dotted line, in a west-east direction, represents a surface projection from the upper mantle of a zone of weakness coming from the Pacific and which once it comes into the continent, raises a lithospheric tearing (Caldas Tear). The gray points show the epicentral solution of earthquakes recorded by the Colombian Geological Service (SGC) from 1993 to 2017. Some seismological features shown on the map are Bucaramanga Nest (BN), Cauca Nest (CN), Murindó Nest (MN) and Puerto Gaitan Cluster (PTGC).

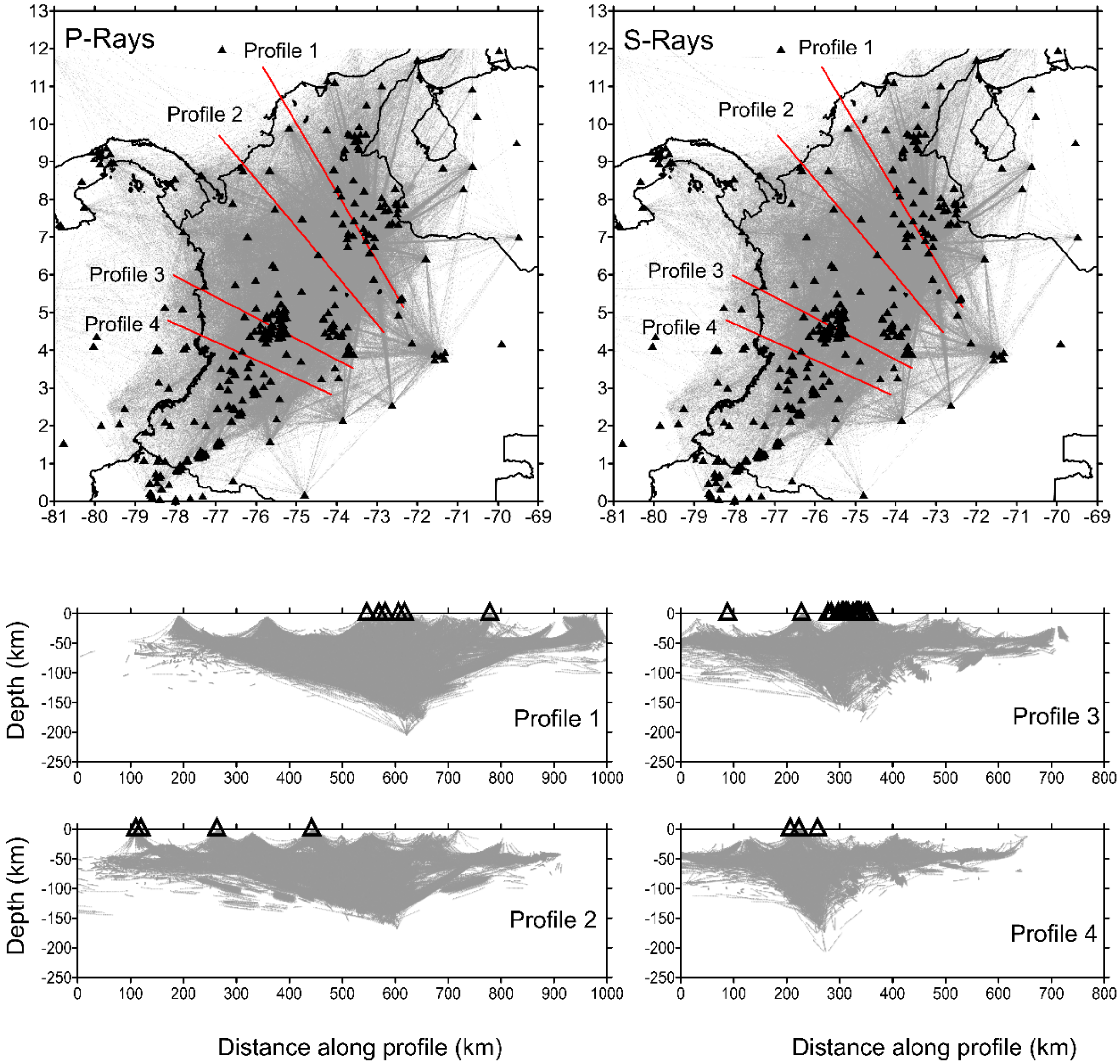

Figure 3. Ray coverage of p and s phases. Red lines show the location of the vertical profiles used in the analysis throughout this study. The black triangles show the distribution of the seismic stations.

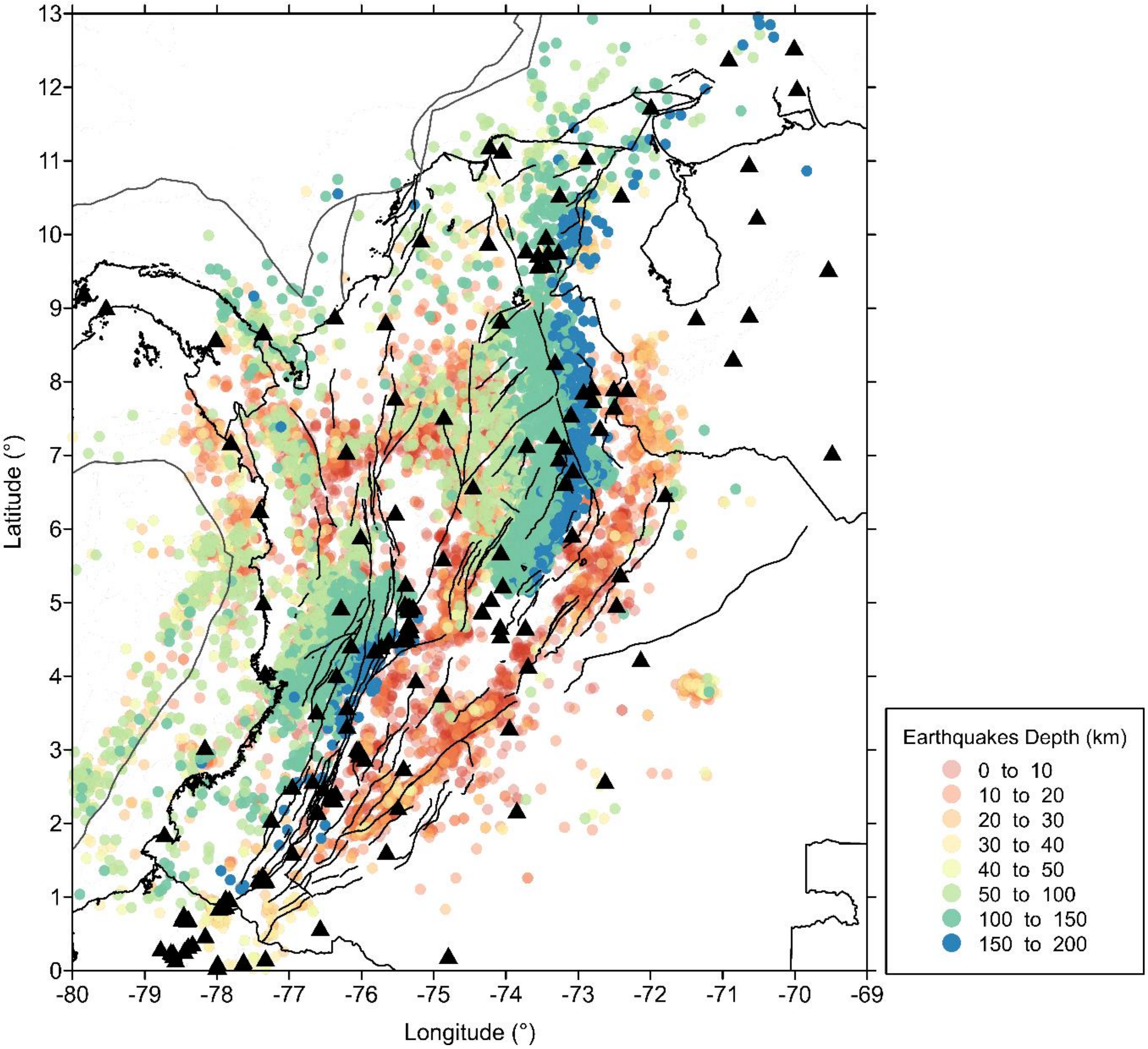

Figure 4. Relocated Seismicity by LOTOS. Earthquakes above 50 km correspond to 18% of the total events of this study and are related with deformation processes and faults in the crust. Below 50 km, events are linked to the activity of the upper mantle (78% of the events used in this study). The black triangles represent the location of the stations used in the relocation process of seismic events.

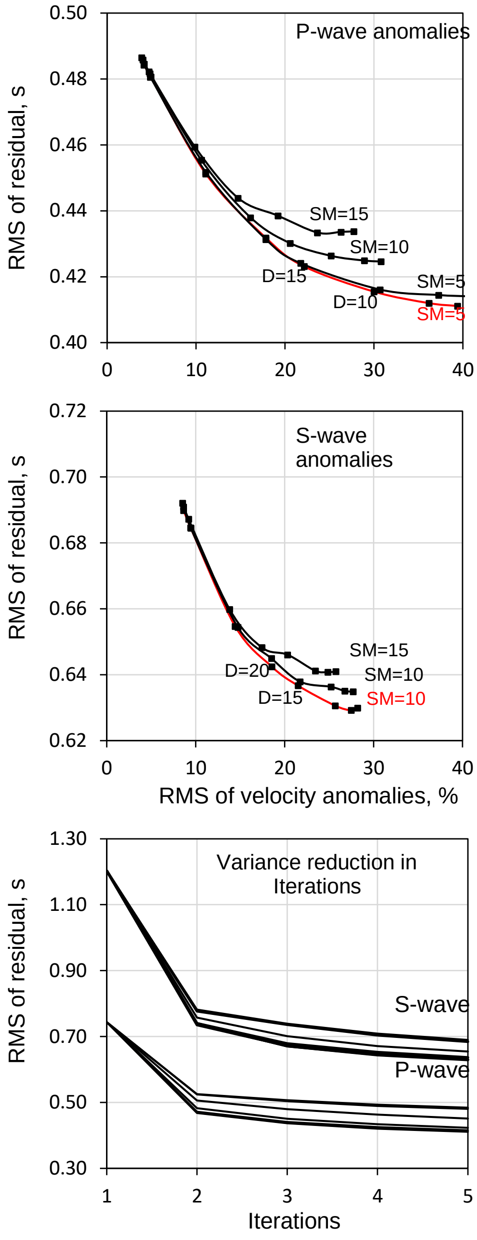

Figure 5. Trade-off curve (TOC) of the Variance of the velocity perturbations and de RMS travel time residuals. Damping parameters are denoted by black dots. Each curve represents different smoothing (SM) values. TOC were performed for both P and S arrival times. Bottom panel shows the Variance reduction Iterations, showing that after second iteration variance is not significant. Both inversions, the isotropic and anisotropic, show the same convergence.

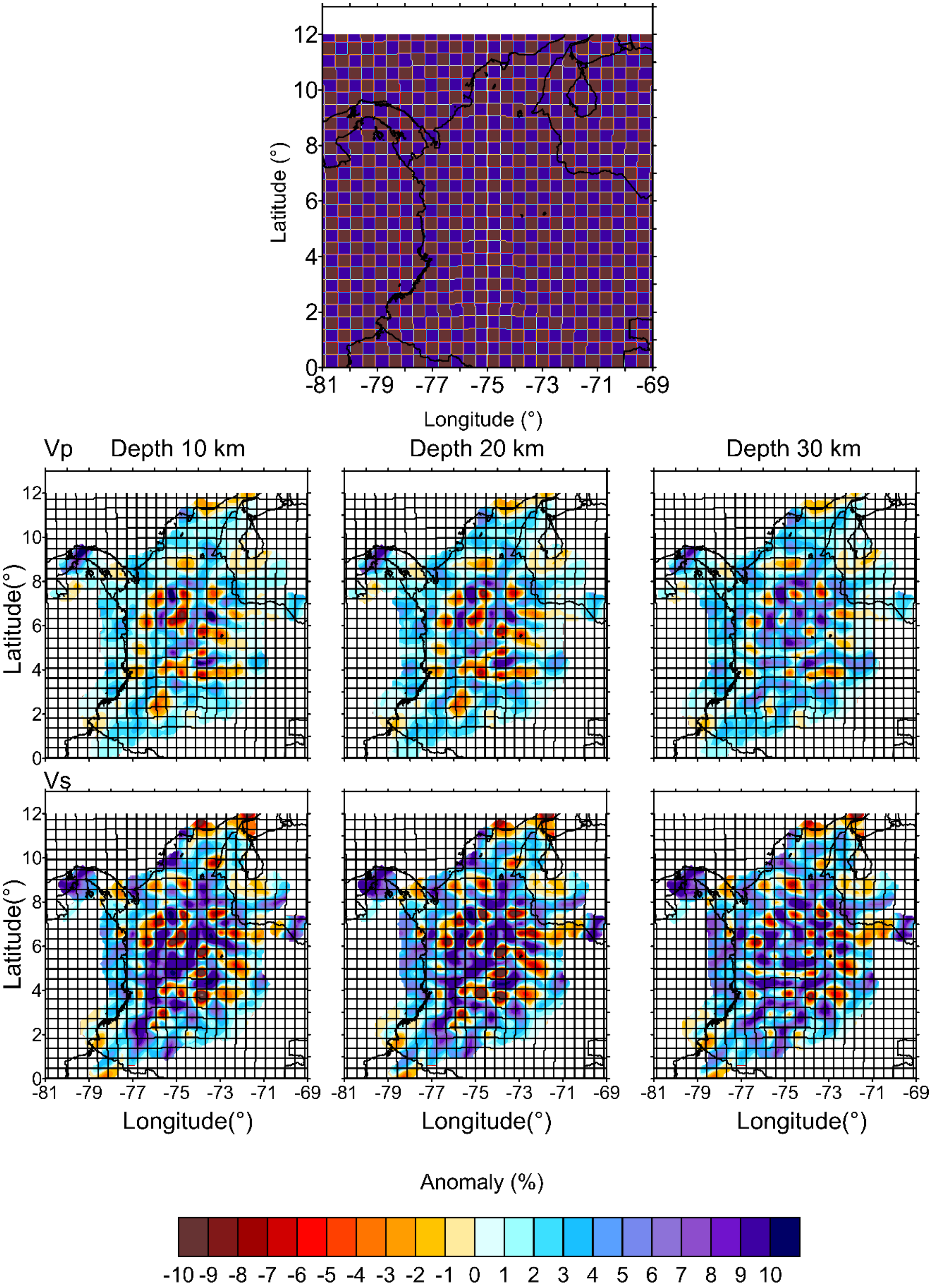
Latitude (°)
Longitude (°)
Vp
Depth 10 km
Depth 20 km
Depth 30 km
Vs
Latitude(°)
Longitude(°)
12
10
8
6
4
2
0
-81
-79
-77
-75
-73
-71
-69
Anomaly (%)
-10 -9 -8 -7 -6 -5 -4 -3 -2 -1 0 1 2 3 4 5 6 7 8 9 10

Figure 6. Checkboard Vp and Vs anomalies. Size anomaly 50km and layers 20km, 30km, 40km

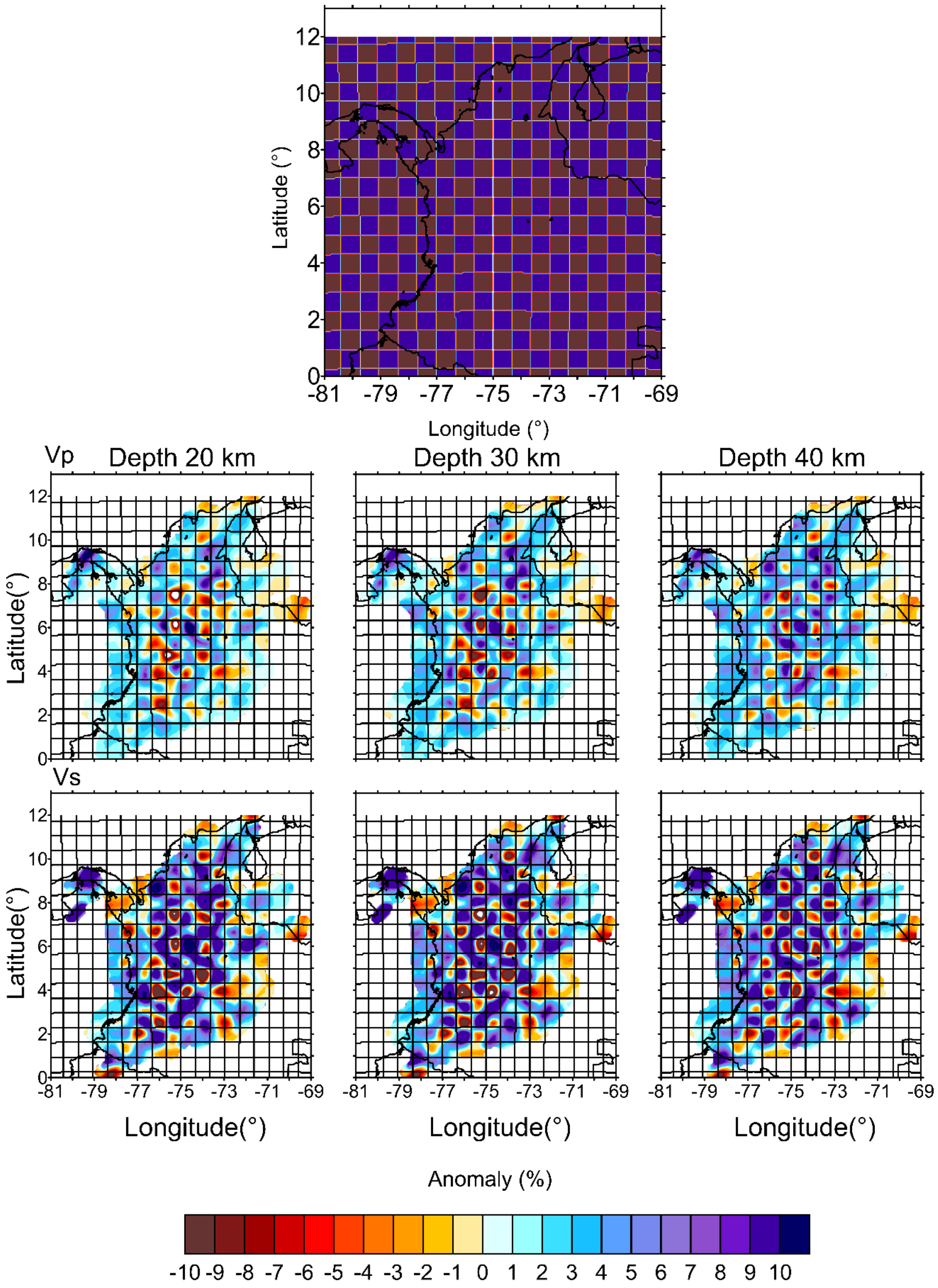
Latitude (°)
Longitude (°)
Vp
Depth 20 km
Depth 30 km
Depth 40 km
Vs
Latitude(°)
Longitude(°)
12
10
8
6
4
2
0
-81
-79
-77
-75
-73
-71
-69
Anomaly (%)
-10 -9 -8 -7 -6 -5 -4 -3 -2 -1 0 1 2 3 4 5 6 7 8 9 10

Figure 7. Checkboard Vp and Vs anomalies. Size anomaly 75km and layers 20km, 30km, 40km

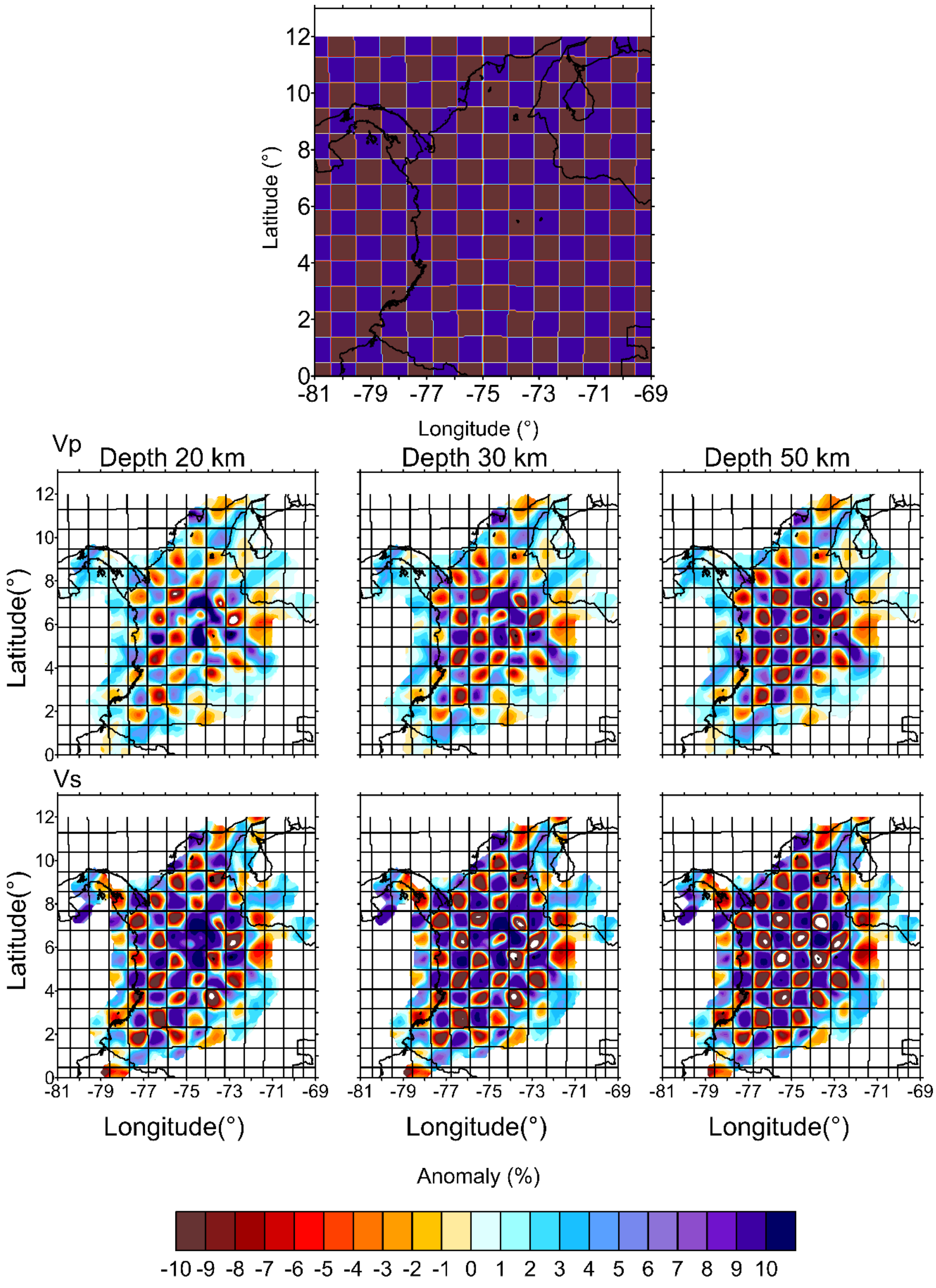
12
10
8
6
4
2
0
Latitude (°)
-81
-79
-77
-75
-73
-71
-69
Longitude (°)
Vp
Depth 20 km
Depth 30 km
Depth 50 km
Vs
Latitude(°)
Longitude(°)
Anomaly (%)
-10 -9 -8 -7 -6 -5 -4 -3 -2 -1 0 1 2 3 4 5 6 7 8 9 10

Figure 8. Checkboard Vp and Vs anomalies. Size anomaly 100km and layers 20km, 30km, 40km.

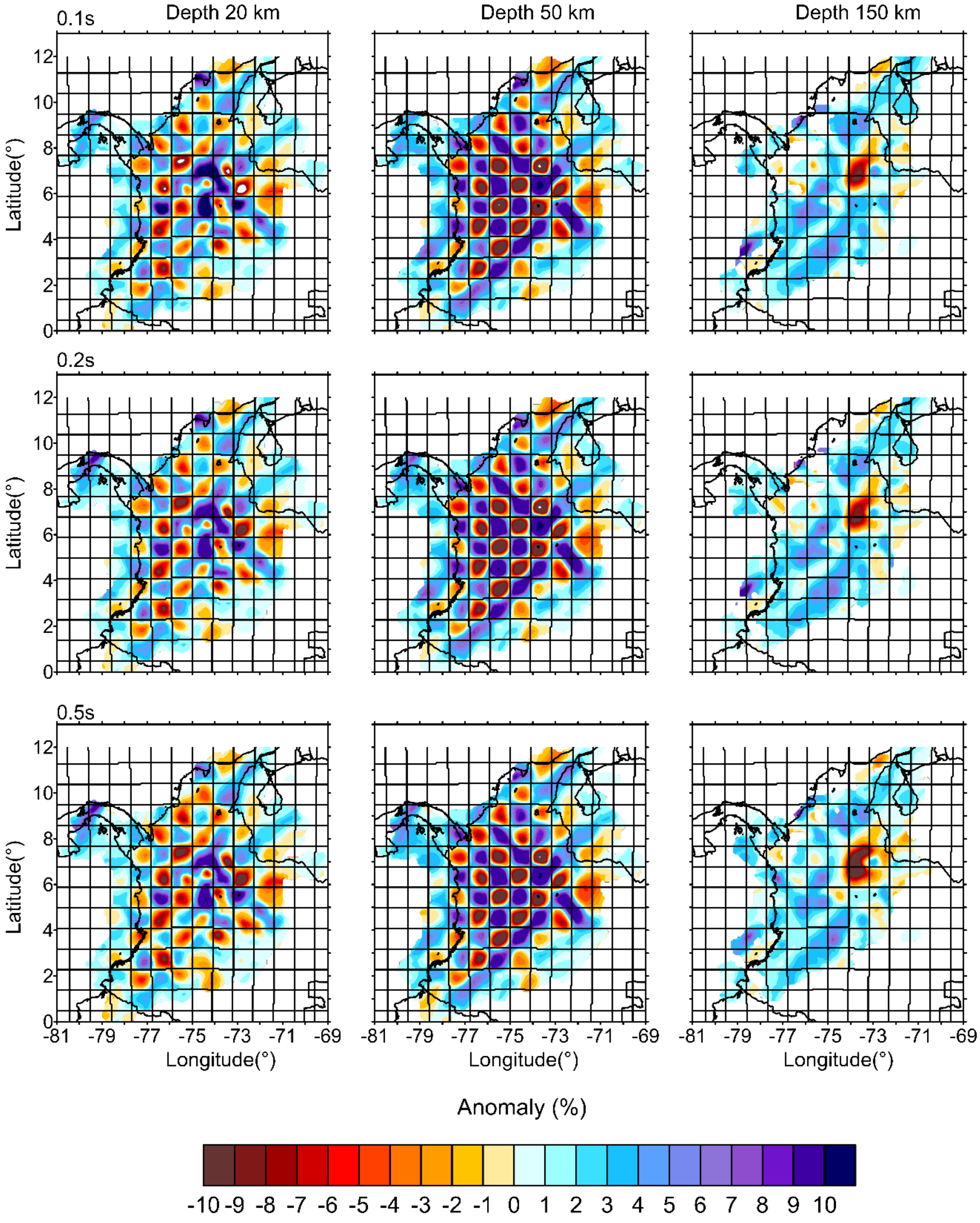

Figure 9. Checkboard Vp anomalies adding noise. selected depths of 20km, 50km and 150km

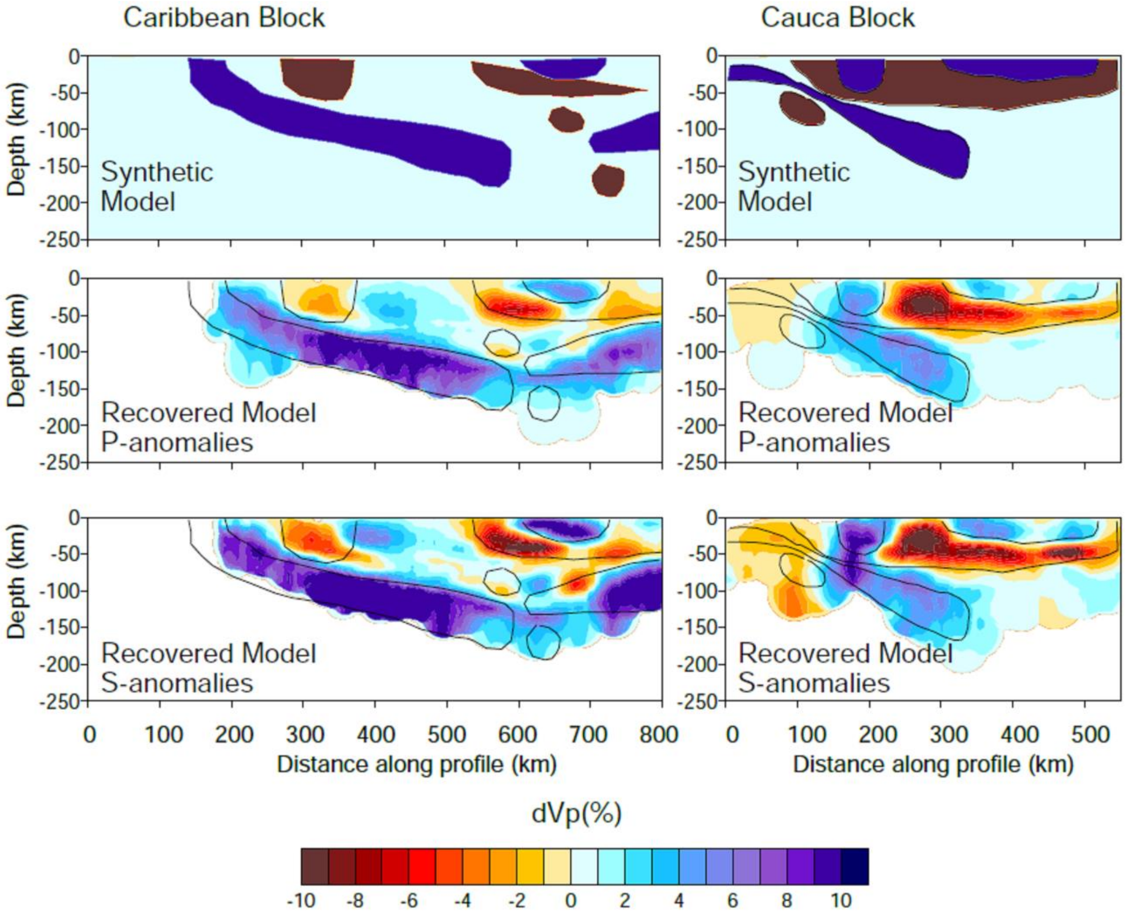

Figure 10. Free shape synthetic test for vertical sections. Slab shape structure may be identified.

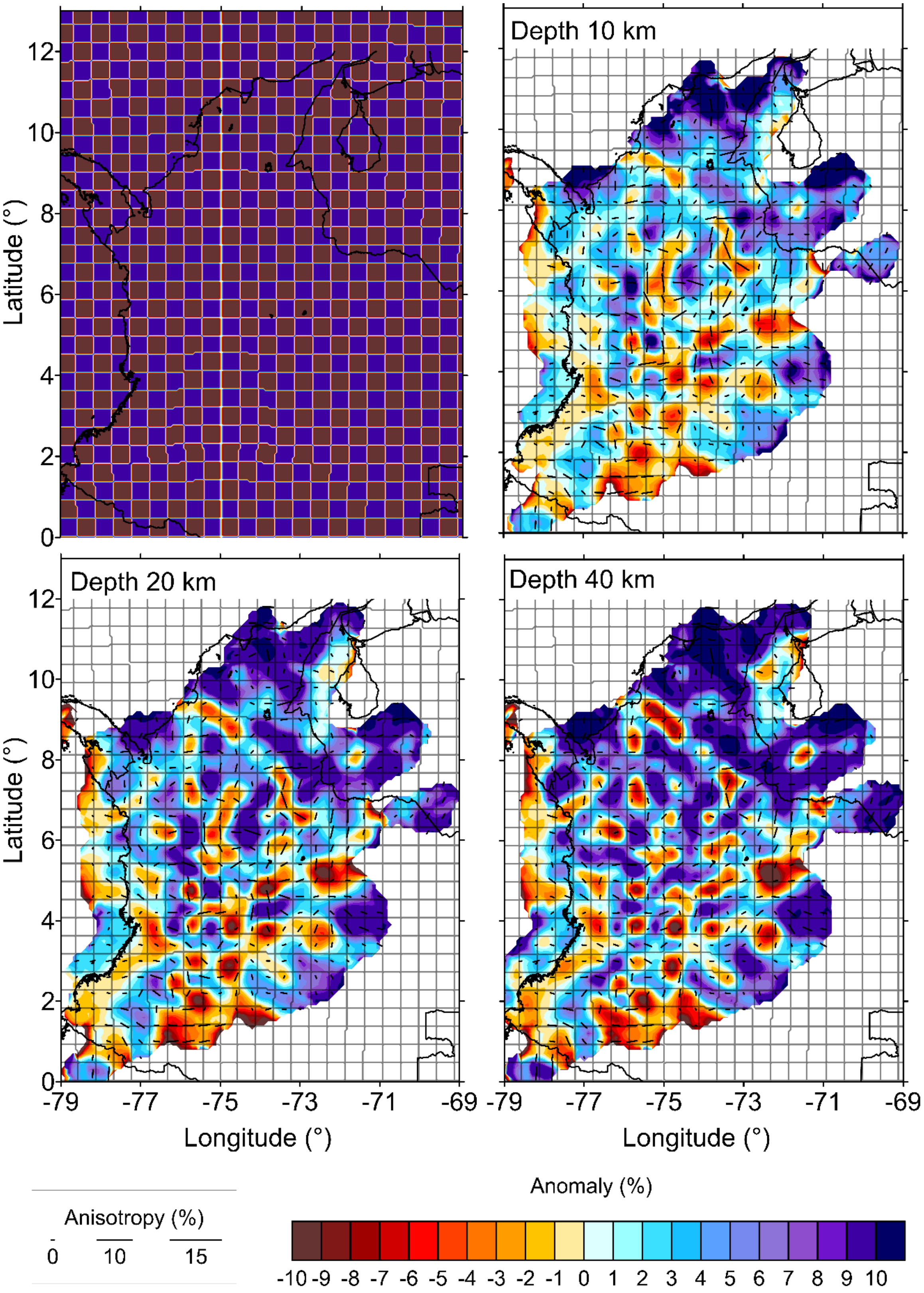
Depth 10 km
Depth 20 km
Depth 40 km
Latitude (°)
0
2
4
6
8
10
12
Longitude (°)
-79
-77
-75
-73
-71
-69
Anisotropy (%)
0
10
15
Anomaly (%)
-10 -9 -8 -7 -6 -5 -4 -3 -2 -1 0 1 2 3 4 5 6 7 8 9 10

Figure 11. Checkboard Vp anisotropy anomaly. Depths 10km, 20 km and 40 km and size anomaly 50km.

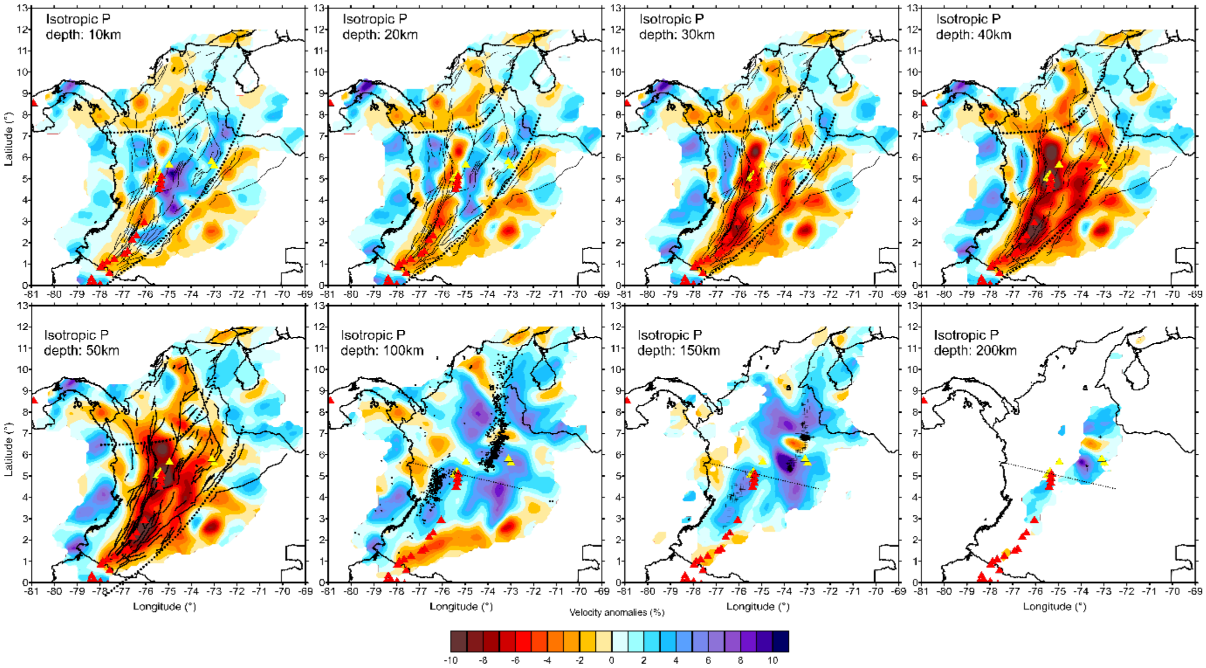

Figure 12. Vp perturbations (%) relative to the initial velocity model. for 10, 20, 30, 40, 50, 100, 150 and 200 km depth, resulting from the 3D inversion. Red triangles represent active volcanoes, while yellow triangles represent inactive volcanoes. Black lines represent major fault systems. The dotted black lines delimit the Caribbean, Andean and Eastern zones in the crust (10 km - 50 km). At mantle depths (> 100 km) the dotted black line represents the lithospheric tear that marks the border between the Cauca and Bucaramanga subduction segments. Black dots represent earthquakes for upper mantle depth.

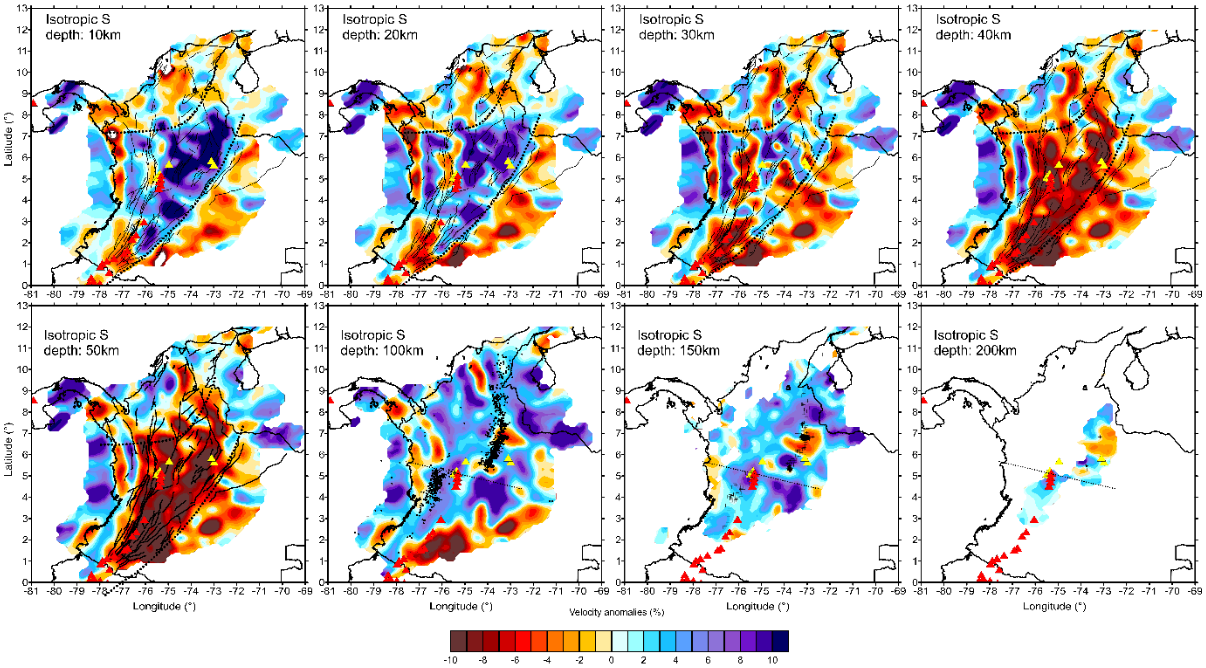

Figure 13. Vs perturbations (%) relative to the initial velocity model for 10, 20, 30, 40, 50, 100, 150 and 200 km depth, resulting from 3D inversion. Same details as Figure 12.

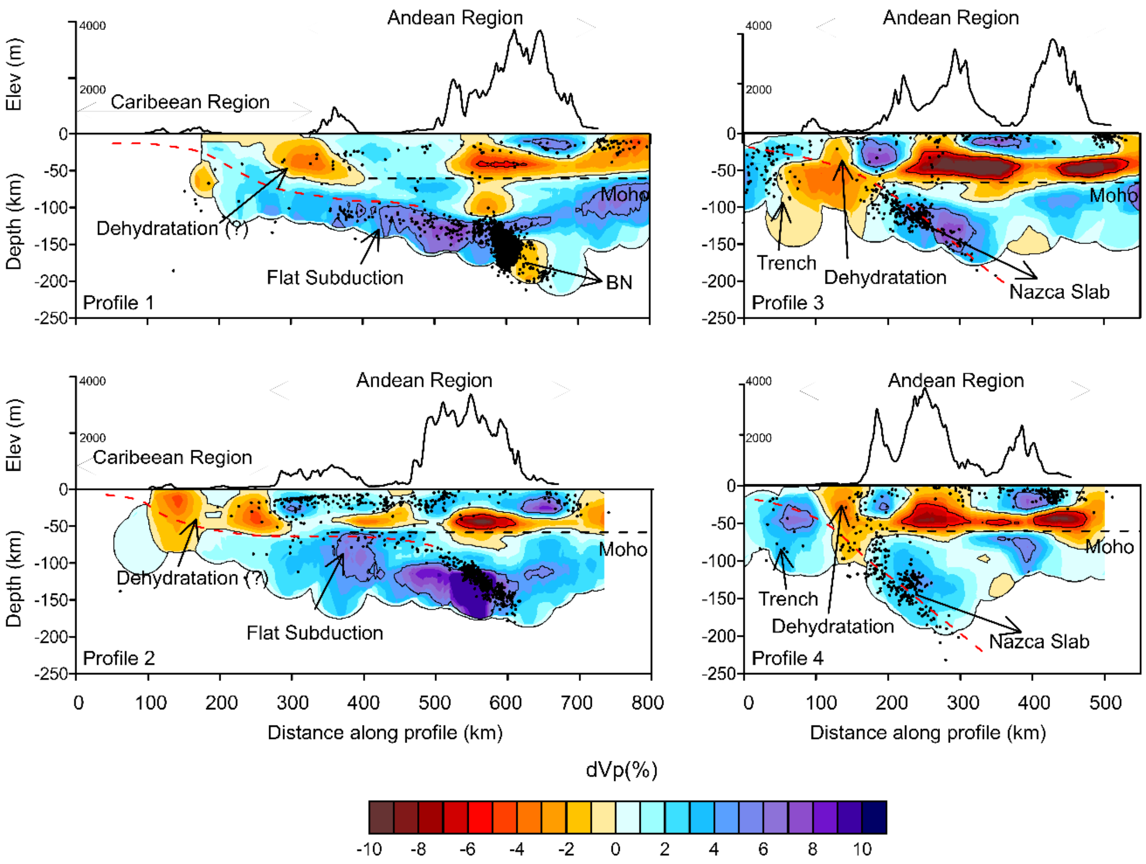

Figure 14. Vertical sections for Vp model (%) relative to the initial velocity model. Relocated earthquakes (black dots) are within ± 5 km from the vertical profiles defined in Figure 2. Black dotted line represents an indicative depth of Moho depth. Red dotted line at each profile is a schematic representation of slab subduction along the profile.

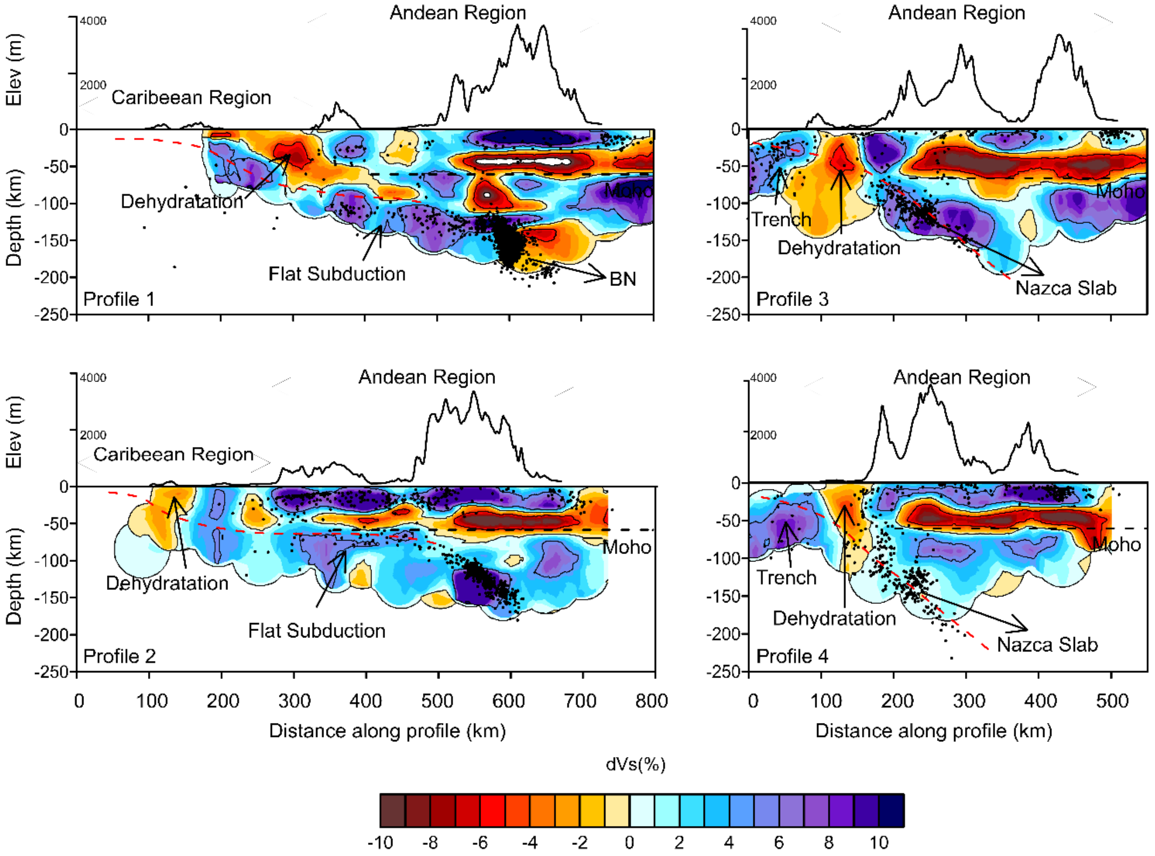

Figure 15. Vertical sections for Vs model (%) relative to the initial velocity model. Same details as Figure 14.

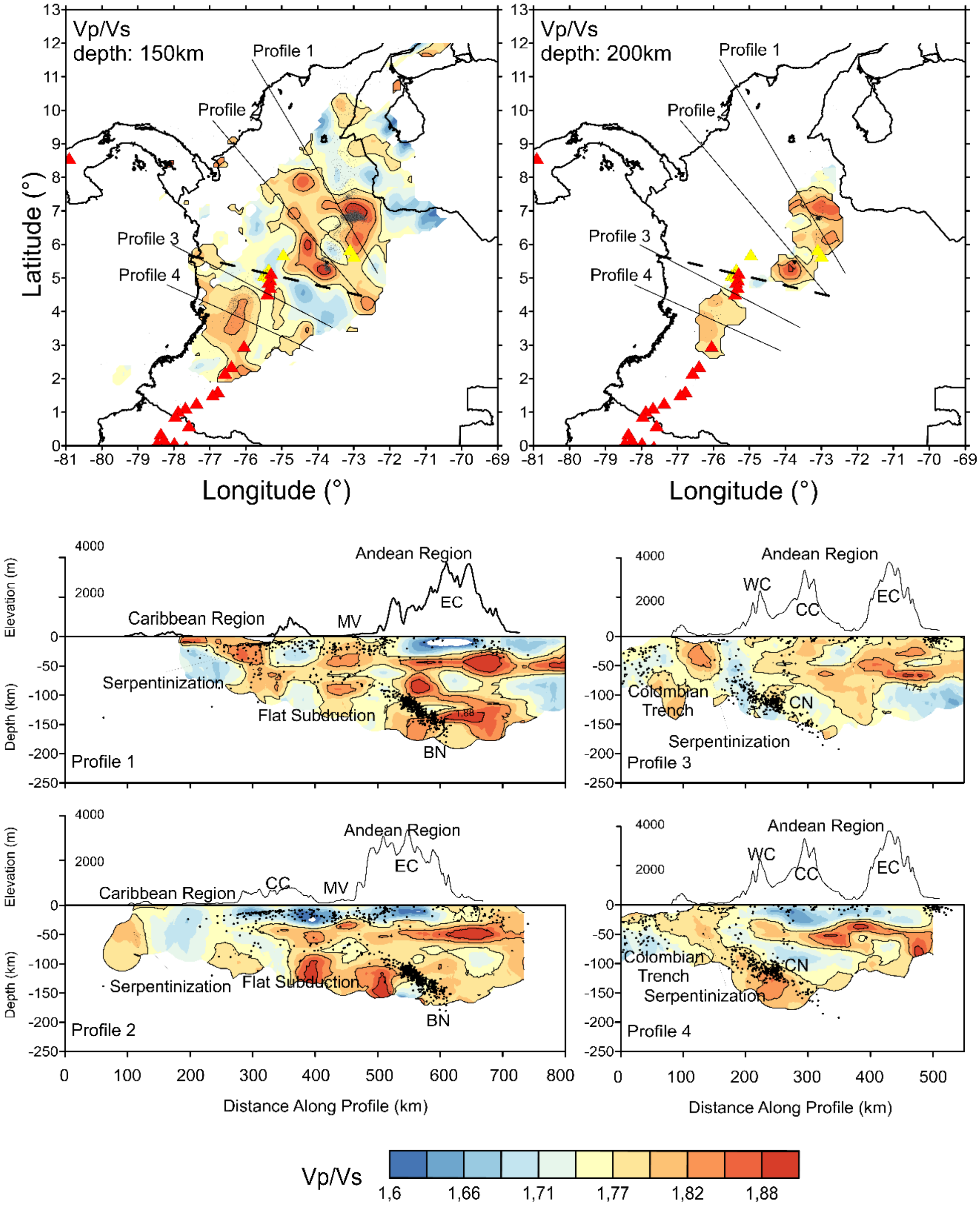

Figure 16. Distribution of Vp/Vs anomalies. The upper panels show the distribution of Vp/Vs at 150km and 200km depth. Dashed black line represents de Caldas Tear. The black dots represent earthquake distribution. Triangles represent volcanoes distribution: red are active and yellow are inactive. The lower panels show the vertical distribution of Vp/Vs anomalies

in the 4 profiles defined in the upper panels. The seismicity associated with each profile within ± 5km (black dots) is shown. Anomalies close to the trench zone are associated with the serpentinization process.

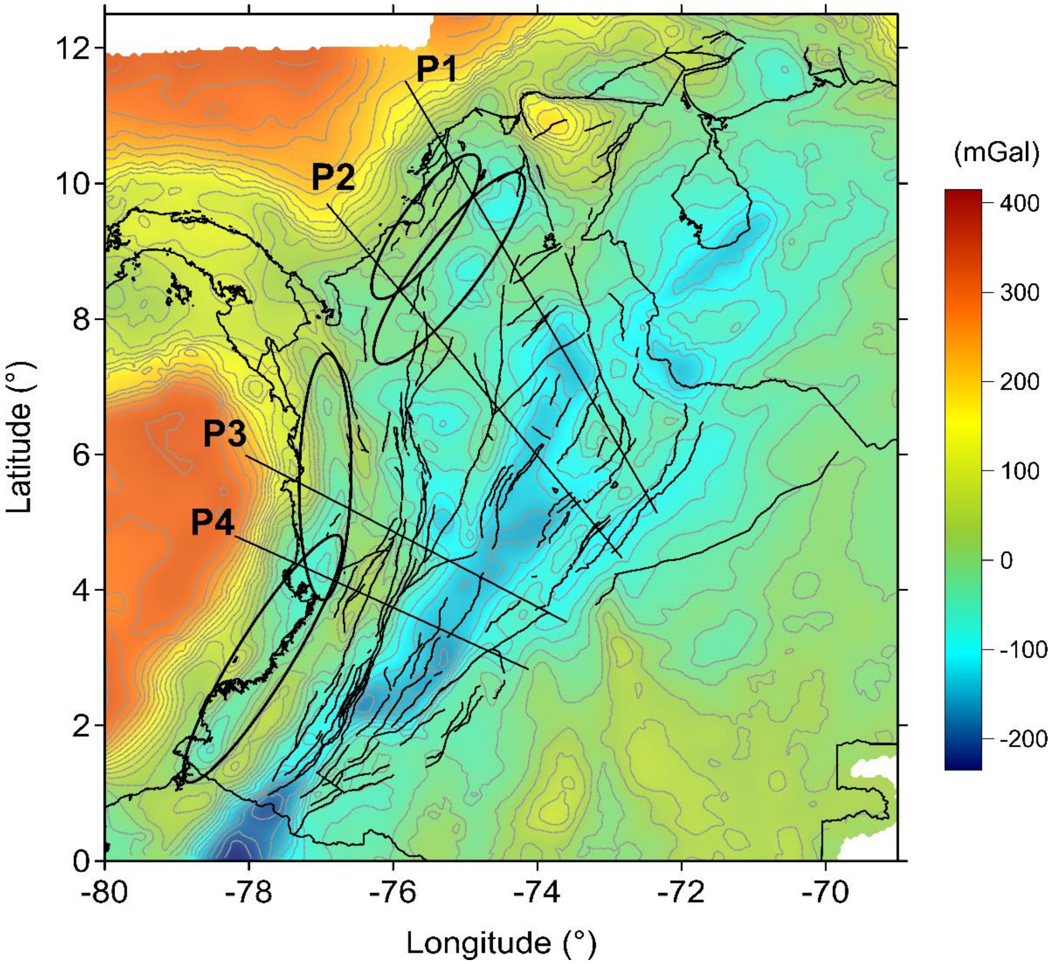

Figure 17. Distribution gravimetric anomalies in the NW corner of South America. Low gravimetric anomalies may correspond to areas with a high hydrothermal presence which reduces rock density. This trend is observed throughout the Nazca and Caribe subduction zone, and their location agrees with the analysis carried out of the distribution of high values of Vp/Vs of the vertical profiles analyzed in Figure 16.

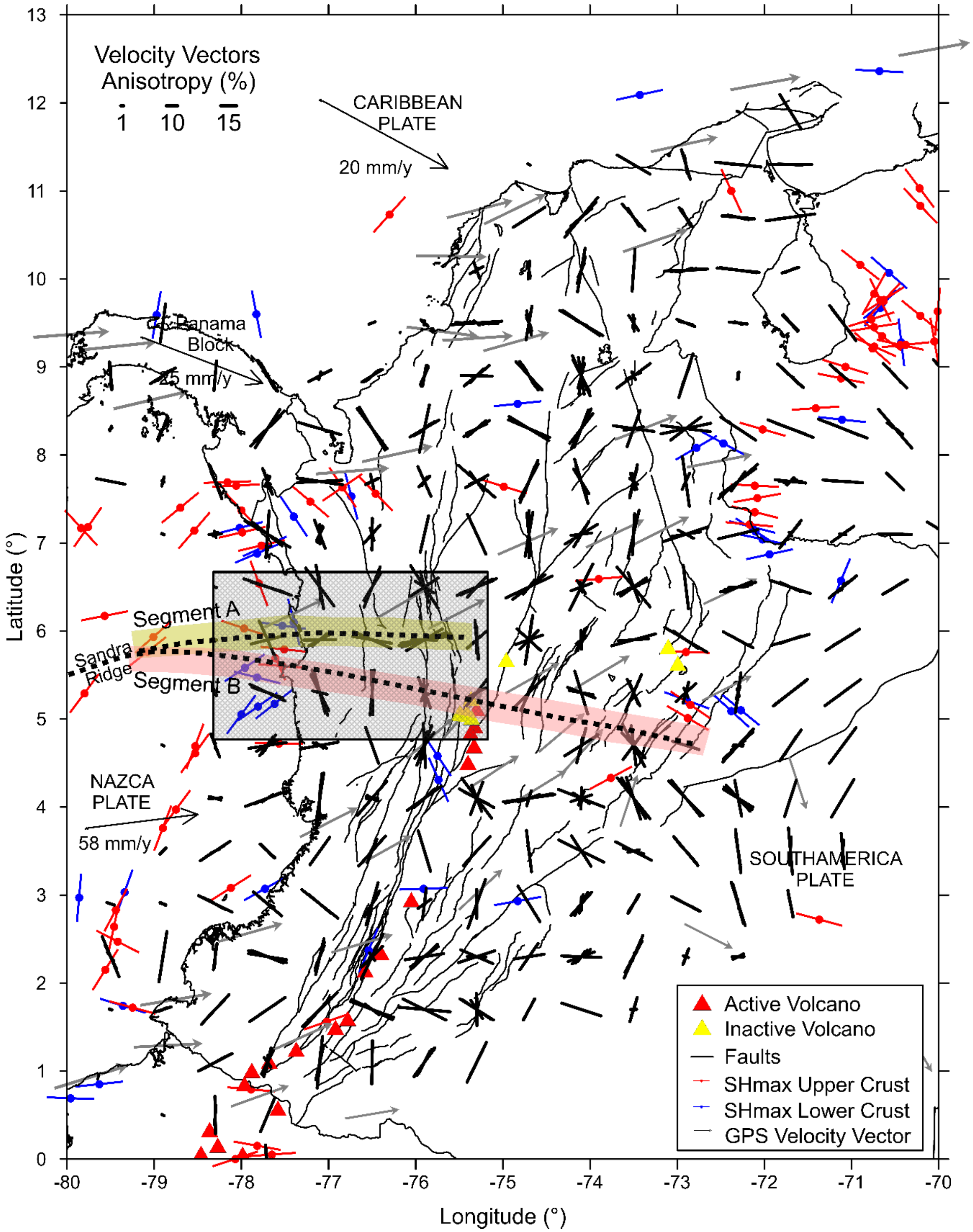

Figure 18. Distribution of P-wave azimuthal anisotropy vectors (Black vectors) along the crust. The direction of the velocity vectors aligned in a north-south direction, change their

orientation around 6°N and then reorient in the direction of the fault system of the Andes (gray box). This change in orientation (Segment A, yellow) is interpreted as a band of weakness where the coupling between the Nazca and Caribbean segments in the crust takes place. Segment B is the projection of the complete lithospheric tear between both blocks and which takes place in the upper mantle proposed by other authors. Although anisotropy in the crust is governed by fault systems, the high anisotropic heterogeneity shown, demonstrates the complex interaction that exists between tectonic stresses, rheology, and mineralogical composition in the NW corner of South America. Vectors of maximum compressional horizontal stress estimated by the WSM Project, and the GPS displacement vectors (gray arrows) are also overlapped.

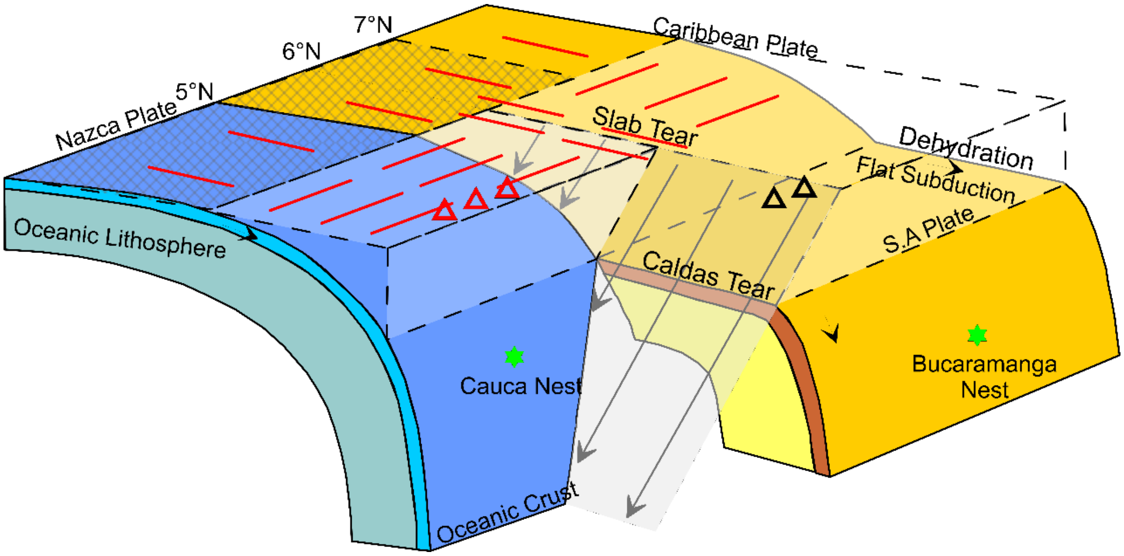

Figure 19. 3D schematic figure summarizing the main features deriving from this study. The angle of subduction of the Nazca plate (blue), favors dehydration of the slab and the appearance of volcanic active chains. In the Caribbean block (yellow), mineral dehydration occurs in a vast region of flat subduction that does not favor the appearance of active volcanoes. The Bucaramanga nest is the product of a slab break-off due to the high-water content and high temperatures in the Caribbean segment. The red lines indicate the direction of the P wave azimuthal anisotropy vectors. Around 6 ° N an abrupt change in their direction is identified, inferring that there is a contact zone between the Nazca and Caribbean segments. This zone of weakness goes deep, while diving southward. Once 5 ° N and the depth of the mantle have been reached, it is evident that there is no connectivity between both segments, suggesting that the lithospheric tear has completely occurred.

Table 1. Colombian layered earth model. Constant $\frac{V_p}{V_s} = 1.78$ (Ojeda and Hasvkov, 2001)

Depth (km)	**V_P (km/s)**	**V_S (Km/s)**	**Density (g/cm^3)**
0	4.8	2.697	2.66
4	6.6	3.708	3.02
25	7	3.933	3.1
32	8	4.494	3.3
40	8.1	4.551	3.32
100	8.2	4.607	3.34

CHAPTER 3. STRESS FIELD ESTIMATION BASED ON FOCAL MECHANISMS AND BACK PROJECTED IMAGING IN THE EASTERN LLANOS BASIN (COLOMBIA)

Introduction

The confluence of declines in the volume of Colombian oil reserves and dynamics in the global hydrocarbon sector prompted the Colombian government to create the National Hydrocarbons Agency (ANH) (www.anh.gov.co) in 2003. The ANH's was tasked with promoting the Latin American nation as an attractive place for investors interested in new Exploration and Production (E&P) contracts, exploratory well drilling, daily production of oil and gas increases and mature field revitalization. Per ANH data, increased production has been driven by the reactivation of heavy oil fields such as Castilla, Chichimene and Rubiales-Pirirí. Today, these three fields boast higher productivity due to the successful implementation of new technologies and enhanced recovery methods, including water injection, internal combustion and steam injection operations.

Recently, the Colombian government has sought to develop Unconventional Reservoirs (UR); thus, the ANH has also been involved in creating special regulations to mitigate the consequences brought about by the development of URs. Notable consequences of URs include water pollution and induced seismicity. Let us focus our attention on the latter situation, induced seismicity. Starting in the mid-20th century, numerous cases have been reported worldwide. Most of these events have been attributed to high-pressure fluid injection into subsurface rock formations (Nicholson et al., 1992; McGarr et al., 2002). Fluid injections are associated with water waste disposal reservoirs, secondary recovery oil, waste fluid from coal bed methane production and brine from hydraulic fracturing of shale gas. With regard to magnitude ranges for these induced events, we find variation: Mw 3.9 at Ashtabula, Ohio, Mw 4.3 at Paradox Valley, Mw 4.7 at Guy, Arkansas, andMw4.9 at Rocky Mountain Arsenal (Herrmann et al., 1981). In Colombia, induced seismicity has not been thoroughly studied, yet recent observations point to an increase in the number of earthquakes in Eastern Colombia. A total of 40 events (Table 2) with magnitudes greater than Mw 3.5 have been recorded since 2013 by the Colombian Geological Survey (SGC) in Puerto Gaitan, Colombia. To put this number in perspective, in the same region, only five events with Mw < 3.0 were recorded in the 20 years prior to 2013. Interestingly, annual reports published by the Colombian Ministry of Mines and Energy (www.minminas.gov.co) show greater oil production in the same area beginning in 2009 (Figure 20). In fact, these reports discuss a maximum average monthly production of 212.000 Bbl/day reached in August 2013. When the study area's seismicity in 2013 and 2014 is compared to average monthly oil production volumes, some level of correlation is found; in other words, there exists a level of correlation between the date of production reports and seismic activity. In response to this correlation, this paper aims to evaluate the hypothesis that relates induced seismicity with increased production within the framework of recent recovery stimulation projects based on available data. To this end, this paper estimates the stress field in the study area, for once the stress field is determined, it is possible to establish whether the impact is significant regionally or only locally.

Tectonic setting

The Eastern Llanos Basin: Geomorphologic boundaries for this basin are the Colombian Venezuela border to the north, the Macarena Peak and Vaupes Arch to the south, the Guaicaramo fault system (GFS) to the west and the Guiana Shield to the east (Casero et al., 1997; Gomez et al., 2005). The major tectonic events that have influenced the development of the Llanos basin are all closely linked to the development of Western South America's active margin. In fact, the region's structural evolution can be understood in terms of eight major events (Cooper et al., 1995):

a. Triassic Early Cretaceous: rift basins developed as a result of the separation of North and South America as the Caribbean opened (~235e130 Ma); these deposits formed a syn-rift mega sequence.
b. Barremiane Maastrichtian: a prolonged period of episodic extension occurred on a series of extensional faults (e.g., the GFS) along with passive regional subsidence in a back-arc basin (~125e74 Ma); these sediments constitute a back-arc mega sequence.

c. Maastrichtian Early Paleocene: the final event in the accretion of the Western Cordillera caused uplift and erosion in the Central Cordillera (~74e65 Ma), thus spurring the onset of the pre-Andean foreland basin mega sequence.
d. Middle Eocene: an early compressional deformation event affected the Magdalena Valley and the western margin of the Eastern Cordillera (~49e42 Ma) on account of an increase in convergence rates of the Nazca and South American plates (Pardo-Casas and Molnar, 1987).
e. Late Eocene Late Oligocene: a prolonged period of subsidence and localized normal faulting occurred in response to lithospheric flexure in the foreland basin created by the deformation load of the Western and Central Cordilleras (~39e29 Ma).
f. Late Oligocene Early Miocene: deformation in the Cauca and Magdalena valleys caused continued subsidence in the Llanos basin (~29e16.5 Ma).
g. Middle Miocene: a phase of rapid subsidence occurred as deformation, uplift and erosion began in the Eastern Cordillera and established the foreland basin depocenter in the Llanos foothills (~16.5e10.5 Ma); this is the Andean foreland basin mega sequence.
h. Late Miocene Today: the latest phase of compression and inversion associated with the formation of the frontal fold and thrust belt of the Eastern Cordillera (10.5 Ma present day).

It is worth mentioning that the oil industry is the principal source of information for developing subsoil models in the Eastern Llanos Basin. Initially, these models are set to small fields during exploration studies and later correlated with adjacent fields to create regional models. Figure 21 presents a structural section encompassing the Eastern Cordillera and the distal zones of the Eastern Llanos basin; likewise, this figure offers a representative stratigraphic column of the study area.

Petroleum Geology: Source rocks for the Llanos Foreland Basin are located beneath the eastern flank of the Eastern Cordillera. Kerogen types II and III are found in the mixed marine continental shales of the Gacheta Formation, with Total Organic Carbon (TOC) ranging from 1% to 3%. Additionally, the primary source has 150e300 ft of effective thickness. Two pulses of migration have been observed: the first in the Upper Eocene-Oligocene; the second in the Miocene and continuing to the present. The Paleogene Carbonera (C-3, C-5 and C-7, Figure 21) and Mirador Sandstones represent excellent reservoir units. Within the Cretaceous sequence, several sandstone intervals also served as excellent reservoirs. Sedimentary thickness increases are east to west in nature, without exception. As for porosity, this aspect decreases in the same direction from 30% to roughly 10%. Pay thickness varies from a few feet to 180 ft, depending on the well's location within the basin. API gravity ranges from 12 to 42. The C-8 unit of the Carbonera formation has traditionally been considered the regional seal of the basin. Still, given the Carbonera C-2 unit's extension, it should be viewed as the best seal. Even-numbered Carbonera units are recognized as local seals, along with the Cretaceous Gacheta and Guadalupe formations, both which may turn out to be self-sealant. Official records indicate more than 1500 MMBO of recoverable oil. Thus far, two giants (Caño Limon and Castilla) three major (Rubiales, Apiay and Tame Complex) and more than fifty fields have been discovered. Exploratory drilling has been concentrated in normal, up-to-the-basin (antithetic) faults. High-potential exploration targets include poorly-tested reverse fault anticlines, low relief anticlines and stratigraphic traps (pinchouts, paleohighs, channels) (Barrera et al., 2007).

Puerto Gaitan: The study area is located on the flat foreland (Figures 2 and 21), a region characterized by a thin sedimentary section onlapping the basement, normal faults and drape structures. The structure can be described as a northwest dipping homocline with a cover of Cenozoic to recent Sediments. This homocline has been slightly deformed by synthetic or antithetic normal faults marked by small displacement.

The main oil accumulation in the area occurs in the Carbonera Basal interval or “C-7” unit of Carbonera Formation at a depth of approximately 2700 ft. Oil has been deposited in a varied succession of fluvial environment genetic units, which hold oil producing columns between 7 ft and 60 ft thick. The main trapping mechanisms combine structural and stratigraphic features. On one hand, proper structural traps may be formed by normal faults up thrown into the basin. On the other, stratigraphic features comprise diverse fluvial regimes in which channel bars are stacked vertically as part of successive fluvial plains; these plains, in turn, display lateral variability (Dasilva et al., 2014). Paleogene and Neogene sediments overlie a

Paleozoic sequence. Diachronic erosion or time-transgressive deposition of Upper Cretaceous to Paleogene sequences produces a basal, onlapping stratigraphic architecture (east-southeastward, see e.g., Yoris and Lugo, 2009). The basal onlapping sections rest directly on a Paleozoic sequence and corresponds to the basal section of Carbonera Formation. The Carbonera Formation includes a succession of sandstones and shales (Gomez et al., 2010). These shales represent the vertical seal for hydrocarbon migration. In this area, younger units of this Paleogene sequence are known as “Arenas Basales,” representing an informal unit to describe the Carbonera basal or “C-7,” an oil-bearing stratigraphic interval in the local fields. Part of the basal onlapping section, this unit is deposited in diverse fluvial regimes in which channel bars are stacked vertically in successive, laterally variable fluvial-plain deposits. Overlying the Carbonera Formation is the Leon Formation, which was deposited during a period of marine transgression. The main lithology in this formation is shale. Subsequent deposits include the Guayabo and Necesidad formations, which are shallow marine and continental sediments, respectively. Overall, the structure in the basal sands can be described as normal, faulted, with homoclinic sections and dipping slightly to the northwest. These normal faults control the distribution of the reservoirs in the area and explain the presence of different compartments for the accumulation of hydrocarbons. Furthermore, lateral variations in facies play a fundamental role in hydrocarbon trapping mechanisms.

Data and methodology

Seismological data: This paper relies on data from the SGC. Operating continuously from June 1993 to the present, the SGC now consists of 52 seismological digital stations located across Colombia, many of which are broad band (Figure 1). In response to the high concentration of seismic activity in the West and Central regions of the country, the majority of SGC's stations are located in these two regions (for the primary characteristics of SGC, see Table 3). Broadly speaking, satellite signals are sent to and processed in real time by a master station in the Colombian capital, Bogota. In 2012, the SGC picked up on a significant increase in seismic activity in the country's eastern region (Figure 20). Previously, a lack of seismic activity had characterized this region, and, as a result, Eastern Colombia had essentially no seismological stations installed by the SGC. The Puerto Gaitan broad band station (PTGC)was installed in September 2013 to study the anomalous seismic activity, and it is located around 70 km from the area; there are, however, other stations in Eastern Colombia, though they are 150 km or more from the study area. Figure 22 presents two maps of isolines with the minimum magnitude recorded by the SGC. Both maps display the contrasting thresholds for two periods: 1) period of anomalous seismic activity, 2011-2012; 2) period of probably-induced seismicity, 2013-2014. When interpreting these data, it is important to keep in mind that on a country-wide scale, no significant changes were observed. In this sense, and from a regional perspective, the study area's threshold is essentially the same from period to period; similarly, hypocentral parameters are comparable for the two periods. Moreover, in order to define the threshold in the study area (70.5°W – 72°W and 3.0°N – 4.5°N), we estimated the Magnitude of Completeness (Mc) based on the Gutenberg-Richter law (Alessandro et al., 2012) for two time periods: 1) pre-installation of the broad band PTGC (September 2013); and 2) post-installation to present. Our results indicate a decrease in the threshold from 2.7 to 2.2, as can be seen in Figure 22. These two values were calculated using the Maximum Curvature method, which arrives at the highest value of the first derivate of the frequency-magnitude function for each time period (Wiemer and Wyss, 2000). Dropping from 2.7 to 2.2 (a M0.5 improvement) in the threshold detection seems reasonable in light of the seismic station PTGC's proximity to the seismic cluster under study.

All local events studied in this paper took place in 2013 and 2014 and were located by means of the SEISAN package (Havskov and Ottemoller, 2000) and the HYPOCENTER algorithm (Lienert and Havskov, 1995). The velocity model used for the location is a typical 1D model for Colombia that consists of six layers (Ojeda and Hasvkov 2001). Table 1 displays the velocity profile. S-wave velocities are estimated to be VP/1.78. All events were located with P and S wave arrival times. principal stations used to locate the events were Puerto Gaitan (PTGC), Guaviare (GUA), Villavicencio (VIL), Chingaza (CHI), Rusia (RUS), Tame (TAM), Macarena (MACC), San Pablo de Borbur (SPBC), Ortega (ORTC) and Florencia (FLO2). Distances between stations fall within a range of 60-300 km and an average azimuthal average gap of about 235° (Figure 1); in other words, location uncertainties are noteworthy: average errors in latitude reach up to 4.5 km, longitude errors reach up to 6.85 km and depth errors 6.59 km (Table 2).

Moment tensor retrieval: We estimated Moment Tensor Retrieval for events in the study area by inverting earthquake waveforms using the ISOLA software package (Sokos and Zahradnik, 2008). This method is based on multiple-point source representation and iterative deconvolution (Kikuchi and Kanamori, 1991) considering full-wave field. Green's functions are calculated by the discrete wavenumber method (Bouchon,1981; Coutant,1989). The Moment Tensor of subevents is found by least-square minimization of misfit between observed and synthetic waveforms, while subevent position and time are optimized through a grid search.

Back projection images (BPI): Recent research has sought to describe the rupture front tracking of large (Mw > 7.0) to megathrust (Mw > 8.0) earthquakes. Techniques have been employed to for a number of phases of the seismic activity in order to gather information such as rupture orientation, path, length and velocity all in an effort to better our understanding of those events. These techniques were heavily utilized to study the Sumatra-Andaman earthquake in 2004 (Ishii et al., 2007; Krüger and Ohrnberger, 2005; Bayer et al., 2012). Constantly under improvement, these techniques are subject to independent attempts to image the rupture process and increase the spatiotemporal resolution and accuracy of event registries. The principles underlying these techniques are generally applied to large teleseismic events. Nevertheless, in this study, these same approaches are employed for the analysis of microseismic rupture imaging at reservoir scale (Folesky, 2013). Although potentially useful at this scale, their applicability depends on a series of factors that warrant further study. A noteworthy example of the techniques being used for microseismic events is the back projection of seismograms recorded by a seismic network array to a grid of possible source locations using calculated travel times for every station location pair as time corrections. The summation stack of all back-projected seismic traces offers a coherent positive stack if the targeted point is indeed the source. Ishii et al. (2007) and Walker and Shearer (2009) utilized this method, and it is referred to as Back- Projection Imaging (BPI) or, as initially conceived, the Source- Scanning Algorithm (Kao and Shan, 2004). In mathematical terms, the idea is to stack all seismograms U(t) received at n receivers as a function of time for every ith potential source grid point, corrected by the individual source-receiver travel time. Using BPI, the complexities resulting from the event that interacts with the ground do not need to be considered separately; instead, they are back projected to estimate their origin in space and time. The following equation mathematically expresses BPI:

$$S_i(t) = \sum_{k=1}^{n} w_k U_k(t - t_{ik}^{p})$$

Where:

$S_i(t)$: Stack at *i*th source grid point.

W_k: Possible station-specific weighting factor at the kth station;

$t^p{}_{ik}$: Predicted P-wave travel time shift, calculated from the *i*th potential grid point location to the *k*th receiver location.

The predicted time shift represents changes in the wavefront's behavior and leads to a coherent, high-amplitude stack if the respective grid point is indeed the source location. By iterating the stacking procedure for all points of an initial grid of possible source points, we can obtain a seismogram-like trace for every point and the stacked value for all time steps (Figure 24). The squared amplitudes of the resultant stack are tied to the energy radiation of the source, but normalization and weighting at the stations means they do not exactly express radiated energy. Rather, this energy is known as back-projected energy. For a unilateral rupture, we would ideally expect one maximum back-projected energy for each time step. This center of back-projected energy is considered the rupture front. Over time, the stack's peak location migrates as the rupture progresses in one direction. Back-projected energy distribution potentially provides estimates for rupture orientation, length and velocity. We used BPI to determine wavefront rupture propagation. The following assumptions were made to model the rupture propagation tracking with an eye towards reducing computational complexity:

a. The experimental area is located around the zone where possible induced seismicity was recorded. The entire area covers stations and source locations. Source events are always placed in the center of the model to avoid boundary effects.

b. The model consists of a homogenous distribution of velocity values. Therefore, paths are straight lines and travel time estimation is simplified. Velocity values are constant (V_p = 4.8 km/s) for the entire study area.

Stress field orientation: Stress field orientation entailed applying the Michael's Method (1984, 1987), for which an instability criterion proposed by Lund and Slunga (1999) was incorporated. To calculate stress inversions from focal mechanisms, we had to discover which nodal planes were related to active faults. Without such information, and if faults and auxiliary nodal planes were interchanged, results would be inaccurate. Michael's linear inversion method proves reasonably accurate when used to find principal stress directions, even in cases where the fault planes in focal mechanisms are incorrectly selected. However, the shape ratio is more sensitive to proper fault choice; thus, substituting the faults using auxiliary nodal planes would introduce significant errors. To avoid the aforementioned errors, Michael's method was modified: joint inversion was carried out for stress and fault orientations. The latter were determined by applying the fault instability constraint, whereas the former involved iterations. In so doing, overall friction on faults is also determined. The package STRESSINVERSE in MATLAB was used for an iterative joint inversion for stress and fault orientations from the estimated focal mechanisms (Vavrycuk, 2014).

Results

Back projection imaging: For BPI estimations, array geometry based on Seismological stations PTGC, GUA, CHI, RUS, TAM and MACC (Figure 1) was used. The closest source-receiver is roughly 70 km away. See Figure 25a for an example of the waveforms used. To carry out BPI, the first step was to identify and separate P-phases for each seismic station; P-wave onset was calculated based on the hypocenter's relation to each respective station. On account of the constant (homogenous) velocity employed by the model, travel times between stations could be easily calculated. Then, depending on the waveforms, we defined a time window for the P-phases and removed the remaining traces (Figure 25b). For back projection, this was the only relevant part of the seismograms. After, the time windows were normalized; to minimize the influence of noise and smooth potential singularities, the envelopes were computed using the Hilbert transformation (Figure 25c). Here, stations were equally weighted, though statin weights can be adjusted given data quality, source-receiver distance or azimuthal station distribution. The squared results of the stack function, obtained for each model grid point, are shown in Figure 26 in the form of six charts that display BPI estimations for the most energetic events recorded in the area for the first half of 2014. The location of maximum back-projected energy was tracked with a SE-NW orientation for all events. Length, however, turned out to be more difficult to determine; results here fell within 100 m and 350 m SE-NW extension, depending on event.

Focal mechanism and stress field orientation derived from strongest events: The earthquakes recorded were large enough to allow us to determine the seismic moment, focal mechanisms and focal depth. These parameters were determined via modeling and inversion of observed seismic records from permanent seismographic stations around the study area. Waveform modeling and inversion results indicate that the focal mechanism of the biggest shock (June 26, 2014) is predominantly normal dip-slip fault with some strike-slip. The best fitting double-couple source mechanism parameters are θ=236°, δ=12°, λ=-24° (second nodal plane θ=98°, δ=62°, λ=-67°) and seismic moment Mo=3.58 x 10^{15} Nm (Mw 4.30). Of the events analyzed, five display this normal dip-slip faulting type, except for the May 13, 2014 event, which exhibited more reverse dip-slip fault with some strike-slip.

For this event, the best fitting double-couple source mechanism parameters are θ=163°, δ=14°, λ=125° (second nodal plane θ=306°, δ=79°, λ=82°) and seismic moment Mo=3.60 x 10^{15} Nm (Mw 4.30). Table 4 contains the most important focal mechanisms parameters for the six largest events recorded. Readers are directed to Figure 27 for a comparison of observed and synthetic waveforms, as well as the variance reduction compared to the best fit of the estimated focal mechanisms. In Figure 26, focal mechanisms are presented. Inversion of the stress field orientation for the six events shows that the principal maximum stress stems from overburden, for it lays in the center of the principal stress and Pressure/ Tension (P/T) axes (Figure 28).

Discussion

At the beginning of this paper, we raised the issue of induced seismicity. The Puerto Gaitan oil fields have seen increased production since 2009, with peak production volume achieved in August 2013 when average monthly oil volume was estimated at 212.000 Bbl. To reach this production in heavy oil fields (Puerto Gaitan) operators employ technologies common for this type of field, such as water injection and thermal stimulation. One of the main characteristics of heavy oil fields is the high-water volume production; this water must be deposited, often in disposal reservoirs.

When Puerto Gaitan's seismicity in 2013 and 2014 is seen through the lens of oil production data, some correlation becomes apparent between production volumes and earthquake occurrence. Prior to 2013, no earthquakes were recorded in this area, save for a peak in production in September 2011 that was followed by earthquakes at the end of said month. Production achieved significant levels in January 2013, and from there the number of seismic events spiked, with a concomitant increase in event magnitudes.

The sharp peak in production during the entire year 2013 appears to be correlated with the occurrence of earthquakes for the same year. Starting in 2014, there was a marked decline in production, yet this year was witness to the largest events recorded which does not contradict the hypothesis presented here, for seismic events result from the release of accumulated energy. Another peak in production took place in May 2014. In line with the hypothesis of this paper, this peak was followed by the occurrence of the highest event recorded that year (Mw 4.4). In an effort to maintain production levels, operators performed actions that probably generated the seismic activity recorded in 2014. In fact, well distribution throughout the field (Figure 20) suggests that events took place near sites where wells were drilled. An important qualification has to do with reported volumes, which correspond to a monthly average; that is to say, during a given period, oil volume may have been higher than the final reported value.

BPI results demonstrate a NW tendency in the direction of wavefront migration. These results are reinforced by focal mechanism estimations, suggesting the same direction tendency as the planes solution in Figure 26. Such findings led us to posit that BPI, despite simplifications inherent to this type of modeling, represents a quick tool for the validation of results obtained via other iterative methods, e.g., Moment Tensor Retrieval. Here, we should pause to point out that wavefront migration is not identical to the fracture itself. Instead, the former represents a stack of radiated energy associated with the rupture process; however, this parameter is crucial for describing and estimating fracture properties, including orientation, path and velocity. Looking at focal mechanisms, all are observed to be of normal faulting type. Therefore, we can state that the seismic events promote normal direction movements of masses (up or down). This faulting type is characteristic of oil fields that undergo water injection in disposal reservoirs or water injection during production. In cases of water injection, rock masses move upwards. Conversely, when oil production is too high and fluids are removed from the reservoir, the rock tends to collapse and thereby generates downward rock displacement. Both water injection and thermal stimulation experiments with high oil volume productions were common in 2013 and 2014 at Puerto Gaitan. Similarly, the stress distribution obtained also validates the focal mechanism results. Primary stress orientation is in the vertical component, such that it is associated with upward and downward rock displacement.

Migration and possible fracture orientation for the study area contrasts with the regional fault orientation trend (Figure 2). In accordance with the focal mechanisms and stress field orientation obtained, we can infer, that earthquakes are not correlated with the reactivation of preexisting faults in the area; rather, they have to do with oil operations. This stark difference raises concerns regarding the effects of induced seismicity in the balance achieved over geologic time in terms of the local stress field relative to the regional stress field (see e.g., Mora et al., 2010; Heidbach et al., 2009). Research has established that stress alters rock volume, geometry and fluid flow paths therein. In sum, the modeling presented in this paper functions as an initial approach to the problem of induced seismicity in stress fields in the study area. Results suggest that a consequence of induced seismicity can be found in the distribution of the study area's local stress field relative to the regional context. In order to further test this hypothesis, more in-depth analysis based on a proper seismological array and supported with other techniques must be conducted.

Conclusions

Based on analysis of the results obtained in this study, we can conclude that:

a. A spatiotemporal relation exists between oil production peaks and significant increases in seismic events.

b. Back Projection Imaging (BPI) offers a good approximation of fracture orientation. Focal mechanisms estimated using Moment Tensor Retrieval confirm results obtained via BPI.
c. Predicted fracture orientation does not match up with regional fracture orientation, likely indicating local stress alteration.

Acknowledgments

We are grateful to the editor in chief Professor Dr. James Nelson Kellogg and two anonymous reviewers for their critical reviews which have improved this paper. We are also grateful to Associate Editors Marcelo Assumpçao and Frank Anderson. We thank Professor Joseph Wager for his help in improving the written English. We recognize the contribution made by the Colombian National Seismological Network and Colombian Ministry of Mines and Energy for providing the data. This work was partially supported by the Universidad Nacional de Colombia under Cooperative agreement (Hermes-25447) as well as corresponding author's fellowship by COLCIENCIAS (Grant: Doctorados Nacionales 617).

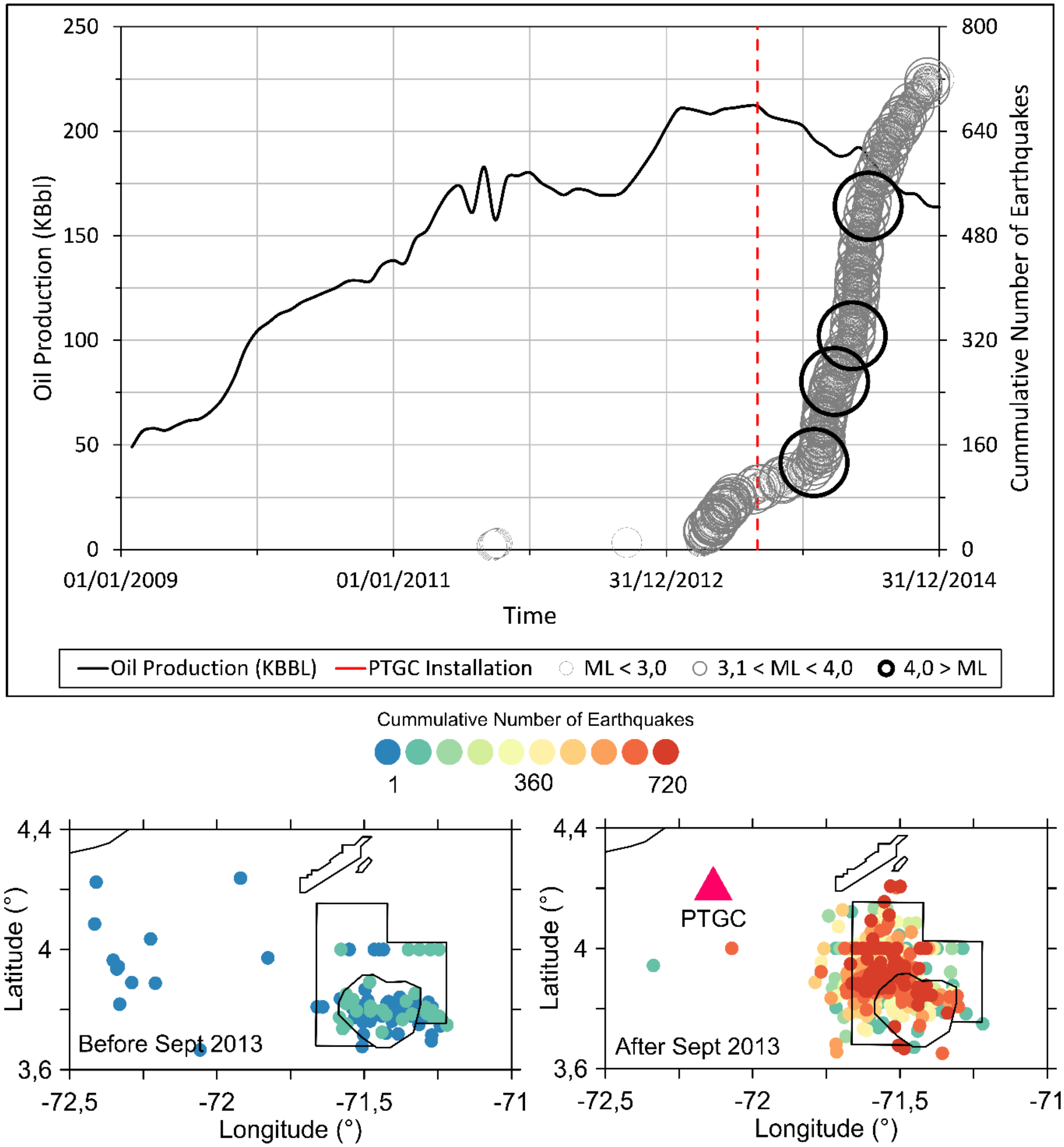

Figure 20. Temporal evolution of recorded seismicity and oil production in Puerto Gaitan oil fields from 2009 to 2013. The upper panel shows the monthly heavy crude oil production and contrasts it with the seismicity recorded in the area. The red line shows the moment when the Puerto Gaitan seismic station (PTGC) was installed in September 2013. Before March 2013 seismicity was considered non-existent. Epicentral events distribution is shown in the bottom panels. The left panel shows the distribution of events before the installation of the PTGC

station, while the right shows the distribution of events recorded afterwards. PTGC is located approximately 70 km from the hydrocarbon production area.

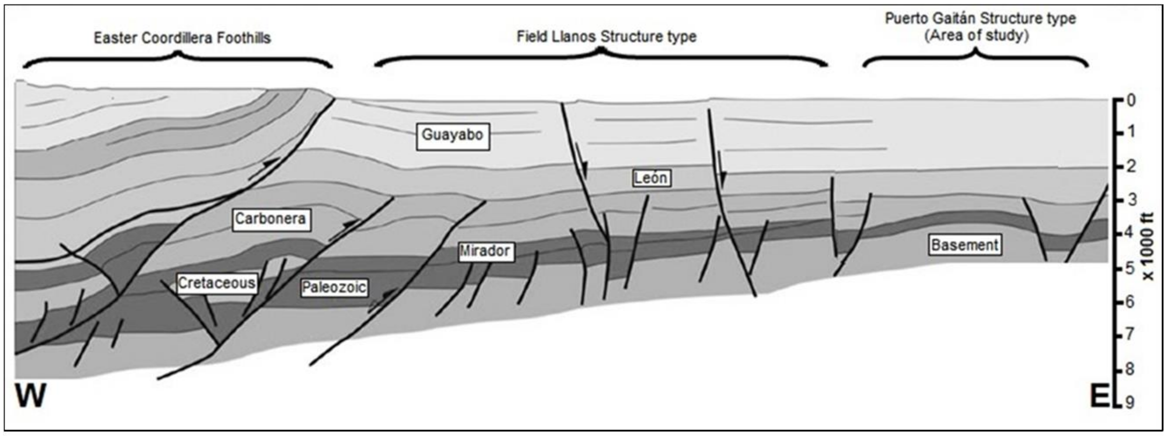
Easter Coordillera Foothills
Field Llanos Structure type
Puerto Gaitán Structure type
(Area of study)
Guayabo
León
Carbonera
Mirador
Cretaceous
Paleozoic
Basement
0
1
2
3
4
5
6
7
8
9
x 1000 ft
W
E

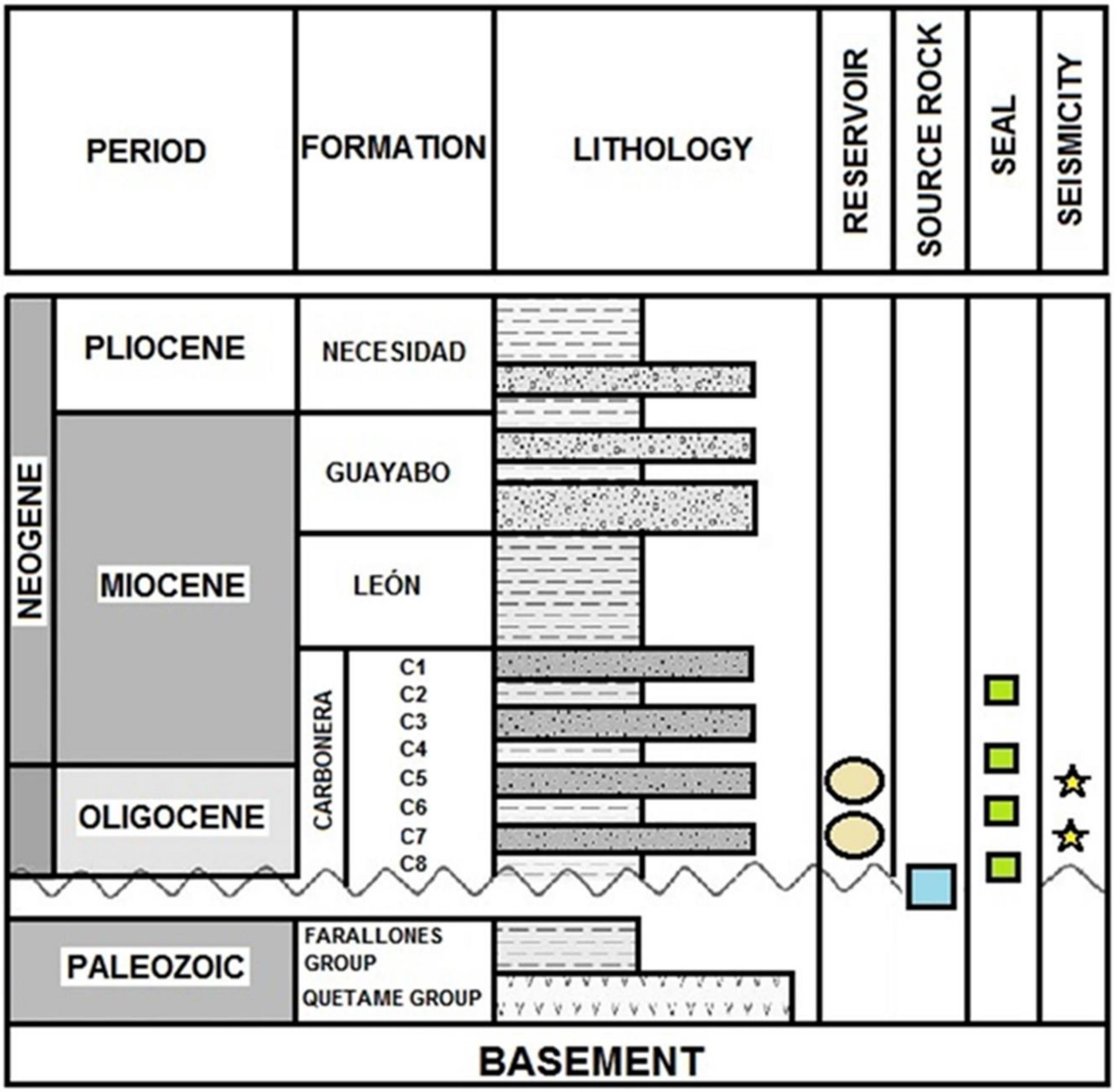
PERIOD
FORMATION
LITHOLOGY
RESERVOIR
SOURCE ROCK
SEAL
SEISMICITY
NEOGENE
PLIOCENE
MIOCENE
OLIGOCENE
NECESIDAD
GUAYABO
LEÓN
CARBONERA
C1
C2
C3
C4
C5
C6
C7
C8
PALEOZOIC
FARALLONES GROUP
QUETAME GROUP
BASEMENT

Figure 21. Structural section of the Llanos Basin and stratigraphic column scheme of typical Puerto Gaitan oil fields (Modified, Gomez, et al., 2010). “C5” and “C7” production formations are probably related to seismic anomalous activity.

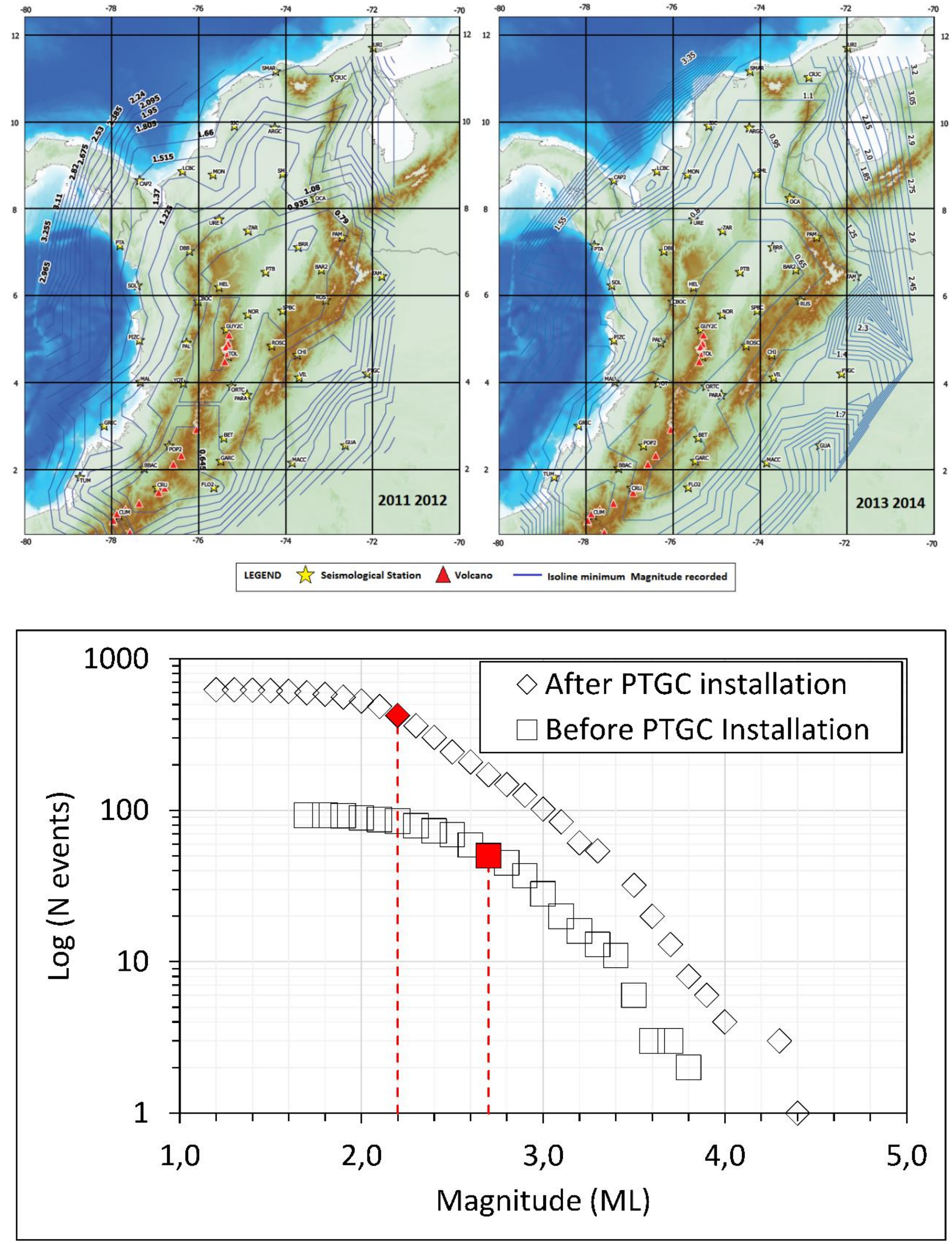

Figure 22. Minimum detected magnitude distribution in Colombia. Changes in detection threshold based on the Gutenberg-Richter law, shows that Magnitude of Completeness (MC)

decreased from 2.7 to 2.2 due to the installation of PTGC station, approximately 70 km from the seismic cluster after September 2013.

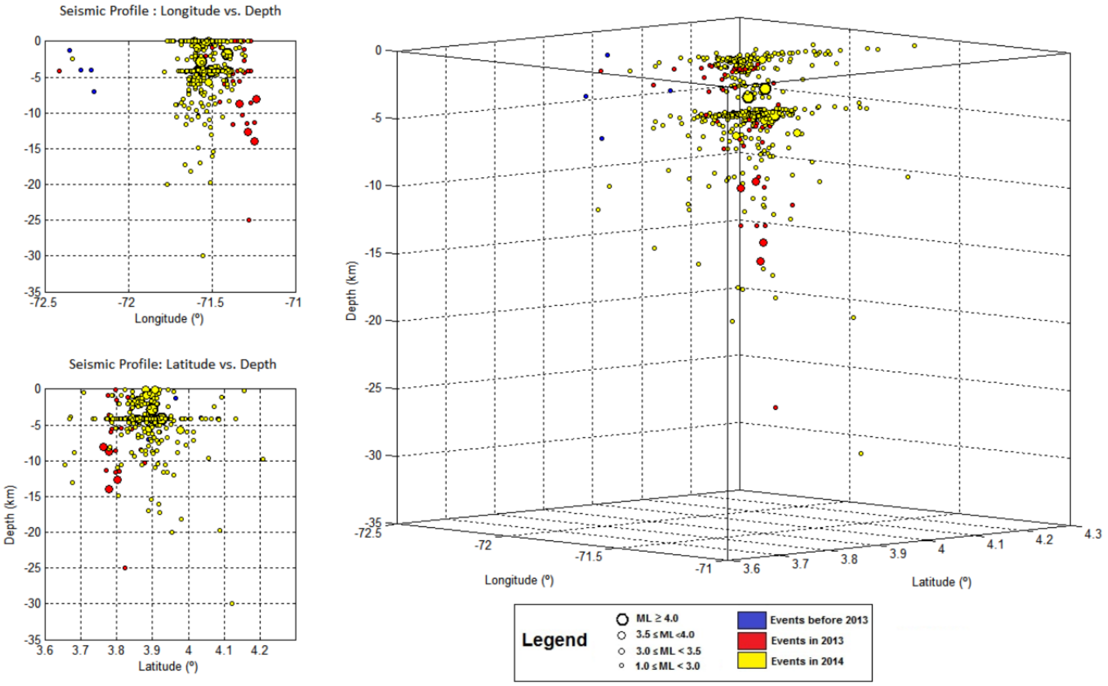

Figure 23. Hypocentral solution for events recorded in Puerto Gaitan from 2007 to 2014. Main seismic activity is grouped above 5 km depth.

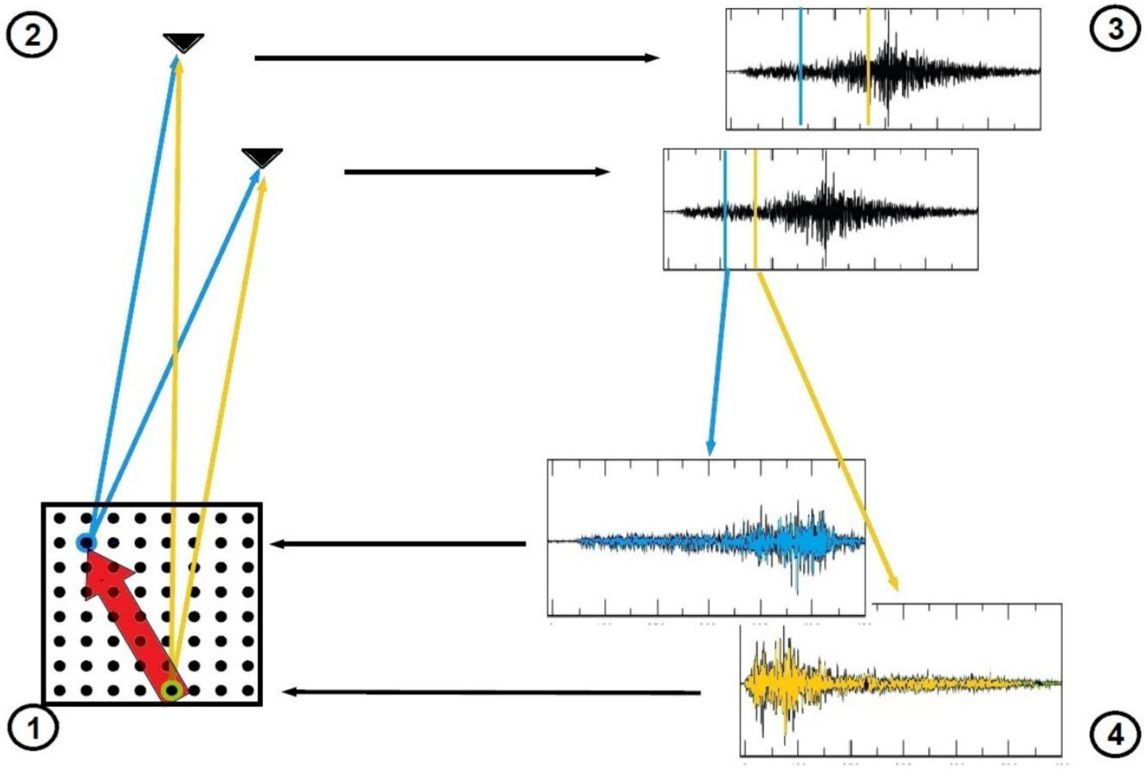

Figure 24. Back Projection Imaging scheme. (1) Grid of possible source locations and rupture; (2) Seismic network recording wavefront arrivals; (3) Theoretical P-wave onset is marked for both records (different source grid points); (4) Seismograms are stacked for each grid point, yielding a back projection energy record per grid point (Folesky, 2013).

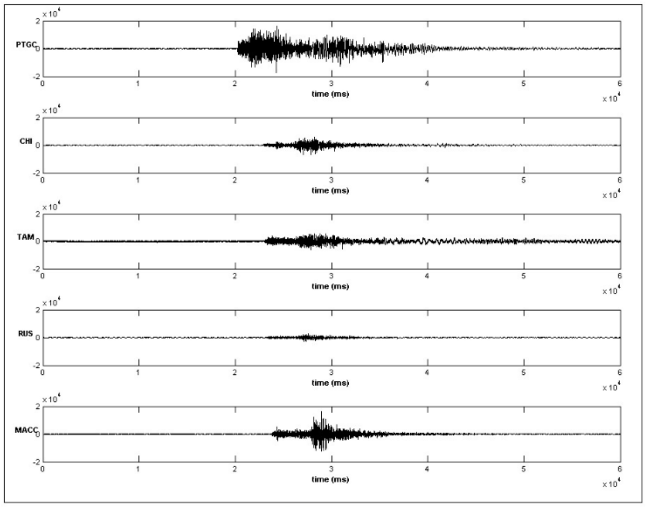
PTGC
CHI
TAM
RUS
MACC
x 10^4
time (ms)
x 10^4

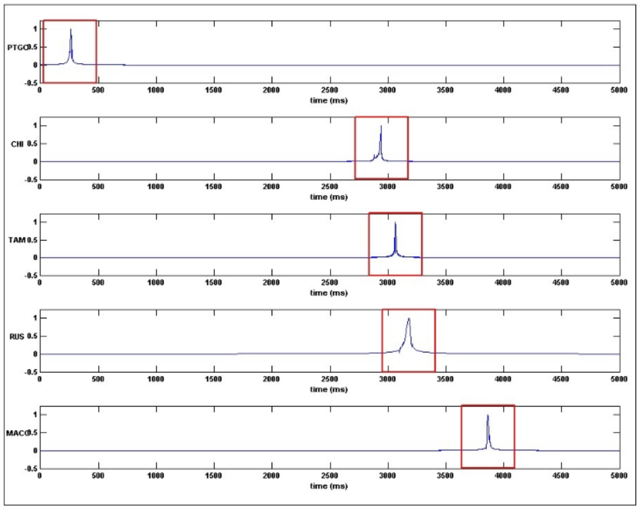
PTGC
CHI
TAM
RUS
MACC
time (ms)

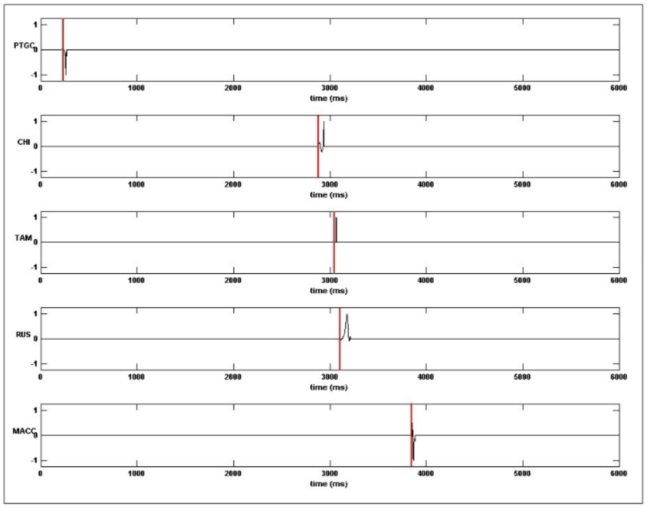
PTGC
CHI
TAM
RUS
MACC
time (ms)

Figure 25. Example of seismograms used for estimating BPI. (a) Raw seismograms; (b) P-phase for each seismic station and the remaining traces are removed; (c) Envelopes are computed.

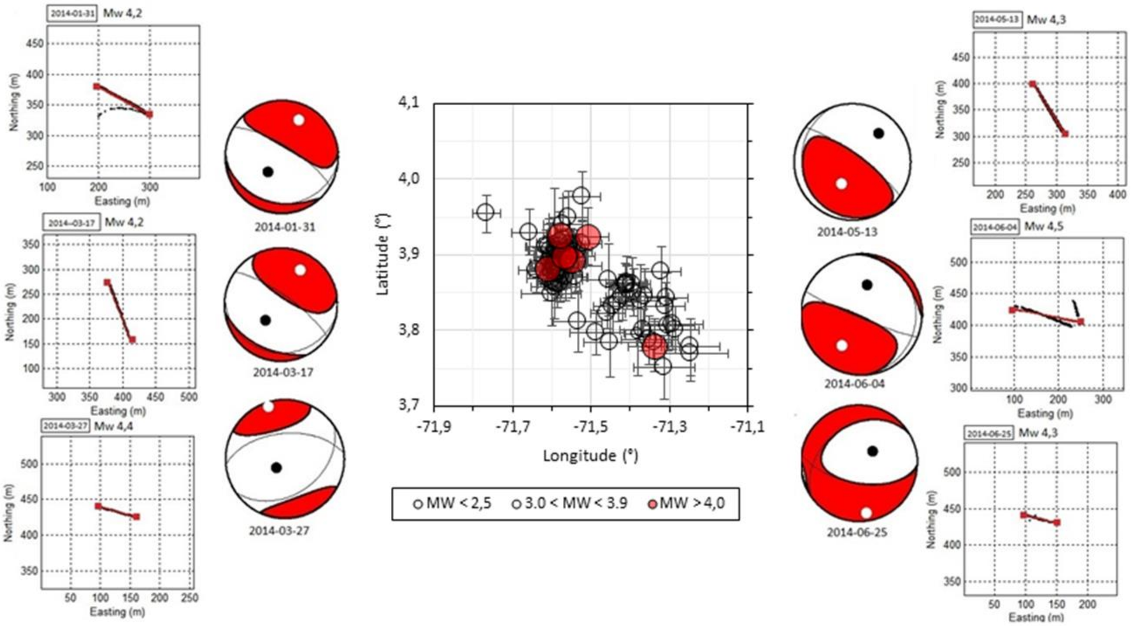

Figure 26. BPI and focal mechanisms result. The position of the maximal back projected energy is shown. Black points belong to the wavefront rupture. The modeled wavefront tracking is indicated by the solid, red line. Focal mechanisms estimated by Moment Tensor Retrieval technique are compared with orientations derived from the BPI approach. Red circles represent epicentral solutions for the six most energetic events in the area (M4.0+) recorded during 2014.

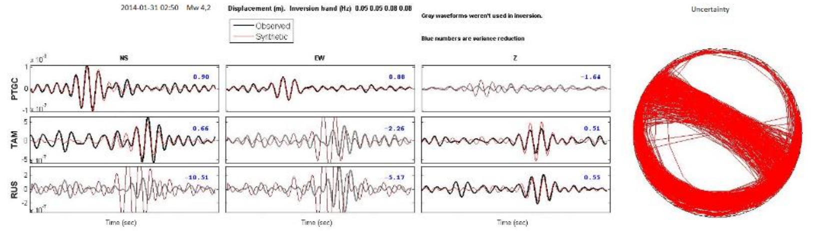
2014-01-31 02:50 Mw 4.2
Displacement (m). Inversion band (Hz) 0.05 0.05 0.08 0.08
Observed
Synthetic
Gray waveforms weren't used in inversion.
Blue numbers are variance reduction
Uncertainty
NS
EW
Z
PTGC
TAM
RUS
0.90
0.88
-1.64
0.66
-2.26
0.51
-10.51
-5.17
0.55
Time (sec)

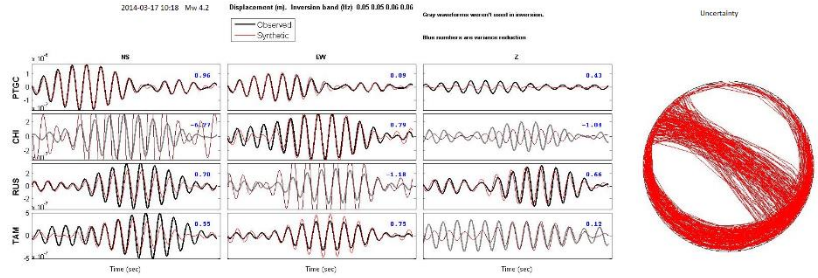
2014-03-17 10:18 Mw 4.2
Displacement (m). Inversion band (Hz) 0.05 0.05 0.06 0.06
Observed
Synthetic
Gray waveforms weren't used in inversion.
Blue numbers are variance reduction
Uncertainty
NS
EW
Z
PTGC
CHI
RUS
TAM
0.96
0.89
0.43
-6.27
0.79
-1.84
0.70
-1.10
0.66
0.55
0.75
0.12
Time (sec)

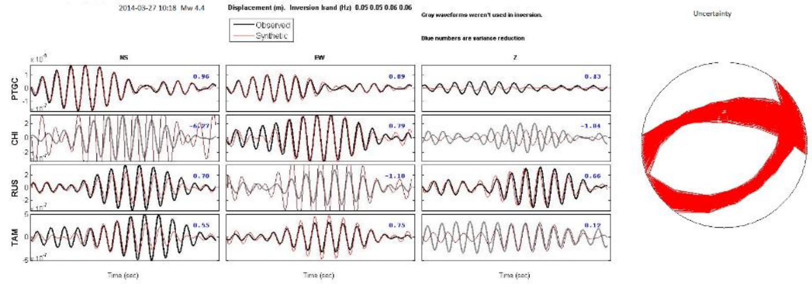
2014-03-27 10:18 Mw 4.4
Displacement (m). Inversion band (Hz) 0.05 0.05 0.06 0.06
Observed
Synthetic
Gray waveforms weren't used in inversion.
Blue numbers are variance reduction
Uncertainty
NS
EW
Z
PTGC
CHI
RUS
TAM
0.96
0.89
0.43
-6.27
0.79
-1.84
0.70
-1.10
0.66
0.55
0.75
0.12
Time (sec)

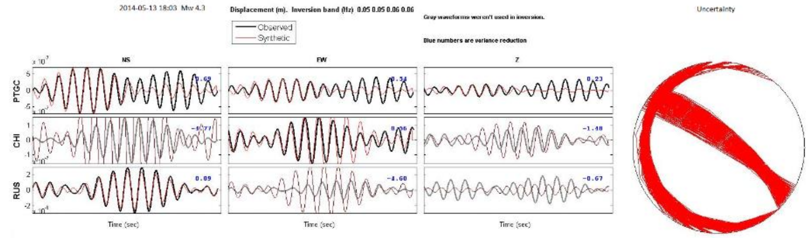
2014-05-13 18:03 Mw 4.3
Displacement (m). Inversion band (Hz) 0.05 0.05 0.06 0.06
Observed
Synthetic
Gray waveforms weren't used in inversion.
Blue numbers are variance reduction
Uncertainty
NS
EW
Z
PTGC
CHI
RUS
0.23
-4.77
0.86
-1.48
0.89
-4.60
-0.67
Time (sec)

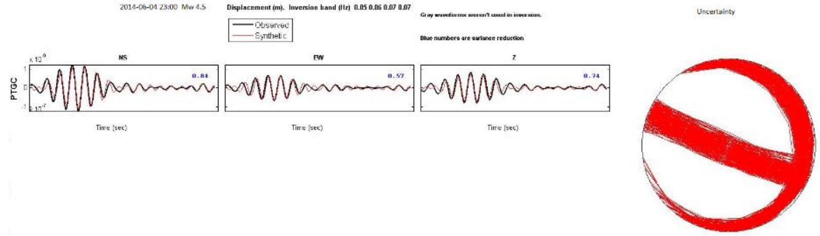
2014-06-04 23:00 Mw 4.5
Displacement (m). Inversion band (Hz) 0.05 0.06 0.07 0.07
Observed
Synthetic
Gray waveforms weren't used in inversion.
Blue numbers are variance reduction
Uncertainty
NS
EW
Z
PTGC
0.84
0.57
0.74
Time (sec)

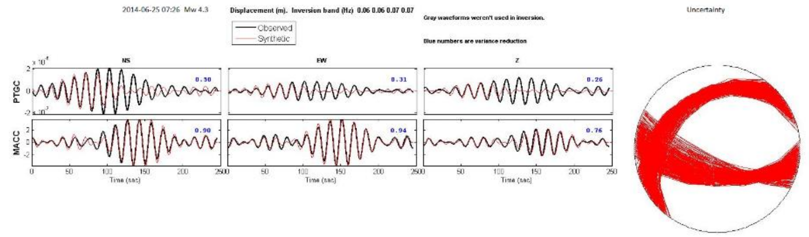
2014-06-25 07:26 Mw 4.3
Displacement (m). Inversion band (Hz) 0.06 0.06 0.07 0.07
Observed
Synthetic
Gray waveforms weren't used in inversion.
Blue numbers are variance reduction
Uncertainty
NS
EW
Z
PTGC
MACC
0.50
0.31
0.26
0.90
0.94
0.76
0
50
100
150
200
250
Time (sec)

Figure 27. Observed and synthetic waveforms. Variance reduction related to the best fit of the estimated focal mechanisms is shown.

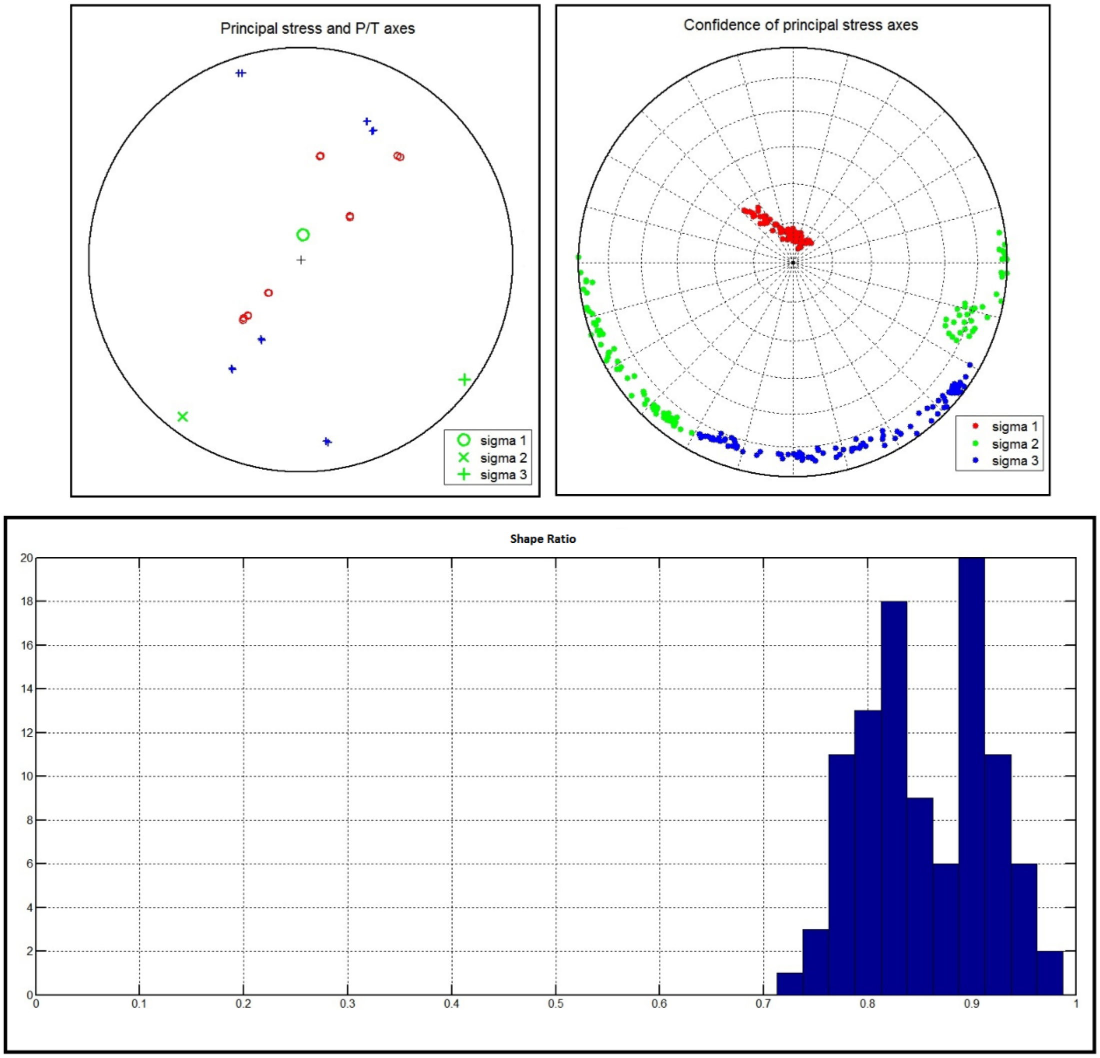

Figure 28. Stress field inversion results based on focal mechanisms estimated with the Moment Tensor Retrieval technique. Note that the principal axis is nearly vertical.

Table 2. Seismic catalogue Puerto Gaitan 2013 – 2014. Mw>3,5. Highlight rows show events that were analyzed with BPI and Moment Tensor techniques. Source: Colombian Geological Survey SGC (www.sgc.gov.co).

Date (dy/mo/year)	Time (hh: mm: ss)	Latitude (° N)	Longitude (° W)	Depth (km)	Magnitude (M_L)	Magnitude (M_W)	rms	gap	E_Lat (km)	E_Long (km)	E_Depth (km)
10/05/2013	1:45:02	3.8010	-71.2850	12.7000	3.50	3.90	0.5	238	3.4	6.8	8.3
11/05/2013	1:19:41	3.7630	-71.2350	8.0000	3.80	4.00	0.5	241	3.4	7.2	7.9
17/05/2013	6:36:39	3.7790	-71.3390	8.7000	3.50	4.10	0.6	231	3.6	7.3	6.6
01/06/2013	23:41:31	3.7970	-71.4850	4.1000	2.90	3.60	0.5	229	3.3	7.6	6
17/06/2013	1:41:19	3.7780	-71.2460	14.0000	3.50	3.90	0.6	240	4.2	8.3	7.7
27/06/2013	2:54:46	3.7850	-71.3380	5.6000	3.40	3.80	0.5	218	3.4	4.8	6.1
31/01/2014	**2:53:08**	**3.8610**	**-71.4090**	**1.8000**	**4.00**	**3.80**	**0.4**	**256**	**2.6**	**6**	**5.2**
20/02/2014	4:14:49	3.8850	-71.5490	4.1000	3.60	3.60	0.7	224	4.7	8.4	9.3
25/02/2014	13:18:10	3.8980	-71.6010	0.5000	3.50	3.50	0.5	222	2.6	4.8	4.9
28/02/2014	7:10:37	3.8880	-71.5860	4.1000	3.20	3.50	0.5	223	3.5	6.2	7
15/03/2014	6:55:43	3.8980	-71.5510	4.1000	3.50	3.70	0.6	224	4.1	6.8	8
17/03/2014	**10:26:05**	**3.8920**	**-71.5460**	**4.1000**	**3.90**	**4.00**	**0.5**	**224**	**2.5**	**3.9**	**4.7**
19/03/2014	11:13:26	3.8730	-71.5750	4.1000	3.40	3.60	0.6	223	3.4	5.9	6
24/03/2014	23:19:31	3.8500	-71.3910	4.1000	3.90	3.90	0.6	232	3.4	5.2	5.9
27/03/2014	**10:21:16**	**3.9260**	**-71.5790**	**4.1000**	**4.30**	**4.30**	**0.5**	**222**	**3.4**	**4.6**	**6.3**
30/03/2014	1:11:12	3.8740	-71.5890	1.3000	3.30	3.50	0.4	223	3.5	7.3	7.2
04/04/2014	4:25:57	3.8860	-71.5920	0.6000	3.60	3.70	0.5	222	3.1	5.5	5.3
10/04/2014	10:13:22	3.8620	-71.3950	4.1000	3.80	3.90	0.5	232	3.7	5.2	5.7
23/04/2014	15:19:28	3.8980	-71.5500	4.1000	3.50	3.80	0.5	224	2.7	4.6	5.3
23/04/2014	18:38:15	3.8850	-71.5950	5.7000	3.70	3.80	0.6	222	3.3	5.4	6.4
13/05/2014	**18:07:32**	**3.8980**	**-71.5670**	**2.8000**	**4.30**	**4.20**	**0.6**	**223**	**3.3**	**5.7**	**5.7**
14/05/2014	2:43:42	3.8630	-71.5910	4.1000	3.40	3.60	0.6	223	2.6	4.1	4.8
25/05/2014	15:25:03	3.9070	-71.5550	4.1000	3.70	3.80	0.4	185	2.6	3.3	4.4
26/05/2014	3:48:15	3.9110	-71.5770	4.1000	3.20	3.80	0.4	223	3.2	6	6.8
26/05/2014	16:03:08	3.9300	-71.6570	11.6000	3.30	3.60	0.6	204	3.3	5	4.8
27/05/2014	17:36:28	3.8900	-71.5730	0.9000	3.30	3.50	0.6	223	3.9	6.4	7.1
04/06/2014	**23:06:20**	**3.8810**	**-71.6110**	**0.1000**	**3.80**	**4.00**	**0.5**	**221**	**3**	**5.2**	**5.3**
04/06/2014	3:17:23	3.8810	-71.5800	4.1000	3.60	3.80	0.5	223	2.8	4.2	5
05/06/2014	1:04:43	3.9040	-71.5550	4.1000	3.60	3.80	0.5	224	3.2	4.7	5.4
20/06/2014	23:31:58	3.8620	-71.5790	4.1000	3.50	3.70	0.5	223	2.8	4.4	5.3
25/06/2014	**7:27:39**	**3.9240**	**-71.5060**	**4.1000**	**4.40**	**4.40**	**0.6**	**226**	**4.2**	**5.6**	**6.9**
26/06/2014	6:20:05	3.8860	-71.5890	4.1000	3.30	3.50	0.6	222	3.1	4.5	5.4
15/07/2014	17:44:33	3.8450	-71.3610	1.0000	3.40	3.60	0.5	234	4	6.7	6.8
20/07/2014	20:47:32	3.8960	-71.5660	0.7000	3.70	3.90	0.5	223	2.8	5.5	5.1
09/08/2014	0:30:58	3.8930	-71.5820	4.1000	3.50	3.80	0.5	223	2.6	3.9	4.6
09/08/2014	12:56:59	3.8840	-71.5920	0.8000	3.50	3.70	0.5	222	3.6	6.5	6.8
14/08/2014	8:04:07	3.8870	-71.5620	4.1000	3.60	3.70	0.6	224	3.4	5.4	6.6
19/10/2014	17:25:29	3.8600	-71.4110	6.4000	3.40	3.50	0.4	231	3.2	4.6	5.2
30/11/2014	19:45:34	3.9060	-71.5340	0.1000	3.60	3.80	0.5	225	2.4	4.1	4.2
30/11/2014	23:22:00	3.9770	-71.5230	5.7000	3.50	3.70	0.8	208	3.7	5.4	6.7

Table 3. Seismic stations deployed by the Colombian Geological Service. Source: www.sgc.gov.co

ID	Name	Latitude (°N)	Longitude (°W)	Altitude (m)	Type of Station	Type of Sensor	Type of Digitizer	Installation Date (dy/mo/year)
ZAR	ZARAGOZA	7.492	-74.858	205	BROAD BAND	KINEMETRICS	KINEMETRICS	29/08/2011
DBB	DABEIBA	7. 018	-76.210	756	SHORT PERIOD	MARK_PRODUCTS	KINEMETRICS	26/11/2008
HEL	HELENA	6. 191	-75.529	2815	BROAD BAND	GURALP	KINEMETRICS	16/06/2011
CBOC	CIUDAD BOLIVAR	5. 864	-76. 012	1401	BROAD BAND	REFTEK	KINEMETRICS	05/08/2013
PTB	PUERTO BERRIO	6. 540	-74.456	260	BROAD BAND	REFTEK	KINEMETRICS	13/11/2011
TAM	TAME	6. 436	-71.791	457	BROAD BAND	NANOMETRICS	KINEMETRICS	25/06/2011
PRV	PROVIDENCIA	13. 376	-81.364	63	BROAD BAND	NANOMETRICS_TRILLIUM	KINEMETRICS	16/05/2011
SJC	SAN JACINTO	9 .897	-75.180	596	BROAD BAND	REFTEK	KINEMETRICS	03/05/2011
SML	SAN MARTIN DE LOBA	8 .801	-74.071	116	BROAD BAND	REFTEK	KINEMETRICS	27/10/2012
RUS	RUSIA	5 .893	-73.083	3697	VERY BROAD BAND	NANOMETRICS	KINEMETRICS	03/04/2009
SPBC	SAN PABLO DE BORBUR	5 .652	-74.072	799	BROAD BAND	REFTEK	KINEMETRICS	16/07/2013
GUY2C	GUYANA2	5 .224	-75.365	3605	BROAD BAND	REFTEK	KINEMETRICS	15/04/2013
NOR	NORCASIA	5 .564	-74.869	536	BROAD BAND	REFTEK	KINEMETRICS	12/09/2010
FLO2	FLORENCIA	1 .583	-75.653	365	BROAD BAND	GURALP	KINEMETRICS	10/09/2008
GRIC	ISLA GORGONA 2	3 .003	-78.167	39	SHORT PERIOD	MARK_PRODUCTS	KINEMETRICS	02/03/2014
BBAC	BALBOA	2 .022	-77.247	1713	BROAD BAND	REFTEK	KINEMETRICS	28/04/2013
POP2	POPAYAN	2 .540	-76.676	1869	BROAD BAND	REFTEK	KINEMETRICS	30/06/2010
SOL	SOLANO	6 .226	-77.409	38	SHORT PERIOD	MARK_PRODUCTS	KINEMETRICS	28/06/1993
PIZC	PIZARRO	4 .965	-77.360	38	BROAD BAND	NANOMETRICS	KINEMETRICS	10/01/2014
CAP2	CAPURGANA	8 .646	-77.359	229	BROAD BAND	GURALP	KINEMETRICS	14/07/2011
PTA	PUNTA ARDITA	7 .147	-77.808	78	BROAD BAND	NANOMETRICS	KINEMETRICS	28/08/2012
PAL	SAN JOSE DEL PALMAR	4 .905	-76.283	675	BROAD BAND	GURALP	KINEMETRICS	30/09/2011
LCBC	LOS CORDOBAS	8 .857	-76.368	75	BROAD BAND	NANOMETRICS	KINEMETRICS	16/11/2013
MON	MONTERIA	8 .778	-75.665	109	BROAD BAND	KINEMETRICS	KINEMETRICS	16/10/2008
URE	SAN JOSE DE URE	7 .752	-75.533	251	BROAD BAND	NANOMETRICS_TRILLIUM	KINEMETRICS	01/05/2012
CHI	CHINGAZA	4 .630	-73.732	3140	BROAD BAND	KINEMETRICS	KINEMETRICS	01/09/2007
ROSC	ROSAL	4 .840	-74.320	2987	BROAD BAND	GURALP	GURALP	31/08/1992
GUA	GUAVIARE	2 .545	-72.627	217	SHORT PERIOD	MARK_PRODUCTS	KINEMETRICS	28/07/2012
BET	BETANIA	2 .723	-75.418	557	BROAD BAND	REFTEK	KINEMETRICS	19/05/2010
GARC	GARZON	2 .187	-75.493	1999	BROAD BAND	REFTEK	KINEMETRICS	24/02/2014
URI	URIBIA	11. 702	-71.993	68	BROAD BAND	KINEMETRICS	KINEMETRICS	16/04/2011
CRJC	CERREJON	11 .020	-72.882	827	BROAD BAND	KINEMETRICS	KINEMETRICS	27/11/2014
SMAR	SANTA MARTA	11 .164	-74.225	122	BROAD BAND	REFTEK	KINEMETRICS	18/09/2012
ARGC	ARIGUANI	9 .858	-74.246	187	BROAD BAND	REFTEK	KINEMETRICS	22/04/2013
PTGC	PUERTO GAITAN	4 .199	-72.134	170	BROAD BAND	NANOMETRICS_TRILLIUM	KINEMETRICS	27/09/2013

MACC	LA MACARENA	2 .145	-73.848	283	BROAD BAND	REFTEK	KINEMETRICS	30/05/2013
VIL	VILLAVICENCIO	4 .112	-73.694	1109	SHORT PERIOD	MARK_PRODUCTS	KINEMETRICS	13/10/2010
CRU	CRUZ	1 .568	-76.951	2761	SHORT PERIOD	GEOSPACE	KINEMETRICS	24/06/2012
CUM	CUMBAL	0.941	-77.825	3420	SHORT PERIOD	GEOSPACE	KINEMETRICS	20/04/2011
TUM	TUMACO	1. 824	-78.727	50	BROAD BAND	KINEMETRICS	KINEMETRICS	05/07/2009
PAM	PAMPLONA	7 .340	-72.700	3676	SHORT PERIOD	MARK_PRODUCTS	KINEMETRICS	18/01/2011
OCA	OCAÑA	8 .239	-73.319	1264	BROAD BAND	KINEMETRICS	KINEMETRICS	02/05/2012
PUAC	OPUERTO ASIS	0.550	-76.570	287	BROAD BAND	REFTEK	KINEMETRICS	------
PTLC	PUERTO LEGUIZAMO	-0.171	-74.797	240	BROAD BAND	REFTEK	KINEMETRICS	03/12/2012
BAR2	BARICHARA	6 .592	-73.182	1864	SHORT PERIOD	MARK_PRODUCTS	KINEMETRICS	01/11/1991
BRR	BARRANCABERMEJA	7 .107	-73.712	137	BROAD BAND	KINEMETRICS	KINEMETRICS	01/02/2008
TOL	TOLIMA	4 .585	-75.320	2577	SHORT PERIOD	MARK_PRODUCTS	GURALP	22/06/2011
PARA	PRADO	3 .714	-74.886	457	BROAD BAND	KINEMETRICS	KINEMETRICS	23/08/2006
ORTC	ORTEGA	3 .909	-75.246	446	BROAD BAND	REFTEK	KINEMETRICS	19/06/2013
MAP	ISLA MALPELO	4 .004	-81.606	137	BROAD BAND	KINEMETRICS	KINEMETRICS	24/05/2009
MAL	MALAGA	4 .013	-77.335	75	SHORT PERIOD	MARK_PRODUCTS	KINEMETRICS	02/11/1994
YOT	YOTOCO	3 .983	-76.345	1040	BROAD BAND	REFTEK	KINEMETRICS	09/12/2011

Table 4. Moment tensor results. Focal mechanisms were estimated using ISOLA software package. Earthquakes used are show as highlighted in Table 2.

Fecha	Latitud	Longitud	Profundidad	Mo	Magnitude	Plane 1			Plane 2		
(dy/mo/year)	(° N)	(° W)	(km)	(Nm)	(M_W)	Strike 1	Dip 1	Rake 1	Strike 2	Dip 2	Rake 2
31/01/2014	3.861	-71.409	4.0	2.28E+15	4.2	302	74	-82	95	18	-116
17/03/2014	3.892	-71.546	3.0	2.45E+15	4.2	305	76	-83	97	15	-117
27/03/2014	3.926	-71.579	5.5	4.57E+15	4.4	265	55	-71	55	39	-115
13/05/2014	3.898	-71.596	4.0	3.60E+15	4.3	163	14	125	306	79	82
25/06/2014	3.924	-71.506	3.0	3.58E+15	4.3	236	35	-127	98	62	-67
04/06/2014	3.881	-71.611	5.0	6.87E+15	4.5	359	12	-24	11	85	-101

CHAPTER 4. EVIDENCING THE RELATIONSHIP BETWEEN INJECTED VOLUME OF WATER AND MAXIMUM EXPECTED MAGNITUDE DURING THE PUERTO GAITAN (COLOMBIA) EARTHQUAKE SEQUENCE FROM 2013 TO 2015

Introduction

Since early to mid-20th-century the Anthropogenic Seismicity (AS) in North America and Europe has been related to underground fluid injections and productions (Ellsworth 2013). There is a general consensus in accepting that AS is generated by two main causes: an increase in pore-fluid pressure and/or a change in the state of the stress that may cause reactivation of existing faults or fractures (Healy et al. 1968; Raleigh et al. 1976). Recent case studies suggest that fluid-induced seismicity results from wastewater disposal (Ellsworth 2013; Keranen et al. 2014), hydraulic fracturing (Bao & Eaton 2016), CO2 sequestration (White & Foxall 2016), gas storage and extraction (Cesca et al. 2014) and geothermal energy (Cornet 2016; Lengliné et al. 2017). In the United States the magnitude and frequency of occurrence of induced earthquakes has increased considerably during the last decades. For instance, in the state of Oklahoma (USA) the injection of waste water associated with the extraction of shale gas, has caused earthquakes with magnitudes up to Mw = 5.8. Moreover, the annual earthquake rate of Mw > 3.0 has increased from 1.6/yr to 850/yr in 2015 (Keranen et al. 2014). Some examples of earthquakes that are suspected to be associated with geothermal activity are those registered in the city of Basel (Switzerland) and Pohang (South Korea). The first was Mw = 3.4 (Mukuhira et al. 2013) and the second Mw = 5.4 (Grigoli et al. 2018; Kimet al. 2018), both in regions considered to have very low seismic activity. The seismicity associated to hydraulic fracturing of sedimentary rocks during shale gas extraction operations, generates very small magnitude earthquakes, compared to those associated with the injection of wastewater or geothermal energy (Davies et al. 2013).

McGarr (1976, 2014) established a mathematical relationship that shows a proportional increase between the induced seismic moment (Mo) and the volume of injected fluid (V). Some other studies have shown that Mo depends on $V^{3/2}$ rather than on V (Galis et al. 2017). Schultz et al (2018) and Eaton & Igonin (2018) came to this last reasoning by comparing the released Mo of induced events with the injected fluid volume in Canada. One more study based on statistical analysis of the seismogenic index (Shapiro et al. 2010), also established that Mo depends on $V^{3/2b}$, where b is the Gutenberg–Richter exponent (Van der Elst et al. 2016). There is a general consensus that the volume of fluid V is the main parameter to estimate the Mo released during injection operations. However, additional case studies have discussed the role of other operational parameters different from V to influence the likelihood of induced seismic events during wastewater fluid injection (Weingarten et al. 2015), which include the injection rate (Frohlich 2012; Keranen et al. 2014), the wellhead injection pressure (Block et al. 2014), the proximity of the injection depth to the crystalline basement (Kim 2013), the state of stress at reservoir depth (Zang et al. 2014), and poroelastic stress (Goebels et al. 2017).

In this study, we focus on estimating the seismic energy efficiency during wastewater injection operations in Colombia’s most productive heavy oilfield from 2013 to 2015 in the municipality of Puerto Gaitan. We have first collected data from simultaneously measurements of injected volume, fluid surface pressure and flow injection rate provided by the Agencia Nacional de Hidrocarburos (Hydrocarbon National Agency of Colombia, ANH), and the catalogue of earthquakes recorded by the SGC. Based on those measurements, we then assessed the relationship between the radiated seismic energy Es and pumped-in hydraulic energy E_{PH}. Through our research, we show that Es constitutes only a small fraction of the total input energy confine within the rock volume. It was also found that it is the reservoir with the lowest energy efficiency compared to other applied technologies, despite being one of the places with the largest volume of fluid injected among those reported in the literature to date.

Seismicity and wastewater injection scenario

Induced seismicity in Puerto Gaitan: Figure 29 shows the distribution of closest seismological stations to Puerto Gaitan, spatiotemporal distribution of earthquakes from 1993 to 2017 and injection clusters. From 1993 to 2011 the number of events recorded in the study area was 10. As of 2012 and until the end of 2013 the number of earthquakes increased to 110. Due to the unexpected increase in recorded events, the SGC deployed the seismological station of Puerto Gaitan (PTGC) in September 2013. During 2014 and 2015 the SGC registered a total of 804 events. Between 2016 and 2017 the number of earthquakes decreased to 149. Regarding the spatial distribution, it can be seen that after 2013 a large number of events spread to the northwest from the original cluster. After 2016 earthquakes regroup again around epicentral solutions registered back in 2013. The SGC recorded a total number of 1108 events in Puerto Gaitan. Catalogue of earthquakes (Table 5) shows that average earthquake depth is 3.62 km. Around 940 events are located between 0 and 4 km in depth. Regarding magnitudes, it was established that average Mw is 3.47, from which 14 earthquakes are Mw + 4.0. Data from 51 injection wells grouped into eight clusters distributed throughout the largest heavy oil producing field in Colombia were considered in this study. It was determined that in March 2013 the cumulative injected water was close to 2.1 × 108 (m^3). By the end of 2015, the cumulative volume of injected water reached 7.0 × 108 (m^3). It was also established that some injection wells started operations 1492 days before to March 2013 (Table 6). A qualitative analysis suggests that cumulative Mo (Nm) and V (m^3) curves have similar shapes but are out of phase in time (Figure 30). When the V curve increases, the cumulative Mo curve also does so time later. Analogically, when V curve does not increase, the upturn of cumulative Mo curve stabilizes. To determine the time lag between both curves, we performed a cross-correlation between both time-series curves and determined that the maximum lag between them is approximately 218 days (Figure 30).

Methodology

To be able to compare both sets of data with each other, we converted injection and seismicity in terms of energy. The following paragraphs describe the energy calculations and the parameters extracted from each stage in order to determine these values. Pumped-in hydraulic energy E_{PH}: The injection energy was calculated to define the total input energy available to perform the waste water injection. Since the pumping data at the surface is available, the total input energy can be calculated by using the following equation:

$$E_{PH} = \int_{t1}^{t2} PQdt \approx \langle P(t) \rangle \langle Q(t) \rangle \Delta t$$

where t1 and t2 are the start and end times of the injection procedure. P(t) and Q(t) denotes the monthly average of surface injection pressure (MPa) and injection rate (m^3/s) of the total number of injection wells. t is the total duration of the water injection cycle. Radiated seismic energy Es: The radiated seismic energy was calculated to determine how much of the output energy was contributed by the recorded events. This is given in units of Joules by:

$$\log_{10}(Es) = 1.5\, Mo + 4.8$$

This equation is modified from Kanamori (1977), who used the Gutenberg–Richter magnitude energy relation calibrated for large earthquakes and expressed the result in units of ergs. *M*O denotes seismic moment and was computed using the following equation:

$$M_W = \left({}^{2}\!/_{3}\right) \log_{10}(Mo) - 6$$

Finally, *E*s is computed by adding the energy for all recorded earthquakes after converting the reported moment magnitudes into energy based on scaling relations developed in earthquake seismology. To estimate both E_{PH} and *E*s we considered some assumptions. For instance, due to the proximity of injection wells we assumed it was reasonable to add all volumes from wells to obtain the total injected volume. The time windows in Puerto Gaitan are not decades old, and the distances are not significant either, so the sum of all the volumes of water is totally adequate. We considered that taking the pressure and injection averages was also acceptable. We also assumed that all seismicity in the area was human related. The above is based on the historical seismicity in the regional context, which we consider as nonexistent before 2013. Furthermore, a suitable distance radius to determine if an event can be induced due to the injection of water at any time after the start of the injection, is ∼20 km according to correlations observed in the literature for the basins of the United States (Rubinstein & Mahani 2015). The previous assumptions had to be made due to the way in which the database presents the average operation parameters. Multiple injection scenarios can be proposed and *E*PH estimations may vary considerably between each other. Moreover, *E*S inaccuracies may be also considered since the radiated seismic energy relations are calibrated for large earthquakes (*M*w > 3.5) and in this study are applied to events that are some magnitudes smaller. In order to determine how reliable, the recording capability of the network is we performed an analysis of *M*c and *b*-value over time (Figure 31). *M*c was estimated by defining the point of the maximum curvature (MAXC). This value is obtained by computing the maximum value of the first derivate of the frequency magnitude curve. In practice, this matches the magnitude bin with the highest frequency of events in the non-cumulative frequency magnitude distribution (Wiemer & Wyss 2000). To estimate the *b*-value we used a maximum-likelihood technique (Aki 1965; Bender 1983):

$$b = \frac{\log_{10}(e)}{\left[M - (Mc - \frac{\Delta M_{bin}}{2})\right]}$$

where *M* is the mean value of the magnitudes greater or equal to *M*c, and M_{bin} = 0.1 is the binning width of the catalogue. The analysis was performed for a total of 7 periods, each with a total of 158 events. The *b* parameter characterizes the ratio of the number of stronger earthquakes to the number of weaker ones, and its value vary from 0.5 to 1.5 depending on the distribution regional stress and tectonics (Mogi 1967; Tsapanos 1990). The lower the *b* coefficient, the larger the probability of have stronger events. According to Figure 31, the largest *b*-value reported in Puerto Gaitan occurs between August 2014 and May 2015. The rest of the reported values is below 1.0, which is considered as a universal value for all tectonic regimes (Frohlich & Davis 1993; Kagan 1997, 1999; Wesnousky 1999; Godano & Pingue 2002; Bird & Kagan 2004; Wech *et al*. 2010). The probability of occurrence of large events in Puerto Gaitan seems to be low. *M*c does not vary drastically, so we consider that the recording capability of the seismic network is good enough to record events over time.

Results: Pumped-in hydraulic energy EPH and radiated seismic energy ES

Main results are shown in Figure 32. The analysis was carried out for 34 periods of time, corresponding to the months between March 2013 and December 2015. To estimate the input hydraulic energy, we used the monthly averages of injection rate and injection pressure. The output elastic energy was assessed by using the energy released of each individual induced event in the study area. The upper panel (Figure 32) shows Q ($m^3\ s^{-1}$) and P (MPa) over time. The injection rate (blue curve) increases steadily over time. The average injection pressure is represented by the black line. It presented two considerable fluctuations in 2013 followed by slightly more moderate variations until the end of 2015. Since both curves show average values, it is not possible to establish with certainty whether the injection of water is done in cycles or if it is done invariably. Figure 32 shows the Mw and Es of induced earthquakes. Events with Mw > 4.0 are marked with red stars. The graph shows two significant accumulations of events. One, during the first half of 2013, and the second throughout 2014. Events with Mw > 4.0 were recorded during the first half of 2014 and second half of 2015. The maximum Es released was 0.0 6259 (MJ). Figure 32 shows the rate of increase of E_{PH} over time. The total cumulative E_{PH} is 3.85E + 09 (MJ) in December 2015 and was calculated through the sum of monthly E_{PH} estimations. The cumulative total of Es equals 0.499325 (MJ) in December 2017. The bottom panel (Figure 32) shows the ratio of both Es and E_{PH} changing with time. Three pick phases of efficient seismic radiation can be identified at the beginning, in the middle and at the end of the injection cycle. In-between, two stages are identified with no very efficient seismic radiation.

Discussion

In this paper, we observed a relation in time and space between the operations of injection of residual water and the sequence of earthquakes in Puerto Gaitan between 2013 and 2015. Previous studies had reported that the seismicity in Puerto Gaitan had its origin as a consequence heavy oil production (Gomez *et al*. 2015). At the time, the available information was that of monthly oil production. In this study, we presented the volume of water injected, the pressure and flow of surface injection, as possible operating factors that induced earthquakes in Puerto Gaitan between 2013 and 2015.

Like many induced events, we hypothesize that Puerto Gaitan earthquakes are generated in the form of swarm like clustering that migrates in space and time in line with the propagation of fluids in the porus media (Shapiro *et al*. 2002). The temporal and spatial distribution of earthquakes seems to demonstrate the prior (Figure 29). It can be evidenced that the oldest events tend to move away from the injection clusters as time passes. The migration of the triggered front of induced seismicity is often described by a pore pressure diffusion process. Measuring the temporal space evolution of the triggered front can allow the estimation of the hydraulic diffusivity of the porus medium (Shapiro *et al*. 1997, 2002). From the distribution of the seismicity registered by the SGC, it is not possible to identify that the migration of fluids reactivates faults or creates new fractures as a mechanism for the generation of induced events. Neither is there enough information to determine if there is a causal relationship between a specific injector well and a particular earthquake.

A qualitative analysis of the slopes of the V and released Mo curves (Figure 30) show that both have the same shape, that is, they evolve in the same way over time. The slopes shown in Figure 30 of the V curve schematically represent the radius between $\Delta V/\Delta t$. The slopes of the released Mo curve represent $\Delta M\mathrm{O}/\Delta t$. Similarities between both curves were identified in three phases that were recognized. The first and the last associated with an increase in ΔV that generated an increase in ΔMo, and an intermediate period where a decrease in ΔV was observed that triggered a decrease in ΔMo. This feature possesses a general discussion that for the case of Puerto Gaitan, the seismicity could be purely influenced by fluids injection other than regional tectonic and stress features. One of the reasons to support this hypothesis has to do with the increase in the recorded event rate. Before 2012 this was 1/annual, when the volumes of water injected were not significant. When water volumes increased abruptly, the rate of recorded events increased to 804/annual. The second reason for this hypothesis has to do with the lag time between both curves. The 218 days established from the cross-correlation between both time-series appear to be a reasonable period for the migration front of the injected fluid volume to generate induced events (Figure 30). Some case studies show that this lag can occur even years after the water has been injected in tectonically stable areas like it has been the case in some areas of the United States (Chen *et al*. 2017).

The panels of Figure 32 show the results of the conversion of the volume of water into hydraulic potential energy, and the Mo released into irradiated seismic energy. The distribution of injection pressure and flow in Figure 32 allow us to identify that another possible operational factor that has an impact on the generation of induced earthquakes in Puerto Gaitan is the injection rate. The average injection rate increases steadily over time just like the Mo is released. On the contrary, the injection pressure due to observed fluctuations does not seem to be a conclusive criterion to establish the causality of the seismicity. One of the advantages of the methodology applied in this research is that it allows to express V and Mo in energy units. This simplifies the assessment between both variables. Figure 32 show the behavior of the input and output energy into the reservoir system over time. Figure 32 shows the distribution of the radius between the output energy of the system and the input energy. The radius is not constant over time but has fluctuations that depend on the variables of operation during the injection of crude oil. We recommend to analyze this energy ratio over time for other fields of fluid-injection-induced seismicity. Peak and plateau values can be used to obtain more insights about the interrelation between seismic radiated energy and operational parameters.

We compared the seismic moment Mo released and energy efficiency of the events with Mw 4.0 + recorded in Puerto Gaitan, with other data collected worldwide in water reservoirs, during hydraulic fracturing operations, geothermal systems and laboratory experiments (Figures 33 and 34). The sequence of events in Puerto Gaitan shows that released seismic moment is found to depend on the pumped-in hydraulic energy. The aforementioned means that the greater the energy injected, the greater the quantification of the energy released after the injection of fluid. There is widespread acceptance that the volume of fluid injected is the main variable to quantify the Mo released resulting from injection operations. McGarr (2014) proposes a linear relation between both parameters ($M_{\mathrm{Otot}}\ \alpha\ V$), while others authors such as van der Elst *et al*. (2016), Galis *et al*. (2017) and De Barros *et al*. (2019) have reported a linear relationship ($M_{\mathrm{Otot}}\ \alpha\ V^{3/2}$). It is also recognized that the prediction of Mo released from only the volume of water injected may be overestimated considering that a large part of these relationships disregard that a large part of the deformation is aseismic (De Barros *et al*. 2018; McGarr *et al*. 2018). Therefore, to assertively estimate the prediction of the released seismic energy, if the geological structures will respond seismically or not must be taken into account. Additionally, the sensitivity of the *M*o induced to the monitoring parameters during the manipulations of industrial fluids in reservoirs should be explored. As mentioned above, an energy efficiency analysis would be a proper evaluation parameter.

Puerto Gaitan seems not to fit with the reported observations in the literature. While the volume of water in our study area surpasses those reported in documented cases, the magnitudes observed are well below the upper bound proposed by McGarr (Figure 33). Figure 34 shows the relationship between *E*PH versus *E*S of the data shown in Figure 33 and other data collected during hydraulic fracturing operations in Canada and laboratory tests. Energy efficiency during the wastewater injection cycle in Puerto Gaitan is the lowest reported among the cases documented in this study except for Groß- Schonebeck case study in Germany (number 17). The only case that has shown an efficiency close to 100 per cent is Denver. The energy ratio for the other cases is very similar. In most cases, the seismic energy released does not exceed 5 per cent of the injected energy. The efficiency in Puerto Gaitan is well below 0.0001 per cent, which indicates that the energy injected into the system is strongly dissipated during the injection cycle, and the expected seismic energy is not released.

The results obtained can be explained by two possible causes. From the point of view of the reservoir, one cause has to do with the aseismic response of the disposal reservoir. That is to say that the deformation in the disposal reservoir does not always generate an earthquake, but only a small portion of the potential energy stored in a reservoir through injection is released through brittle deformation with associated radiation of seismic energy (McGarr 2014). Another explanation may be associated with the geometry of fluid propagation and the diffusion of fluid pressure in the reservoir. Studies carried out by Dieterich *et al* (2015), have estimated that the escalation between *M*o and *V* is determined by the systems of formation faults, permeability and 3-D diffusion through the Bulk. In the case of Puerto Gaitan, it is possible that fraction of *V* is damped/filtered through fractures that connect with deeper structures of the crystalline basement and is not confined solely in the reservoir. Figure 35 gives an independent support for this hypothesis based on gravity data inversion (Graterol & Rey 2009). Injection clusters and earthquakes are located on a structural high where we assume the crystalline basement to be superficial and gravity data is higher. To the southeast and northwest, we find two depocenters where no seismic activity has been recorded. It seems that earthquakes are grouped in areas where the basement is shallower. The experience of large-scale wastewater injection in Oklahoma (USA) shows that seismicity occurs mainly in the highest part of the crystalline basement. McNamara *et al*. (2015), state that earthquakes in Oklahoma are due to the reactivation of subsurface faults that extend into the crystalline basement. Similar observations have also taken place in CO_2 injection operations at Decatur, Illinois (Goertz-Allmann *et al*. 2017). The Puerto Gaitan basement seems to play two fundamental roles: the first one is to set the seismicity in the current cluster of events in the structural high, that is, when the basement is shallow. The second role has to do with the possible hydraulic connection (permeability) of faults that allow the percolation of water in deeper structures, precisely where the basement is deeper and where the seismicity has not yet spread. Adequate mitigation of risk in Puerto Gaitan, and in general of areas where long-term Injection experiments are made, requires the prior mapping of faulted structures with hydraulic connection between the disposal reservoir and the crystalline basement.

Conclusions

The relationship between oilfield operations and seismicity between 2013 and 2015 in the municipality of Puerto Gaitan is suggestive. Our analysis and results propose that the sequence of events in Puerto Gaitan are the result of the release of the elastic energy stored in the reservoir due to the continuous action of the work exerted by the injection of water. The released Mo in Puerto Gaitan depends on the injected volume, but also on injection rate, surface pressure, depth of crystalline basement and stress conditions of the reservoir. Establishing the relationship between the previous operative criteria and Mo are necessary for understanding and control of long-term injection experiments in the field. The behavior of the V and Mo curves in Puerto Gaitan show us that a reduction of the total pumped volume or slow injection operations may reduce seismic hazard in the area. A hydromechanical analysis allows us to determine that the energy efficiency of the injection cycle is well compared to other documented long-term injection operations. The high seismic deformation of the reservoirs and the possible filtration of large volumes of fluid injected into deeper structures are the main causes that generate low energy efficiency in Puerto Gaitan. These two conditions have allowed long-term injection of large volumes to have not led to significant larger events. However, it is essential to settle if there is a hydraulic connection (high permeability) between the reservoir and the crystalline basement, most likely through basement faults reaching into the reservoir.

Acknowledgements

We want to thank NEXCOA Workshop funding for bringing us together. This work is partially supported by the Universidad Nacional de Colombia, Departamento de Geociencias. S. Gómez-Alba thanks a fellowship by COLCIENCIAS (Grant: Doctorados Nacionales 617-2). C.A Vargas thanks to COLCIENCIAS for partial funding through grant FP44842-006-2016 (Análisis 4-D de *Vp*, *Vs* y la relación *Vp*/*Vs* en la Esquina NW de Suramérica). We wish to acknowledge the work of the Colombian Geological Survey (SGC) for providing the seismological data, as well as the National Hydrocarbon Agency (ANH) for providing water injection information. Comments from Editor Professor Gabi Laske, reviewer Volkey Oye and one more anonymous reviewer, all are acknowledged.

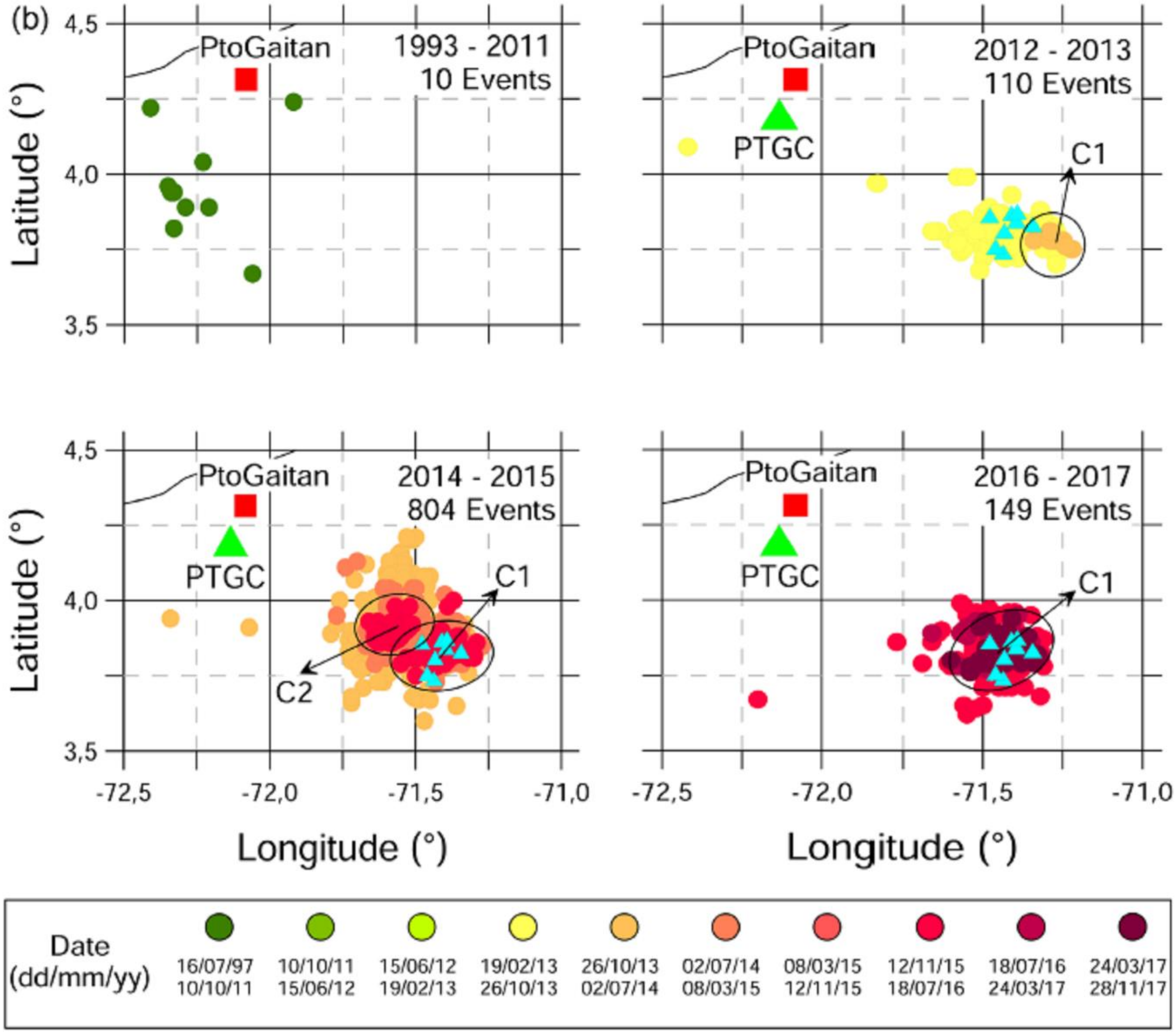

Figure 29. Seismicity distribution in Puerto Gaitan from 1993 to 2018. Each panel shows the distribution of seismicity in Puerto Gaitan as a function of time from 1993 to 2017. The red square represents the location of the city of Puerto Gaitan, and the green triangle is the closest seismological station to the study area (PTGC). The largest number of recorded events took place between 2014 and 2015, with a total of 804 events. The blue triangles represent the 8 injection clusters, which group a total of 51 injection wells. Given the proximity between the events and the injection wells, the seismicity has been catalogued as human related.

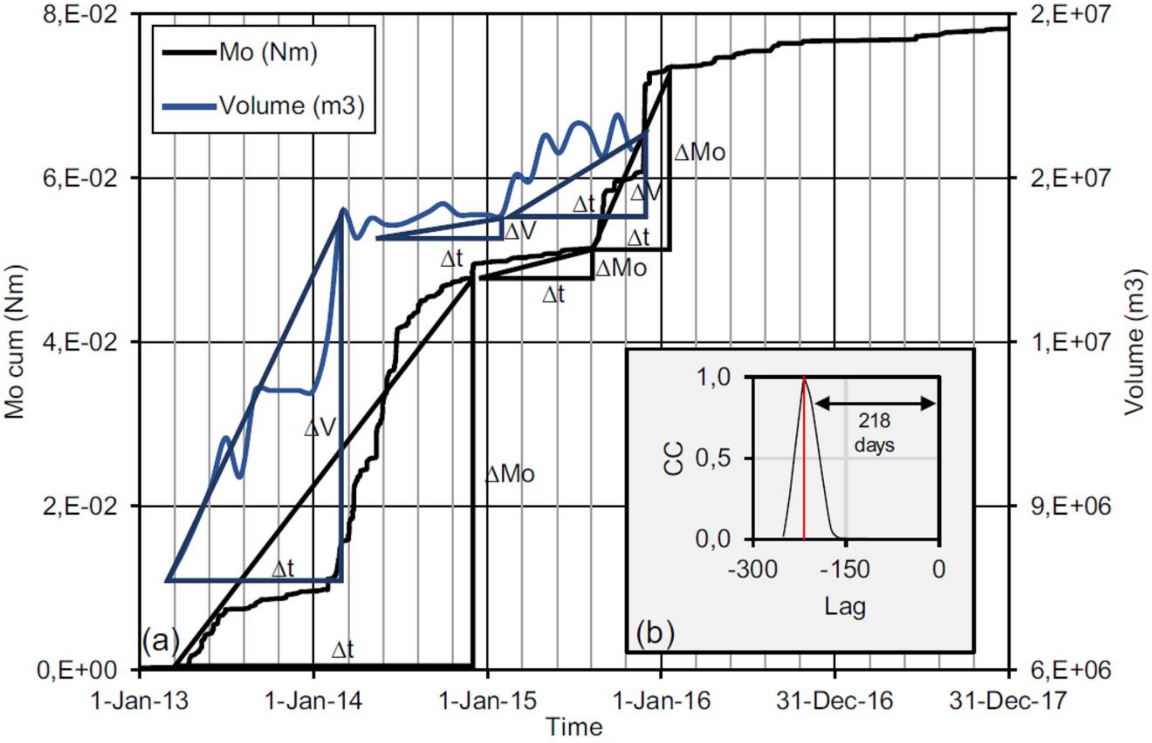

Figure 30. Relationship between seismicity and water injection curves. Data sets have similar shapes but out of phase in time. (a) The blue line and black line represent Water Injection, V, (m^3) and seismic moment, MO, (Nm), respectively. Slopes are a schematic representation of input energy into the system (ΔV/Δt) and output energy from the system (ΔMO/Δt). (b) Cross-correlation between both injection and seismic moment curves from Mo and Volume. Red line shows the lag at maximum correlation. Maximum lag is ∼218 d.

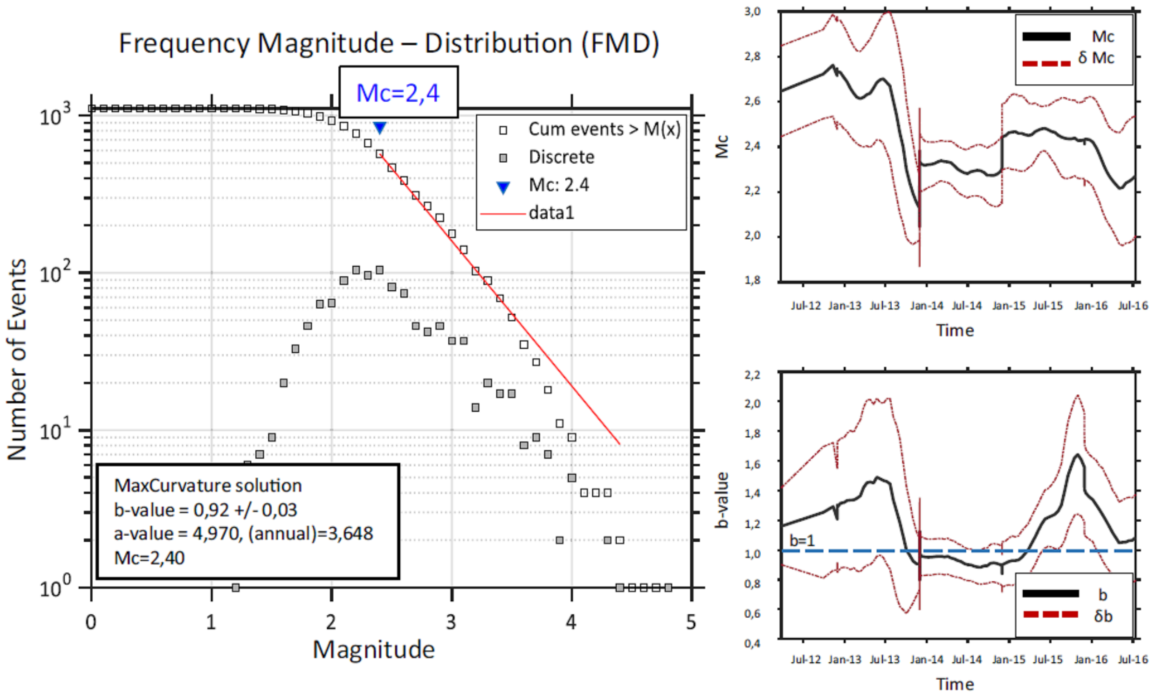

Figure 31. Cumulative frequency magnitude distribution (FMD) plots in Puerto Gaitan. The right-hand panels show the evolution of Mc and b-value over time.

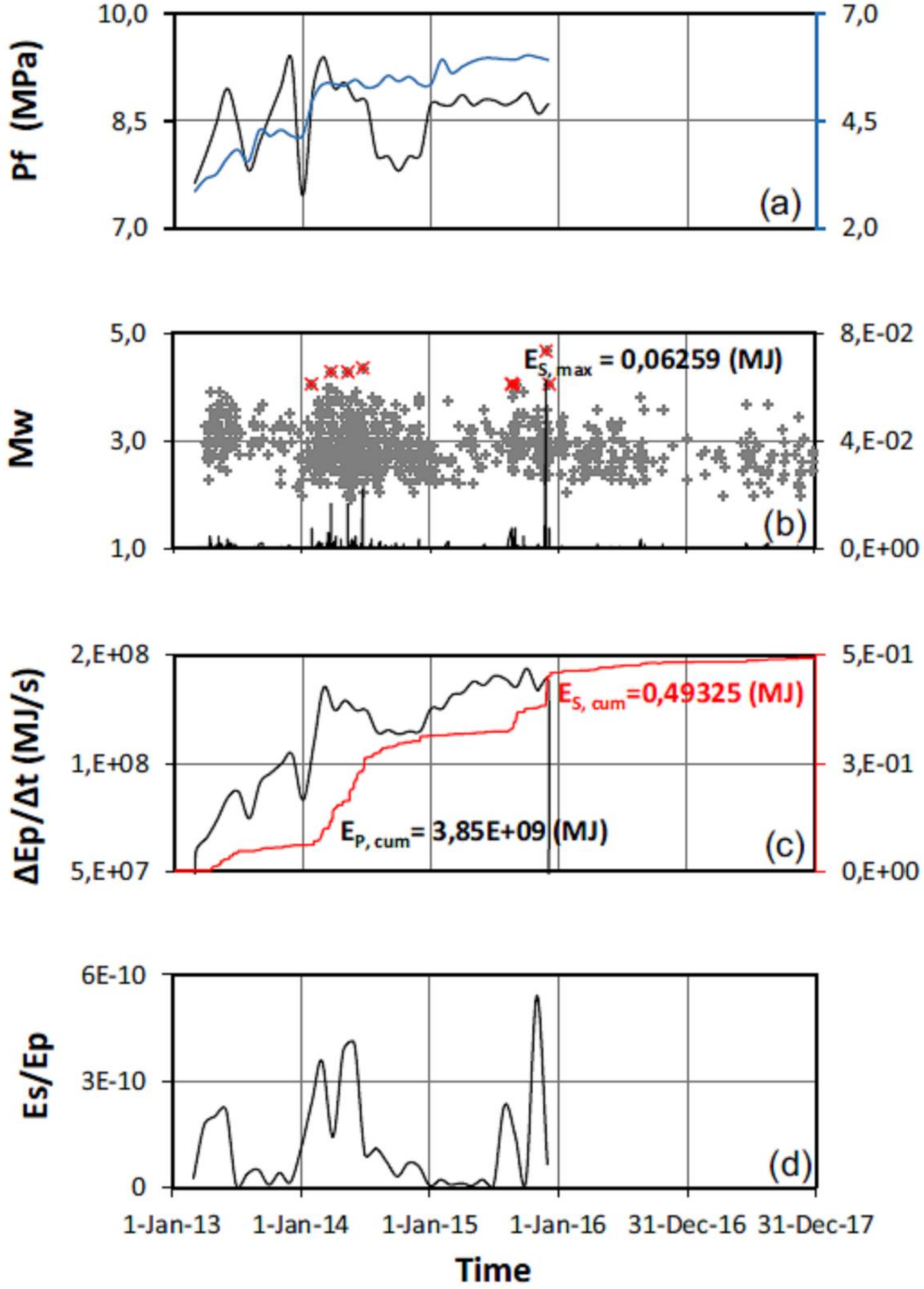

Figure 32. Input and output energy results. (a) Time variation of Injection rate (blue line) Q, (m^3s^{-1}) and fluid Pressure (black line) P_f, at injection point (MPa) (b) Moment Magnitude (grey crosses), Mw and radiated seismic energy, ES (MJ) of all sequence of induced events (black

line). ES, max corresponds to the highest ES of the largest single event (Mw = 4.8). Red crosses are induced events with MW4.0+. (c) Time variation of rate of pumped-in hydraulic energy (black line), EP (MJ) and cumulative radiated seismic energy (red line) ES, cum (MJ). The area under the black curve represents the total amount of pumped-in energy EP, cum (MJ). (d) Ratio of ES to EP changing with time.

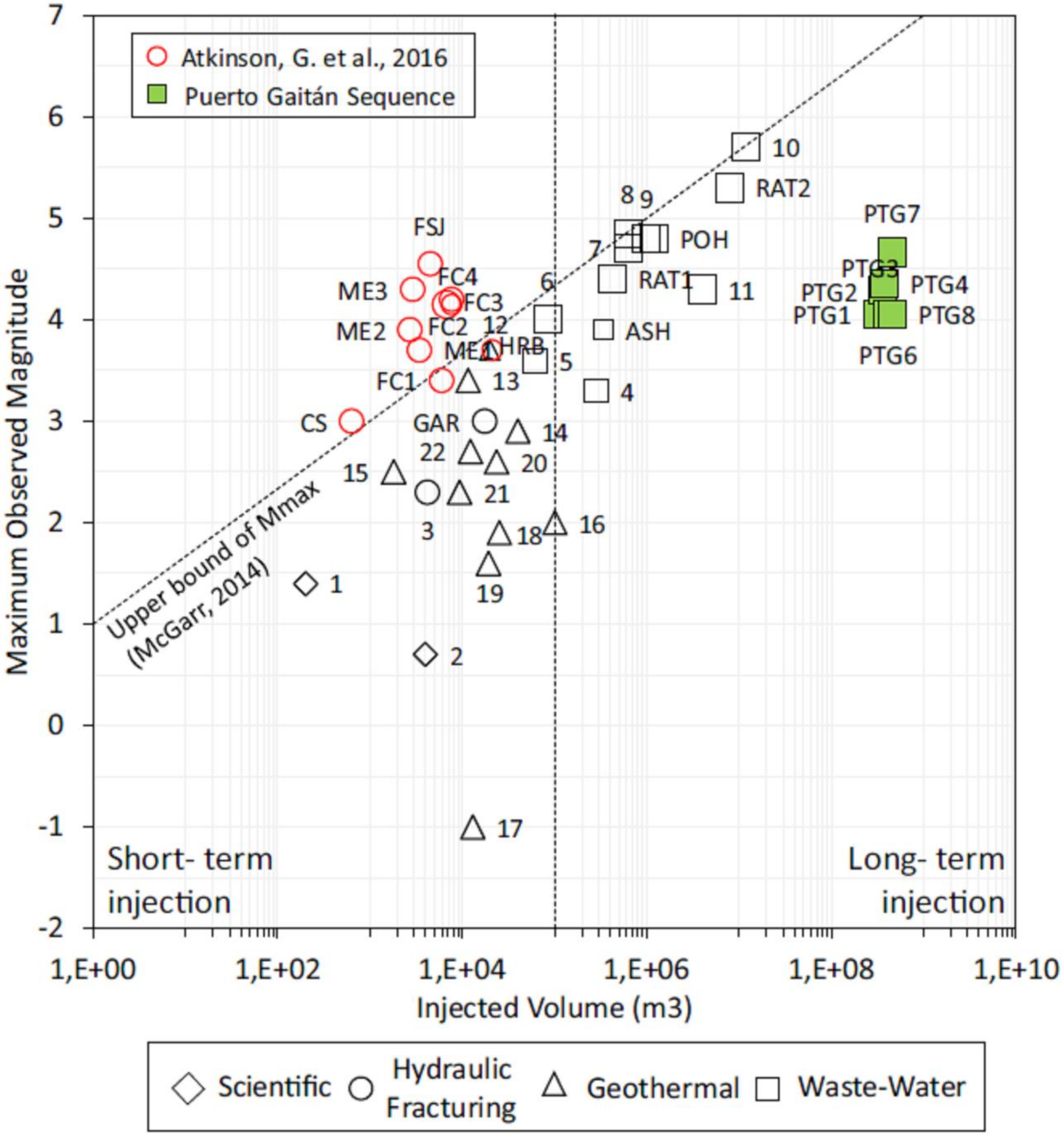

Figure 33. Relationship between maximum observed seismic magnitudes and fluid volume injected during different technology operations. Symbols indicate technology type. Numbers and characters correspond to studies listed by Zhang et al. (2014). Red circles indicate calculations from shale gas reservoirs in Western Canada Sedimentary Basin (Atkinson et al. 2016): (CS) Cardston swarm, (FC1) Fox Creek event 1, (FC2) Fox Creek event 2, (FC3) Fox Creek event 3, (FC4) Fox Creek event 4, (ME1) Montney event 1, (ME2) Montney event 2, (ME3) Montney event 3, (HRB) Horn River Basin, (FSJ) Fort St. John. Upper bound is the

linear relationship postulated by McGarr (2014). Green squares show the relationship between injected volume and observed magnitude for waste water induced events MW 4.0+ reported in this study (PTG) Puerto Gaitan.

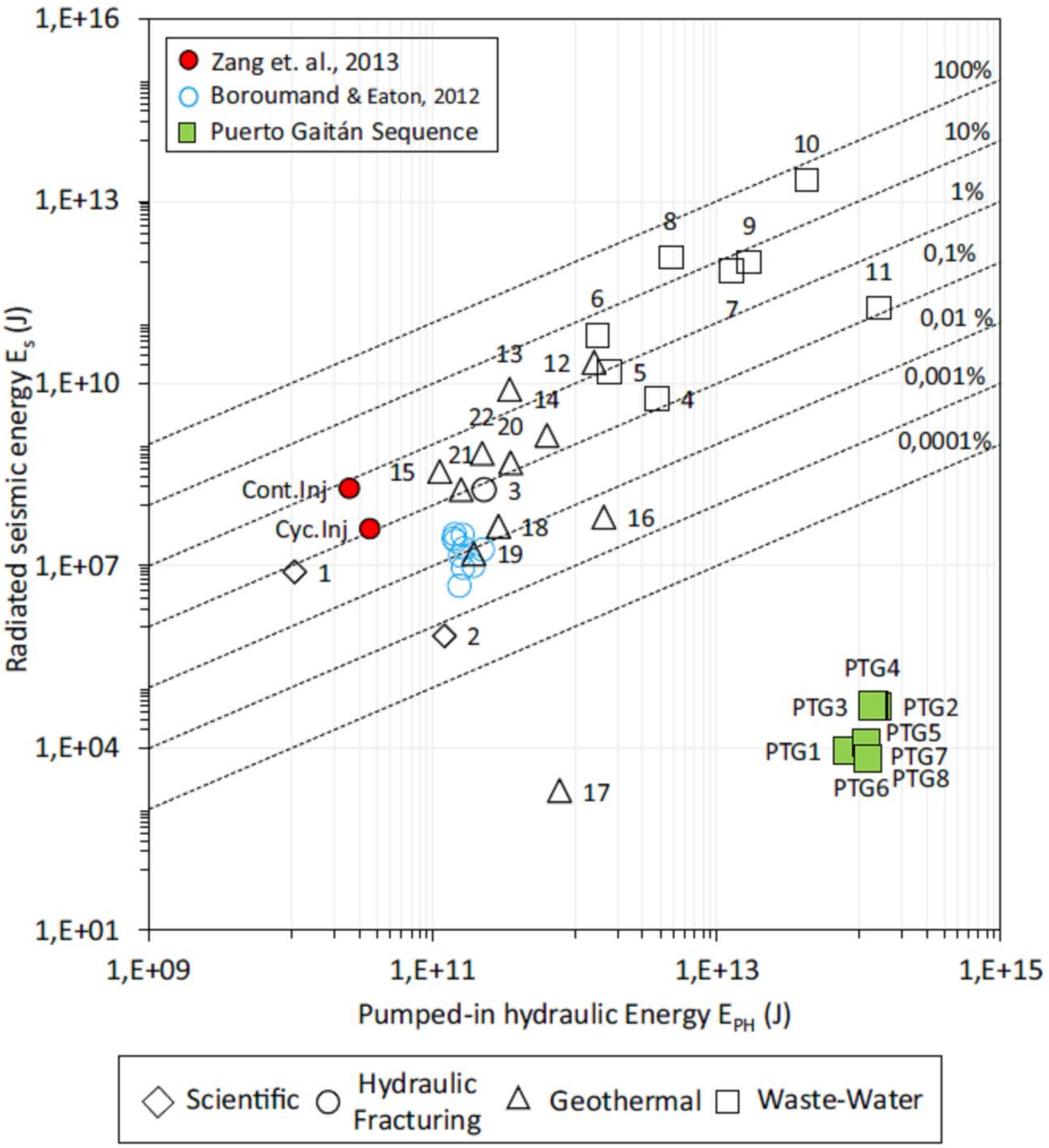

Figure 34. Relationship between total pumped-in energy, EPH, and total radiated seismic energy, ES. Numbers and Characters correspond to the same database used in Fig. 4(a). Blue circles indicate calculations from shale gas reservoirs (hydraulic fracturing) that are based on all induced events (Boroumand & Eaton 2012). Red circles show two stimulation models for continuous and cyclic injection procedures by Zang et al. (2013). The dotted lines represent the energy efficiency.

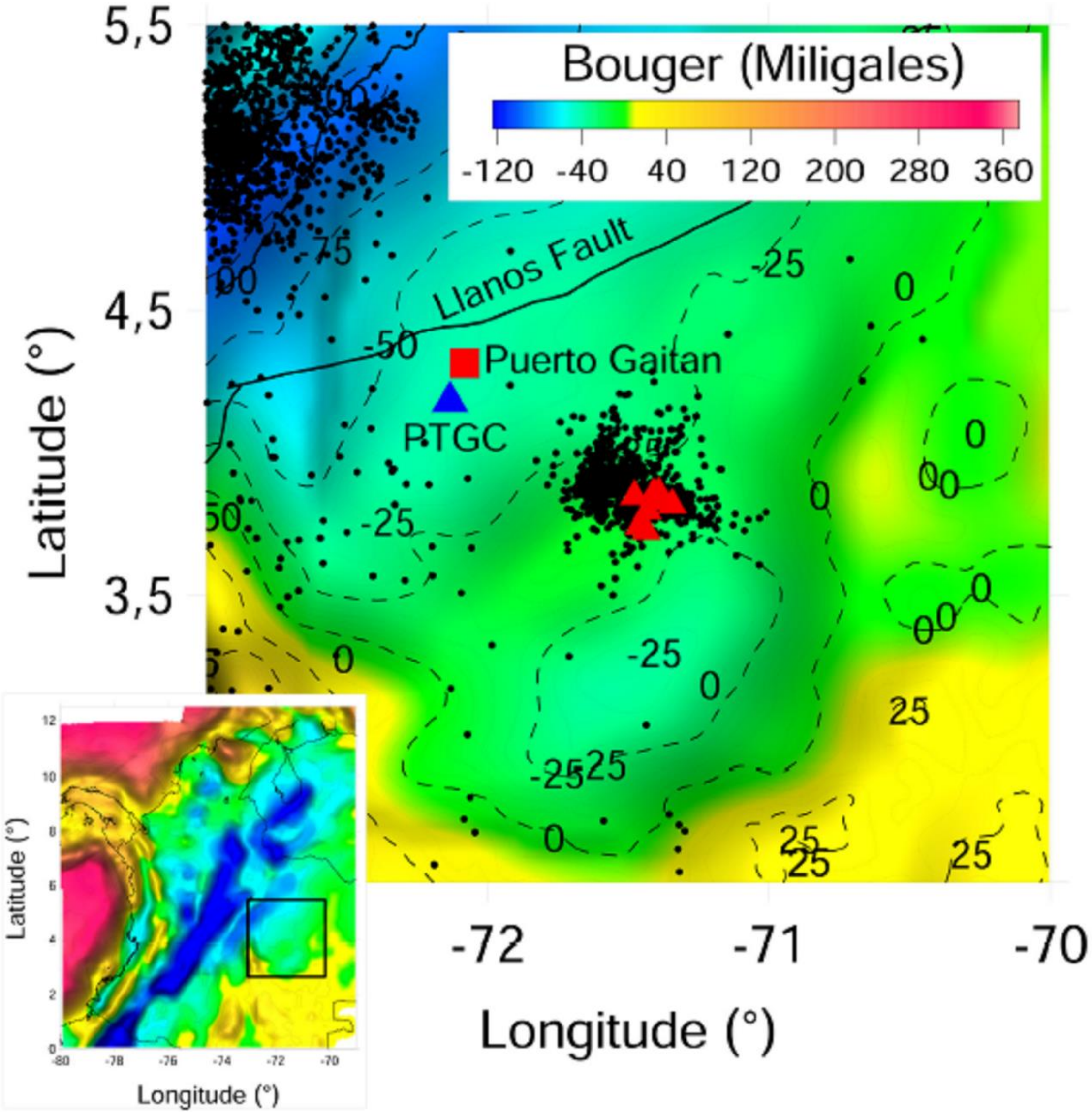

Figure 35. Inversion map of gravity data for Colombia. Seismic events and Injection clusters are set at a structural height. The events are distributed northwest of the study area. To the south where the basement is deeper there has not been seismic activity recorded until to date (modified from Graterol & Rey 2009).

Table 5. Seismic catalogue Puerto Gaitán 1997 - 2018. Source: www.sgc.gov.co

Event	Date	Latitude	Longitude	Depth	Magnitude	Magnitude	Rms	GAP	Error		
ID	mm/dd/yy	(°)	(°)	(km)	ML	MW			Latitude (km)	Longitude (km)	Depth (km)
1	07/16/97	4,24	-71,92	156,0	3,00		0,1	304,0	18,7	21,5	32,7
2	05/31/98	3,67	-72,06	32,0	2,80		0,4	231,0	37,0	19,4	99,9
3	08/02/03	4,22	-72,41	20,9	1,90		0,3	260,0	13,5	19,5	35,2
4	04/04/03	3,82	-72,33	0,0	2,20		1,0	287,0	22,2	24,9	32,2
5	11/18/07	4,04	-72,23	4,0	2,60		0,6	215,0	3,8	8,9	9,7
6	09/21/11	3,89	-72,21	7,0	2,00		0,3	287,0	5,1	9,2	9,6
7	09/24/11	3,94	-72,33	0,0	2,10		0,5	281,0	17,9	12,4	19,2
8	09/28/11	3,94	-72,34	0,0	2,30		0,4	281,0	15,8	11,7	17,2
9	01/10/11	3,96	-72,35	1,3	1,90		0,3	285,0	5,2	5,1	5,9
10	05/10/11	3,89	-72,29	4,0	2,40		0,4	199,0	2,2	5,7	6,3
11	09/16/12	3,97	-71,83	16,4	2,30		0,3	233,0	2,7	7,5	11,0
12	02/04/13	3,79	-71,33	5,3	3,00	3,20	0,4	236,0	3,6	6,5	11,3
13	03/04/13	3,80	-71,54	2,0	2,60		0,5	226,0	4,7	8,8	7,6
14	06/04/13	3,83	-71,42	26,0	2,20		0,5	232,0	5,7	11,4	20,0
15	09/04/13	3,83	-71,34	14,0	2,50		0,5	235,0	3,4	10,8	14,8
16	10/04/13	3,72	-71,50	0,0	2,80		0,3	230,0	3,2	6,2	5,4
17	10/04/13	3,83	-71,33	10,7	2,90		0,5	236,0	5,3	9,1	14,7
18	11/04/13	3,80	-71,45	32,1	2,20		0,2	262,0	2,4	10,1	17,1
19	12/04/13	3,81	-71,66	0,2	2,80		0,8	183,0	5,4	7,9	11,3
20	12/04/13	3,79	-71,44	32,1	1,70		0,3	262,0	6,6	16,3	31,8
21	12/04/13	3,79	-71,34	39,9	2,60		0,6	236,0	5,8	11,9	37,1
22	12/04/13	3,82	-71,38	24,9	2,40		0,6	234,0	9,7	10,3	10,2
23	12/04/13	3,80	-71,41	1,5	2,50		0,5	233,0	4,0	8,0	8,0
24	04/13/13	3,82	-71,42	14,0	2,50		0,6	232,0	5,7	10,1	17,6
25	04/14/13	3,79	-71,34	32,1	2,50		0,5	236,0	5,8	8,7	99,9
26	04/14/13	3,87	-71,50	12,0	2,30		0,5	227,0	4,2	8,5	15,6
27	04/14/13	3,78	-71,47	12,0	2,10		0,5	230,0	4,9	10,2	18,5
28	04/16/13	3,81	-71,29	6,3	3,80	3,80	0,6	238,0	4,3	8,7	13,4
29	04/19/13	3,76	-71,41	4,1	3,40		0,9	234,0	8,5	15,6	18,9
30	04/19/13	3,81	-71,52	0,0	3,10		0,5	274,0	18,5	19,9	18,9
31	04/20/13	3,78	-71,29	12,0	2,60		0,8	238,0	6,4	16,0	27,0
32	04/24/13	3,68	-71,51	0,6	2,90	3,00	0,7	255,0	7,2	26,1	21,3
33	04/28/13	3,70	-71,27	10,8	3,00		1,0	241,0	10,7	17,1	18,4
34	04/28/13	3,77	-71,53	5,3	2,30		0,3	228,0	2,6	7,2	11,5
35	04/30/13	3,80	-71,38	11,6	3,20		0,3	234,0	2,6	6,9	9,8
36	01/05/13	3,76	-71,50	9,4	2,50		0,7	229,0	5,1	13,2	17,5
37	01/05/13	3,75	-71,24	13,3	2,70		0,5	241,0	5,3	11,4	19,4
38	04/05/13	3,83	-71,49	0,0	2,90		0,7	275,0	22,4	25,0	22,4
39	06/05/13	3,81	-71,35	0,0	3,00		0,6	235,0	4,9	12,6	8,2
40	06/05/13	3,81	-71,27	4,1	3,10		0,5	239,0	5,2	12,7	7,3
41	10/05/13	3,80	-71,29	12,7	3,50	3,90	0,5	238,0	3,4	6,8	8,3
42	11/05/13	3,79	-71,46	0,0	2,80		0,4	231,0	3,9	9,3	10,4
43	11/05/13	3,76	-71,24	8,0	3,80	4,00	0,5	241,0	3,4	7,2	7,9
44	11/05/13	3,72	-71,27	0,0	2,80		0,5	240,0	4,7	9,8	7,8
45	05/13/13	3,72	-71,43	4,1	3,30	3,70	0,7	233,0	5,0	11,2	10,4
46	05/14/13	3,78	-71,50	3,6	2,00		0,3	229,0	3,2	6,6	5,3
47	05/16/13	3,79	-71,51	0,0	2,20		0,4	228,0	3,8	8,1	8,5
48	05/17/13	3,78	-71,34	8,7	3,50	4,10	0,6	231,0	3,6	7,3	6,6
49	05/18/13	4,09	-72,42	4,1	2,20		0,5	173,0	2,5	4,5	6,9
50	05/18/13	3,75	-71,31	0,0	2,60	3,20	0,5	220,0	4,7	8,6	8,2
51	05/19/13	3,78	-71,31	4,4	3,40		0,6	237,0	4,9	9,2	8,3
52	05/21/13	3,81	-71,64	0,0	2,50		0,5	245,0	5,9	18,7	15,5
53	05/23/13	3,81	-71,47	5,7	2,20		0,7	230,0	9,9	13,7	11,4
54	05/23/13	3,79	-71,45	0,0	2,70	3,20	0,6	192,0	5,1	7,6	8,6

55	05/24/13	3,79	-71,33	4,1	2,60	3,20	0,5	236,0	4,7	11,3	10,1
56	05/28/13	3,72	-71,39	6,3	2,40		0,6	235,0	5,0	10,9	15,3
57	01/06/13	3,80	-71,49	4,1	2,90	3,60	0,5	229,0	3,3	7,6	6,0
58	02/06/13	3,84	-71,58	4,2	2,90		0,6	224,0	5,0	10,8	10,0
59	02/06/13	3,83	-71,42	5,1	3,30	3,50	0,6	192,0	4,0	6,3	13,1
60	02/06/13	3,87	-71,44	4,1	1,90		0,3	268,0	2,6	6,7	4,5
61	03/06/13	3,99	-71,55	0,0	3,20	3,30	1,0	197,0	7,7	19,1	19,2
62	04/06/13	3,82	-71,35	4,1	2,40		0,4	235,0	2,9	8,3	9,8
63	05/06/13	3,76	-71,48	0,0	2,90		0,6	230,0	4,7	12,8	8,7
64	05/06/13	3,78	-71,29	12,1	3,70	3,80	0,4	238,0	3,9	8,3	14,1
65	12/06/13	3,82	-71,28	25,0	3,10		0,6	238,0	4,1	9,1	7,6
66	12/06/13	3,81	-71,42	5,4	2,60		0,3	232,0	2,4	6,5	6,5
67	12/06/13	3,78	-71,44	0,0	2,50		0,4	256,0	3,3	14,9	11,1
68	06/14/13	3,79	-71,45	0,9	2,90		0,5	231,0	4,2	15,9	9,8
69	06/14/13	3,84	-71,38	5,6	3,40		0,5	233,0	3,5	7,6	7,2
70	06/15/13	3,79	-71,31	10,0	3,40	3,50	0,7	237,0	4,8	12,3	15,7
71	06/15/13	3,79	-71,50	0,0	2,70		0,5	229,0	3,8	9,1	7,3
72	06/15/13	3,83	-71,54	2,0	2,70		0,5	226,0	3,7	13,9	9,9
73	06/17/13	3,78	-71,25	14,0	3,50	3,90	0,6	240,0	4,2	8,3	7,7
74	06/19/13	3,77	-71,37	0,0	2,90	3,40	0,8	235,0	5,4	14,4	10,2
75	06/24/13	3,79	-71,29	4,1	2,50		0,4	238,0	2,7	8,4	7,5
76	06/27/13	3,79	-71,34	5,6	3,40	3,80	0,5	218,0	3,4	4,8	6,1
77	06/28/13	3,78	-71,35	0,0	2,70		0,5	236,0	4,8	12,8	8,6
78	06/29/13	3,85	-71,33	2,0	2,50		0,2	286,0	11,9	13,2	12,0
79	06/30/13	3,80	-71,53	4,1	2,80	3,50	0,7	227,0	6,0	8,1	12,0
80	06/30/13	3,80	-71,27	8,6	2,80		0,6	239,0	4,7	9,1	8,7
81	06/30/13	3,83	-71,36	11,0	3,20	3,60	0,5	260,0	4,1	10,1	11,4
82	06/30/13	3,77	-71,25	11,3	2,90	3,20	0,5	265,0	4,1	10,6	9,4
83	06/30/13	3,81	-71,29	11,5	3,00	3,30	0,5	238,0	3,7	8,5	7,4
84	07/07/13	3,78	-71,43	6,0	2,30		0,7	232,0	4,9	12,5	8,8
85	07/13/13	3,78	-71,58	27,6	2,80		0,8	187,0	5,5	9,3	17,6
86	07/08/13	3,80	-71,48	0,0	2,30		0,5	229,0	4,3	8,3	7,7
87	11/08/13	3,83	-71,28	35,4	2,50		0,5	238,0	4,1	7,7	31,9
88	08/14/13	3,80	-71,44	26,2	2,60		0,8	256,0	7,6	29,8	42,7
89	08/20/13	3,77	-71,58	4,0	3,10	3,30	0,7	187,0	5,9	7,5	15,7
90	08/20/13	3,85	-71,56	10,1	3,00	3,20	0,5	186,0	3,8	5,7	12,6
91	08/23/13	3,86	-71,31	24,9	3,00	3,10	1,1	195,0	9,4	11,9	16,1
92	08/26/13	3,78	-71,27	8,0	2,60		0,4	239,0	4,2	9,7	16,4
93	08/30/13	3,81	-71,48	0,4	3,00	3,20	0,8	229,0	5,9	15,4	12,2
94	01/09/13	3,74	-71,57	0,0	2,50	2,80	0,7	189,0	6,5	14,1	16,2
95	02/09/13	3,75	-71,22	0,0	3,40		1,0	242,0	8,9	22,1	15,0
96	09/13/13	3,78	-71,28	24,7	3,50		1,8	239,0	14,1	43,5	64,2
97	09/13/13	3,73	-71,44	0,0	3,00		1,9	195,0	17,6	31,7	26,2
98	09/13/13	3,75	-71,56	0,0	2,70		0,8	257,0	7,4	44,7	37,8
99	09/28/13	3,82	-71,56	8,1	2,30		0,7	187,0	7,4	7,6	16,7
100	09/29/13	3,89	-71,48	32,1	2,30		1,6	228,0	15,8	24,5	14,0
101	11/10/13	3,79	-71,35	0,0	2,90	3,10	0,5	247,0	3,5	8,1	7,0
102	10/13/13	3,80	-71,38	0,0	2,60	2,90	0,4	234,0	3,4	6,1	6,0
103	10/26/13	3,85	-71,39	0,0	2,50		0,5	297,0	19,5	10,1	17,4
104	04/11/13	3,84	-71,31	2,7	3,00	3,00	0,5	236,0	3,8	6,0	5,7
105	04/11/13	3,88	-71,32	10,3	3,10	3,10	0,5	235,0	3,7	5,8	5,8
106	05/11/13	3,93	-71,41	0,0	1,60		0,6	274,0	7,1	12,7	11,6
107	05/11/13	3,99	-71,58	0,0	1,90		0,8	196,0	9,0	8,1	12,0
108	05/11/13	3,87	-71,46	8,4	3,10	3,10	0,9	190,0	5,3	7,4	9,5
109	05/11/13	3,78	-71,50	0,8	2,60		0,7	229,0	4,2	8,6	9,2
110	05/11/13	3,81	-71,42	0,0	2,50		0,3	232,0	2,8	3,9	4,9
111	07/11/13	3,84	-71,37	4,5	3,00	3,10	0,5	233,0	5,2	5,7	8,7
112	12/11/13	3,81	-71,34	0,0	2,40		0,4	235,0	2,6	5,4	5,2
113	11/29/13	3,80	-71,37	0,0	3,30	3,40	0,4	234,0	3,1	6,7	5,5
114	01/12/13	3,80	-71,48	0,0	2,90	3,30	0,5	229,0	5,7	10,7	11,9

115	05/12/13	3,83	-71,31	1,1	3,00	3,20	0,5	236,0	3,4	5,6	5,8
116	05/12/13	3,81	-71,38	0,0	2,60		0,5	264,0	9,7	24,6	18,3
117	12/21/13	3,86	-71,44	0,0	1,50		0,5	230,0	4,5	7,2	6,5
118	12/22/13	3,84	-71,43	4,0	2,80	3,10	0,3	231,0	2,8	5,3	6,2
119	12/22/13	3,78	-71,60	0,0	1,50		0,6	224,0	6,5	10,1	10,5
120	12/25/13	3,80	-71,41	0,1	2,20		0,4	233,0	5,8	6,7	6,9
121	03/01/14	3,81	-71,48	5,5	2,20		0,6	260,0	9,9	12,0	10,9
122	05/01/14	4,12	-71,67	0,0	1,70		0,7	231,0	9,5	11,4	14,1
123	06/01/14	3,94	-72,34	2,4	1,30		0,5	182,0	4,9	3,8	7,5
124	09/01/14	3,83	-71,29	0,0	1,90		0,2	237,0	2,1	3,4	3,5
125	01/19/14	3,83	-71,41	0,0	3,10		0,6	232,0	5,1	8,5	9,2
126	01/20/14	3,67	-71,45	3,9	2,40		0,3	233,0	3,0	6,3	5,1
127	01/20/14	3,78	-71,41	3,8	2,10		0,5	233,0	3,0	5,5	5,3
128	01/20/14	3,84	-71,50	1,6	2,00		0,4	228,0	2,7	6,2	6,3
129	01/20/14	3,84	-71,43	3,2	2,60		0,3	231,0	3,0	4,6	4,8
130	01/24/14	3,94	-71,66	0,0	2,00		0,5	234,0	4,3	5,5	9,0
131	01/26/14	3,81	-71,52	0,0	2,40		0,5	228,0	3,4	6,3	7,3
132	01/31/14	3,90	-71,62	0,0	2,10		0,6	236,0	8,7	9,9	11,8
133	01/31/14	3,86	-71,41	1,8	4,00	3,80	0,4	256,0	2,6	6,0	5,2
134	01/31/14	3,92	-71,46	0,0	2,90		0,6	274,0	10,5	8,4	10,1
135	01/02/14	4,02	-71,61	0,0	2,20		0,6	195,0	6,7	8,0	9,1
136	05/02/14	3,97	-71,64	0,0	2,10		0,8	234,0	8,6	9,7	11,1
137	05/02/14	3,85	-71,43	1,8	2,20		0,7	231,0	5,1	8,5	9,3
138	05/02/14	3,76	-71,60	0,0	1,70		0,7	224,0	5,9	16,7	18,0
139	07/02/14	3,80	-71,50	0,0	2,60		0,7	228,0	5,0	10,1	9,3
140	10/02/14	3,86	-71,72	0,1	1,80		0,6	216,0	6,7	9,7	10,6
141	10/02/14	3,84	-71,42	5,4	2,40		0,5	231,0	4,7	6,5	6,9
142	02/13/14	4,04	-71,50	0,0	2,70		1,0	183,0	11,7	12,5	14,7
143	02/13/14	3,80	-71,72	0,0	2,00		0,6	234,0	9,6	10,0	11,7
144	02/13/14	3,90	-71,59	0,0	3,30		0,8	222,0	5,2	9,0	10,1
145	02/13/14	4,04	-71,59	0,0	2,70		0,5	235,0	5,2	6,5	8,1
146	02/15/14	3,88	-71,61	0,0	2,40		0,4	222,0	2,7	4,5	4,5
147	02/15/14	3,84	-71,46	0,0	2,40		0,4	230,0	3,6	7,0	6,3
148	02/15/14	3,92	-71,33	0,1	2,40		0,4	277,0	7,1	9,6	9,7
149	02/16/14	3,87	-71,73	0,0	2,20		0,5	232,0	5,0	4,7	7,8
150	02/16/14	3,86	-71,41	2,0	3,30	3,40	0,5	231,0	3,8	5,8	6,1
151	02/17/14	3,76	-71,32	0,0	2,30		0,5	300,0	17,1	8,4	14,0
152	02/18/14	3,90	-71,53	0,0	3,50	3,60	0,9	225,0	6,0	12,2	11,7
153	02/18/14	3,71	-71,68	0,4	2,20		0,5	296,0	12,1	7,4	9,6
154	02/19/14	3,92	-71,59	4,1	2,40		0,7	254,0	9,4	14,9	15,8
155	02/19/14	3,88	-71,60	0,0	3,00		0,5	222,0	3,4	5,3	5,3
156	02/20/14	3,89	-71,55	4,1	3,60	3,60	0,7	224,0	4,7	8,4	9,3
157	02/20/14	4,13	-71,54	0,0	2,10		0,5	249,0	7,6	9,5	10,0
158	02/20/14	3,92	-71,60	4,1	2,00		0,4	222,0	5,7	7,7	8,2
159	02/20/14	3,99	-71,61	0,0	2,00		0,5	235,0	6,1	7,0	7,8
160	02/20/14	3,96	-71,59	0,0	2,40		0,5	236,0	5,7	6,6	7,3
161	02/20/14	3,90	-71,58	2,0	2,60		0,6	223,0	4,4	8,5	7,9
162	02/21/14	3,90	-71,57	4,1	3,30	3,40	0,4	223,0	3,3	6,0	6,2
163	02/21/14	3,91	-71,61	4,1	3,00	3,20	0,4	221,0	2,6	5,5	6,1
164	02/22/14	3,89	-71,59	4,1	3,10	3,40	0,4	223,0	3,0	5,0	5,7
165	02/22/14	3,89	-71,57	4,1	2,60		0,6	224,0	4,9	7,2	7,9
166	02/22/14	3,87	-71,60	0,0	2,10		0,5	222,0	4,0	6,4	6,9
167	02/22/14	3,86	-71,61	0,0	1,70		0,5	222,0	4,2	7,0	7,4
168	02/22/14	3,88	-71,66	0,0	1,90		0,5	219,0	4,0	6,7	7,2
169	02/22/14	3,89	-71,58	2,0	1,90		0,4	223,0	3,7	6,1	6,3
170	02/22/14	3,93	-71,59	0,0	1,90		0,4	293,0	15,0	9,0	12,4
171	02/22/14	3,91	-71,60	0,3	2,90	3,20	0,5	221,0	4,1	6,4	6,9
172	02/22/14	3,91	-71,58	4,1	2,50		0,5	236,0	4,7	7,7	7,0
173	02/22/14	3,89	-71,58	4,1	2,90	3,20	0,5	223,0	3,4	5,4	7,1
174	02/22/14	3,89	-71,58	4,1	3,10	3,40	0,8	223,0	4,6	7,7	8,7

175	02/22/14	3,91	-71,57	0,0	3,30		0,9	223,0	5,3	8,8	8,9
176	02/22/14	3,92	-71,59	0,0	2,30		0,4	293,0	11,5	7,0	9,5
177	02/23/14	3,80	-71,70	4,1	2,10		0,6	218,0	5,9	8,9	8,1
178	02/23/14	3,89	-71,59	4,1	2,30		0,6	222,0	4,6	8,0	8,9
179	02/23/14	3,88	-71,60	0,0	1,60		0,5	222,0	6,5	8,1	8,1
180	02/23/14	3,97	-71,52	8,8	1,80		0,5	257,0	6,6	11,7	7,6
181	02/23/14	3,91	-71,57	4,1	1,80		0,7	294,0	15,6	9,3	12,2
182	02/23/14	3,88	-71,60	0,0	2,40		0,6	222,0	4,2	10,2	8,3
183	02/23/14	3,90	-71,61	4,1	1,80		0,4	221,0	4,2	5,3	5,5
184	02/23/14	3,84	-71,65	0,0	1,80		0,5	294,0	12,6	7,4	10,8
185	02/23/14	3,77	-71,69	0,0	1,90		0,4	295,0	10,1	7,5	9,0
186	02/23/14	3,96	-71,57	0,0	2,10		0,5	292,0	16,5	9,6	13,5
187	02/24/14	3,90	-71,61	0,0	2,90		0,5	221,0	4,5	7,4	8,3
188	02/24/14	3,84	-71,50	4,1	2,00		0,7	227,0	5,8	9,8	10,5
189	02/24/14	3,88	-71,59	0,0	2,50		0,5	222,0	4,2	9,5	8,8
190	02/24/14	3,87	-71,54	0,8	2,80	3,00	0,3	225,0	2,2	3,4	3,5
191	02/24/14	3,88	-71,59	0,0	3,30	3,40	0,5	223,0	2,7	5,1	5,0
192	02/24/14	3,86	-71,59	0,0	3,20	3,30	0,5	223,0	3,4	5,5	5,6
193	02/25/14	3,91	-71,59	4,2	3,50	3,60	1,3	222,0	7,3	10,3	10,5
194	02/25/14	3,90	-71,60	0,5	3,50	3,50	0,5	222,0	2,6	4,8	4,9
195	02/25/14	3,89	-71,57	4,1	2,00		0,5	255,0	5,2	9,9	8,2
196	02/25/14	3,89	-71,59	0,0	3,10	3,20	0,5	222,0	4,1	6,8	6,9
197	02/25/14	4,13	-71,59	4,1	2,20		0,6	269,0	10,1	9,6	10,0
198	02/26/14	3,85	-71,67	4,1	2,70		1,1	219,0	7,4	12,4	13,5
199	02/26/14	3,90	-71,72	4,2	2,20		0,7	216,0	4,8	9,2	10,1
200	02/26/14	3,88	-71,58	4,1	3,10		0,5	223,0	3,2	5,7	6,5
201	02/26/14	3,88	-71,56	4,1	1,90		0,8	294,0	14,2	11,2	12,2
202	02/26/14	4,11	-71,74	0,0	2,50		0,8	228,0	9,4	9,0	9,1
203	02/26/14	3,85	-71,58	5,3	1,80		0,5	224,0	4,2	7,1	7,5
204	02/27/14	3,85	-71,60	4,1	2,40	3,10	0,6	223,0	4,7	8,4	8,8
205	02/27/14	3,85	-71,69	4,1	2,10		0,7	181,0	4,4	9,8	10,0
206	02/28/14	3,87	-71,58	4,1	3,10		0,5	223,0	3,2	5,2	5,8
207	02/28/14	3,92	-71,59	4,1	2,00		0,5	254,0	6,5	12,0	11,3
208	02/28/14	3,89	-71,59	4,1	2,30		0,5	222,0	4,3	6,7	7,7
209	02/28/14	3,87	-71,70	4,1	2,30		0,7	217,0	6,2	10,0	11,0
210	02/28/14	3,89	-71,59	4,1	3,20	3,50	0,5	223,0	3,5	6,2	7,0
211	02/28/14	3,88	-71,63	4,1	2,30		0,6	221,0	3,8	6,3	7,3
212	02/28/14	3,88	-71,61	4,1	1,90		0,5	254,0	4,9	9,5	7,7
213	02/28/14	3,92	-71,61	4,1	2,00		0,6	253,0	6,2	12,7	9,6
214	01/03/14	3,91	-71,62	8,6	2,40		0,3	234,0	3,1	7,2	4,8
215	01/03/14	3,90	-71,63	4,1	2,30		0,2	182,0	3,5	6,0	5,8
216	01/03/14	3,89	-71,61	0,0	3,50		0,5	222,0	2,7	4,7	4,8
217	02/03/14	3,83	-71,59	4,1	2,20		0,6	185,0	6,3	8,7	9,3
218	02/03/14	3,88	-71,58	4,1	2,10		0,6	223,0	6,1	9,5	10,9
219	02/03/14	3,89	-71,63	0,0	2,20		0,4	220,0	3,8	6,0	6,8
220	03/03/14	3,87	-71,69	4,1	2,10		0,3	218,0	3,1	6,3	5,8
221	03/03/14	3,89	-71,45	7,0	2,30		0,4	229,0	3,7	4,7	5,0
222	03/03/14	3,86	-71,56	4,1	2,60		0,5	225,0	5,2	8,4	9,6
223	03/03/14	3,91	-71,59	4,1	2,40		0,4	222,0	3,7	6,0	7,0
224	03/03/14	3,88	-71,54	0,5	2,50		0,6	225,0	5,5	10,6	10,5
225	05/03/14	3,84	-71,72	4,1	2,10		1,2	293,0	19,3	19,6	17,0
226	09/03/14	3,78	-71,51	4,1	2,10		0,4	229,0	4,2	7,3	6,9
227	10/03/14	3,90	-71,58	4,1	2,10		0,6	255,0	7,9	12,3	10,1
228	12/03/14	3,90	-71,59	4,1	2,30		0,7	280,0	12,8	8,6	10,4
229	12/03/14	3,88	-71,62	4,1	2,40		0,4	221,0	3,1	5,9	5,6
230	03/13/14	3,89	-71,55	4,1	2,10		0,6	225,0	7,4	9,1	10,8
231	03/13/14	4,03	-71,57	4,1	2,50		0,8	270,0	10,0	12,4	12,1
232	03/14/14	3,97	-71,65	0,0	2,20		0,3	277,0	7,6	5,6	9,3
233	03/15/14	3,93	-71,58	4,1	1,60		0,6	222,0	6,6	9,2	9,9
234	03/15/14	3,90	-71,55	4,1	3,50	3,70	0,6	224,0	4,1	6,8	8,0

235	03/15/14	3,91	-71,55	0,0	1,60		0,6	224,0	5,6	6,9	8,1
236	03/15/14	3,90	-71,57	4,1	3,40		0,5	313,0	10,5	9,6	8,3
237	03/15/14	3,81	-71,58	4,1	2,30		0,5	283,0	9,7	6,7	7,5
238	03/16/14	3,83	-71,32	4,1	2,30		0,4	236,0	3,2	4,7	5,6
239	03/16/14	3,89	-71,57	4,1	2,50		0,5	280,0	9,2	13,4	11,2
240	03/17/14	3,88	-71,55	4,1	3,70	3,70	1,1	225,0	7,8	11,6	13,5
241	03/17/14	3,89	-71,55	4,1	3,90	4,00	0,5	224,0	2,5	3,9	4,7
242	03/17/14	3,89	-71,59	4,1	2,60		0,5	222,0	4,3	6,2	7,0
243	03/17/14	3,83	-71,60	4,1	2,60		0,6	223,0	7,3	8,7	10,5
244	03/17/14	4,00	-71,55	4,1	2,30		0,5	279,0	9,7	7,1	8,2
245	03/18/14	4,05	-71,59	4,1	2,40		0,6	235,0	10,3	8,9	11,5
246	03/18/14	3,94	-71,65	4,1	2,10		0,7	278,0	10,3	10,2	13,0
247	03/18/14	3,93	-71,64	4,1	2,10		0,6	219,0	5,3	8,4	10,2
248	03/19/14	3,87	-71,58	4,1	3,40	3,60	0,6	223,0	3,4	5,9	6,0
249	03/19/14	3,92	-71,51	4,1	2,30		0,5	225,0	4,8	6,5	6,6
250	03/20/14	3,86	-71,63	0,0	3,30		0,7	221,0	4,0	10,5	7,5
251	03/22/14	3,86	-71,61	4,9	2,20		0,3	237,0	3,5	4,5	5,2
252	03/24/14	3,86	-71,47	4,6	2,40		0,5	229,0	4,6	6,5	7,0
253	03/24/14	3,85	-71,39	4,1	3,90	3,90	0,6	232,0	3,4	5,2	5,9
254	03/25/14	3,85	-71,39	4,1	1,90		0,5	233,0	4,4	6,4	6,6
255	03/26/14	3,82	-71,41	0,1	2,70		0,5	232,0	3,8	6,2	6,4
256	03/26/14	3,80	-71,45	0,0	2,80		0,4	231,0	3,1	5,4	5,5
257	03/26/14	3,86	-71,38	6,7	3,00		0,4	233,0	4,2	5,6	5,8
258	03/27/14	3,93	-71,58	4,1	4,30	4,30	0,5	222,0	3,4	4,6	6,3
259	03/27/14	4,08	-71,47	4,1	2,40		0,6	307,0	17,5	11,8	9,7
260	03/27/14	3,89	-71,63	4,1	2,80		0,5	221,0	4,3	7,6	8,1
261	03/28/14	3,86	-71,40	4,0	2,80		0,4	232,0	3,7	5,5	5,8
262	03/28/14	3,86	-71,41	4,5	3,30	3,40	0,4	232,0	3,0	4,4	4,9
263	03/28/14	3,92	-71,44	0,0	2,40		0,5	283,0	11,9	9,1	10,6
264	03/29/14	3,87	-71,62	4,1	2,20		0,5	294,0	12,6	9,7	9,3
265	03/30/14	3,87	-71,59	1,3	3,30	3,50	0,4	223,0	3,5	7,3	7,2
266	03/30/14	3,88	-71,59	0,0	2,80		0,4	223,0	3,2	5,6	5,9
267	03/31/14	3,88	-71,58	0,4	2,90		0,5	223,0	4,5	8,1	8,7
268	03/31/14	3,85	-71,65	0,0	2,40		0,4	252,0	3,9	11,2	8,6
269	03/31/14	3,91	-71,60	2,6	3,00		0,5	222,0	3,8	6,1	6,2
270	01/04/14	3,86	-71,57	0,0	2,90		0,5	224,0	3,7	6,2	6,8
271	01/04/14	3,88	-71,58	0,0	3,10	3,30	0,5	223,0	3,2	5,4	5,7
272	01/04/14	4,02	-71,54	0,0	2,00		0,5	312,0	13,0	12,5	11,6
273	03/04/14	4,08	-71,45	4,1	2,20		0,3	273,0	5,7	5,1	4,9
274	04/04/14	3,89	-71,59	0,6	3,60	3,70	0,5	222,0	3,1	5,5	5,3
275	04/04/14	3,90	-71,57	0,0	2,40		0,4	223,0	2,8	4,5	5,2
276	06/04/14	4,04	-71,57	0,0	2,20		0,5	236,0	6,7	7,2	7,9
277	07/04/14	3,92	-71,57	5,3	2,10		0,3	223,0	7,6	12,4	11,9
278	07/04/14	3,89	-71,65	4,1	1,90		0,5	220,0	5,3	7,3	8,9
279	08/04/14	3,89	-71,51	7,9	2,40		0,3	226,0	2,9	4,3	4,0
280	10/04/14	3,86	-71,40	4,1	3,80	3,90	0,5	232,0	3,7	5,2	5,7
281	10/04/14	3,87	-71,38	4,1	2,50		0,5	233,0	7,0	6,9	8,8
282	04/15/14	3,84	-71,38	0,0	2,20		0,3	289,0	8,7	21,1	14,6
283	04/15/14	3,86	-71,39	2,4	2,80		0,3	232,0	2,7	4,6	4,8
284	04/18/14	3,93	-71,59	4,1	2,20		0,6	222,0	6,0	7,4	9,0
285	04/19/14	3,90	-71,59	4,1	1,60		0,4	279,0	8,3	13,2	11,1
286	04/19/14	3,92	-71,56	4,1	2,20		0,5	313,0	12,6	8,4	8,2
287	04/20/14	3,86	-71,64	4,1	2,40		0,5	252,0	7,5	11,2	10,9
288	04/21/14	3,90	-71,64	0,0	1,90		0,6	252,0	5,7	15,4	11,9
289	04/22/14	3,84	-71,50	10,0	2,40		0,6	189,0	8,0	13,3	12,3
290	04/23/14	3,81	-71,42	0,0	2,10		0,5	262,0	5,6	12,9	11,0
291	04/23/14	3,82	-71,39	0,0	2,50		0,2	233,0	1,9	3,2	3,5
292	04/23/14	3,92	-71,44	4,0	2,30		0,4	261,0	6,1	8,0	7,5
293	04/23/14	3,90	-71,55	4,1	3,50	3,80	0,5	224,0	2,7	4,6	5,3
294	04/23/14	4,04	-71,56	4,1	2,20		0,6	311,0	13,4	9,3	9,2

295	04/23/14	3,95	-71,60	4,1	2,70		0,5	236,0	5,0	6,2	7,0
296	04/23/14	3,99	-71,56	4,1	2,20		0,5	312,0	11,2	8,1	7,6
297	04/23/14	3,89	-71,60	5,7	3,70	3,80	0,6	222,0	3,3	5,4	6,4
298	04/23/14	4,01	-71,64	7,1	1,90		0,6	310,0	11,2	9,5	8,4
299	04/23/14	3,93	-71,58	4,6	2,30		0,6	183,0	11,6	20,7	18,0
300	04/25/14	3,98	-71,60	0,0	2,00		0,5	235,0	4,4	6,0	6,2
301	04/25/14	3,86	-71,32	1,8	2,60		0,6	236,0	3,9	8,1	7,1
302	04/25/14	4,00	-71,68	2,0	1,80		0,4	285,0	8,1	16,1	11,7
303	04/26/14	3,81	-71,53	4,1	3,20	3,40	0,6	227,0	4,4	6,9	7,9
304	04/27/14	3,83	-71,44	4,1	2,90	3,20	0,4	230,0	3,8	5,5	6,5
305	04/28/14	3,90	-71,63	4,1	2,10		0,5	220,0	5,2	8,4	8,4
306	04/28/14	3,86	-71,43	4,1	2,90		0,5	230,0	4,0	5,7	6,3
307	04/30/14	3,85	-71,43	4,1	2,40		0,4	231,0	4,0	6,0	6,2
308	04/30/14	3,84	-71,44	4,1	2,40		0,4	230,0	3,6	6,1	6,9
309	02/05/14	3,91	-71,55	4,1	2,60		0,5	224,0	4,3	6,7	7,5
310	02/05/14	3,88	-71,69	8,6	1,80		0,4	218,0	4,2	6,9	8,6
311	03/05/14	3,90	-71,55	4,1	2,30		0,6	224,0	5,0	6,8	8,0
312	03/05/14	3,90	-71,52	4,1	1,60		0,5	257,0	5,9	8,8	7,4
313	03/05/14	3,88	-71,52	4,1	1,60		0,7	327,0	20,0	13,1	12,4
314	06/05/14	3,82	-71,53	0,0	2,00		0,5	227,0	4,3	6,9	7,3
315	07/05/14	3,93	-71,67	0,0	1,70		0,5	234,0	5,8	7,1	7,8
316	08/05/14	3,94	-71,60	0,0	2,00		0,4	304,0	9,5	14,6	13,0
317	08/05/14	3,85	-71,44	4,1	2,40		0,4	230,0	4,2	8,2	8,2
318	09/05/14	3,83	-71,39	2,0	2,40		0,4	233,0	3,7	5,7	5,9
319	10/05/14	3,73	-71,61	0,0	1,60		0,4	284,0	8,4	7,9	7,9
320	11/05/14	4,09	-71,57	0,0	2,20		0,5	270,0	7,1	11,0	9,4
321	11/05/14	3,93	-71,60	4,1	2,50		0,5	221,0	5,2	6,4	7,4
322	11/05/14	3,95	-71,49	0,0	2,40		0,4	240,0	4,7	5,7	6,4
323	11/05/14	3,86	-71,55	0,0	2,60		0,6	239,0	5,4	7,1	8,3
324	11/05/14	3,99	-71,63	4,1	2,20		0,6	277,0	8,0	6,7	7,2
325	05/13/14	3,79	-71,65	0,0	1,30		0,5	295,0	11,8	8,3	10,3
326	05/13/14	3,92	-71,58	3,8	3,10	3,20	0,6	222,0	3,7	5,6	5,7
327	05/13/14	3,90	-71,60	1,8	2,70		0,5	221,0	3,8	5,9	5,9
328	05/13/14	3,90	-71,57	2,8	4,30	4,20	0,6	223,0	3,3	5,7	5,7
329	05/13/14	3,94	-71,59	0,0	2,50		0,6	279,0	11,5	9,2	10,9
330	05/13/14	3,87	-71,57	0,0	3,30		0,5	224,0	3,5	6,1	6,4
331	05/13/14	3,95	-71,60	0,0	2,70		0,5	279,0	10,5	8,4	9,9
332	05/13/14	3,97	-71,63	0,0	2,10		0,5	311,0	10,4	12,0	11,2
333	05/13/14	3,93	-71,63	0,0	3,00		0,5	220,0	5,1	5,7	7,5
334	05/14/14	3,87	-71,59	6,0	2,00		0,4	223,0	10,5	12,7	14,2
335	05/14/14	3,86	-71,59	4,1	3,40	3,60	0,6	223,0	2,6	4,1	4,8
336	05/14/14	3,88	-71,64	4,1	2,80	3,10	0,6	220,0	3,3	5,1	5,8
337	05/14/14	3,90	-71,63	4,1	2,20		0,5	220,0	3,3	6,2	7,1
338	05/14/14	3,87	-71,59	4,1	1,50		0,6	223,0	6,5	10,3	9,7
339	05/14/14	3,89	-71,61	4,1	2,60		0,6	183,0	4,6	6,9	8,1
340	05/14/14	3,83	-71,59	4,0	2,20		0,5	224,0	3,9	6,5	6,5
341	05/14/14	3,93	-71,63	0,0	2,30		0,5	279,0	10,3	9,1	9,9
342	05/14/14	3,98	-71,62	0,0	2,30		0,6	311,0	12,7	14,3	13,5
343	05/14/14	4,00	-71,65	0,0	2,30		0,4	233,0	5,2	6,0	7,4
344	05/15/14	3,87	-71,59	4,1	2,10		0,5	281,0	8,6	6,3	7,1
345	05/15/14	3,87	-71,58	4,1	2,80		0,6	223,0	4,3	6,4	7,1
346	05/15/14	3,92	-71,53	4,1	2,10		0,5	225,0	3,6	6,6	6,3
347	05/15/14	3,86	-71,59	4,1	3,10		0,6	223,0	3,5	5,3	6,3
348	05/15/14	3,88	-71,61	4,1	2,80		0,4	221,0	3,3	5,3	6,1
349	05/15/14	3,85	-71,62	4,1	1,60		0,6	222,0	5,8	8,1	7,9
350	05/15/14	3,92	-71,53	4,1	1,50		0,5	257,0	5,5	9,2	8,5
351	05/16/14	3,89	-71,52	4,1	2,40		0,5	187,0	4,8	6,0	7,7
352	05/16/14	3,88	-71,66	4,2	2,50		0,5	181,0	2,6	3,7	4,7
353	05/16/14	3,83	-71,59	4,6	1,90		0,5	185,0	3,0	4,0	4,8
354	05/16/14	3,90	-71,48	8,7	1,80		0,4	274,0	5,5	5,0	3,8

355	05/16/14	3,89	-71,60	4,1	2,00		0,5	222,0	4,6	7,5	7,4
356	05/17/14	4,09	-71,51	19,7	1,40		0,2	312,0	6,4	5,7	2,7
357	05/17/14	3,88	-71,64	6,0	2,00		0,5	220,0	3,5	5,3	5,8
358	05/17/14	3,84	-71,71	8,9	1,60		0,6	217,0	4,6	7,4	7,1
359	05/17/14	3,91	-71,64	6,8	2,20		0,3	220,0	2,8	3,9	4,4
360	05/17/14	3,87	-71,60	1,2	3,00	3,30	0,4	222,0	2,8	4,7	4,8
361	05/17/14	4,00	-71,59	0,0	2,40		0,4	278,0	8,6	6,9	8,0
362	05/17/14	3,98	-71,56	2,5	2,40		0,5	308,0	11,4	12,6	12,2
363	05/17/14	4,05	-71,59	0,0	1,90		0,4	311,0	10,6	10,9	10,6
364	05/18/14	4,01	-71,60	4,1	1,70		0,5	235,0	5,9	7,5	6,8
365	05/18/14	3,88	-71,63	4,1	3,10		0,4	220,0	1,7	2,5	3,0
366	05/18/14	3,79	-71,40	4,7	2,40		0,5	233,0	3,4	4,7	4,7
367	05/18/14	3,91	-71,66	4,1	2,20		0,4	219,0	2,6	3,7	4,4
368	05/19/14	4,00	-71,50	0,0	1,90		0,4	313,0	13,4	11,8	11,3
369	05/20/14	3,93	-71,52	4,1	2,10		0,5	285,0	8,3	12,0	9,7
370	05/20/14	3,92	-71,57	7,1	2,00		0,4	223,0	4,3	6,8	6,8
371	05/20/14	3,95	-71,66	0,0	2,30		0,5	277,0	9,8	8,0	9,4
372	05/21/14	3,98	-71,63	0,0	2,00		0,4	234,0	4,9	5,5	8,4
373	05/22/14	3,97	-71,64	7,4	2,00		0,5	278,0	7,8	5,9	5,9
374	05/22/14	3,88	-71,63	4,1	1,90		0,4	253,0	3,4	7,4	5,9
375	05/22/14	3,93	-71,52	4,1	2,20		0,5	225,0	3,7	5,3	5,9
376	05/22/14	3,86	-71,40	4,1	3,60		0,6	232,0	3,7	5,8	6,1
377	05/23/14	3,99	-71,49	7,8	1,20		0,3	272,0	5,1	6,6	5,6
378	05/23/14	3,92	-71,52	4,1	2,00		0,5	225,0	5,1	7,3	8,5
379	05/23/14	3,83	-71,62	5,6	1,30		0,1	254,0	1,9	3,8	3,0
380	05/23/14	3,78	-71,40	8,3	1,70		0,4	233,0	4,1	6,7	6,7
381	05/23/14	3,90	-71,56	4,1	2,60		0,3	185,0	2,7	2,8	4,1
382	05/23/14	3,89	-71,59	4,1	2,20		0,5	222,0	4,2	6,7	7,3
383	05/23/14	3,91	-71,52	10,9	2,60		0,4	226,0	2,9	5,5	9,5
384	05/24/14	4,05	-71,58	4,1	2,20		0,6	235,0	7,3	7,4	8,2
385	05/24/14	3,90	-71,58	0,0	2,40		0,5	223,0	3,4	6,0	6,6
386	05/25/14	3,92	-71,58	4,2	2,10		0,5	183,0	12,1	18,2	16,7
387	05/25/14	3,90	-71,62	5,0	1,80		0,3	221,0	4,6	6,9	6,7
388	05/25/14	3,87	-71,39	4,1	2,40		0,5	192,0	7,8	10,3	10,8
389	05/25/14	4,12	-71,55	30,0	2,10		0,3	270,0	6,3	6,3	3,8
390	05/25/14	3,91	-71,56	4,1	3,70	3,80	0,4	185,0	2,6	3,3	4,4
391	05/25/14	3,80	-71,58	14,9	2,00		0,2	283,0	4,8	4,5	3,1
392	05/25/14	3,88	-71,59	0,0	2,20		0,5	223,0	4,0	6,2	6,5
393	05/25/14	3,95	-71,61	0,0	2,00		0,5	279,0	10,1	8,2	9,6
394	05/25/14	3,95	-71,59	0,0	1,90		0,4	279,0	10,2	8,4	8,7
395	05/25/14	3,91	-71,58	0,0	2,50		0,5	222,0	3,9	6,0	6,4
396	05/25/14	3,91	-71,56	2,9	2,60		0,5	224,0	4,0	6,1	6,4
397	05/26/14	3,83	-71,65	4,1	1,80		0,4	221,0	4,5	7,1	7,7
398	05/26/14	3,87	-71,56	4,1	3,00	3,30	0,5	224,0	3,5	5,8	5,9
399	05/26/14	3,89	-71,53	0,0	2,70		0,4	225,0	3,3	7,6	4,9
400	05/26/14	3,78	-71,49	0,0	1,50		0,5	297,0	14,7	9,5	12,1
401	05/26/14	3,91	-71,58	4,1	3,20	3,80	0,4	223,0	3,2	6,0	6,8
402	05/26/14	3,84	-71,42	3,8	2,10		0,4	262,0	3,7	9,0	6,7
403	05/26/14	3,95	-71,58	0,0	2,10		0,2	279,0	7,4	4,4	7,2
404	05/26/14	3,93	-71,58	10,9	2,00		0,4	296,0	17,8	10,5	11,3
405	05/26/14	3,91	-71,59	4,2	3,20	3,40	0,6	222,0	3,6	5,3	6,3
406	05/26/14	3,93	-71,66	11,6	3,30	3,60	0,6	204,0	3,3	5,0	4,8
407	05/26/14	3,73	-71,63	4,1	2,40		0,4	224,0	2,8	4,3	4,1
408	05/26/14	3,91	-71,54	4,1	2,60		0,5	224,0	3,3	4,9	4,9
409	05/26/14	3,85	-71,64	9,4	2,10		0,5	221,0	4,3	6,0	6,2
410	05/26/14	3,91	-71,56	4,1	3,70		0,5	223,0	2,9	3,9	4,7
411	05/27/14	3,89	-71,58	4,1	2,20		0,5	223,0	4,3	6,6	6,9
412	05/27/14	3,95	-71,61	4,9	1,50		0,3	292,0	7,0	5,9	6,4
413	05/27/14	3,92	-71,55	4,1	2,30		0,5	224,0	4,8	6,7	7,2
414	05/27/14	3,87	-71,59	0,0	2,50		0,5	184,0	7,3	12,5	11,5

415	05/27/14	3,80	-71,44	5,5	1,80		0,6	286,0	9,5	7,3	7,9
416	05/27/14	3,89	-71,61	4,1	1,90		0,5	222,0	5,8	7,4	9,0
417	05/27/14	3,92	-71,59	4,7	2,30	2,80	0,5	183,0	5,2	7,8	8,7
418	05/27/14	3,98	-71,56	4,1	1,90		0,4	237,0	9,2	6,5	6,5
419	05/27/14	3,98	-71,58	4,1	2,20		0,6	221,0	6,9	6,9	9,1
420	05/27/14	3,83	-71,34	12,0	2,90	3,30	0,5	235,0	4,9	9,6	15,3
421	05/27/14	3,98	-71,60	4,1	2,50		0,6	270,0	10,5	7,3	8,8
422	05/27/14	3,98	-71,57	0,9	3,30	3,50	0,6	223,0	3,9	6,4	7,1
423	05/27/14	3,98	-71,60	0,0	2,60		0,4	303,0	13,2	12,8	13,5
424	05/27/14	3,94	-71,57	5,5	2,40		0,6	222,0	4,6	6,9	6,7
425	05/27/14	3,92	-71,50	4,1	2,20		0,5	226,0	4,8	6,3	5,9
426	05/28/14	3,79	-71,52	4,1	2,40		0,7	189,0	6,3	7,5	9,2
427	05/28/14	3,89	-71,57	4,1	2,80		0,5	223,0	3,1	4,3	4,7
428	05/28/14	3,91	-71,58	4,1	3,10		0,4	222,0	2,8	3,8	4,2
429	05/28/14	4,07	-71,71	2,4	2,10		0,5	266,0	5,8	4,6	3,0
430	05/29/14	3,92	-71,57	6,0	3,10	3,40	0,6	184,0	3,2	4,7	5,2
431	05/29/14	3,95	-71,77	20,0	2,90	3,10	0,3	212,0	2,7	3,8	3,0
432	05/29/14	3,89	-71,63	4,1	2,20		0,5	253,0	4,9	8,5	7,4
433	05/29/14	3,91	-71,59	1,1	3,00	3,30	0,6	222,0	3,6	6,2	6,1
434	05/30/14	3,90	-71,60	6,2	2,10		0,7	222,0	5,1	8,0	8,3
435	05/30/14	3,89	-71,67	5,4	2,10		0,6	251,0	7,9	13,8	12,6
436	05/30/14	3,93	-71,56	4,1	2,60		0,6	223,0	4,4	5,9	6,9
437	05/30/14	3,88	-71,66	4,1	2,60		0,6	252,0	10,2	15,3	14,4
438	05/30/14	3,86	-71,62	4,1	3,00		0,6	221,0	4,8	7,0	7,9
439	05/30/14	3,87	-71,64	4,1	3,00		0,5	252,0	5,3	9,3	8,0
440	05/30/14	3,89	-71,62	4,1	2,80		0,3	221,0	3,0	5,3	4,9
441	05/30/14	3,87	-71,63	4,1	2,40		0,4	221,0	3,1	4,2	4,7
442	05/30/14	4,02	-71,59	6,0	1,90		0,4	303,0	8,9	6,9	5,5
443	05/30/14	3,86	-71,63	4,1	2,10		0,3	236,0	3,7	3,9	4,1
444	05/30/14	3,93	-71,60	4,1	2,10		0,5	269,0	6,2	7,6	6,2
445	05/30/14	3,89	-71,62	4,1	2,60		0,5	221,0	3,1	4,1	4,7
446	05/31/14	3,88	-71,54	4,1	2,10		0,2	225,0	1,8	2,4	2,7
447	05/31/14	3,89	-71,57	17,0	2,10		0,6	223,0	5,4	9,1	6,9
448	02/06/14	3,78	-71,61	4,1	2,10		0,9	238,0	15,9	12,7	17,6
449	02/06/14	3,86	-71,61	4,1	2,00		0,3	222,0	2,8	4,1	4,6
450	02/06/14	3,89	-71,56	4,1	2,10		0,5	280,0	9,8	15,5	11,6
451	02/06/14	3,77	-71,42	4,1	2,20		0,6	287,0	12,9	10,5	9,1
452	03/06/14	3,94	-71,57	6,7	2,80	3,10	0,6	183,0	3,8	5,5	5,8
453	04/06/14	3,88	-71,58	4,1	3,60	3,80	0,5	223,0	2,8	4,2	5,0
454	04/06/14	3,91	-71,59	4,1	2,00		0,5	222,0	4,6	6,7	6,7
455	04/06/14	3,87	-71,61	4,1	3,10	3,40	0,5	222,0	3,3	5,8	6,8
456	04/06/14	3,88	-71,64	4,1	2,00		0,5	253,0	5,5	10,1	8,8
457	04/06/14	3,91	-71,58	10,4	2,50		0,5	235,0	5,0	7,8	6,7
458	04/06/14	3,86	-71,55	4,1	2,80		0,6	225,0	4,8	6,9	7,7
459	04/06/14	3,87	-71,60	6,6	2,30		0,6	222,0	5,1	8,6	9,0
460	04/06/14	3,91	-71,61	4,0	3,10	3,40	0,6	221,0	4,2	6,8	7,1
461	04/06/14	4,04	-71,61	0,0	2,70		0,6	234,0	6,9	8,3	8,3
462	04/06/14	3,88	-71,61	0,1	3,80	4,00	0,5	221,0	3,0	5,2	5,3
463	05/06/14	3,90	-71,56	4,1	3,60	3,80	0,5	224,0	3,2	4,7	5,4
464	05/06/14	3,90	-71,57	4,1	2,60		0,6	223,0	4,5	6,3	7,2
465	05/06/14	3,90	-71,55	4,1	2,00		0,5	281,0	8,8	6,4	7,2
466	05/06/14	3,89	-71,62	0,0	1,80		0,4	293,0	10,9	6,2	9,1
467	05/06/14	3,89	-71,57	0,0	1,60		0,4	294,0	15,7	8,9	11,4
468	05/06/14	3,89	-71,62	4,1	1,90		0,5	221,0	4,2	6,4	7,2
469	05/06/14	3,90	-71,62	4,1	1,80		0,5	221,0	5,4	8,7	9,7
470	05/06/14	3,91	-71,59	4,1	2,40		0,5	222,0	3,7	6,7	7,8
471	05/06/14	3,89	-71,79	4,2	1,70		0,7	277,0	10,2	10,4	9,9
472	05/06/14	3,81	-71,65	10,6	2,30		0,6	252,0	5,7	12,4	8,4
473	05/06/14	3,78	-71,67	8,0	2,10		0,5	252,0	5,3	12,0	8,4
474	05/06/14	4,00	-71,61	0,0	1,90		0,6	235,0	9,9	8,6	9,9

475	06/06/14	3,87	-71,62	4,1	2,10		0,7	221,0	5,7	11,0	10,4
476	06/06/14	3,89	-71,59	4,1	2,20		0,6	223,0	3,8	6,3	7,5
477	06/06/14	3,89	-71,61	4,1	2,70		0,6	221,0	5,1	6,6	8,1
478	06/06/14	3,82	-71,63	4,1	2,90		0,5	222,0	4,7	8,7	7,7
479	06/06/14	3,92	-71,58	4,1	2,60		0,5	222,0	4,1	5,8	6,7
480	06/06/14	4,13	-71,70	0,0	2,60		0,5	272,0	11,1	9,3	12,2
481	06/06/14	3,94	-71,64	4,1	2,30		0,6	235,0	5,5	10,1	9,8
482	08/06/14	3,89	-71,54	4,1	2,50		0,5	225,0	4,3	6,1	6,8
483	08/06/14	3,89	-71,65	4,1	1,90		0,4	220,0	4,1	7,7	8,5
484	08/06/14	3,86	-71,59	4,1	2,90	3,30	0,6	185,0	4,7	6,9	7,3
485	08/06/14	3,81	-71,60	6,4	2,50		0,6	223,0	5,3	7,9	8,4
486	08/06/14	3,90	-71,63	4,2	2,30		0,6	253,0	6,2	10,5	9,2
487	08/06/14	3,89	-71,60	4,1	2,10		0,7	280,0	11,5	9,4	8,6
488	08/06/14	3,99	-71,58	0,0	2,50		0,6	278,0	13,0	9,7	11,8
489	09/06/14	3,89	-71,59	0,0	3,30		0,5	248,0	5,6	10,9	9,7
490	09/06/14	3,99	-71,60	4,1	2,20		0,5	283,0	6,9	6,6	6,9
491	10/06/14	3,89	-71,59	4,1	3,10		0,5	222,0	3,5	5,5	6,6
492	11/06/14	4,02	-71,53	0,0	2,30		0,4	237,0	5,4	6,4	7,3
493	11/06/14	3,79	-71,58	4,1	2,30		0,4	283,0	8,8	7,4	6,3
494	06/13/14	3,93	-71,49	4,0	2,00		0,3	226,0	2,5	3,6	4,5
495	06/13/14	3,84	-71,58	4,1	2,20		0,6	224,0	4,4	5,9	6,5
496	06/14/14	3,88	-71,62	4,1	2,30		0,4	221,0	3,4	5,9	6,0
497	06/14/14	3,79	-71,64	4,1	2,50		0,4	222,0	4,1	5,6	6,6
498	06/14/14	3,80	-71,63	10,9	2,30		0,3	237,0	7,4	6,0	4,4
499	06/15/14	4,00	-71,76	0,0	1,90		0,6	274,0	9,3	7,4	5,4
500	06/15/14	3,90	-71,64	4,1	2,30		0,5	275,0	7,8	12,5	10,9
501	06/16/14	4,08	-71,59	0,0	2,30		0,5	269,0	8,8	13,6	12,3
502	06/16/14	3,87	-71,58	0,0	2,00		0,3	255,0	3,6	8,9	6,9
503	06/16/14	3,81	-71,47	0,0	2,70		0,5	260,0	4,9	13,7	8,9
504	06/18/14	3,87	-71,59	0,0	2,00		0,4	223,0	3,8	5,9	6,6
505	06/19/14	3,88	-71,63	0,6	2,20		0,5	221,0	4,0	6,6	7,5
506	06/19/14	3,89	-71,56	0,0	2,40		0,5	224,0	3,5	6,0	6,4
507	06/19/14	3,85	-71,46	0,0	2,50		0,5	229,0	4,7	6,7	6,4
508	06/19/14	3,91	-71,63	5,1	2,70		0,5	220,0	5,6	7,5	9,5
509	06/19/14	3,90	-71,60	1,6	2,90		0,5	222,0	4,3	8,2	7,5
510	06/19/14	3,88	-71,58	4,1	3,00		0,5	223,0	3,6	5,3	6,6
511	06/19/14	3,90	-71,61	4,1	2,30		0,6	221,0	4,9	7,7	7,7
512	06/19/14	3,77	-71,42	4,1	2,10		0,5	286,0	9,9	7,0	7,4
513	06/20/14	3,82	-71,33	0,0	2,40		0,3	236,0	2,6	3,8	4,0
514	06/20/14	3,86	-71,58	4,1	3,50	3,70	0,5	223,0	2,8	4,4	5,3
515	06/21/14	4,04	-71,51	0,0	2,50		0,3	272,0	4,9	5,9	6,1
516	06/21/14	3,90	-71,59	4,0	3,10	3,40	0,5	222,0	3,3	5,9	6,1
517	06/21/14	3,86	-71,40	4,0	2,40		0,4	263,0	3,7	8,7	7,1
518	06/21/14	3,87	-71,62	2,2	2,80		0,5	221,0	3,5	6,5	6,7
519	06/21/14	3,83	-71,73	0,0	2,40		0,5	216,0	3,6	8,0	9,0
520	06/21/14	3,87	-71,59	0,0	2,80		0,5	223,0	3,8	6,7	7,4
521	06/21/14	3,91	-71,56	4,0	2,60		0,5	224,0	4,3	6,7	7,2
522	06/21/14	3,87	-71,60	1,2	2,10		0,3	222,0	2,2	3,5	3,8
523	06/21/14	3,92	-71,55	4,1	2,20		0,6	256,0	6,5	9,5	8,2
524	06/22/14	4,01	-71,51	0,0	2,20		0,5	272,0	7,4	10,2	9,6
525	06/22/14	3,85	-71,45	0,3	2,50		0,4	230,0	2,8	4,7	5,0
526	06/25/14	3,92	-71,51	4,1	4,40	4,40	0,6	226,0	4,2	5,6	6,9
527	06/25/14	3,91	-71,53	4,1	2,50		0,6	257,0	6,3	9,5	8,4
528	06/25/14	3,95	-71,63	4,1	2,00		0,7	219,0	6,0	10,6	10,5
529	06/25/14	3,92	-71,68	4,1	1,90		0,8	217,0	7,3	11,6	13,7
530	06/25/14	3,96	-71,48	4,4	2,70		0,5	227,0	3,4	5,3	5,9
531	06/25/14	3,91	-71,52	4,0	3,10	3,30	0,5	225,0	3,5	5,8	5,9
532	06/26/14	3,92	-71,56	4,1	2,10		0,4	273,0	5,0	7,6	6,4
533	06/26/14	3,89	-71,58	4,1	2,60		0,6	223,0	3,7	5,9	6,6
534	06/26/14	3,89	-71,59	4,1	3,30	3,50	0,6	222,0	3,1	4,5	5,4

535	06/26/14	3,86	-71,57	4,1	2,70		0,5	224,0	3,0	4,7	5,1
536	06/26/14	3,92	-71,66	17,2	2,30		0,6	218,0	4,3	7,0	6,4
537	06/26/14	3,90	-71,60	4,1	1,90		0,5	222,0	3,7	5,7	5,6
538	06/26/14	3,90	-71,67	9,0	2,60		0,5	218,0	3,5	5,9	5,9
539	06/26/14	3,91	-71,55	4,1	2,50		0,5	224,0	3,4	5,1	6,0
540	06/26/14	3,91	-71,54	4,1	2,80		0,4	224,0	3,1	4,9	5,8
541	06/26/14	4,05	-71,46	0,0	2,20		0,6	313,0	14,4	14,5	13,8
542	06/26/14	3,86	-71,63	0,0	2,70		0,5	221,0	3,8	6,2	6,6
543	06/27/14	3,92	-71,56	0,0	2,70		0,4	256,0	4,3	9,4	7,5
544	06/28/14	3,88	-71,64	4,1	2,70		0,5	220,0	2,7	4,0	4,8
545	06/28/14	3,66	-71,72	10,5	1,40		0,3	327,0	7,2	8,6	4,5
546	06/28/14	3,94	-71,47	4,1	1,60		0,4	259,0	4,3	7,7	6,2
547	06/29/14	3,92	-71,62	6,0	2,70		0,5	220,0	4,3	8,0	8,4
548	06/29/14	3,89	-71,65	2,5	2,00		0,4	219,0	3,5	6,6	6,6
549	06/30/14	3,88	-71,55	5,5	2,60		0,5	225,0	3,5	4,4	4,9
550	01/07/14	3,90	-71,56	4,1	2,20		0,5	224,0	4,0	5,1	5,8
551	03/07/14	3,92	-71,57	2,0	2,80		0,5	223,0	3,3	6,0	6,3
552	03/07/14	3,88	-71,61	4,1	2,30		0,7	221,0	5,0	8,5	9,8
553	04/07/14	3,88	-71,66	0,0	2,30		0,6	219,0	4,7	10,0	9,5
554	04/07/14	3,85	-71,49	1,6	2,30		0,3	228,0	2,6	4,0	5,5
555	04/07/14	4,00	-71,61	6,0	1,80		0,5	235,0	5,9	5,3	5,3
556	04/07/14	4,06	-71,60	9,7	1,80		0,5	235,0	5,5	5,9	5,5
557	04/07/14	3,87	-71,57	8,6	1,80		0,3	313,0	7,1	6,1	4,7
558	04/07/14	3,88	-71,61	0,0	2,10		0,5	221,0	4,0	7,3	6,7
559	05/07/14	3,86	-71,51	0,0	2,30		0,5	283,0	12,6	10,7	10,0
560	05/07/14	3,82	-71,66	0,0	2,20		0,5	281,0	9,6	8,3	9,6
561	06/07/14	3,90	-71,68	4,1	2,20		0,5	260,0	6,2	7,1	6,2
562	06/07/14	3,90	-71,56	7,3	1,70		0,3	313,0	5,9	5,1	3,8
563	07/07/14	3,90	-71,60	4,1	2,30		0,6	280,0	9,6	7,6	8,2
564	08/07/14	3,68	-71,72	8,9	2,30		0,4	297,0	8,7	6,6	7,2
565	09/07/14	3,92	-71,50	16,0	2,80		0,6	239,0	5,1	8,1	6,7
566	09/07/14	3,88	-71,62	4,1	2,00		0,6	221,0	7,2	8,3	11,3
567	10/07/14	3,92	-71,58	5,1	2,40		0,5	255,0	5,0	8,4	7,5
568	07/15/14	3,91	-71,51	4,1	2,50		0,5	226,0	3,6	5,5	5,7
569	07/15/14	3,89	-71,57	4,1	2,10		0,5	256,0	5,4	10,8	8,3
570	07/15/14	3,85	-71,36	1,0	3,40	3,60	0,5	234,0	4,0	6,7	6,8
571	07/15/14	3,91	-71,51	4,1	2,10		0,5	314,0	13,0	9,3	7,7
572	07/15/14	3,95	-71,57	4,1	2,40		0,6	255,0	6,0	11,3	9,7
573	07/16/14	3,94	-71,46	4,1	2,20		0,5	260,0	4,4	8,7	7,1
574	07/19/14	3,89	-71,59	4,1	2,00		0,6	281,0	9,4	7,6	8,0
575	07/19/14	3,84	-71,45	4,1	1,90		0,5	230,0	4,9	7,4	7,4
576	07/20/14	3,90	-71,57	0,7	3,70	3,90	0,5	223,0	2,8	5,5	5,1
577	07/20/14	3,93	-71,59	0,0	2,30		0,5	271,0	13,7	8,7	13,0
578	07/21/14	3,89	-71,61	0,0	3,30	3,50	0,5	248,0	5,0	11,1	10,7
579	07/21/14	3,85	-71,54	4,1	2,40		0,6	225,0	5,9	7,3	8,3
580	07/22/14	3,96	-71,52	0,3	2,00		0,5	257,0	4,5	9,7	8,3
581	07/22/14	3,94	-71,48	6,0	2,10		0,6	288,0	9,3	13,0	12,3
582	07/23/14	3,90	-71,55	4,1	2,60		0,6	224,0	5,6	7,9	8,9
583	07/26/14	3,89	-71,59	4,1	2,50		0,5	222,0	3,4	5,8	6,3
584	07/26/14	3,85	-71,68	4,1	1,70		0,6	219,0	5,0	9,1	8,2
585	07/26/14	3,91	-71,58	4,1	1,80		0,6	255,0	5,5	12,2	9,9
586	07/26/14	3,89	-71,54	4,1	2,40		0,5	225,0	3,5	5,2	6,1
587	07/27/14	4,06	-71,57	0,0	2,20		0,5	236,0	5,8	7,3	7,7
588	07/27/14	3,90	-71,64	5,3	3,00		0,5	220,0	3,2	5,3	5,9
589	07/30/14	3,92	-71,57	4,0	3,10		0,6	255,0	5,4	12,8	9,5
590	07/30/14	3,91	-71,56	0,7	3,10	3,30	0,4	224,0	3,1	5,1	5,5
591	07/31/14	3,94	-71,56	4,1	2,90		0,5	223,0	5,4	5,4	8,4
592	07/31/14	3,92	-71,57	0,0	1,70		0,4	255,0	4,6	9,3	7,8
593	07/31/14	3,90	-71,57	4,1	2,10		0,6	255,0	5,4	8,1	7,4
594	07/31/14	3,82	-71,49	4,1	2,10		0,5	253,0	4,4	7,3	6,1

595	02/08/14	3,91	-71,54	0,0	2,20		0,4	271,0	9,7	11,7	8,9
596	02/08/14	3,88	-71,53	4,1	2,10		0,5	327,0	14,0	9,5	7,6
597	05/08/14	3,91	-71,54	7,1	3,00	3,20	0,5	224,0	2,2	3,2	3,5
598	05/08/14	3,92	-71,52	0,0	2,70		0,4	225,0	2,6	4,1	4,3
599	05/08/14	3,89	-71,63	0,0	2,00		0,5	220,0	4,5	7,2	7,6
600	06/08/14	3,88	-71,60	0,0	2,30		0,5	237,0	8,3	7,1	9,7
601	07/08/14	3,88	-71,59	0,0	2,30		0,5	255,0	4,5	11,5	8,9
602	08/08/14	3,80	-71,61	5,4	1,50		0,4	269,0	5,7	7,8	6,1
603	08/08/14	3,92	-71,56	4,1	2,20		0,4	256,0	4,2	7,0	6,2
604	08/08/14	3,86	-71,57	4,0	2,40		0,5	224,0	4,1	6,1	7,0
605	09/08/14	3,89	-71,58	4,1	3,50	3,80	0,5	223,0	2,6	3,9	4,6
606	09/08/14	3,89	-71,60	4,1	2,90		0,4	222,0	2,3	3,7	4,0
607	09/08/14	3,88	-71,60	4,1	2,80		0,5	222,0	2,8	3,8	4,2
608	09/08/14	3,96	-71,51	12,0	2,00		0,4	225,0	3,1	5,5	4,5
609	09/08/14	3,89	-71,59	4,1	2,70		0,5	222,0	3,2	5,1	5,6
610	09/08/14	3,92	-71,77	0,0	1,70		0,5	230,0	5,0	5,0	3,9
611	09/08/14	4,09	-71,54	4,3	2,20		0,4	271,0	5,2	6,3	5,5
612	09/08/14	3,84	-71,62	4,1	2,10		0,3	268,0	6,7	5,8	5,3
613	09/08/14	3,90	-71,61	4,1	2,00		0,5	280,0	8,0	7,4	7,1
614	09/08/14	3,91	-71,59	1,2	2,40		0,5	222,0	3,6	6,5	6,9
615	09/08/14	3,88	-71,59	0,8	3,50	3,70	0,5	222,0	3,6	6,5	6,8
616	10/08/14	3,90	-71,52	4,1	1,70		0,4	282,0	8,7	5,8	6,2
617	10/08/14	4,07	-71,55	4,1	1,70		0,5	270,0	6,4	8,5	6,8
618	10/08/14	3,91	-71,62	4,1	2,30		0,4	220,0	3,2	5,1	5,1
619	10/08/14	3,88	-71,53	4,1	1,40		0,4	314,0	8,8	7,2	6,1
620	11/08/14	3,85	-71,45	0,0	2,20		0,4	230,0	3,5	6,2	5,9
621	12/08/14	3,84	-71,33	4,0	2,40		0,4	266,0	4,6	9,5	7,7
622	08/13/14	3,93	-71,45	4,1	2,10		0,6	241,0	7,0	8,7	10,2
623	08/14/14	3,89	-71,56	4,1	3,60	3,70	0,6	224,0	3,4	5,4	6,6
624	08/15/14	3,92	-71,46	4,1	1,80		0,4	314,0	9,8	6,7	5,8
625	08/16/14	3,98	-71,47	4,1	1,90		0,5	291,0	8,0	10,1	10,0
626	08/16/14	4,20	-71,51	0,0	1,80		0,5	308,0	12,0	14,2	13,4
627	08/21/14	3,84	-71,49	2,5	2,20		0,4	259,0	3,8	13,5	9,8
628	08/22/14	3,86	-71,65	15,3	2,20		0,3	252,0	2,3	8,0	10,7
629	08/24/14	3,81	-71,30	2,0	3,10	3,30	0,4	237,0	3,6	7,6	6,5
630	08/25/14	3,88	-71,47	3,5	2,30		0,5	228,0	4,2	8,9	8,2
631	08/25/14	3,89	-71,50	6,2	2,10		0,1	227,0	1,5	4,0	5,8
632	08/25/14	3,85	-71,59	0,0	2,40		0,5	255,0	3,7	13,6	10,0
633	08/25/14	3,83	-71,37	6,0	2,60		0,3	234,0	2,5	5,2	8,8
634	08/28/14	3,90	-71,56	16,0	3,30		0,4	224,0	4,6	9,1	15,0
635	08/28/14	3,86	-71,50	0,0	2,80		0,5	227,0	3,8	7,8	7,1
636	08/29/14	4,00	-71,68	0,0	2,30		0,4	218,0	3,0	5,9	7,9
637	08/29/14	3,93	-71,62	25,8	2,40		0,6	181,0	5,9	11,6	20,7
638	08/30/14	3,91	-72,07	0,0	2,10		0,4	229,0	3,1	11,6	11,4
639	08/30/14	3,81	-71,54	24,0	2,10		0,4	257,0	3,1	12,5	19,5
640	08/30/14	3,86	-71,69	0,0	2,10		0,2	218,0	2,4	5,9	6,8
641	08/30/14	3,84	-71,31	2,6	2,00		0,5	267,0	3,8	18,5	12,5
642	01/09/14	3,93	-71,52	4,5	2,20		0,4	271,0	4,8	13,5	19,2
643	02/09/14	3,65	-71,36	4,0	2,40		0,8	238,0	7,1	18,0	13,0
644	06/09/14	3,86	-71,54	0,0	2,60		0,5	225,0	3,7	7,9	6,8
645	11/09/14	3,90	-71,49	21,2	2,30		0,6	227,0	4,8	9,4	16,6
646	12/09/14	3,74	-71,43	15,0	2,20		0,4	233,0	6,5	9,5	13,3
647	12/09/14	3,86	-71,58	22,3	2,40		0,4	223,0	2,7	6,3	11,2
648	09/15/14	3,82	-71,46	0,0	3,20	3,40	0,3	230,0	2,3	4,8	4,2
649	09/15/14	3,88	-71,48	3,5	2,70		0,5	259,0	4,4	14,5	9,7
650	09/17/14	3,86	-71,62	0,0	2,60		0,5	222,0	4,3	6,6	7,3
651	09/20/14	3,78	-71,43	0,0	2,90		0,4	232,0	4,4	8,8	7,4
652	09/21/14	3,90	-71,61	4,1	2,60		0,6	221,0	3,6	5,4	6,4
653	09/21/14	3,89	-71,60	4,1	2,90	3,30	0,5	222,0	2,5	4,2	5,0
654	09/21/14	3,88	-71,60	2,0	3,10	3,40	0,5	222,0	4,3	6,8	7,0

655	09/22/14	3,89	-71,57	4,1	2,70		0,5	223,0	2,9	5,1	5,4
656	09/22/14	3,88	-71,57	4,1	2,30		0,4	223,0	3,8	5,9	5,7
657	09/22/14	3,92	-71,55	5,1	2,30		0,5	224,0	4,7	6,3	6,6
658	09/25/14	3,92	-71,55	4,1	2,40		0,5	224,0	4,3	6,5	6,5
659	09/26/14	3,88	-71,56	0,0	2,50		0,5	256,0	4,5	10,2	8,3
660	09/27/14	3,84	-71,42	4,3	3,20	3,40	0,5	231,0	3,4	4,8	5,6
661	09/27/14	3,85	-71,44	4,1	2,90		0,5	230,0	3,8	5,5	6,8
662	09/27/14	3,91	-71,52	0,0	3,50		0,4	225,0	2,7	4,7	5,0
663	09/28/14	3,86	-71,61	4,1	2,00		0,5	237,0	9,3	7,1	7,6
664	09/29/14	3,88	-71,66	0,0	2,30		0,3	272,0	9,8	28,4	19,5
665	09/29/14	3,92	-71,55	7,5	2,90		0,7	184,0	4,1	6,1	7,2
666	09/29/14	3,87	-71,56	4,1	2,60		0,6	185,0	9,7	13,2	14,2
667	01/10/14	3,81	-71,44	0,9	2,40		0,5	231,0	4,5	7,8	6,9
668	05/10/14	3,95	-71,51	4,1	1,80		0,5	287,0	8,0	11,1	8,8
669	06/10/14	3,88	-71,55	4,7	2,40		0,6	185,0	6,0	9,7	8,2
670	06/10/14	3,94	-71,48	9,0	2,30		0,7	186,0	10,0	12,9	12,8
671	07/10/14	3,95	-71,56	3,8	3,00	3,30	0,7	183,0	3,7	5,4	6,1
672	10/10/14	3,79	-71,34	0,9	2,10		0,5	266,0	4,4	10,8	8,3
673	11/10/14	3,87	-71,44	10,5	2,10		0,2	261,0	2,4	4,0	3,0
674	12/10/14	3,89	-71,60	0,0	1,90		0,6	254,0	5,9	13,6	10,4
675	10/13/14	4,05	-71,59	0,0	2,20		0,7	273,0	12,5	11,1	11,9
676	10/14/14	3,90	-71,50	15,4	2,30		0,5	259,0	5,2	8,5	6,1
677	10/15/14	3,84	-71,39	2,0	2,40		0,4	232,0	4,4	6,2	6,3
678	10/16/14	3,89	-71,54	0,0	2,30		0,5	225,0	4,7	6,8	6,9
679	10/17/14	3,94	-71,52	0,1	2,50		0,5	225,0	4,0	6,1	6,4
680	10/18/14	3,92	-71,65	4,1	2,20		0,6	252,0	5,9	11,7	9,9
681	10/19/14	3,86	-71,41	6,4	3,40	3,50	0,4	231,0	3,2	4,6	5,2
682	10/20/14	4,03	-71,51	0,0	2,10		0,3	272,0	3,9	10,9	7,4
683	10/21/14	4,11	-71,54	0,0	1,70		0,5	271,0	8,2	11,1	11,0
684	10/22/14	3,94	-71,55	11,6	2,10		0,4	256,0	4,8	7,7	7,0
685	10/27/14	3,97	-71,61	0,0	2,30		0,6	235,0	10,3	10,7	14,3
686	10/27/14	3,93	-71,44	0,0	2,20		0,4	261,0	9,1	17,9	13,7
687	10/30/14	3,98	-71,56	0,0	2,70		0,7	237,0	7,2	8,7	10,5
688	01/11/14	3,92	-71,60	0,0	2,50		0,6	221,0	4,4	6,8	7,4
689	04/11/14	4,03	-71,59	0,0	1,90		0,6	269,0	7,3	11,4	10,2
690	05/11/14	3,91	-71,60	4,6	2,00		0,5	222,0	4,8	8,0	8,7
691	06/11/14	3,88	-71,55	0,0	2,90		0,4	224,0	3,0	5,5	5,9
692	07/11/14	4,21	-71,50	0,0	2,00		0,4	272,0	5,9	9,0	8,0
693	07/11/14	3,91	-71,51	2,0	2,40		0,3	226,0	2,5	4,1	4,6
694	07/11/14	3,92	-71,48	0,6	1,60		0,4	259,0	4,1	8,5	7,1
695	07/11/14	3,91	-71,55	1,3	2,30		0,4	224,0	3,4	5,7	6,3
696	07/11/14	3,89	-71,56	0,6	2,60		0,4	224,0	2,9	5,1	5,5
697	07/11/14	3,91	-71,57	2,0	2,20		0,4	223,0	2,9	4,5	4,8
698	07/11/14	3,88	-71,64	0,0	2,90		0,4	220,0	3,5	5,8	6,2
699	07/11/14	3,94	-71,50	4,1	2,50		0,5	226,0	3,3	6,1	5,5
700	08/11/14	3,67	-71,49	4,1	2,10		0,4	299,0	8,5	7,6	6,7
701	12/11/14	3,93	-71,59	4,0	2,30		0,6	222,0	4,5	7,0	7,5
702	11/14/14	3,88	-71,55	4,7	1,40		0,8	256,0	7,3	12,4	10,9
703	11/14/14	3,88	-71,41	6,0	2,90		0,6	231,0	4,2	6,2	6,9
704	11/18/14	3,95	-71,67	2,0	2,10		0,7	251,0	6,3	16,3	12,8
705	11/23/14	3,95	-71,57	4,0	2,20		0,8	222,0	5,9	9,4	10,4
706	11/27/14	3,85	-71,40	4,8	2,60		0,4	232,0	2,7	4,0	4,6
707	11/29/14	3,87	-71,58	0,0	1,70		0,5	281,0	10,6	8,8	10,3
708	11/30/14	3,98	-71,63	18,1	1,90		0,4	219,0	3,9	8,0	6,6
709	11/30/14	3,87	-71,54	0,0	2,80		0,4	225,0	3,0	5,3	5,4
710	11/30/14	3,91	-71,53	0,1	3,60	3,80	0,5	225,0	2,4	4,1	4,2
711	11/30/14	3,68	-71,51	13,1	1,90		0,5	287,0	8,4	7,6	6,8
712	11/30/14	3,88	-71,56	9,1	2,50		0,4	224,0	2,8	4,3	4,7
713	11/30/14	4,00	-71,57	0,0	1,90		0,7	236,0	8,1	9,2	10,1
714	11/30/14	3,88	-71,64	2,0	1,80		0,6	252,0	5,7	13,5	11,0

715	11/30/14	4,21	-71,53	9,8	2,30		0,7	308,0	14,5	12,2	8,9
716	11/30/14	4,16	-71,55	0,2	2,00		0,4	307,0	7,8	9,8	8,4
717	11/30/14	4,09	-71,60	1,1	1,80		0,3	310,0	7,4	7,6	7,2
718	11/30/14	3,94	-71,58	10,5	2,40		0,6	222,0	4,3	6,5	7,0
719	11/30/14	3,98	-71,52	5,7	3,50	3,70	0,8	208,0	3,7	5,4	6,7
720	01/12/14	4,07	-71,54	0,0	2,30		0,5	236,0	8,7	8,2	10,1
721	01/12/14	4,05	-71,50	0,0	1,90		0,3	279,0	7,4	6,1	6,8
722	01/12/14	3,88	-71,57	0,0	3,00		0,5	224,0	3,0	5,4	5,6
723	01/12/14	3,87	-71,59	0,0	1,70		0,4	255,0	3,8	9,1	7,1
724	01/12/14	3,87	-71,61	0,0	2,20		0,6	222,0	4,2	7,4	7,7
725	01/12/14	3,95	-71,49	0,8	1,90		0,3	258,0	5,1	10,2	9,5
726	01/12/14	3,97	-71,60	0,0	2,30		0,8	312,0	17,4	19,0	17,4
727	01/12/14	3,98	-71,63	4,1	2,10		0,7	311,0	13,7	11,5	10,2
728	01/12/14	3,85	-71,63	0,0	2,40		0,4	281,0	7,7	6,4	8,6
729	01/12/14	3,98	-71,50	0,0	2,10		0,3	272,0	5,5	7,3	6,5
730	01/12/14	3,90	-71,65	0,1	2,80		0,8	219,0	9,2	15,7	14,8
731	02/12/14	3,87	-71,42	0,7	2,50		0,3	231,0	2,1	3,9	3,9
732	02/12/14	3,94	-71,54	4,0	1,90		0,4	224,0	4,5	5,6	6,1
733	02/12/14	3,91	-71,54	4,2	3,70	3,80	0,5	224,0	2,1	3,4	4,0
734	02/12/14	3,94	-71,56	7,9	2,60		0,3	223,0	2,4	4,0	4,5
735	02/12/14	3,87	-71,65	4,1	2,30		0,5	220,0	3,6	6,4	7,2
736	03/12/14	3,95	-71,48	4,0	2,20		0,4	259,0	3,8	8,7	7,2
737	03/12/14	3,88	-71,56	0,0	1,90		0,4	256,0	4,6	10,4	8,3
738	04/12/14	4,00	-71,50	0,0	2,50		0,5	225,0	4,7	6,5	7,5
739	04/12/14	3,92	-71,52	4,1	2,40		0,4	225,0	4,5	6,6	6,8
740	08/12/14	3,86	-71,40	3,9	2,60		0,7	232,0	5,6	8,5	7,8
741	09/12/14	3,96	-71,51	5,2	2,20		0,5	225,0	3,9	5,9	6,6
742	09/12/14	3,89	-71,53	0,1	2,10		0,4	225,0	3,1	5,6	5,8
743	12/12/14	3,99	-71,56	0,0	2,00		0,4	279,0	8,0	6,5	7,4
744	12/12/14	3,79	-71,40	4,1	1,90		0,4	233,0	3,3	4,8	5,0
745	12/13/14	3,90	-71,59	0,0	1,80		0,8	222,0	6,1	10,7	10,5
746	12/14/14	3,97	-71,57	0,0	2,40		0,4	279,0	8,6	6,9	8,0
747	12/15/14	4,15	-71,56	0,0	2,00		0,5	270,0	6,1	9,5	8,8
748	12/20/14	3,79	-71,45	4,1	1,70		0,7	286,0	12,8	9,9	11,8
749	12/22/14	3,84	-71,36	8,2	2,40		0,6	234,0	5,2	8,4	8,5
750	12/23/14	3,84	-71,47	4,0	2,50		0,4	229,0	3,4	5,5	5,6
751	12/24/14	3,82	-71,39	0,0	2,40		0,5	233,0	11,9	18,4	17,8
752	12/26/14	3,89	-71,57	0,0	2,60		0,8	224,0	8,2	14,8	13,8
753	12/26/14	3,84	-71,42	0,0	1,80		0,5	285,0	12,5	10,1	11,2
754	12/30/14	3,97	-71,60	0,0	1,80		0,6	278,0	13,9	10,5	11,8
755	12/30/14	3,88	-71,47	3,5	2,00		0,6	283,0	14,1	11,0	13,1
756	12/31/14	3,92	-71,51	10,0	1,80		0,6	258,0	7,2	10,9	9,1
757	12/31/14	3,82	-71,42	0,0	2,30		0,6	232,0	4,3	7,5	7,2
758	12/31/14	3,74	-71,52	4,1	2,20		0,6	229,0	5,4	8,6	8,5
759	06/01/15	4,07	-71,47	0,0	1,90		0,2	313,0	13,5	7,9	6,9
760	07/01/15	3,91	-71,45	4,2	1,80		0,5	242,0	7,6	7,5	7,7
761	07/01/15	3,83	-71,35	1,5	2,50		0,4	235,0	3,1	5,2	5,3
762	08/01/15	4,03	-71,60	0,0	2,30		0,6	235,0	6,3	7,7	7,6
763	12/01/15	3,86	-71,39	4,3	2,50		0,2	289,0	3,2	4,5	4,0
764	01/16/15	3,77	-71,51	0,0	1,60		0,4	228,0	3,2	5,4	5,5
765	01/17/15	3,88	-71,64	0,0	1,90		0,5	220,0	3,8	6,5	6,7
766	01/18/15	3,83	-71,38	0,0	1,70		0,6	245,0	9,5	8,9	11,3
767	01/18/15	3,81	-71,54	0,0	2,20		0,6	240,0	9,6	9,7	12,2
768	01/19/15	3,92	-71,52	4,1	2,20		0,5	281,0	8,4	7,6	7,5
769	01/23/15	3,91	-71,49	0,0	2,10		0,5	240,0	9,7	8,1	11,8
770	02/02/15	3,93	-71,60	4,0	2,20		0,8	221,0	6,1	9,9	11,7
771	07/02/15	3,90	-71,58	0,0	1,70		0,7	255,0	6,6	16,1	12,8
772	09/02/15	3,83	-71,47	0,0	1,70		0,4	260,0	3,8	9,4	7,3
773	02/24/15	3,92	-71,54	3,0	3,60		0,3	224,0	2,2	3,6	4,2
774	02/24/15	3,99	-71,55	0,0	2,10		0,5	237,0	5,6	7,0	7,9

775	05/03/15	3,84	-71,29	4,1	2,20		0,4	237,0	3,2	5,2	5,5
776	05/03/15	3,83	-71,30	4,1	2,10		0,5	237,0	3,9	6,2	7,0
777	08/03/15	3,81	-71,36	4,1	1,70		0,4	289,0	7,8	10,8	8,8
778	03/23/15	3,87	-71,68	0,0	1,90		0,5	250,0	5,3	13,4	11,4
779	03/26/15	3,94	-71,54	2,0	3,00		0,5	224,0	3,9	6,1	5,6
780	03/27/15	4,00	-71,61	0,0	1,60		0,6	235,0	6,1	7,8	9,0
781	03/30/15	3,82	-71,37	0,0	2,50		0,5	234,0	4,0	6,4	7,0
782	03/30/15	3,77	-71,42	0,0	2,50		0,8	233,0	7,9	14,1	14,2
783	08/04/15	3,84	-71,29	4,0	2,60		0,5	267,0	4,4	10,1	8,7
784	04/25/15	3,88	-71,36	4,0	2,90		0,6	233,0	4,5	7,4	7,7
785	04/27/15	3,89	-71,41	4,1	2,80	3,20	0,7	243,0	8,3	7,8	8,6
786	04/27/15	3,94	-71,40	0,0	2,70		0,7	243,0	7,7	9,1	10,7
787	04/28/15	3,81	-71,35	0,0	2,50		0,3	265,0	3,1	7,4	5,8
788	04/29/15	3,85	-71,42	3,7	2,70		0,6	191,0	6,4	10,6	9,2
789	04/29/15	3,82	-71,43	4,1	2,40		0,4	262,0	4,8	9,9	7,2
790	02/05/15	3,81	-71,45	4,4	2,90		0,5	231,0	3,3	5,8	5,9
791	03/05/15	3,86	-71,56	0,0	1,60		0,4	314,0	9,9	11,3	9,3
792	08/05/15	3,83	-71,43	5,7	2,50		0,5	192,0	3,7	5,1	5,7
793	05/15/15	3,81	-71,62	0,0	2,20		0,4	237,0	4,8	6,3	6,8
794	05/20/15	3,86	-71,43	2,2	2,00		0,6	191,0	6,3	12,6	8,5
795	05/30/15	3,81	-71,41	2,8	2,00		0,5	263,0	5,5	14,2	10,3
796	06/06/15	3,98	-71,39	0,0	3,40	3,50	0,5	242,0	5,4	8,2	6,8
797	07/06/15	3,80	-71,41	0,0	2,30		0,5	263,0	4,7	11,7	9,2
798	07/06/15	3,86	-71,29	4,1	3,10	3,40	0,5	248,0	2,9	5,0	5,1
799	06/20/15	3,75	-71,50	4,0	2,90		0,3	260,0	3,9	12,1	8,5
800	06/25/15	3,89	-71,38	0,0	2,80		0,5	271,0	5,5	10,7	8,6
801	09/07/15	3,83	-71,37	0,0	2,10		0,5	264,0	4,5	10,9	8,5
802	10/07/15	3,91	-71,38	4,0	2,50		0,5	292,0	8,3	10,9	9,8
803	07/13/15	3,82	-71,40	4,1	2,50		0,6	263,0	6,1	9,8	8,0
804	07/23/15	3,82	-71,52	0,0	2,40		0,5	258,0	4,8	11,6	9,3
805	07/24/15	3,86	-71,36	4,0	2,80		0,5	193,0	4,4	5,4	5,9
806	09/08/15	3,84	-71,41	2,0	2,70		0,5	232,0	3,7	6,6	6,0
807	09/08/15	3,85	-71,41	10,3	2,60		0,5	232,0	4,2	6,8	5,8
808	08/23/15	3,84	-71,36	4,1	4,00	4,00	0,6	194,0	2,8	3,2	4,0
809	08/23/15	3,82	-71,33	4,1	2,20		0,3	290,0	6,0	8,3	7,7
810	08/23/15	3,83	-71,39	2,0	2,20		0,4	233,0	4,2	8,0	7,1
811	08/23/15	3,83	-71,36	4,0	2,40		0,5	194,0	4,3	4,6	6,5
812	08/23/15	3,83	-71,37	4,5	2,40		0,5	194,0	3,7	4,3	5,1
813	08/23/15	3,83	-71,43	0,6	3,00	3,40	0,5	231,0	2,2	3,8	3,7
814	08/23/15	3,80	-71,33	2,7	2,20		0,4	196,0	3,8	5,3	5,9
815	08/24/15	3,84	-71,31	4,1	4,00	4,40	0,6	191,0	4,0	4,4	6,1
816	08/24/15	3,81	-71,46	9,0	3,00	3,10	0,6	230,0	4,8	7,4	7,7
817	08/24/15	3,86	-71,29	7,4	2,40		0,5	294,0	7,7	9,3	8,7
818	08/24/15	3,81	-71,41	0,4	1,90		0,3	263,0	3,2	7,8	6,1
819	08/24/15	3,79	-71,35	4,1	2,00		0,6	266,0	5,4	9,9	7,4
820	08/24/15	3,77	-71,48	4,1	2,70		0,6	230,0	3,9	6,1	6,2
821	08/24/15	3,85	-71,35	6,0	2,50		0,4	291,0	5,7	8,3	6,6
822	08/24/15	3,81	-71,44	0,0	2,50		0,4	231,0	3,6	8,1	7,2
823	08/25/15	3,91	-71,34	6,0	2,60		0,7	245,0	7,4	9,2	9,4
824	08/25/15	3,83	-71,37	3,6	3,70	3,60	0,3	234,0	1,8	3,3	3,1
825	08/26/15	3,88	-71,32	4,0	2,30		0,5	266,0	4,2	9,7	7,6
826	08/27/15	3,83	-71,39	2,3	2,10		0,4	263,0	4,1	10,6	6,9
827	08/27/15	3,81	-71,46	0,3	1,90		0,5	261,0	5,2	14,4	9,6
828	08/28/15	3,83	-71,39	0,0	1,90		0,1	288,0	5,3	13,1	9,1
829	08/30/15	3,82	-71,39	0,0	2,40		0,5	257,0	4,4	10,8	7,9
830	08/30/15	3,79	-71,55	0,0	3,10	3,50	0,5	227,0	3,5	6,6	6,2
831	08/31/15	3,82	-71,40	5,0	3,80	4,00	0,6	190,0	2,1	2,8	3,1
832	08/31/15	3,77	-71,44	4,1	2,40		0,5	232,0	3,4	5,2	5,4
833	08/31/15	3,84	-71,41	10,0	2,90		0,9	192,0	5,3	6,2	7,6
834	08/31/15	3,85	-71,33	2,5	2,20		0,4	195,0	3,7	4,5	5,0

835	08/31/15	3,88	-71,35	5,1	3,80	4,10	0,6	190,0	2,1	2,7	3,1
836	08/31/15	3,82	-71,37	1,7	2,40		0,4	194,0	3,1	3,7	5,0
837	08/31/15	3,84	-71,36	4,0	2,40		0,5	194,0	3,7	4,7	5,8
838	08/31/15	3,85	-71,35	4,0	2,80	3,20	0,5	194,0	3,5	4,2	4,5
839	08/31/15	3,81	-71,34	3,8	2,20		0,6	196,0	4,8	5,4	6,8
840	01/09/15	4,00	-71,37	1,3	2,90	3,20	0,6	201,0	6,4	5,1	6,8
841	01/09/15	3,83	-71,39	4,1	3,00	3,30	0,5	233,0	2,2	3,4	3,3
842	02/09/15	3,87	-71,39	5,9	2,70	3,10	0,4	192,0	4,7	4,3	5,3
843	02/09/15	3,82	-71,36	4,9	4,00	4,10	0,6	194,0	2,2	2,8	2,9
844	02/09/15	3,81	-71,45	0,0	2,50		0,4	255,0	2,6	5,9	4,8
845	03/09/15	3,86	-71,38	4,9	2,50		0,4	192,0	3,4	3,6	4,6
846	04/09/15	3,81	-71,38	4,1	3,10	3,40	0,7	194,0	2,9	3,6	4,1
847	04/09/15	3,81	-71,39	4,5	3,10		0,7	194,0	4,2	3,9	4,9
848	04/09/15	3,82	-71,42	8,0	2,40		0,6	232,0	3,4	4,8	4,7
849	05/09/15	3,83	-71,38	4,0	3,00	3,30	0,6	234,0	4,3	7,5	7,0
850	06/09/15	3,83	-71,44	0,0	2,70		0,7	231,0	5,2	9,9	9,3
851	07/09/15	3,83	-71,35	4,0	2,30		0,3	290,0	5,9	7,2	6,6
852	08/09/15	3,86	-71,37	10,0	3,30	3,50	0,7	193,0	3,7	4,6	5,6
853	09/16/15	3,83	-71,38	0,0	2,50		0,5	275,0	7,9	12,2	8,8
854	09/20/15	3,70	-71,46	4,0	2,30		0,6	233,0	4,8	7,9	9,4
855	09/24/15	3,84	-71,38	4,1	2,60		0,7	233,0	6,2	7,9	8,2
856	09/24/15	3,98	-71,59	3,9	2,30		0,4	196,0	4,1	4,3	8,3
857	09/25/15	3,81	-71,30	0,0	3,80	3,90	0,6	237,0	4,3	7,5	6,6
858	09/25/15	3,84	-71,35	5,5	2,40		0,5	234,0	5,1	7,8	7,1
859	09/25/15	3,83	-71,35	0,1	3,30	3,50	0,3	217,0	2,4	4,1	4,4
860	09/27/15	3,82	-71,30	16,7	3,20	3,40	0,3	197,0	2,5	3,3	7,4
861	07/10/15	3,87	-71,42	4,1	3,00	3,20	0,5	231,0	2,9	3,9	4,4
862	09/10/15	3,87	-71,38	7,2	1,90		0,3	290,0	5,4	7,6	6,3
863	09/10/15	3,82	-71,42	2,0	1,80		0,4	263,0	3,6	8,9	6,7
864	10/10/15	3,83	-71,36	2,9	2,60		0,5	194,0	3,6	4,8	5,6
865	10/10/15	3,83	-71,46	0,4	1,80		0,5	230,0	4,5	7,1	8,3
866	11/10/15	3,83	-71,41	4,1	2,50	2,70	0,6	263,0	4,5	7,4	6,0
867	10/17/15	3,79	-71,38	4,1	2,60		0,6	258,0	3,4	5,7	4,9
868	10/18/15	3,60	-71,47	0,0	1,80		0,2	318,0	5,9	7,6	5,9
869	10/20/15	3,80	-71,39	7,4	3,10	3,20	0,4	233,0	2,1	3,8	3,5
870	10/25/15	3,82	-71,51	0,0	2,20		0,5	228,0	4,0	8,3	7,2
871	10/31/15	3,81	-71,51	0,0	3,10	3,20	0,5	228,0	3,7	6,9	6,8
872	01/11/15	3,85	-71,46	0,0	2,50		0,5	229,0	4,9	7,6	8,1
873	06/11/15	3,85	-71,42	1,4	3,40	3,60	0,5	231,0	2,7	5,0	5,2
874	06/11/15	3,81	-71,49	2,0	3,20	3,30	0,6	229,0	3,8	7,8	8,4
875	06/11/15	3,78	-71,42	0,0	2,20		0,4	263,0	5,3	11,8	8,2
876	06/11/15	3,78	-71,54	1,7	2,10		0,1	227,0	2,1	3,0	5,6
877	06/11/15	3,81	-71,40	12,1	2,70		0,4	263,0	5,9	7,5	6,3
878	07/11/15	3,97	-71,47	0,0	2,30		0,4	240,0	4,0	5,9	6,3
879	08/11/15	3,85	-71,37	5,0	2,70		0,4	260,0	3,5	6,1	5,6
880	08/11/15	3,79	-71,40	0,0	2,90	3,10	0,5	233,0	3,4	6,1	6,1
881	10/11/15	3,84	-71,33	3,6	2,10		0,5	236,0	3,8	6,3	6,9
882	10/11/15	3,90	-71,41	0,0	2,90		0,6	231,0	5,6	7,6	7,2
883	11/11/15	3,86	-71,48	0,0	2,40		0,7	241,0	9,0	9,3	11,0
884	12/11/15	4,00	-71,37	0,0	2,00		0,3	308,0	7,8	12,7	9,8
885	11/13/15	3,83	-71,36	0,0	2,00		0,3	288,0	5,3	6,4	3,5
886	11/14/15	3,81	-71,42	0,0	2,00		0,6	232,0	4,6	6,2	7,3
887	11/15/15	3,86	-71,42	0,0	2,70		0,7	210,0	6,5	10,0	5,0
888	11/15/15	3,85	-71,38	4,1	2,20		0,5	290,0	7,9	8,4	7,8
889	11/19/15	3,83	-71,34	0,0	1,80		0,5	290,0	7,9	9,5	5,2
890	11/19/15	3,83	-71,38	0,0	2,00		0,4	264,0	4,2	7,2	3,4
891	11/21/15	3,86	-71,38	0,4	2,50		0,5	233,0	3,9	4,4	2,6
892	11/22/15	3,83	-71,36	4,1	2,30		0,6	234,0	4,4	7,8	7,2
893	11/22/15	3,80	-71,33	1,9	1,70		0,0	266,0	1,6	4,2	2,9
894	11/23/15	3,91	-71,51	4,1	2,80		0,6	122,0	3,1	2,8	5,2

895	11/24/15	3,87	-71,40	0,0	2,70		0,6	275,0	6,3	6,3	4,1
896	11/28/15	3,82	-71,36	4,1	4,80	4,70	0,6	191,0	2,4	3,4	4,3
897	11/28/15	3,79	-71,34	4,1	2,70		0,6	236,0	3,5	5,7	4,9
898	11/28/15	3,80	-71,45	4,1	2,90	3,00	0,6	231,0	3,6	7,1	6,1
899	11/28/15	3,88	-71,42	10,2	3,40	3,50	0,7	215,0	3,2	4,7	4,5
900	11/28/15	3,87	-71,45	5,0	2,80	3,10	0,5	242,0	3,5	6,4	5,3
901	11/28/15	3,81	-71,32	4,1	3,10	3,30	0,7	220,0	3,6	5,2	5,8
902	11/28/15	3,84	-71,41	2,0	2,60		0,5	232,0	3,7	6,1	6,3
903	11/28/15	4,02	-71,40	4,1	2,50		0,7	242,0	6,4	8,5	7,9
904	11/29/15	3,81	-71,37	4,1	2,80	3,20	0,6	195,0	2,7	3,8	4,5
905	11/29/15	3,84	-71,36	4,0	2,40		0,4	194,0	2,5	3,3	4,0
906	11/29/15	3,81	-71,45	0,0	2,20		0,7	192,0	4,3	8,6	8,1
907	11/29/15	3,81	-71,43	0,0	2,20		0,4	231,0	3,3	7,0	6,2
908	11/29/15	3,96	-71,53	4,1	2,40		0,6	238,0	6,7	7,2	9,5
909	11/30/15	3,73	-71,43	0,0	2,50		0,5	263,0	4,3	11,9	9,3
910	01/12/15	3,80	-71,54	0,0	2,20		0,6	227,0	4,7	7,9	8,6
911	04/12/15	3,81	-71,41	3,7	2,10		0,4	232,0	3,8	6,5	7,0
912	04/12/15	3,76	-71,59	0,0	1,80		0,6	188,0	7,6	6,8	10,1
913	05/12/15	3,75	-71,50	1,8	2,90		0,2	260,0	2,2	6,6	5,7
914	07/12/15	3,81	-71,44	0,0	2,20		0,5	231,0	4,0	6,9	7,7
915	07/12/15	3,82	-71,31	2,0	4,00	4,00	0,7	220,0	4,3	7,9	8,4
916	09/12/15	3,76	-71,50	0,0	2,40		0,3	229,0	2,2	4,0	3,7
917	12/14/15	3,85	-71,46	0,0	2,40		0,5	261,0	4,1	10,3	8,6
918	12/15/15	4,00	-71,45	0,0	2,30		0,3	231,0	2,9	5,0	5,8
919	12/17/15	3,85	-71,58	0,0	2,40		0,4	255,0	4,6	9,2	8,7
920	12/17/15	3,85	-71,27	4,1	2,40		0,2	283,0	3,8	5,9	4,0
921	12/22/15	3,93	-71,36	4,1	2,40		0,6	264,0	7,0	7,9	7,6
922	12/24/15	3,86	-71,32	4,1	2,40		0,6	292,0	7,4	10,4	8,1
923	12/24/15	3,83	-71,35	4,1	2,60		0,4	265,0	4,0	6,6	5,3
924	12/24/15	3,88	-71,44	3,5	2,40		0,8	230,0	6,2	10,7	11,5
925	04/01/16	3,83	-71,41	2,5	2,70		0,4	232,0	2,9	5,9	5,9
926	08/01/16	3,85	-71,42	6,0	3,10	3,40	0,5	231,0	3,3	5,1	5,6
927	08/01/16	3,82	-71,47	2,6	3,00		0,4	229,0	3,0	5,4	5,6
928	09/01/16	3,81	-71,47	5,2	2,60		0,4	242,0	2,8	5,5	4,3
929	10/01/16	3,87	-71,41	7,7	2,50		0,7	231,0	6,0	8,4	8,9
930	10/01/16	3,77	-71,49	0,0	2,50		0,6	229,0	4,7	10,2	10,8
931	11/01/16	3,96	-71,40	0,0	1,80		0,5	275,0	6,8	11,9	9,7
932	01/13/16	3,84	-71,43	1,5	2,30		0,5	231,0	4,2	7,8	7,4
933	01/13/16	3,79	-71,48	0,0	2,80	3,30	0,4	230,0	3,6	5,5	6,2
934	01/13/16	3,78	-71,53	0,0	3,20	3,50	0,5	227,0	5,2	6,8	7,8
935	01/17/16	3,83	-71,44	0,0	2,80		0,4	231,0	3,2	7,1	6,5
936	01/19/16	3,80	-71,34	4,1	2,60		0,6	236,0	5,2	8,7	7,1
937	01/19/16	3,83	-71,36	0,0	2,30		0,5	234,0	3,5	5,9	6,3
938	01/19/16	3,86	-71,35	6,5	2,50		0,8	234,0	6,8	8,7	9,4
939	01/23/16	3,78	-71,58	0,0	2,50		0,7	225,0	5,8	10,2	9,1
940	01/25/16	3,71	-71,43	0,0	1,40		0,2	288,0	4,9	4,2	5,5
941	01/25/16	3,79	-71,39	0,0	1,40		0,2	264,0	2,5	6,9	4,6
942	08/02/16	3,86	-71,66	16,6	1,70		0,6	252,0	5,5	13,4	8,2
943	02/14/16	3,76	-71,45	0,0	1,70		0,3	262,0	4,3	8,4	6,2
944	02/15/16	3,65	-71,56	0,0	1,90		0,3	259,0	3,3	13,7	10,0
945	02/20/16	3,89	-71,45	11,5	2,60		0,7	189,0	5,7	6,4	8,3
946	02/26/16	3,83	-71,44	0,0	2,30		0,4	262,0	3,5	8,5	6,7
947	02/29/16	3,81	-71,38	0,1	2,20		0,6	264,0	5,1	12,7	9,6
948	03/03/16	3,78	-71,54	0,0	2,60		0,6	227,0	4,7	9,1	8,0
949	03/13/16	3,79	-71,37	1,0	2,00		0,4	235,0	3,3	5,1	4,9
950	03/13/16	3,97	-71,48	0,0	1,70		0,3	281,0	7,7	5,9	6,7
951	03/14/16	3,85	-71,43	3,6	2,30		0,5	231,0	4,8	9,6	7,4
952	03/17/16	3,88	-71,43	0,0	2,20		0,5	284,0	9,4	8,1	8,8
953	03/18/16	3,80	-71,53	0,0	1,80		0,6	227,0	4,7	7,8	9,0
954	03/18/16	3,82	-71,39	6,1	2,20		0,2	264,0	2,6	4,6	3,6

955	03/18/16	3,82	-71,38	0,0	2,40		0,2	264,0	2,8	6,2	4,9
956	03/20/16	3,81	-71,47	0,0	2,10		0,4	230,0	2,9	5,4	4,7
957	03/22/16	3,82	-71,32	0,0	2,00		0,4	236,0	3,0	5,2	6,9
958	03/25/16	3,89	-71,41	4,1	2,40		0,6	243,0	6,6	6,4	8,1
959	03/25/16	3,75	-71,50	0,0	2,20		0,5	229,0	6,3	9,7	8,2
960	03/26/16	3,78	-71,48	4,1	2,20		0,5	230,0	4,0	6,7	7,7
961	03/27/16	3,77	-71,47	0,0	1,80		0,4	286,0	9,9	6,3	7,3
962	03/27/16	3,80	-71,39	0,0	2,30		0,5	233,0	3,6	6,1	6,5
963	03/27/16	3,84	-71,39	4,1	3,00	3,30	0,7	232,0	5,1	6,2	6,7
964	01/04/16	3,80	-71,35	0,3	2,50		0,3	235,0	2,1	4,1	4,0
965	02/04/16	3,85	-71,46	0,0	2,50		0,4	260,0	4,3	9,8	7,9
966	08/04/16	3,83	-71,41	0,0	2,30		0,4	263,0	3,9	8,8	7,0
967	11/04/16	3,79	-71,51	0,0	2,60		0,5	228,0	3,9	7,3	7,1
968	04/15/16	3,65	-71,50	0,0	1,90		0,4	300,0	11,6	7,2	10,3
969	04/15/16	3,64	-71,52	0,0	2,20		0,5	300,0	11,7	7,3	9,7
970	04/15/16	3,82	-71,39	0,0	2,60		0,3	233,0	3,1	6,0	5,7
971	04/16/16	3,83	-71,32	4,1	2,20		0,5	236,0	3,0	4,6	4,1
972	04/17/16	3,79	-71,50	0,2	2,90	3,30	0,6	190,0	3,7	5,3	5,6
973	04/18/16	3,81	-71,45	4,1	2,70		0,6	230,0	5,6	8,1	8,5
974	04/18/16	3,81	-71,39	1,3	2,30		0,4	264,0	3,8	9,3	7,4
975	04/18/16	3,81	-71,39	4,0	2,40		0,4	233,0	3,2	5,8	5,8
976	04/18/16	3,95	-71,39	0,0	2,40		0,4	275,0	4,7	8,8	6,5
977	04/22/16	3,78	-71,46	0,0	2,60		0,3	231,0	2,7	4,8	4,7
978	04/22/16	3,82	-71,38	4,0	2,80		0,4	233,0	3,2	4,2	4,9
979	04/22/16	3,78	-71,52	0,0	2,40		0,5	190,0	4,0	5,6	6,0
980	04/22/16	3,78	-71,57	0,0	2,50		0,3	265,0	3,4	8,6	6,1
981	04/22/16	3,76	-71,54	4,1	2,60		0,7	190,0	5,0	5,7	6,5
982	04/22/16	3,82	-71,33	4,1	3,40	3,50	0,5	235,0	2,4	3,4	3,8
983	04/23/16	3,82	-71,37	2,0	2,50		0,5	234,0	4,0	6,4	6,4
984	04/24/16	3,79	-71,34	0,5	2,50		0,4	236,0	2,8	4,8	4,4
985	04/24/16	3,82	-71,37	4,5	2,10		0,4	234,0	3,5	5,7	5,2
986	04/24/16	3,80	-71,45	0,0	2,50		0,4	231,0	3,5	6,3	6,0
987	04/25/16	3,80	-71,53	9,0	1,90		0,4	258,0	5,3	11,7	8,4
988	04/27/16	3,80	-71,44	0,0	2,50		0,3	231,0	2,9	7,5	4,9
989	04/29/16	3,80	-71,60	0,0	2,60		0,6	224,0	4,1	8,7	9,5
990	02/05/16	3,84	-71,49	0,0	2,50		0,4	259,0	2,9	7,9	5,4
991	04/05/16	3,79	-71,50	0,0	1,80		0,4	260,0	4,3	11,3	8,7
992	10/05/16	3,71	-71,50	0,0	1,80		0,2	260,0	2,6	9,1	6,2
993	05/14/16	3,80	-71,54	0,2	1,90		0,5	258,0	4,5	12,4	9,6
994	01/06/16	3,77	-71,42	0,0	2,10		0,5	233,0	4,4	7,8	8,1
995	01/06/16	3,81	-71,36	0,0	2,40		0,3	235,0	2,7	4,6	4,8
996	01/06/16	3,80	-71,37	0,0	3,00		0,4	264,0	3,8	9,6	7,5
997	01/06/16	3,79	-71,43	0,0	3,10	3,50	0,5	232,0	4,4	8,7	8,1
998	01/06/16	3,80	-71,41	4,1	2,40		0,5	233,0	3,9	6,4	7,1
999	02/06/16	3,89	-71,56	0,0	1,80		0,5	238,0	4,8	6,5	7,2
1000	02/06/16	3,79	-71,54	3,1	2,10		0,6	227,0	4,8	9,7	9,0
1001	02/06/16	3,77	-71,45	1,0	2,10		0,1	231,0	1,4	2,5	2,4
1002	02/06/16	3,80	-71,47	0,0	1,90		0,4	230,0	2,9	6,2	5,7
1003	02/06/16	3,90	-71,56	15,6	2,00		0,6	238,0	5,3	7,8	8,8
1004	03/06/16	3,85	-71,37	0,0	1,70		0,4	233,0	4,3	6,0	7,1
1005	03/06/16	3,82	-71,35	4,0	3,00		0,8	235,0	5,8	9,8	9,5
1006	07/06/16	3,79	-71,52	0,0	2,70		0,5	228,0	3,9	8,6	8,1
1007	08/06/16	3,82	-71,39	2,1	2,90	3,20	0,2	233,0	2,0	3,4	3,7
1008	06/13/16	3,78	-71,31	0,0	2,20		0,7	237,0	5,4	7,2	8,3
1009	06/17/16	3,82	-71,48	6,4	2,90	3,30	0,8	229,0	5,2	7,4	8,2
1010	06/24/16	3,91	-71,40	8,3	1,70		0,0	291,0	3,0	4,3	3,2
1011	06/25/16	3,83	-71,43	0,1	3,10		0,8	231,0	4,5	7,7	7,4
1012	06/26/16	3,84	-71,36	9,2	2,60		0,6	234,0	4,0	5,7	5,9
1013	06/28/16	3,86	-71,77	0,9	1,70		0,4	214,0	2,5	5,9	6,1
1014	06/29/16	3,96	-71,48	0,0	2,10		0,3	240,0	3,0	4,0	4,2

1015	06/29/16	3,86	-71,42	0,0	1,80		0,3	243,0	3,8	4,9	5,5
1016	02/07/16	3,81	-71,38	2,0	2,60		0,6	264,0	4,0	10,6	8,1
1017	04/07/16	3,80	-71,58	0,0	2,00		0,3	225,0	4,2	5,5	7,3
1018	05/07/16	3,83	-71,53	2,0	2,20		0,5	226,0	3,8	6,0	7,0
1019	06/07/16	3,83	-71,47	1,5	2,60		0,7	214,0	5,5	8,2	8,3
1020	07/19/16	3,85	-71,42	1,4	2,40		0,3	328,0	15,5	11,9	11,1
1021	07/27/16	3,71	-71,41	0,0	1,70		0,2	317,0	5,4	6,4	5,4
1022	07/31/16	3,86	-71,37	2,5	1,60		0,4	264,0	4,0	9,4	8,0
1023	06/08/16	3,83	-71,48	0,0	2,20		0,4	260,0	3,6	9,6	7,6
1024	08/15/16	3,94	-71,41	0,0	2,50		0,5	227,0	8,5	7,2	6,7
1025	08/17/16	3,81	-71,44	4,1	2,00		0,6	262,0	6,5	12,7	8,8
1026	08/24/16	3,85	-71,32	8,0	3,70	3,90	0,6	215,0	2,2	3,3	3,4
1027	08/24/16	3,82	-71,46	0,0	2,10		0,4	230,0	4,9	9,7	11,7
1028	08/25/16	3,81	-71,42	0,0	2,00		0,4	263,0	3,5	8,5	6,7
1029	08/25/16	3,81	-71,43	0,0	1,90		0,4	262,0	4,5	11,1	8,0
1030	08/26/16	3,85	-71,38	4,1	2,60		0,6	233,0	3,7	5,6	5,4
1031	08/27/16	3,81	-71,35	4,1	2,20		0,5	259,0	3,0	6,4	4,5
1032	08/28/16	3,87	-71,33	4,9	2,30		0,4	246,0	2,3	3,9	3,5
1033	08/29/16	3,81	-71,32	0,0	2,40		0,4	236,0	3,5	6,4	5,7
1034	08/29/16	3,83	-71,40	0,0	2,10		0,5	232,0	3,5	5,9	6,6
1035	01/09/16	3,84	-71,40	2,7	2,20		0,5	232,0	3,7	8,1	7,5
1036	03/09/16	3,98	-71,56	0,0	1,70		0,3	270,0	3,6	6,8	6,5
1037	03/09/16	3,82	-71,40	4,0	3,40	3,60	0,5	217,0	3,0	5,9	6,0
1038	08/09/16	3,83	-71,50	4,1	1,70		0,8	228,0	7,2	10,6	12,8
1039	09/26/16	3,62	-71,55	2,0	2,10		0,1	300,0	11,5	3,0	6,7
1040	10/21/16	3,82	-71,45	0,6	1,90		0,7	230,0	5,0	8,7	9,6
1041	10/25/16	3,86	-71,40	2,0	3,40	3,50	0,5	232,0	4,8	8,0	7,6
1042	10/28/16	3,82	-71,40	0,0	2,20		0,3	233,0	2,4	4,5	4,3
1043	11/21/16	3,81	-71,40	0,0	2,50		0,5	257,0	5,1	12,9	9,6
1044	02/01/17	3,83	-71,47	0,0	2,70		0,5	229,0	4,5	8,9	8,6
1045	04/01/17	3,81	-71,35	2,3	1,70		0,2	298,0	9,7	5,0	7,0
1046	02/14/17	3,88	-71,51	4,1	2,30		0,5	314,0	9,0	7,8	6,2
1047	02/21/17	3,93	-71,52	0,0	2,40		0,7	239,0	7,8	8,4	9,4
1048	02/21/17	3,89	-71,53	2,7	1,80		0,2	239,0	2,6	3,2	3,4
1049	02/22/17	3,88	-71,48	0,0	2,40		0,4	241,0	6,0	5,7	8,0
1050	03/27/17	3,96	-71,42	0,0	2,20		0,5	274,0	6,9	9,0	11,0
1051	02/04/17	3,80	-71,39	0,0	2,40		0,3	257,0	3,5	7,3	5,8
1052	11/04/17	3,77	-71,38	0,1	2,20		0,4	257,0	5,4	11,3	8,9
1053	04/14/17	3,67	-72,20	4,8	1,30		0,2	279,0	5,0	3,2	3,5
1054	04/21/17	3,82	-71,44	0,0	2,00		0,4	254,0	2,8	5,9	5,4
1055	04/06/17	3,79	-71,38	0,0	2,60		0,4	257,0	3,4	7,8	5,9
1056	07/06/17	3,91	-71,48	0,6	2,30		0,3	282,0	8,3	8,6	9,3
1057	07/06/17	3,91	-71,55	3,8	2,30		0,5	224,0	4,1	7,9	6,4
1058	11/06/17	3,83	-71,44	0,0	1,90		0,5	243,0	8,5	7,6	9,5
1059	06/18/17	3,87	-71,31	7,9	2,00		0,5	286,0	9,6	6,8	7,0
1060	06/19/17	3,80	-71,51	0,0	2,60		0,6	228,0	3,6	9,5	6,0
1061	06/19/17	3,83	-71,42	3,5	3,50		0,6	232,0	3,3	6,7	6,4
1062	06/24/17	3,80	-71,41	0,0	2,40		0,8	232,0	3,1	7,2	6,4
1063	06/25/17	3,95	-71,45	2,0	1,60		0,4	266,0	4,3	7,1	7,0
1064	06/29/17	3,94	-71,50	0,0	2,20		0,4	264,0	7,0	7,0	6,9
1065	06/30/17	3,80	-71,47	0,0	2,10		0,5	230,0	4,4	9,3	7,8
1066	01/07/17	3,82	-71,41	0,0	2,80		0,2	256,0	2,4	5,4	4,3
1067	10/07/17	3,92	-71,41	3,1	2,40		0,8	231,0	5,7	9,2	10,0
1068	10/07/17	3,96	-71,40	0,0	1,30		0,4	243,0	5,4	7,6	7,7
1069	07/14/17	3,89	-71,42	0,0	2,60		0,4	284,0	9,2	6,9	8,4
1070	07/16/17	3,99	-71,57	0,0	2,00		0,7	261,0	5,6	8,9	9,3
1071	07/28/17	3,84	-71,46	0,0	2,50		0,5	230,0	3,4	6,5	6,5
1072	07/29/17	3,78	-71,60	0,0	1,90		0,7	296,0	15,2	10,0	11,8
1073	01/08/17	3,81	-71,43	0,0	1,60		0,5	254,0	4,4	7,0	6,5
1074	04/08/17	3,71	-71,45	0,1	1,90		0,5	266,0	7,0	6,9	5,8

1075	08/20/17	3,87	-71,55	0,8	3,50	3,80	0,4	225,0	2,2	4,8	3,7
1076	08/20/17	3,79	-71,69	4,2	1,40		0,6	316,0	10,9	10,4	8,3
1077	08/20/17	3,89	-71,64	0,0	1,90		0,5	280,0	11,4	9,5	10,2
1078	08/20/17	3,90	-71,63	0,0	1,80		0,5	316,0	16,2	11,4	14,4
1079	08/23/17	3,79	-71,48	0,0	2,10		0,5	229,0	4,0	6,7	6,3
1080	01/09/17	3,89	-71,57	0,1	2,30		0,8	223,0	5,2	8,7	9,1
1081	05/09/17	3,86	-71,45	0,0	2,30		0,6	230,0	4,0	8,6	8,3
1082	05/09/17	3,86	-71,45	0,0	2,30		0,6	230,0	4,0	8,6	8,3
1083	09/30/17	3,91	-71,51	0,6	2,90		0,7	226,0	3,0	5,1	4,9
1084	09/30/17	3,71	-71,37	4,1	1,70		0,4	300,0	7,2	5,9	5,6
1085	07/10/17	3,74	-71,44	0,0	2,10		0,4	255,0	3,0	7,7	6,2
1086	07/10/17	3,73	-71,41	0,0	1,80		0,4	310,0	7,0	6,7	7,7
1087	08/10/17	3,89	-71,43	4,6	2,60		0,8	243,0	7,5	7,2	9,5
1088	10/13/17	3,80	-71,44	0,0	2,30		0,4	286,0	8,7	8,7	8,7
1089	06/11/17	3,88	-71,55	0,0	2,30		0,6	225,0	4,1	6,6	6,8
1090	11/14/17	3,89	-71,45	4,1	3,20	3,20	0,9	275,0	11,3	9,9	11,7
1091	11/14/17	3,85	-71,53	0,0	1,60		0,4	318,0	11,5	8,0	9,6
1092	11/14/17	3,79	-71,61	7,1	1,50		0,6	317,0	11,3	10,3	8,6
1093	11/16/17	3,93	-71,49	0,0	2,50		0,6	248,0	9,4	8,5	9,9
1094	11/20/17	3,87	-71,50	0,0	1,90		0,5	319,0	15,0	10,2	12,8
1095	11/20/17	3,80	-71,54	0,0	1,30		0,3	318,0	9,4	6,7	8,1
1096	11/21/17	3,68	-71,32	7,8	1,50		0,2	301,0	4,9	3,1	3,4
1097	11/21/17	3,83	-71,37	0,1	1,80		0,4	245,0	9,6	8,1	7,8
1098	11/21/17	3,88	-71,33	0,0	1,80		0,5	246,0	19,1	14,4	14,8
1099	11/21/17	3,95	-71,55	0,0	1,90		0,6	285,0	9,8	10,5	9,9
1100	11/26/17	3,88	-71,38	0,0	2,10		0,5	269,0	8,9	9,9	8,4
1101	11/30/17	3,88	-71,36	0,0	2,70		0,6	289,0	8,6	10,1	9,6
1102	12/20/17	3,95	-71,35	0,0	1,90		0,4	309,0	9,4	8,8	9,5
1103	12/24/17	3,89	-71,42	0,0	2,10		0,6	284,0	12,7	9,7	12,1
1104	12/25/17	3,79	-71,47	0,0	2,40		0,2	285,0	12,1	4,3	7,7
1105	12/27/17	3,96	-71,52	4,3	1,90		0,7	280,0	13,1	10,1	11,7
1106	12/28/17	3,89	-71,66	0,0	2,30		0,5	270,0	8,6	7,7	9,5

Table 6. Water injection report from 2013 to 2015 in Puerto Gaitan Oilfields. Source: National Hydrocarbon Agency ANH (www.anh.gov.co).

Water Injection Report from 2013 to 2015 in Puerto Gaitan Oilfields. Source: National Hydrocarbon Agency (ANH)						
Date	Average pressure (lb/inch^2)	Well average volume (Bbl)	Average pressure (MPa)	Total monthly volume (m^3)	Cumulative volume (m^3)	Monthly average injection rate (m^3/s)
01/03/2013	1.106,67	1,34E+06	7,63	7,66E+06	2,10E+08	2,86
01/04/2013	1.163,29	1,42E+06	8,02	8,16E+06	2,18E+08	3,15
01/05/2013	1.226,64	1,53E+06	8,46	8,73E+06	2,27E+08	3,26
01/06/2013	1.298,52	1,64E+06	8,95	9,40E+06	2,36E+08	3,63
01/07/2013	1.228,41	1,79E+06	8,47	1,03E+07	2,46E+08	3,83
01/08/2013	1.132,19	1,67E+06	7,81	9,55E+06	2,56E+08	3,57
01/09/2013	1.188,71	1,79E+06	8,20	1,11E+07	2,67E+08	4,29
01/10/2013	1.245,24	1,79E+06	8,59	1,11E+07	2,78E+08	4,15
01/11/2013	1.301,76	1,79E+06	8,98	1,11E+07	2,89E+08	4,29
01/12/2013	1.358,29	1,79E+06	9,37	1,11E+07	3,00E+08	4,15
01/01/2014	1.081,92	1,79E+06	7,46	1,11E+07	3,12E+08	4,15
01/02/2014	1.301,02	1,96E+06	8,97	1,22E+07	3,24E+08	5,03
01/03/2014	1.363,02	2,32E+06	9,40	1,44E+07	3,38E+08	5,36
01/04/2014	1.299,37	2,24E+06	8,96	1,39E+07	3,52E+08	5,36
01/05/2014	1.310,34	2,30E+06	9,03	1,43E+07	3,66E+08	5,33
01/06/2014	1.274,25	2,23E+06	8,79	1,42E+07	3,80E+08	5,46
01/07/2014	1.274,25	2,23E+06	8,79	1,42E+07	3,95E+08	5,28
01/08/2014	1.161,15	2,04E+06	8,01	1,43E+07	4,09E+08	5,32
01/09/2014	1.161,15	2,06E+06	8,01	1,44E+07	4,23E+08	5,55
01/10/2014	1.131,56	2,08E+06	7,80	1,45E+07	4,38E+08	5,43
01/11/2014	1.161,14	2,05E+06	8,01	1,43E+07	4,52E+08	5,53
01/12/2014	1.161,14	2,05E+06	8,01	1,43E+07	4,66E+08	5,35
01/01/2015	1.267,89	2,10E+06	8,74	1,43E+07	4,81E+08	5,35
01/02/2015	1.265,19	2,05E+06	8,72	1,43E+07	4,95E+08	5,93
01/03/2015	1.265,21	2,15E+06	8,72	1,51E+07	5,10E+08	5,62
01/04/2015	1.285,52	2,14E+06	8,86	1,50E+07	5,25E+08	5,77
01/05/2015	1.264,84	2,26E+06	8,72	1,58E+07	5,41E+08	5,89
01/06/2015	1.276,08	2,21E+06	8,80	1,55E+07	5,56E+08	5,97
01/07/2015	1.274,22	2,28E+06	8,79	1,60E+07	5,72E+08	5,96
01/08/2015	1.264,83	2,28E+06	8,72	1,59E+07	5,88E+08	5,94
01/09/2015	1.274,79	2,20E+06	8,79	1,54E+07	6,04E+08	5,94
01/10/2015	1.289,03	2,31E+06	8,89	1,62E+07	6,20E+08	6,03
01/11/2015	1.247,93	2,22E+06	8,60	1,55E+07	6,35E+08	5,99
01/12/2015	1.267,05	2,27E+06	8,74	1,59E+07	6,51E+08	5,92

CHAPTER 5. CONCLUSIONS

This dissertation characterizes subsurface attributes, through the use of seismological techniques to analyze data from tectonic and anthropogenic earthquakes. The following subsections summarize the main contributions of this dissertation and discuss limitations and potential future research opportunities.

Contributions

a. Local earthquake isotropic tomography model of Colombia: Chapter 2 is mainly divided in two parts. The first, estimates velocity anomaly variations and relocation of regional earthquakes by using a local tomography algorithm (Koulakov, 2009). Our model suggests the existence of two clearly differentiated subduction segments: Caribbean and Nazca. These results are in line with previously published studies (Pennington, 1981; van der Hilst and Mann, 1994; Taboada et al., 2000; Cortés and Angelier, 2005; Chiarabba et al., 2016; Syracuse et al., 2016). High-quality images of Vp/Vs anomalies towards the south of the Caldas Tear (Vargas and Mann, 2013), support the evidence of the steep subduction of Nazca Plate, which favors the hydration of minerals and the appearance of active volcanoes chains along the Andean Cordillera. On the other hand, towards the north the distribution of these anomalies suggests that mineral dehydration occupies a vast region. This feature not only shows that the subduction angle in the Caribbean segment is not as distinct as it is in Nazca (Bernal-Olaya, 2015; Sanchez et al., 2015; Mora-Bohórquez et al., 2017), but also supports the hypothesis that the origin of the Bucaramanga seismic nest is Caribbean and it's generated by a massive dehydration process of this slab (Taboada et al., 2000; Zafiri et al., 2007; Vargas and Mann, 2013; Syracuse et al., 2016).
b. Local earthquake anisotropic tomography model of Colombia: The second part of Chapter 2, estimates the magnitude and direction of the high-velocity P-wave vectors of the isotropic model defined in the first section of chapter 2 (Koulakov et al., 2009b). This P-wave anisotropic model is the first of its kind for Colombia. As expected, the azimuthal distributions of high-velocity P-wave vectors are linked to the

alignment of geological structures and fault systems in the upper crust (Bokelmann, 1995; Zhang and Schwartz, 1994). In those regions where there are no mapped faults, the direction of the obtained vectors is a source of valuable information linked with the distribution of tectonic stresses. The most important anisotropic feature suggests the coupling of both subduction segments, Caribbean and Nazca. We propose that both blocks couple at the surface around 6°N and dives south to 5°N into the upper mantle where there is no longer a connection between both segments.

c. Predicted impact of induced earthquakes on stress field distribution: Chapter 3 of this dissertation is the first published article that documented the induced seismicity in Puerto Gaitan. Making use of available public information, it was possible to establish a spatial and temporal correlation between industrial activities of hydrocarbon production (extraction and injection of fluids) and the seismicity reported by the Colombian Geological Service (SGC) at that time. However, we consider that the importance of the article lay so much more in demonstrating that the techniques and methodologies to characterize large tectonic events are also useful to describe the mechanics of small anthropogenic events. Back Projection Imaging (BPI) was used to obtain the rupture direction and velocity of some recorded earthquakes (Ishii et al., 2007; Krüger and Ohrnberger, 2005; Bayer et al., 2012; Folesky, 2013; Ishii et al., 2007; Walker and Shearer, 2009; Kao and Shan, 2004). The focal mechanisms of the six largest events were estimated and the stress tensor was determined (Vavrycuk, 2014). The BPI, the focal mechanisms, and the stress tensor results demonstrated that the predicted fractures did not align to regional fracture orientation. This is an indication that the recorded anomalous seismicity was a consequence of a local alteration on the regional stress field.

d. Hydromechanical analysis allows us to determine the energy efficiency in Puerto Gaitan oilfields: The relationship between oilfield operations and seismicity between 2013 and 2015 in the municipality of Puerto Gaitan is suggestive. Our analysis and results propose that the sequence of events in Puerto Gaitan are the result of the release of the elastic energy stored in the reservoir due to the continuous action of the work exerted by the injection of water. The released Mo in Puerto Gaitan depends on the injected volume, but also on injection rate, surface pressure, depth of crystalline basement and stress conditions of the reservoir. Establishing the relationship between the previous operative criteria and Mo are necessary for understanding and control of long-term injection experiments in the field. The behavior of the V and Mo curves in Puerto Gaitan show us that a reduction of the total pumped volume or slow injection operations may reduce seismic hazard in the area. The energy efficiency of the injection cycle is well compared to other documented long-term injection operations. The high seismic deformation of the reservoirs and the possible filtration of large volumes of fluid injected into deeper structures are the main causes that generate low energy efficiency in Puerto Gaitan. These two conditions have allowed long-term injection of large volumes to have not led to significant larger events. However, it is essential to settle if there is a hydraulic connection (high permeability) between the reservoir and the crystalline basement, most likely through basement faults reaching into the reservoir. Additionally, gravimetric information is used to demonstrate that basement heights mitigate the propagation of seismicity and control the dissipation of earthquake energy (McNamara et al., 2015; Goertz-Allmann et al., 2017).

Limitations and future work

We believe that there are areas for improvement and opportunities for future research.

a. Data Sources: The information used in this research is public and can be consulted through the information channels of the Colombian Geological Service (SGC) and the National Hydrocarbons Agency (ANH). The information available from regional earthquakes was adequate to develop the methodology proposed in Chapter 1, and to obtain the results of seismic tomography and azimuthal anisotropy for P wave. However, for the other chapters, we are aware that the gotten results may have a load. of uncertainty. Moreover, in our studies, we only consider the relationship between average water injection volumes and the seismic occurrence from a regional network. As mentioned in Chapter 1, it is essential to have dense station networks on the surface as well as downhole instrumentation. The study carried out by Molina et al., (2020) for instance, used detailed information given from the operator company including: 2D and

3D seismic data, injection rates and surface pressure data, 3 years of seismic data from a network of 28 local stations around the field. This information was useful to build a local velocity model, relocate earthquakes, and recalculate magnitudes. Industry-academy cooperation is important to develop detailed studies. Open-source datasets may be published to increases the development of independent research and enhances knowledge related to anthropogenic seismicity.

b. Field experiments: In a wide range of tectonic regimes, fluids are involved in faulting activation and seismic processes: fluid intrusion into subduction zones (Saffer & Tobin, 2011; Sibson, 1992, 2000), mineralization processes involving high-pressure fluids (Weatherley & Henley, 2013), dehydration of fluids along faults (Connolly, 1997; Hacker, 1997). The above processes were shown in Chapter 2. Areas with reported induced earthquakes may become natural laboratories for large-scale experiments to further understand earthquakes in natural fault systems.

c. Precursor signals: Earthquake prediction and hazard evaluation may has to do with the analysis of precursor signals. In some rare cases there is evidence of precursor signals prior to failure of a fault (Dodge et al., 1996; Savage et al. 2017a). Considering that injection protocols are controlled operations, induced seismicity can become a research area in this topic. High-precision instrumentation located in dense networks is required to allow recording and later testing if there are signals that anticipate the occurrence of an earthquake.

d. Improve pressure diffusion simulation: Hydrogeological models (including poroelasticity) and the resulting estimates of pressure disturbances endure the most consistent way to determine the probability of fluids triggering seismicity. These models, however, rely on parameters such as injection unit thickness and permeability/conductivity. These parameters are often not in the public domain, and as a result the models often remain relatively simplistic (Keranen et al. 2014). In Chapter 4 we demonstrate that, by means of a simple energy balance, the Puerto Gaitán area is an inefficient medium to release energy in the form of earthquakes. We argue that this inefficiency was due to the low rock conductivity. Although it is a simple analysis, the results are revealing. Molina et al., (2020) reported a value for the hydraulic conductivity of 5.3×10^{-5} ms^{-1} fits the relationship between the elapsed time since injection started, and the distance reached by the pore pressure disturbance. It is important to note that hydrogeological parameters are not stationary. Shallow groundwater studies indicate that permeability is not constant with changes over time (Manga et al. 2016). Molina et al., (2020) suggested that as July 2016 injection is likely to affect reservoir pressure at distances where seismicity is not occurring, neither the amplitude of the pressure disturbance, nor the conditions and orientation of stresses, are sufficient for faults to be activated. The study finally concludes that earthquakes have released most of the tectonic stress, and given the short period of time and modest tectonic loading rate, faults in the area have not re-loaded enough to produce new earthquakes. However, the Colombian Geological Service (SGC) reported the occurrence of 90 earthquakes in March 2021, including one with M5.0 on March 21, the largest event recorded ever in the area. Is the seismicity in Puerto Gaitan no longer induced, to be now triggered?

REFERENCES

Abercrombie, R.E. (1995). J. Geophys. Res. 100, 24015-24036.

Adamek, S., Frohlich, C., and Pennington, W.D. (1988). Seismicity of the Caribbean-Nazca boundary: Constraints on microplate tectonics of the Panama region. Journal of Geophysical Research 93: doi: 10.1029/88JB01269. ISSN: 0148-0227.

Ake J, Mahrer K, O'Connell D, Block L. 2005. Deep-injection and closely monitored induced seismicity at Paradox Valley, Colorado. Bull. Seismol. Soc. Am. 95:664–83

Aki, K., 1965. Maximum likelihood estimate of b in the formula log N = a - b M and its confidence limits, Bull. seism. Soc. Am., 43, 237–239.

Alessandro, A., Danet, A., Grecu, B., 2012. Location performance and detection magnitude threshold of the Romanian national seismic network. Pure Appl. Geophys. 169 (2012), 2149e2164. http://dx.doi.org/10.1007/s00024-012-0475-7.

Alghannam, M., Juanes, R., 2020. Understanding rate effects in injection-induced earthquakes. Nature communications 11, 1–6.

Alt RC, Zoback MD. 2016. In situ stress and active faulting in Oklahoma. Bull. Seismol. Soc. Am. 107:216–28

Aspden, J.A., McCourt, W.J., 1986. Mesozoic oceanic terrane in the central Andes of Colombia. Geology 14, 415e418.

Aspectos hidrodinámicos, estructurales y estratigráficos del Campo Rubiales. Cuenca de los Llanos Orientales, Colombia. In: VI Simposio Bolivariano-Exploración Petrolera en las Cuencas Subandinas, Cartagena de Indias, vol. 9, pp. 4e10.

Atkinson GM, Eaton DW, Ghofrani H, Walker D, Cheadle B, et al. 2016. Hydraulic fracturing and seismicity in the Western Canada Sedimentary Basin. Seismol. Res. Lett. 87:631–47

Atkinson, G.M., 2015. Ground-motion prediction equation for small-to-moderate events at short hypocentral distances, with application to induced-seismicity hazards. Bulletin of the Seismological Society of America 105, 981–992.

Atkinson, G.M., 2020. The intensity of ground motions from induced earthquakes with implications for damage potential. Bulletin of the Seismological Society of America 110, 2366–2379.

Atkinson, G.M., Eaton, D.W., Ghofrani, H., Walker, D., Cheadle, B., Schultz, R. & Liu, Y., 2016. Hydraulic fracturing and seismicity in the Western Canada Sedimentary Basin, Seismol. Res. Lett., 87, 631–647.

Atkinson, G.M., Wald, D., Worden, C.B., Quitoriano, V., 2018. The intensity signature of induced seismicity. Bulletin of the Seismological Society of America 108, 1080–1086.

Baisch, S., Koch, C., Muntendam-Bos, A., 2019. Traffic light systems: To what extent can induced seismicity be controlled? Seismological Research Letters 90, 1145–1154.

Bao, X. & Eaton, D.W., 2016. Fault activation by hydraulic fracturing in western Canada, Science, 354(6318), 1046–1409.

Barnhart WD, Benz HM, Hayes GP, Rubinstein JL, Bergman E. 2014. Seismological and geodetic constraints on the 2011 Mw5.3 Trinidad, Colorado earthquake and induced deformation in the Raton Basin. J. Geophys. Res. 119:7923–33

Barrera, D., Pardo, A., Vargas, C.A., Martínez, J., 2007. Petroleum geology of Colombian basins. Colombian Sedimentary Basins: Nomenclature, Boundaries and Petroleum Geology, a New Proposal. Agencia Nacional de Hidrocarburos ANH.

Barros, L, Cappa, F., Guglielmi, Y., Duboeuf, L. & Grasso, J.R., 2019. Energy of injection-induced seismicity predicted from in-situ experiments, Scientific Reports, 9, 10.1038/s41598-019-41306-x.

Bayer, B., Kind, R., Hoffmann, M., Yuan, X., Meier, T., 2012. Tracking unilateral earthquake rupture by P-wave polarization analysis. Geophys. J. Int. 188, 1141e1153.

Ben-Avraham, Z., Nur, A., 1987. Effects of collisions at trenches on oceanic ridges and passive margins. In: Monger, J.W.H., Francheteau, J. (Eds.), Circum-Pacific Orogenic Belts and Evolution of the Pacific Ocean Basin: American Geophysical Union, Geodynamics Series, vol. 18, pp. 9e18.

Bender, B., 1983. Maximum likelihood estimation of b values for magnitude grouped data, Bull. seism. Soc. Am., 73, 831–851.

Bernal-Olaya, R., Mann, P., & Escalona, A. (2015). Cenozoic tectonostratigraphic evolution of the Lower Magdalena Basin, Colombia: An example of an under- to overfilled forearc basin. In C. Bartolini & P. Mann (Eds.), Petroleum geology and potential of the Colombian Caribbean Margin, AAPG Memoir (Vol. 108, pp. 345–398). Tulsa, OK: American Association of Petroleum Geologists. https://doi.org/10.1306/13531943M1083645

Bernal-Olaya, R., Mann, P., & Vargas, C. A. (2015). Earthquake, tomographic, seismic reflection, and gravity evidence for a shallowly dipping subduction zone beneath the Caribbean margin of northwestern Colombia. In C. Bartolini & P. Mann (Eds.), Petroleum geology and potential of the Colombian Caribbean Margin, AAPG Memoir (Vol. 108, pp. 247–270). Tulsa, OK: Association of Petroleum Geologists. https://doi.org/10.1306/13531939M1083642

Bird, P & Kagan, Y, 2004. Plate-Tectonic Analysis of Shallow Seismicity: Apparent boundary Width, Beta, Corner Magnitude, Coupled Lithosphere Thickness, and Coupling in Seven Tectonic Settings, Bull. seism. Soc. Am., 94 (6), 2380–2399.

Block, L.V., Wood, C.K., Yeck, W.L. & King, V.M., 2014. The 24 January 2013 ML earthquake near Paradox, Colorado, and its relation to deep well injection, Seismol. Res. Lett., 85(3), 609–624.

Bokelmann, G., 1995. P-wave array polarization analysis and effective anisotropy of the brittle crust. Geophysical Journal International 120, 145–162.

Bommer, J.J., Crowley, H., Pinho, R., 2015. A risk-mitigation approach to the management of induced seismicity. Journal of Seismology 19, 623–646.

Bommer, J.J., Dost, B., Edwards, B., Staord, P.J., van Elk, J., Doornhof, D., Ntinalexis, M., 2016. Developing an application-specific ground-motion model for induced seismicity. Bulletin of the Seismological Society of America 106, 158–173.

Bommer, J.J., Stafford, P.J., Edwards, B., Dost, B., van Dedem, E., Rodriguez-Marek, A., Kruiver, P., van Elk, J., Doornhof, D., Ntinalexis, M., 2017. Framework for a ground-motion model for induced seismic hazard and risk analysis in the Groningen gas field, the Netherlands. Earthquake Spectra 33, 481–498.

Boroumand, N. & Eaton, D.W., 2012 Comparing energy calculation: hydraulic fracture and Microseismic monitoring, in Proceedings of the Geo-Convention: Vision, Calgary, Canada, 14–18 May 2012.

Bossu, R., et al. (1996). Bull. Seismol. Soc. Am. 86, 959-971.

Bouchon, M., 1981. A Simple Method to calculate Green's functions in Elastic Layered Media, Bull. Seismol. Soc. Am. 71, 959e971.

Bourne, S., Oates, S., Van Elk, J., 2018. The exponential rise of induced seismicity with increasing stress levels in the Groningen gas field and its implications for controlling seismic risk. Geophysical Journal International 213, 1693–1700.

Bourne, S.J., Oates, S.J., 2017. Development of statistical geomechanical models for forecasting seismicity induced by gas production from the Groningen field. Netherlands Journal of Geosciences 96, s175–s182.

Brace, W. F. y D. L. Kohlstedt (1980), Limits on lithospheric stress impossed by laboratory experiments, Journal of Geophysical Research, 85, 6248-6252.

Brantut, N., Passelègue, F. X., Deldicque, D., Rouzaud, J. N. & Schubnel, A. Dynamic weakening and amorphization in serpentinite during laboratory earthquakes. Geology 44, 607–610, doi:10.1130/G37932.1 (2016).

Broccardo, M., Mignan, A., Wiemer, S., Stojadinovic, B., Giardini, D., 2017. Hierarchical Bayesian modeling of fluid-induced seismicity. Geophysical Research Letters 44, 11–357.

Brooks, E.M., Stein, S., Spencer, B.D., Salditch, L., Petersen, M.D., McNamara, D.E., 2018. Assessing earthquake hazard map performance for natural and induced seismicity in the central and eastern United States. Seismological Research Letters 89, 118–126.

Brudy, M., et al. (1997). J. Geophys. Res. 102, 18453-18475.

Bürgl, H., 1961. Sedimentación cíclica en el geosinclinal Cretáceo de la Cordillera Oriental de Colombia. Servicio Geológico Nacional, p. 60. Informe No. 1347.

Burke, K., 1988. Tectonic evolution of the Caribbean. Annu. Rev. Earth Planet. Sci. 16, 201e230.

Butler, K., Schamel, S., 1988. Structure along the eastern margin of the Central cordillera, upper Magdalena Valley, Colombia. J. S. Am. Earth Sci. 1, 109e120.

Bydlon, S.A., Gupta, A., Dunham, E.M., 2017. Using simulated ground motions to constrain near source ground-motion prediction equations in areas experiencing induced seismicity. Bulletin of the Seismological Society of America 107, 2078–2093.

Bydlon, S.A., Withers, K.B., Dunham, E.M., 2019. Combining Dynamic Rupture Simulations with Ground-Motion Data to Characterize Seismic Hazard from Mw 3 to 5.8 Earthquakes in Oklahoma and Kansas. Bulletin of the Seismological Society of America 109, 652–671.

Byerlee, J. D. (1978), Friction of rocks, Pure and Applied Geophysics, 116, 615-626.

Casero, P., Salel, J.F., Rosato, A., 1997. Multidisciplinary correlative evidences for pholyphase geological evolution of the foot-hills of the Cordillera oriental. In: VI Simposio Bolivariano- Exploración Petrolera en las Cuencas Subandinas, Cartagena de Indias, vol. 1, pp. 100e118.

Cediel, F., Shaw, R.P. & Cáceres, C., 2003. Tectonic assembly of the northern Andean block, in the circum-Gulf of Mexico and the Caribbean: Hydrocarbon habitats, basin formation, and plate tectonics, AAPG Mem., 79, 1–34.

Cesca, S. et al., 2014. The 2013 September–October seismic sequence offshore Spain: a case of seismicity triggered by gas injection? Geophys. J. Int., 182(2), 941–953.

Chan, A.W. & Zoback, M.D., 2007. The role of hydrocarbon production on land subsidence and fault reactivation in the Louisiana coastal zone, Journal of Coastal Research, 23, 771-786.

Chang, K.W., Yoon, H., Martinez, M.J., 2018. Seismicity rate surge on faults after shut-in: Poroelastic response to fluid injection. Bulletin of the Seismological Society of America 108, 1889–1904.

Chang, Ying & Warren, Linda & Prieto, German. (2017). Precise Locations for Intermediate-Depth Earthquakes in the Cauca Cluster, Colombia. Bulletin of the Seismological Society of America. 107. 1-15. 10.1785/0120170127.

Chen, R., Xue, X., Park, J., Datta-Gupta, A., King, M.J., 2020. New insights into the mechanisms of seismicity in the Azle area, North Texas. Geophysics 85, EN1–EN15.

Chen, X. et al., 2017. The Pawnee earthquake as a result of the interplay among injection, faults and foreshocks, Sci. Rep., 7. doi:10.1038/s41598-017-04992-z.

Chiarabba, C., De Gori, P., Faccena, C., Speranza, F., Deccia, D., Dionicio, V., Prieto, G.A., 2015. Subduction system and flat slab beneath the Eastern Cordillera of Colombia. Geochem. Geophys. Geosyst.17, 16–27. http://dx.doi.org/10.1002/2015GC006048.

Connolly JAD. 1997. Devolatilization-generated fluid pressure and deformation-propagated fluid flow during prograde regional metamorphism. J. Geophys. Res. 102:18149–73

Cooper, M.A., Addison, F.T., Álvarez, R., Coral, M., Graham, R.H., Hayward, A.B., Howe, S., Martínez, J., Naar, J., Peñas, R., Pulham, A., Taborda, A., 1995a. Basin development and tectonic history of the Llanos basin, Eastern Cordillera and middle Magdalena Valley, Colombia. AAPG Bull. 79 (10), 1421e1443.

Cooper, M.A., Addison, F.T., Alvarez, R., Hayward, A.B., Howe, S., Pulham, A.J., Taborda, A., 1995b. Basin development and tectonic history of the Llanos basin, Colombia. In: Tankard, A.J., Suárez, R., Welsink, H.J. (Eds.), Petroleum Basins of South America: AAPG Memoir 62, pp. 659e665.

Cornet, F.H., 2016. Seismic and aseismic motions generated by fluid injections, Geomech. Ener. Environ., 5, 42–54.

Cortés, M., Angelier, J., 2005. Current state of stress in the northern Andes as indicated by focal mechanisms of earthquakes. Tectonophysics403, 29–58. http://dx.doi.org/10.1016/j.tecto.2005.03.020.

Coutant, O., 1989. Numerical Study of the diffraction of elastic waves by fluid-filled cracks. J. Geophys. Res. 94, 17805e17818.

Cremen, G., Gupta, A., Baker, J., 2017. Evaluation of ground motion intensities from induced earthquakes using “Did You Feel It?” data, in: 16th World Conf. on Earthquake Engineering.

Cremen, G., Werner, M.J., Baptie, B., 2020. A new procedure for evaluating ground-motion models, with application to hydraulic-fracture-induced seismicity in the United Kingdom. Bulletin of the Seismological Society of America 110, 2380–2397.

Dasilva, A., Gómez, Y., Villa, M.A., Yoris, F., Morales, D., 2014. Oil distribution in the carbonera formation, Arenas Basales unit. A case study in the Quifa and Rubiales Fields, Eastern Llanos basin, Colombia. In: Adapted from Extended Abstract Prepared for a Poster

Presentation at AAPG International Conference & Exhibition, Cartagena, Colombia, September 8-11, 2013.

Davies, R., Foulger, G., Bindley, A. & Styles, P., 2013. Induced seismicity and hydraulic fracturing for the recovery of hydrocarbons, Mar. Petrol. Geol., 45, 171–185

Davis SD, Frohlich C. 1993. Did (or will) fluid injection cause earthquakes? Criteria for a rational assessment. Seismol. Res. Lett. 64:207–24

Davis SD, Pennington WD. 1989. Induced seismic deformation in the Cogdell oil field of west Texas. Bull. Seismol. Soc. Am. 79:1477–95

De Barros, L., Guglielmi, Y.D., Cappa, F. & Duboeuf, L., 2018. Seismicity and fault aseismic deformation caused by fluid injection in decametric in-situ experiments, Comptes Rendus Geoscience, 350 (8), 464–475.

Dempsey, D., Suckale, J., 2017. Physics-based forecasting of induced seismicity at Groningen gas field, the Netherlands. Geophysical Research Letters 44, 7773–7782.

Dengo, C., and M. Covey (1993), Structure of the eastern cordillera of Colombia: Implications for trap styles and regional tectonics, AAPG Bull., 77, 1315–1315.

Dieterich, J.H., Richards-Dinger, K.B. & Kroll, K.A., 2015. Modeling injection-induced seismicity with the physics-based earthquake simulator RSQ Sim, Seismol. Res. Lett., 86(4), 1102–1109.

Dodge DA, Beroza GC, Ellsworth WL. 1996. Detailed observations of California foreshock sequences: implications for the earthquake initiation process. J. Geophys. Res. 101:22371–92

Dost, B., Ruigrok, E., Spetzler, J., 2017. Development of seismicity and probabilistic hazard assessment for the Groningen gas field. Netherlands Journal of Geosciences 96, s235–s245.

Duque-Caro, H., 1991. Contributions to the geology of the Pacific and Caribbean coastal areas of northwestern Colombia and South America: Princeton University, PhD. thesis, 132 p.

Eaton, D.W. & Igonin, N., 2018. What controls the maximum magnitude of injection-induced earthquakes? Leading Edge, 37(2), 135–140.

Eberhart-Phillips, D. (1986). Three-dimensional velocity structure in northern California Coast Ranges from inversion of local earthquake arrival times, Bull. Seismol. Soc. Am. 76, 1025–1052.

Ellsworth, W., 2013. Injection-induced earthquakes, Science, 341, 1225942.

Ellsworth, W.L., Llenos, A.L., McGarr, A.F., Michael, A.J., Rubinstein, J.L., Mueller, C.S., Petersen, M.D., Calais, E., 2015. Increasing seismicity in the US midcontinent: Implications for earthquake hazard. The Leading Edge 34, 618–626.

Espurt, N., F. Funiciello, J. Martinod, B. Guillaume, V. Regard, C. Faccenna, and S. Brusset (2008), Flat subduction dynamics and deformation of the South American plate: Insights from analog modeling, Tectonics, 27, TC3011, doi:10.1029/2007TC002175.

Etayo-Serna, F., 1979. Zonation of the Cretaceous of Central Colombia by ammonites, vol. 2. Publicación Especial INGEOMINAS, pp. 1e186.

Fabre, A., 1983. La subsidencia de la Cuenca del Cocuy (Cordillera Oriental de Colombia) durante el Cretáceo y el Terciario, Segunda parte: Esquema de Evolución Tectónica. Geol. NorAndina 8, 49e61.

Farhadi, A., Pezeshk, S., Khoshnevis, N., 2018. Assessing the Applicability of Ground-Motion Models for Induced Seismicity Application in Central and Eastern North America. Bulletin of the Seismological Society of America 108, 2265–2277.

Farris, D. W., Jaramillo, C., Bayona, G., Restrepo-moreno, S. A., Montes, C., Cardona, A., Valencia, V. (2011). Fracturing of the Panamanian Isthmus during initial collision with South America. Geology, 39(11), 1007–1010.

Faul, U.H., Jackson, I., 2005. The seismological signature of temperature and grain size variations in the upper mantle. Earth Planet. Sci. Lett.234 (1–2), 119–134. http://dx.doi.org/10.1016/j.epsl.2005.02.008.

Flinch, J. F. (2003). Structural evolution of the Sinu-Lower Magdalena area (northern Colombia). AAPG Memoir, 79(1), 776–796.

Folesky, J.T., 2013. Rupture Propagation Imaging at Microseismic Scale. Berlin Freie University, Berlin.

Fouch, M., Rondenay, S., 2006. Seismic anisotropy beneath stable continental interiors. Physics of the Earth and Planetary Interiors 158, 292–320.

Freymuller, J., Kellogg, J., Vega, V., 1993. Plate motions in the North Andean region. J. Geophys. Res. 98 (21), 21853e21863.

Frohlich C, Walter JI, Gale JF. 2015. Analysis of transportable array (USArray) data shows earthquakes are scarce near injection wells in the Williston Basin, 2008–2011. Seismol. Res. Lett. 86:492–99

Frohlich, C. & Davis, S., 1993. Teleseismic b-values: or, much ado about 1.0, J. geophys. Res., 98, 631–644.

Frohlich, C., 2012. Two-year survey comparing earthquake activity and injection-well locations in Barnett Shale, Texas, Proc. Natl Acad. Sci. USA, 109, 13934–13938

Gailler, A., P. Charvis, and E. R. Flueh (2007), Segmentation of the Nazca and South American plates along the Ecuador subduction zone from wide angle seismic profiles, Earth Planet. Sci. Lett., 260, 444–464.

Galis, M., Ampuero, J.P., Mai, P.M. & Cappa, F., 2017. Induced seismicity provides insight into why earthquake ruptures stop, Sci. Adv., 3(12)

Ghofrani, H., Atkinson, G.M., Schultz, R., Assatourians, K., 2019. Short-term hindcasts of seismic hazard in the western Canada sedimentary basin caused by induced and natural earthquakes. Seismological Research Letters 90, 1420–1435.

Gobel T. 2015. A comparison of seismicity rates and fluid-injection operations in Oklahoma and California: ¨ implications for crustal stresses. Lead. Edge 34:640–48

Godano, C. & Pingue, F., 2002. Is the seismic moment-frequency relation universal? Geophys. J. Int., 142, 193–198, 10.1046/j.1365-246x.2000.00149. x.

Goebel THW, Hosseini SM, Cappa F, Hauksson E, Ampuero JP, et al. 2016. Wastewater disposal and earthquake swarm activity at the southern end of the Central Valley, California. Geophys. Res. Lett. 43:1092–99

Goebels, T.H.W, Weingartenb, M., Chenc, X., Haffenerc, J. & Brodskya, E.E., 2017. The 2016 Fair view Oklahoma earthquakes: Evidence for long range poroelastic stress triggering at >40 km from fluid disposal wells, Earth planet. Sci. Lett., 472, 50–61.

Goertz-Allmann, B.P., Gibbons, S.J., Oye, V., Bauer, R. & Will, R., 2017. Characterization of induced seismicity patterns derived from internal structure in event clusters, J. geophys. Res., 122, 3875–3894.

Gómez, E.T., Jordan, R.W., Allmendinger, Cardozo, N., 2005. Development of the Colombian foreland-basin system as a consequence of diachronous exhumation of northern Andes. Geol. Soc. Am. Bull. 117, 1272e1292.

Gómez, Y., Yoris, F., Rodríguez, J., Portillo, F., Araujo, Y., Pacific Rubiales Energy, 2010.

Gómez-Alba, S., Fajardo-Zarate, C.E. & Vargas, C.A., 2015. Stress field estimation based on focal mechanisms and back projected imaging in the Eastern Llanos Basin (Colombia), J. S. Am. Earth Sci., 71, 320–332

Gono, V., Olson, J.E., Gale, J.F., et al., 2015. Understanding the correlation between induced seismicity and wastewater injection in the Fort Worth basin, in: 49th US Rock Mechanics/Geomechanics Symposium, American Rock Mechanics Association.

Grasso, J.R., 1992. Mechanics of seismic instabilities induced by the recovery of hydrocarbons, Pure and Applied Geophysics, 139, 507-534.

Graterol, V. & Rey, C.A., 2009. Mediciones Aero gravimétricas y magnetométricas en los Llanos Orientales de Colombia, X Simposio Bolivariano Exploración Petrolera en Cuencas Subandinas, Cartagena, Colombia.

Grigoli, F. et al., 2018. The November 2017 Mw 5.5 Pohang earthquake: a possible case of induced seismicity in South Korea, Science, 360(6392), 1003–1006.

Grigoratos, I., Rathje, E., Bazzurro, P., Savvaidis, A., 2020a. Earthquakes induced by wastewater injection, part I: Model development and hindcasting. Bulletin of the Seismological Society of America 110, 2466–2482.

Grigoratos, I., Rathje, E., Bazzurro, P., Savvaidis, A., 2020b. Earthquakes induced by wastewater injection, part II: Statistical evaluation of causal factors and seismicity rate forecasting. Bulletin of the Seismological Society of America 110, 2483–2497.

Gupta, A., Baker, J.W., 2017. Estimating spatially varying event rates with a change point using Bayesian statistics: Application to induced seismicity. Structural safety 65, 1–11.

Gupta, A., Baker, J.W., 2019. A framework for time-varying induced seismicity risk assessment, with application in Oklahoma. Bulletin of Earthquake Engineering 17, 4475–4493.

Gutscher, M. A., W. Spakman, H. Bijward, and E. R. Engdahl (2000), Geodynamics of flat subduction: Seismicity and tomographic constraints from the Andean margin, Tectonics, 19, 814–833.

Gutscher, M., J. Malavieille, S. Lallemand, and J. Collot (1999), Tectonic segmentation of the North Andean margin: Impact of the Carnegie ridge collision, Earth Planet. Sci. Lett., 168, 255–270.

Hacker BR. 1997. Diagenesis and fault valve seismicity of crustal faults. J. Geophys. Res. 102:24459–67

Hacker, B. R., Peacock, S. M., Abers, G. A. & Holloway, S. D. Subduction factory 2. Are intermediate-depth earthquakes in subducting slabs linked to metamorphic dehydration reactions? J. Geophys. Res. 108, B12030, doi:10.1029/2001JB001129 (2003).

Haddad, M., Eichhubl, P., et al., 2020. Poroelastic Modeling of Basement Fault Reactivation Caused by Saltwater Disposal Near Venus, Johnson County, Texas, in: 54th US Rock Mechanics/Geomechanics Symposium, American Rock Mechanics Association.

Hammond, W.C., Humphreys, E.D., 2000. Upper mantle seismic wave velocity: effects of realistic partial melt geometries. J. Geophys. Res.105 (B5), 10,975–10,986. http://dx.doi.org/10.1029/2000JB900041.

Havskov, J., Ottemoller, L., 2000. SEISAN. The earthquake analysis software. Institute of solid Earth Physics. University of Bergen, Bergen, Norway, p. 250.

Healy, J., Rubey, W., Griggs, D. & Raleigh, C., 1968. The Denver earthquakes, Science, 161, 1301–1310.

Heidbach O, Tingay M, Barth A, Reinecker J, Kurfeß D, Muller B. 2010. Global crustal stress pattern based ¨ on the World Stress Map database release 2008. Tectonophysics 482:3–15

Heidbach, O., M. Rajabi, X. Cui, K. Fuchs, B. Müller, J. Reinecker, K. Reiter, M. Tingay, F. Wenzel, F. Xie, M. O. Ziegler, M.-L. Zoback, and M. D. Zoback. 2018, The World Stress Map database release 2016: Crustal stress pattern across scales. Tectonophysics, 744,484-498. http://doi.org/10.1016/j.tecto.2018.07.007

Heidbach, O., Tingay, M., Barth, A., Reinecker, J., Kurfeß, D., Müller, B., 2009. The World Stress Map Based on the Database Release 2008, Equatorial Scale 1:46,000,000, Commission for the Geological Map of the World, Paris. http://dx.doi.org/10.1594/GFZ.WSM.Map2009.

Hennings, P.H., Lund Snee, J.E., Osmond, J.L., DeShon, H.R., Dommisse, R., Horne, E., Lemons, C., Zoback, M.D., 2019. Injection-induced seismicity and fault-slip potential in the Fort Worth Basin, Texas. Bulletin of the Seismological Society of America 109, 1615–1634.

Herrmann, R.B., Park, S.-K., Wang, C.-Y., 1981. The Denver earthquakes of 1967e1968. Bull. Seismol. Soc. Am. 71, 731e745.

Hettner, A., 1892. Die kordillere von Bogota: Ergzh zu Petermanns Mitteilungen Bd. 22. Erganzungsheft 104, 1e131.

Hickman SH, Healy JH, ZobackMD. 1985. In situ stress, natural fracture distribution, and borehole elongation in the Auburn geothermal well, Auburn, New York. J. Geophys. Res. 90:5497–512

Hitzman, M.W. et al., 2012. Induced Seismicity Potential in Energy Technologies, The National Academies Press, Washington D.C.

Holland AA. 2013a. Earthquakes triggered by hydraulic fracturing in south-central Oklahoma. Bull. Seismol. Soc. Am. 103:1784–92

Holland AA. 2013b. Optimal fault orientations within Oklahoma. Seismol. Res. Lett. 84:876–90

Hornbach MJ, Jones M, Scales M, DeShon HR, Magnani MB, et al. 2016. Ellenburger wastewater injection and seismicity in North Texas. Phys. Earth Planet. Inter. 261:54–68

Horton, S., 2012. Disposal of hydrofracking waste fluid by injection into subsurface aquifers triggers earthquake swarm in central Arkansas with potential for damaging earthquake. Seismological Research Letters 83, 250–260.

Houston, H. 4.13 - Deep Earthquakes. In: Schubert, G. (ed). Treatise on Geophysics (Second Edition). Elsevier, Oxford, pp 329–354 (2015).

Hsieh PA, Bredehoeft JD. 1981. A reservoir analysis of the Denver earthquakes: a case of induced seismicity. J. Geophys. Res. 86:903–20

Huang Y, Beroza GC, Ellsworth WL. 2016. Stress drop estimates of potentially induced earthquakes in the Guy-Greenbrier sequence. J. Geophys. Res. 121:6597–607

Huang, Y., Ellsworth, W.L., Beroza, G.C., 2017. Stress drops of induced and tectonic earthquakes in the central United States are indistinguishable. Science advances 3, e1700772.

Hubach, E., 1957. Contribución a las unidades estratigráficas de Colombia, (enumeración regional, de más reciente a más antiguas). Servicio Geológico Nacional, p. 165. Informe no. 1212.

Idárraga-García, J., Kendall, J.-M., & Vargas, C. A. (2016). Shear wave anisotropy in northwestern South America and its link to the Caribbean and Nazca subduction geodynamics. Geochemistry, Geophysics, Geosystems, 17(9), 3655–3673. https://doi.org/10.1002/2016GC006323.

Ishii, M., Shearer, P., Houston, H., Vidale, J., 2007. Teleseismic P wave imaging of the 26 December 2004 Sumatra-Andaman and 28 March 2005 Sumatra earthquake ruptures using the Hi-net array. JGR 112.

Jadamec, M.A., Billen, M.I., 2010. Reconciling surface plate motions with rapid three-dimensional mantle flow around a slab edge. Nature465 (7296), 338–341. http://dx.doi.org/10.1038/nature09053.

Jung, H., and S. Karato (2001), Water-induced fabric transitions in olivine, Science, 293(5534), 1460–1463.

Jung, H., Green, H. W. & Dobrzhinetskaya, L. F. Intermediate-depth earthquake faulting by dehydration embrittlement with negative volume change. Nature 428, 545–549, doi:10.1038/nature02412 (2004).

Kagan, Y.Y., 1997. Seismic moment-frequency relation for shallow earthquakes: regional comparison, J. geophys. Res., 102, 2835–2852, doi:10.1029/96JB03386.

Kagan, Y.Y., 1999. Universality of the seismic moment-frequency relation, Pure appl. Geophys., 15, 537–573.

Kanamori, H., 1977. The energy release in great earthquakes, J. geophys. Res., 82 (20), 2981–2987.

Kang, J.Q., Zhu, J.B., Zhao, J., 2019. A review of mechanisms of induced earthquakes: from a view of rock mechanics. Geomechanics and Geophysics for Geo-Energy and Geo-Resources 5, 171–196.

Kao, H., Shan, S.-J., 2004. The source-scanning algorithm: mapping the distribution of seismic sources in time and space. GJI 157, 589e594.

Karato, S., 1993. Importance of anelasticity in the interpretation of seismic tomography. Geophys. Res. Lett.20 (15), 1623–1626. http://dx.doi.org/10.1029/93GL01767.

Kawakatsu, H. & Watada, S. Seismic Evidence for Deep-Water. Science **316**, 1468–1471, doi:10.1126/science.1140855 (2007).

Keleman, P.B., Hirth, G., 2007. A periodic shear-heating mechanism for intermediate-depth earthquakes in the mantle. Nature446, 787–790.

Kellogg, J., Vega, V., 1995. Tectonic development of Panama, Costa Rica, and Colombian Andes: constraints from global positioning system geodetic studies and gravity. Spec. Pap. Geol. Soc. Am. 295, 75e90.

Keranen KM, Savage HM, Abers GA, Cochran ES. 2013. Potentially induced earthquakes in Oklahoma, USA: links between wastewater injection and the 2011 Mw 5.7 earthquake sequence. Geology 41:699–702

Keranen, K.M., Weingarten, M., 2018. Induced seismicity. Annual Review of Earth and Planetary Sciences 46, 149–174.

Keranen, K.M., Weingarten, M., Abers, G.A., Bekins, B.A. & Ge, S., 2014. Sharp increase in central Oklahoma seismicity since 2008 induced by massive wastewater injection, Science, 345(6195), 448–451.

Khosravikia, F., Clayton, P., Nagy, Z., 2019. Artificial neural network-based framework for developing ground-motion models for natural and induced earthquakes in Oklahoma, Kansas, and Texas. Seismological Research Letters 90, 604–613.

Kikuchi, M., Kanamori, H., 1991. Inversion of complex body waves III. Bull. Seismol. Soc. Am. 81, 2335e2350.

Kim, K.H., Ree, J.H., Kim, Y.H., Kim, S., Kang, S.Y. & Seo, W., 2018. Assessing whether the 2017 Mw 5.4 Pohang earthquake in South Korea was an induced event, Science, 360(6392), 1007–1009.

Kim, W.Y., 2013. Induced seismicity associated with fluid injection into deep well in Youngstown, Ohio, J. geophys. Res., 18, 3506–3518.

King VM, Block LV, Yeck WL, Wood CK, Derouin SA. 2014. Geological structure of the Paradox Valley Region, Colorado, and relationship to seismicity induced by deep well injection. J. Geophys. Res. 119:4955– 78

Kirby, S.H., Stein, S., Okal, E., Rubie, D.C., 1996. Metastable mantle phase transformations and deep earthquakes in subducting oceanic lithosphere. Rev. Geophys.34, 261–306.

Kneller, E.A., van Keken, P.E., Karato, S.-I., Park, J., 2005. B-type olivine fabric in the mantle wedge: insights from high-resolution non-Newtonian subduction zone models. Earth Planet. Sci. Lett.429, 781–797. http://dx.doi.org/10.1016/j.epsl.2005.06.049.

Kohlstedt, D. L., B. Evans y S. J. Mackwell (1995), Strength of the lithosphere: Constraints imposed by laboratory experiments, Journal of Geophysical Research, 100, 17587-17602.

Korhonen, J.V. & Fairhead, J. & Hamoudi, M. & Hemant, K. & Lesur, V. & Mandea, Mioara & Maus, Steffany & Purucker, M. & Ravat, Dhananjay & Sazonova, T. & Erwan, Thebault & Ccgm, Cgmw. (2007). Magnetic Anomaly Map of the World 1:50M (Release: July 2007).

Koulakov I. (2009), LOTOS code for local earthquake tomographic inversion. Benchmarks for testing tomographic algorithms, Bulletin of the Seismological Society of America, 99(1), 194-214, doi: 10.1785/0120080013.

Koulakov, I., A. Jakovlev, and B. G. Luehr (2009b), Anisotropic structure beneath central Java from local earthquake tomography, Geochem. Geophys. Geosyst., 10 Q02011, doi:10.1029/2008GC002109.

Koulakov, I., and S. Sobolev (2006). Moho depth and three-dimensional P and S structure of the crust and uppermost mantle in the Eastern Mediterranean and Middle East derived from tomographic inversion of local ISC data, Geophys. J. Int. 164, no. 1 218–235.

Krüger, F., Ohrnberger, M., 2005. Tracking the rupture of the Mw ¼ 9.3 Sumatra earthquake over 1,150 km at teleseismic distance. Nature 435, 937e941.

Lambert C. 2017. Structural controls on fluid migration and seismic variability in northern Oklahoma. Master’s Thesis, Dep. Earth Atmos. Sci., Cornell Univ., Ithaca, NY

Langenbruch, C., Shapiro, S.A., 2015. Quantitative analysis of rock stress heterogeneity: Implications for the seismogenesis of fluid-injection-induced seismicity. Geophysics 80, WC73–WC88.

Langenbruch, C., Weingarten, M., Zoback, M.D., 2018. Physics-based forecasting of man-made earthquake hazards in Oklahoma and Kansas. Nature communications 9, 3946.

Langenbruch, C., Zoback, M.D., 2016. How will induced seismicity in Oklahoma respond to decreased saltwater injection rates? Science advances 2, e1601542.

Lara, M., Cardona, A., Monsalve, G., Yarce, J., Montes, C., Valencia, V López-Martínez, M. (2013). Middle Miocene near trench volcanism in northern Colombia: A record of slab tearing due to the simultaneous subduction of the Caribbean Plate under South and Central America Journal of South American Earth Sciences, 45, 24–41. https://doi.org/10.1016/j.jsames.2012.12.006

Lengliné, O., Boubacar, M. & Schmittbuhl, J., 2017. Seismicity related to the hydraulic stimulation of GRT1, Rittershoffen, France, Geophys. J. Int., 208(3), 1704–1715.

Liener, B.R., Havskov, J., 1995. A computer program for locating earthquakes locally, regionally and globally. Seismol. Res. Lett. 66, 26e36. http://dx.doi.org/10.1785/gssrl.66.5.26.

Liu E, Crampin S, Queen JH. 1991. Fracture detection using crosshole surveys and reverse vertical seismic profiles at the Conoco Borehole Test Facility, Oklahoma. Geophys. J. Int. 107:449–63

Llenos AL, Michael AJ. 2013. Modeling earthquake rate changes in Oklahoma and Arkansas: possible signatures of induced seismicity. Bull. Seismol. Soc. Am. 103:285

Lui, S.K., Huang, Y., 2019. Do injection-induced earthquakes rupture away from injection wells due to fluid pressure change? Bulletin of the Seismological Society of America 109, 358–371.

Lund, B., Slunga, R., 1999. Stress tensor inversion using detailed microearthquake information and stability constraints: application to Olfus in southwest Iceland. J. Geophys. Res. 104, 14 947e14 964.

Majer EL, Baria R, Stark M, Oates S, Bommer J, et al. 2007. Induced seismicity associated with enhanced geothermal systems. Geothermics 36:185–222

Malin, P.E., et al. (1988). Bull. Seismol. Soc. Am. 78, 401-420.

Manga M, Wang CY, Shirzaei M. 2016. Increased stream discharge after the 3 September 2016 Mw 5.8 Pawnee, Oklahoma earthquake. Geophys. Res. Lett. 43:11588–94

Maxwell, S., Zhang, F., Damjanac, B., 2015. Geomechanical modeling of induced seismicity resulting from hydraulic fracturing. The Leading Edge 34, 678–683.

Maxwell, S.C., Rutledge, J., Jones, R., & Fehler, M., 2010, Petroleum reservoir characterization using downhole microseismic monitoring, Geophysics, 75, 75A129-75A137.

McCourt, W.J., Aspden, J.A., Brook, M., 1984. New geological and geochronological data from the Colombian Andes: continental growth by multiple accretion. J. Geol. Soc. Lond. 141, 831e845.

McGarr, A. & Barbour, A.J., 2018. Injection-induced moment released can also be aseismic, Geophys. Res. Lett., 45(11)5344–5311.

McGarr, A. (1992). Pure Appl. Geophys. 139, 781-800.

McGarr, A. and D. Simpson (1997). In: "Rock bursts and Seismicity in Mines," pp. 385-396, Balkema.

McGarr, A., 1976. Seismic moments and volume changes, J. geophys. Res., 81(1):1487–1494.

McGarr, A., 2014. Maximum magnitude earthquakes induced by fluid injection, J. geophys. Res., 119, 1008–1019.

McGarr, A., Simpson, D., Seeber, L., 2002. Case histories of induced and triggered seismicity. In: Lee, W., Kanamori, H., Jennings, P., Kisslinger, C. (Eds.), International Handbook of Earthquake and Engineering Seismology Academic Press, London, pp. 647e664. Chapter 40.

McNamara, D. et al., 2015. Efforts to monitor and characterize the recent increasing seismicity in central Oklahoma, Lead. Edge, 34(6), 628–639.

Megard, F., 1987. Cordillera Andes and Marginal Andes: A Review of Andean Geology North of the Arica Elbow (18 Deg. S), in J. W. H.

Michael, A.J., 1984. Determination of stress from slip data: faults and folds. J. Geophys. Res. 89, 11 517e11 526.

Michael, A.J., 1987. Use of focal mechanisms to determine stress: a control study. J. Geophys. Res. 92 (B1), 357e368.

Mignan, A., 2016. Static behaviour of induced seismicity. Nonlinear Processes in Geophysics 23, 107–113.

Mignan, A., Broccardo, M., Wiemer, S., Giardini, D., 2017. Induced seismicity closed-form traffic light system for actuarial decision-making during deep fluid injections. Scientific reports 7, 1–10.

Mishra, O. P. & Zhao, D. P. Seismic evidence for dehydration embrittlement of the subducting Pacific slab. Geophys. Res. Lett. **31**, L09610, doi: 10.1029/2004GL019489 (2004).

Miyazawa, M., Venkataraman, A., Snieder, R., & Payne, M.A., 2008. Analysis of microearthquake data at Cold Lake and its applications to reservoir monitoring, Geophysics, 73, 015-021.

Mogi, K., 1967. Regional variation in magnitude - frequency relation of earthquake, Bull. Earthq. Res. Inst., 45, 313–325.

Molina, Indira & Velasquez, Juan & Rubinstein, Justin & Garcia, Alexander & DIONICIO, VIVIANA. (2020). Seismicity induced by massive wastewater injection near Puerto Gaitán, Colombia. Geophysical Journal International. 223. 777-791. 10.1093/gji/ggaa326.

Montes, C., Guzmán, G., Bayona, G., Cardona, A., Valencia, V., & Jaramillo, C. (2010). Clockwise rotation of the Santa Marta Massif and simultaneous Paleogene to Neogene deformation of the Plato-San Jorge and Cesar-Ranchería Basins. Journal of South American Earth Sciences, 29(4), 832–848. https://doi.org/10.1016/j.jsames.2009.07.010

Montgomery, S., 1992. Petroleum potential of upper and middle Magdalena basins, Colombia, part 2: plate tectonics, reservoirs, source rocks, and field histories. Pet. Front. 9, 67.

Mora, A., et al., 2010. The eastern foothills of the eastern cordillera of Colombia: an example of multiple factors controlling structural styles and active tectonics, Bull. Geol. Soc. Am., 122 (11–12), 1846–1864.

Mora-Bohórquez, J. A., Ibánez-Mejia, M., Oncken, O., de Freitas, M., Vélez, V., Mesa, A., & Serna, L. (2017). Structure and age of the Lower Magdalena Valley Basin basement, northern Colombia: New reflection-seismic and U-Pb-Hf insights into the termination of the central Andes against the Caribbean basin. Journal of South American Earth Sciences, 74, 1–26. https://doi.org/10.1016/j.jsames.2017.01.001

Mousavi, S.M., Beroza, G.C., Hoover, S.M., 2018. Variabilities in probabilistic seismic hazard maps for natural and induced seismicity in the central and eastern United States. The Leading Edge 37, 141a1–141a9.

Mukuhira, Y., Asanuma, H., Niitsuma, H. & Haring, M.O., 2013. Characteristics of large-magnitude microseismic events recorded during and after stimulation of a geothermal reservoir at Basel, Switzerland, Geothermics, 45, 1–17.

Nicholson, C., Roeloffs, E., Wesson, R.L., 1992. Triggered earthquakes and deep well activities. Pure Appl. Geophys. 139, 561e578.

Novakovic, M., Atkinson, G.M., Assatourians, K., 2018. Empirically calibrated ground-motion prediction equation for Oklahoma. Bulletin of the Seismological Society of America 108, 2444– 2461.

Ojeda, A., & Havskov, J. (2001). Crustal structure and local seismicity in Colombia. Journal of Seismology, 5(4), 575–593. https://doi.org/10.1023/A:1012053206408

Pardo, A., Barrero, D., Vargas, C.A., Martínez, J., 2007. Sedimentary Basins of Colombia: Geological Framework. Colombian Sedimentary Basins: Nomenclature, Boundaries and Petroleum Geology, a New Proposal. Agencia Nacional de Hidrocarburos ANH.

Pardo-Casas, F., Molnar, P., 1987. Relative motion of the Nazca (Farallon) and South American plates since Late Cretaceous time. Tectonics 6, 233e248.

Pennington, W. D. (1981), Subduction of the eastern Panama basin and seismotectonics of northwestern South America, J. Geophys. Res., 86(B11), 10753-10770, doi: 10.1029/JB086iB11p10753.

Petersen, M.D., Mueller, C.S., Moschetti, M.P., Hoover, S.M., Llenos, A.L., Ellsworth, W.L., Michael, A.J., Rubinstein, J.L., McGarr, A.F., Rukstales, K.S., 2016. Seismic-hazard forecast for 2016 including induced and natural earthquakes in the central and eastern United States. Seismological Research Letters 87, 1327–1341.

Petersen, M.D., Mueller, C.S., Moschetti, M.P., Hoover, S.M., Rubinstein, J.L., Llenos, A.L., Michael, A.J., Ellsworth, W.L., McGarr, A.F., Holland, A.A., et al., 2015.

Incorporating induced seismicity in the 2014 United States National Seismic Hazard Model: Results of 2014 workshop and sensitivity studies.

Petersen, M.D., Mueller, C.S., Moschetti, M.P., Hoover, S.M., Shumway, A.M., McNamara, D.E., Rennolet, S.B., Moschetti, M.P., Thompson, E.M., Yeck, W.L., 2018. A flatfile of ground motion intensity measurements from induced earthquakes in Oklahoma and Kansas. Earthquake Spectra 34, 1–20.

Pilger Jr., R.H., 1984. Cenozoic plate kinematics subduction and magmatism: south American Andes. J. Geol. Soc. Lond. 141, 793e802.

Porritt, R. W., T. W. Becker, and G. Monsalve (2014), Seismic anisotropy and slab dynamics from SKS splitting recorded in Colombia, Geophys. Res. Lett., 41, 8775-8783, doi: 10.1002/2014GL061958.

Poveda, E., Julià, J., Schimmel, M., & Perez-Garcia, N. (2018). Upper and middle crustal velocity structure of the Colombian Andes from ambient noise tomography: Investigating subduction related magmatism in the overriding plate. Journal of Geophysical Research: Solid Earth, 123, 1459–1485. https://doi.org/10.1002/2017JB014688

Poveda, E., Monsalve, G., & Vargas, C. A. (2015). Receiver functions and crustal structure of the northwestern Andean region, Colombia. Journal of Geophysical Research: Solid Earth, 120, 2408–2425. https://doi.org/10.1002/2014JB011304

Prieto, G.A., Beroza, G.C., Barrett, S.A., López, G.A., Florez, M., 2012. Earthquake nests as natural laboratories for the study of intermediate-depth earth-quake mechanics. Tectonophysics 570–571, 42–56. http://dx.doi.org/10.1016/j.tecto.2012.07.019.

Raleigh CB, Healy JH, Bredehoeft JD. 1976. An experiment in earthquake control at Rangely, Colorado. Science 191:1230–37

Rubinstein JL, Ellsworth WL, McGarr A, Benz HM. 2014. The 2001–present induced earthquake sequence in the Raton basin of northern New Mexico and southern Colorado. Bull. Seismol. Soc. Am. 104:2162–81

Rubinstein, J.L. & Babaie Mahani, A., 2015. Myths and Facts on Wastewater Injection, Hydraulic Fracturing, Enhaced Oil Recovery, and Induced Seismicity, Seismol. Res. Lett., 86, 1060–1067, 10.1785/0220150067.

Rubinstein, J.L., Ellsworth, W.L., Dougherty, S.L., 2018. The 2013–2016 Induced Earthquakes in Harper and Sumner Counties, Southern Kansas. Bulletin of the Seismological Society of America 108, 674–689.

Rubinstein, J.L., Ellsworth, W.L., McGarr, A., Benz, H.M., 2014. The 2001–present induced earthquake sequence in the Raton Basin of northern New Mexico and southern Colorado. Bulletin of the Seismological Society of America 104, 2162–2181.

Rutledge, J.T. & Phillips, W.S., 2003. Hydraulic stimulation of natural fractures as revealed by induced microearthquakes, Carthage Cotton Valley gas field, east Texas, Geophysics, 68, 441-452.

Saffer DM, Tobin HJ. 2011. Hydrogeology and mechanics of subduction zone forearcs: fluid flow and pore pressure. Annu. Rev. Earth Planet. Sci. 39:157–86

Salazar, J. M., and C. A. Vargas (2015). Fractal dimension and seismotectonic deformation rates along an inter-plate setting: Seismic regime along the Caribbean plate boundary zone, in Petroleum Geology and Potential of the Colombian Caribbean Margin, C. Bartolini and P. Mann (Editors), AAPG Memoir 108, Chapt. 11, 271–294, ISBN13: 978-0-89181-388-0.

Sanchez, J., & Mann, P. (2015). Integrated structural and basinal analysis of the Cesar-Rancheria Basin, Colombia: Implications for its tectonic history and petroleum systems. In C. Bartolini & P. Mann (Eds.), Petroleum geology and potential of the Colombian Caribbean Margin, AAPG Memoir (Vol. 108, pp. 431–470). Tulsa, OK: American Association of Petroleum Geologists. https://doi.org/10.1306/13531945M1083648

Sarkar, S., 2008. Reservoir monitoring using induced seismicity at a petroleum field in Oman: PhD thesis, Massachusetts Institute of Technology, Cambridge, Massachusetts, US.

Savage HM, Keranen KM, Schaff D, Dieck C. 2017a. Possible precursory signals in damage zone foreshocks. Geophys. Res. Lett. 44:5411–17

Savvaidis, A., Lomax, A., Breton, C., 2020. Induced Seismicity in the Delaware Basin, West Texas, is Caused by Hydraulic Fracturing and Wastewater Disposal. Bulletin of the Seismological Society of America 110, 2225–2241.

Scanlon, B.R., Weingarten, M.B., Murray, K.E., Reedy, R.C., 2019. Managing basin-scale fluid budgets to reduce injection-induced seismicity from the recent US shale oil revolution. Seismological Research Letters 90, 171–182.

Schoenball, M., Ellsworth, W.L., 2017. A systematic assessment of the spatiotemporal evolution of fault activation through induced seismicity in Oklahoma and southern Kansas. Journal of Geophysical Research: Solid Earth 122, 10–189.

Schultz, R., Atkinson, G., Eaton, D.W., Gu, Y.J. & Kao, H., 2018. Hydraulic fracturing volume is associated with induced earthquake productivity in the Duvernay play, Science, 359(6373), 304–308.

Schultz, R., Beroza, G., Ellsworth, W., Baker, J., 2020. Risk-Informed Recommendations for Managing Hydraulic Fracturing–Induced Seismicity via Traffic Light Protocols. Bulletin of the Seismological Society of America 110, 2411–2422.

Schultz, R., Quitoriano, V., Wald, D.J., Beroza, G.C., 2021. Quantifying nuisance ground motion thresholds for induced earthquakes. Earthquake Spectra, 8755293020988025.

Sella, G., Dixon, T.H., Mao, A., 2002. REVEL: a model of recent plate velocities from space geodesy. J. Geophys. Res.107 (B4). http://dx.doi.org/10.1029/2000JB000033. 2081.

Shapiro, S.A., Dinske, C., Langenbruch, C. & Wenzel, F., 2010. Seismogenic index and magnitude probability of earthquakes induced during reservoir fluid stimulations, Leading Edge, 29(3), 304–309.

Shapiro, S.A., Huenges, E. & Borm, G., 1997. Estimating the crust permeability from fluid-injection-induced seismic emission at the KTB site, Geophys. J. Int., 131(2), F15–F18.

Shapiro, S.A., Rothert, E., Rath, V. & Rindschwentner, J., 2002. Characterization of fluid transport properties of reservoirs using induced microseismicity, Geophysics, 67, 212–220.

Shelly DR, Moran SC, Thelen WA. 2013. Evidence for fluid-triggered slip in the 2009 Mount Rainier, Washington earthquake swarm. Geophys. Res. Lett. 40:1506–12

Sibson RH. 2000. Fluid involvement in normal faulting. J. Geodyn. 29:469–99

Skoumal RJ, Brudzinski MR, Currie BS. 2015a. Distinguishing induced seismicity from natural seismicity in Ohio: demonstrating the utility of waveform template matching. J. Geophys. Res. 120:6284–96

Skoumal RJ, Brudzinski MR, Currie BS. 2015b. Earthquakes induced by hydraulic fracturing in Poland Township, Ohio. Bull. Seismol. Soc. Am. 105:189–97

Skoumal RJ, Brudzinski MR, Currie BS. 2016. An efficient repeating signal detector to investigate earthquake swarms. J. Geophys. Res. 121:5880–97

Skoumal, R.J., Barbour, A.J., Brudzinski, M.R., Langenkamp, T., Kaven, J.O., 2020. Induced seismicity in the Delaware Basin, Texas. Journal of Geophysical Research: Solid Earth 125, e2019JB018558.

Smalley PC, Muggeridge AH. 2010. Reservoir compartmentalization: Get it before it gets you. Geol. Soc. Lond. Spec. Publ. 347:25–41

Snee, J.E.L., Zoback, M.D., 2018. State of stress in the Permian Basin, Texas and New Mexico: Implications for induced seismicity. The Leading Edge 37, 127–134.

Sokos, E.N., Zahradnik, J., August 2008. ISOLA a Fortran code and a MATLAB GUI to perform multiple-point source inversion of seismic data. Comp. Geosci 34 (8), 967e977. http://dx.doi.org/10.1016/j.cageo.2007.07.005. ISSN 0098-3004.

Spottiswoode, S.M. and A. McGarr (1975). Bull. Seismol. Soc. Am. 65, 93-112.

Suckale, J., 2010. Induced seismicity in hydrocarbon fields, Chapter 2 in advances in Geophysics, 51.

Sumy DF, Cochran ES, Keranen KM, Wei M, Abers GA. 2014. Observations of static Coulomb stress triggering of the November 2011 M5.7 Oklahoma earthquake sequence. J. Geophys. Res. 119:1904–23

Sumy DF, Neighbors CJ, Cochran ES, Keranen KM. 2017. Low stress drops observed for aftershocks of the 2011 Mw 5.7 Prague, Oklahoma, earthquake. J. Geophys. Res. 122:3813–34

Syracuse, E. M., Maceira, M., Prieto, G. A., Zhang, H., & Ammon, C. J. (2016). Multiple plates subducting beneath Colombia, as illuminated by seismicity and velocity from the joint inversion of seismic and gravity data. Earth and Planetary Science Letters, 444, 139–149. https://doi.org/10.1016/j.epsl.2016.03.050

Taboada, A., L.A. Rivera, A. Fuenzalida, A. Cisternas, H. Philip, H. Bijwaard, J. Olaya, and C. Rivera, 2000. Geodynamics of the northern Andes: Subductions and intracontinental deformation (Colombia). Tectonics. v.19, no. 5, p. 787-813.

Takei, Y., 2002. Effect of pore geometry on VP/VS: from equilibrium geometry to crack. J. Geophys. Res.107 (B2), 2043. http://dx.doi.org/10.1029/2001JB000522.

Townend J, Zoback MD. 2000. How faulting keeps the crust strong. Geology 28:399–402

Trenkamp, R., J. Kellogg, J. Freymueller and H. Mora, (2002). Wide plate margin, southern Central America and northwestern South America, CASA GPS observations, Journal of South American Earth Sciences 15, 157-171, Elsevier.

Trugman, D.T., Savvaidis, A., 2021. Source Spectral Properties of Earthquakes in the Delaware Basin of West Texas. Seismological Research Letters

Tsapanos, T., 1990. b-Value of two tectonic parts in the circum-Pacific belt, Pure appl. Geophys, 143, 229–242, doi: 10.1007/BF00876999.

van der Elst NJ, Savage HM, Keranen KM, Abers GA. 2013. Enhanced remote earthquake triggering at fluid-injection sites in the midwestern United States. Science 341:164–67

van der Elst, N.J., Page, M.T., Weiser, D.A., Goebel, T.H.W. & Hosseini, S.M., 2016. Induced earthquake magnitudes are as large as (statistically) expected, J. geophys. Res., 121, 4575–4590.

van der Hilst, R., Mann, P., 1994. Tectonic implications of tomographic images of subducted lithosphere beneath northwestern South America. Geology22, 451–454.

van der Sluis, A., and H. A. van der Vorst (1987). Numerical solution of large, sparse linear algebraic systems arising from tomographic problems, in Seismic Tomography, G. Nolet (Editor), Reidel, Dordrecht, 49–83.

van Elk, J., Doornhof, D., Bommer, J.J., Bourne, S.J., Oates, S.J., Pinho, R., Crowley, H., 2017. Hazard and risk assessments for induced seismicity in Groningen. Netherlands Journal of Geosciences 96, s259–s269

van Thienen-Visser, K., Breunese, J., 2015. Induced seismicity of the Groningen gas field: History and recent developments. The Leading Edge 34, 664–671.

Vargas, C.A. & Mann, P., 2013. Tearing and breaking off of subducted slabs as the result of collision of the Panama arc-indenter with northwestern South America Bull, Seismol. Soc. Am., 103(3) 2025–2046.

Vavrycuk, V., 2014. Seismology iterative joint inversion for stress and fault orientations from focal mechanisms. GJI Geophys. J. Int. 199, 69e77 (Praha, Czech Republic).

Verdon, J.P., Bommer, J.J., 2020. Green, yellow, red, or out of the blue? An assessment of Traffic Light Schemes to mitigate the impact of hydraulic fracturing-induced seismicity. Journal of Seismology, 1–26.

Walker, K., Shearer, P., 2009. Illuminating the near-sonic rupture velocities of the intracontinental Kokoxili Mw 7.8 and Denali fault Mw 7.9 strike-slip earthquakes with global P wave back projection imaging. J. Geophys. Res. 114.

Walsh, F.R., Zoback, M.D., 2015. Oklahoma's recent earthquakes and saltwater disposal. Science advances 1, e1500195.

Walters, R.J., Zoback, M.D., Baker, J.W., Beroza, G.C., 2015. Characterizing and responding to seismic risk associated with earthquakes potentially triggered by fluid disposal and hydraulic fracturing. Seismological Research Letters 86, 1110–1118.

Wang, R., Gu, Y.J., Schultz, R., Chen, Y., 2018. Faults and non-double-couple components for induced earthquakes. Geophysical Research Letters 45, 8966–8975.

Wang, Z., Carpenter, N.S., Zhang, L., Woolery, E.W., 2017. Assessing potential ground-motion hazards from induced earthquakes. Natural Hazards Review 18, 04017018

Weatherley DK, Henley RW. 2013. Flash vaporization during earthquakes evidenced by gold deposits. Nat. Geosci. 6:294

Wech, A., Kenneth, W., Creager, C., Houston, H. & Vidale, J., 2010. An earthquake like magnitude–frequency distribution of slow slip in Northern Cascadia, Geophys. Res. Lett., 37, L22310, doi:10.1029/2010GL044881.

Weingarten M, Ge S, Godt JW, Bekins BA, Rubinstein JL. 2015. High-rate injection is associated with the increase in US mid-continent seismicity. Science 348:1336–40

Wesnousky, S.G., 1999. Crustal deformation processes and the stability of the Gutenberg-Richter relationship. Bull. seism. Soc. Am., 89 (4),1131–1137.

White, J.A. & Foxall, W., 2016. Assessing induced seismicity risk at CO2 storage projects: recent progress and remaining challenges, Int. J. Greenhouse Gas Control, 49, 413–424.

Wibberley CA, Gonzalez-Dunia J, Billon O. 2017. Faults as barriers or channels to production-related flow: insights from case studies. Pet. Geosci. 23:134–47

Wiemer, S. & Wyss, M., 2000. Minimum magnitude of complete reporting in earthquake catalogs: examples from Alaska, the Western United States, and Japan, Bull. Seism. Soc. Am., 90, 859–869.

Wu, Q., Chapman, M., Chen, X., 2018. Stress-Drop Variations of Induced Earthquakes in Oklahoma Stress-Drop Variations of Induced Earthquakes in Oklahoma. Bulletin of the Seismological Society of America 108, 1107–1123.

Yeck WL, Weingarten M, Benz HM, McNamara DE, Bergman EA, et al. 2016. Far-field pressurization likely caused one of the largest injections induced earthquakes by reactivating a large preexisting basement fault structure. Geophys. Res. Lett. 43:10198–207

Yoris, F., Lugo, J., 2009. Características de la trampa estratigráfica de Carbonera basal en el Sureste de Llanos Orientales. In: X Simposio Bolivariano Exploración Petrolera en Cuencas Subandinas, Cartagena, Colombia, Julio, 2009.

Zakharova NV, Goldberg DS. 2014. In situ stress analysis in the northern Newark Basin: implications for induced seismicity from CO2 injection. J. Geophys. Res. 119:2362–74

Zang, A., Oye, V., Jousset, P., Deichmann, N., Gritto, R., McGarr, A., Majer, E. & Bruhn, D., 2014. Analysis of induced seismicity in geothermal reservoirs—an overview, Geothermics, 52, 6–21.

Zang, A., Yoon, J.S., Stephansson, O. & Heidbach, O., 2013. Fatigue hydraulic fracturing by cyclic reservoir treatment enhances permeability and reduces induced seismicity, Geophys. J. Int., 195(2), 1282–1287.

Zarifi, Z., J. Havskov, and A. Hanyga (2007), An insight into the Bucaramanga nest, Tectonophysics, 443, 93–105.

Zhang Y, Person M, Rupp J, Ellett K, Celia MA, et al. 2013. Hydrogeologic controls on induced seismicity in crystalline basement rocks due to fluid injection into basal reservoirs. Groundwater 51:525–38

Zhang, Z., Schwartz, S., 1994. Seismic anisotropy in the shallow crust of the Loma Prieta segment of the San Andreas fault system. Journal of Geophysical Research 99, 9651–9661.

Zoback, M.D. and J.H. Healy (1984). Ann. Geophys. 2, 689-698.